SUPERCRITICAL FLUIDS, OSCILLATORY FLOW, AND PARTIALLY SATURATED POROUS MEDIA BY MAGNETIC RESONANCE MICROSCOPY

by

Erik Michael Rassi

A dissertation submitted in partial fulfillment
of the requirements for the degree

of

Doctor of Philosophy

in

Engineering

MONTANA STATE UNIVERSITY
Bozeman, Montana

November 2011

©COPYRIGHT

by

Erik Michael Rassi

2011

All Rights Reserved

APPROVAL

of a dissertation submitted by

Erik Michael Rassi

This dissertation has been read by each member of the dissertation committee and has been found to be satisfactory regarding content, English usage, format, citation, bibliographic style, and consistency and is ready for submission to The Graduate School.

Dr. Sarah L. Codd

Approved for the Department of Mechanical and Industrial Engineering

Dr. Christopher H. M. Jenkins

Approved for The Graduate School

Dr. Carl A. Fox

STATEMENT OF PERMISSION TO USE

In presenting this dissertation in partial fulfillment of the requirements for a doctoral degree at Montana State University, I agree that the Library shall make it available to borrowers under rules of the Library. I further agree that copying of this dissertation is allowable only for scholarly purposes, consistent with "fair use" as prescribed in the U.S. Copyright Law. Requests for extensive copying or reproduction of this dissertation should be referred to ProQuest Information and Learning, 300 North Zeeb Road, Ann Arbor, Michigan 48106, to whom I have granted "the exclusive right to reproduce and distribute my dissertation in and from microform along with the non-exclusive right to reproduce and distribute my abstract in any format in whole or in part."

Erik Michael Rassi

November 2011

ACKNOWLEDGEMENTS

The motivation behind this work is no different than that for many who have come before; a desire to understand the world in which we were created and to enjoy life that God has decreed. To my wife, I give you thanks for your unending patience and love. To my children and family, I thank you for the support. To my country, I thank those who have come before and allowed this opportunity and to my university, I extend this thanks. To Sarah L. Codd and Joseph D. Seymour, thank you for your time, patience, and wisdom. I am also appreciative to the U.S. National Science Foundation award NSF CAREER CBET-0642328 for financial support provided to Dr. Sarah L. Codd.

TABLE OF CONTENTS

1. INTRODUCTION 1

Critical and Supercritical Fluids 1
Partially Saturated Porous Media 4
Oscillatory Flow 5

2. BACKGROUND-NMR AND MRI 9

Larmor Frequency and Net Magnetization 9
Energy, Spin States, and the Rotating Frame 11
Excitation and Relaxation 13
Spectral Density and Correlation Time 18
Inversion Recovery and Measurement of T_1 relaxation 21
k-space Spatial Resolution, Signal, 1D and 2D Imaging, Slice Selection 23

3. TRANSLATIONAL DYNAMICS IN NMR 30

Propagators 30
Pulsed Field Gradient NMR 32
PGSE NMR 33
PGSTE NMR 35
Correlation Functions 37
Echo Signal of Narrow-Pulse Self-Diffusion and Flow 39
Resolution of ***q***-space and Comparison to ***k***-space 40
Restricted Diffusion 42
Partially Connected Structures 47
Susceptibility Inhomogeneities 51
Velocity Maps 53

4. FLUID DYNAMICS IN COMPLEX SYSTEMS 55

Introduction to Critical and Supercritical Fluids 55
Equations and Modeling of Critical Fluids 57
Partially Saturated Porous Media Theory 63
Oscillatory Flow Phenomena in Simple and Complex Fluids 66

5. MR VELOCITY MAPS AND PROPAGATORS OF A SUB, CRITICAL, AND SUPERCRITICAL FLUORINATED GAS, C_2F_6, IN A CAPILLARY 69

Methods 69
Results 71
Discussion 90

TABLE OF CONTENTS- CONTINUED

Conclusions....100

6. MR VELOCITY MAPS AND PROPAGATORS OF A SUB, CRITICAL, AND SUPERCRITICAL FLUORINATED GAS, C_2F_6, IN A POROUS MEDIA....101

Introduction....101
Methods....103
Results....107
No Flow Results....107
Flow Results....117
Conclusions....124

7. MR CHARACTERIZATION OF THE STATIONARY DYNAMICS OF PARTIALLY SATURATED MEDIA DURING STEADY STATE INFILTRATION FLOW....126

Introduction....126
Methods....128
Results and Discussion....132
Conclusion....141
Acknowledgements....141

8. OSCILLATORY FLOW PHENOMENA IN SIMPLE AND COMPLEX FLUIDS....142

Introduction....142
Methods....143
Oscillatory apparatus....143
MRI Experiments....144
Trigger....145
Fluids and Flow Frequencies....145
Setup....146
Results and Discussion....147
Conclusions....154

9. FUTURE WORK....155

Introduction....155
Methods....156
Preliminary Results and Discussion....157

TABLE OF CONTENTS- CONTINUED

Conclusion 159

REFERENCES CITED.....160

APPENDICES 176

APPENDIX A: MR Propagators of a Near Critical Gas, Critical Fluid, And Supercritical Fluorinated Fluid, C_2F_6, in a Dead End Sample Holder 177

APPENDIX B: Signal Processing and Data Analysis Notes.....191

LIST OF TABLES

Table Page

2.1 Gyromagnetic ratios for some common isotopes....10

5.1 Fluids considered for supercritical study....70

5.2 *Re* numbers for various pressures and temperatures of flowing C_2F_6....78

5.3 *Gr* and *Ri* numbers for flowing C_2F_6 at T_s = 25 ^oC and T_{fluid} = 21 ^oC....78

7.1 Experimental flow rate and NMR experiments run at each flow rate....130

8.1 MRI experimental parameters for oscillatory flow....144

8.2 Fluid properties for the four fluids and experimental parameters at each of the frequencies tested....149

LIST OF FIGURES

Figure Page

2.1 Water molecules in the absence and presence of a magnetic field $\boldsymbol{B}_o$ 10

2.2 Two energy states for spin ½ 12

2.3 Affect of a 90^o RF Pulse on the magnetization $\boldsymbol{M}$ 14

2.4 Two spins interacting by method of translational motion. 18

2.5 Spectral density plot as a function of frequency for increasing temperature. 19

2.6 T_1 and T_2 relaxation as a function of 1/Temperature. 21

2.7 Inversion Recovery Pulse Sequence 21

2.8 Longitudinal magnetization for an inversion recovery pulse sequence. 22

2.9 A gradient's effect on the magnetic field strength $\boldsymbol{B}_o$ 23

2.10 H_20 inside a coil with a gradient applied in one dimension. 24

2.11 Voxels discretized through the sample and signal intensity 25

2.12 N^2 steps for a $\boldsymbol{k}$-space image without a read gradient 27

2.13 N steps for a $\boldsymbol{k}$-space image with a read gradient 28

2.14 Image slice showing thickness and resolution 29

3.1 Displacement of a single particle 30

3.2 Propagator for Brownian motion 32

3.3 PGSE sequence 33

3.4 Condition of spins in PGSE sequence at times a-g in Figure 3.3 34

3.5 The pulsed gradient stimulated echo sequence 36

LIST OF FIGURES- CONTINUED

Figure Page

3.6 Particle representation of a motional correlation function.....37

3.7 Particle representation of a motional self-correlation function.....37

3.8 Long time limit restricted diffusion in a square box of dimension a 42

3.9 Spin density as a function of the *z* coordinate.....42

3.10 Average propagator for a square box as a function of $\boldsymbol{Z}$.....43

3.11 Connected network of square boxes aligned with the *z*-direction 45

3.12 The convoluted functions that represent the box connected network.....46

3.13 Signal from the connected box network 47

3.14 Partially connected pore network.....48

3.15 Diffusion coefficient in a porous media.....49

3.16 Echo signal from the connected box network.....51

3.17 Diffusion of 2 molecules to show low and high $\boldsymbol{q}$ encoding.....51

5.1 Pressure vs. Density Diagram for C_2F_6.....69

5.2 Supercritical flow loop schematic.....71

5.3 Diffusion coefficient as a function of pressure for C_2F_6.....72

5.4 Velocity maps of C_2F_6 for upward flow against gravity 73

5.5 Velocity maps of C_2F_6 for downward flow with gravity 74

5.6 Velocity profiles of C_2F_6 below, near, and above the critical pressure.....74

5.7 Velocity profiles of C_2F_6 at T_f = 21 ^oC for various pressures 75

LIST OF FIGURES- CONTINUED

Figure Page

5.8 Velocity profiles of C_2F_6 at T_f = 21 ^oC for various temperatures.....76

5.9 Velocity profiles for upward flow of C_2F_6 near the critical point.....77

5.10 Velocity map and density map of two-phase C_2F_6 79

5.11 Upward flow propagators and velocity maps of C_2F_6 at P = 25 bar.....81

5.12 Upward flow propagators and velocity maps of C_2F_6 at P = 29 bar.....82

5.13 Upward flow propagators and velocity maps of C_2F_6 at P = 45 bar.....83

5.14 Upward flow propagators as a function of pressure 83

5.15 Velocity maps showing the time to steady state flow near the critical point.....84

5.16 Propagators showing the time to steady state flow near the critical point.....85

5.17 Propagators and Velocity maps during a temperature shift.....85

5.18 25 bar dPGSE signal attenuation plots of C_2F_6.....86

5.19 29 bar dPGSE signal attenuation plots of C_2F_6.....87

5.20 45 bar dPGSE signal attenuation plots of C_2F_6.....87

5.21 Diffusion and dispersion coefficients of C_2F_6 88

5.22 T_1-T_2 plots of C_2F_6 89

5.23 T_2-T_2 plots at of C_2F_6 25 bar 89

5.24 T_2-T_2 plots at of C_2F_6 29 bar 90

6.1 Velocity map pulse sequence using a stimulated echo 105

6.2 Single pulsed gradient stimulated echo pulse sequence 106

LIST OF FIGURES- CONTINUED

Figure Page

6.3 Double pulsed gradient stimulated echo pulse sequence 106

6.4 Pulse sequence for MRI density maps 107

6.5 No flow sPGSE propagators of C_2F_6 in 55 µm beads.....108

6.6 No flow sPGSE and dPGSE propagators of C_2F_6 in 230 µm beads at 25 bar 110

6.7 Superposition of two Gaussian Curves 110

6.8 No flow sPGSE and dPGSE propagators of C_2F_6 in 230 µm beads at 29 bar 111

6.9 No flow sPGSE and dPGSE propagators of C_2F_6 in 230 µm beads at 45 bar 111

6.10 No flow Stejskal-Tanner plots of C_2F_6 in 230 µm beads at 25 bar.....112

6.11 No flow Stejskal-Tanner plots of C_2F_6 in 230 µm beads at 29 bar.....113

6.12 No flow Stejskal-Tanner plots of C_2F_6 in 230 µm beads at 45 bar.....113

6.13 No flow *q*-space plots of C_2F_6 in 230 µm beads at 25 bar.....114

6.14 No flow *q*-space plots of C_2F_6 in 230 µm beads at 29 bar.....114

6.15 No flow *q*-space plots of C_2F_6 in 230 µm beads at 45 bar.....115

6.16 MR images of C_2F_6 in 230 µm beads 116

6.17 MR image of C_2F_6 in 550 µm beads 116

6.18 Non-flowing velocity maps of C_2F_6 at various pressures 117

6.19 Velocity maps of C_2F_6 at 45 bar in 55 µm beads.....118

6.20 Velocity maps of C_2F_6 in 55 µm beads as a function of temperature 118

6.21 Propagators of C_2F_6 in 55 µm beads as a function of pressure.....119

6.22 Propagators showing the time to steady state flow in porous media 121

LIST OF FIGURES- CONTINUED

Figure Page

6.23 Stejskal-Tanner plots of C_2F_6 in 55 μm beads as a function of pressure.....122

6.24 *q*-space plots of flowing C_2F_6 in 55 μm beads at 25 bar.....123

6.25 *q*-space plots of flowing C_2F_6 in 55 μm beads at 29 bar.....123

6.26 *q*-space plots of flowing C_2F_6 in 55 μm beads at 45 bar.....124

7.1 Pulse sequences used for partially saturated porous media 131

7.2 MR image density maps for a 1.5 mm slice.....133

7.3 Total FID normalized area vs. flow rate 135

7.4 Velocity maps from a 10 mm slice 137

7.5 Average steady-state pressure drop vs. Capillary number.....138

7.6 Displacement propagators for the fully or partially saturated states.....138

7.7 Displacement propagators comparing before and after max flow 140

8.1 Apparatus used to create an oscillatory flow 143

8.2 Experimental setup of the oscillatory flow loop 146

8.3 Average velocity data for the four rotation rates 148

8.4 Velocity map with the corresponding velocity profile 148

8.5 Comparison of velocity profiles for several fluids 151

8.6 Normalized velocity of the four fluids with α close to three.....152

8.7 Velocity profiles collected at eight points in the oscillation cycle 153

9.1 Image of Supercritical CO_2 in 230 μm beads at 80 bar 157

LIST OF FIGURES- CONTINUED

Figure Page

9.2 sPGSE and dPGSE propagators of CO_2 at 80 bar 100 ^{o}C 158

ABSTRACT

The research presented in this dissertation used Magnetic Resonance (MR) techniques to study fluid dynamics in complex systems. The systems investigated were critical and supercritical fluids, partially saturated porous media, and oscillatory flow. Supercritical fluids (SCF) are useful solvents in green chemistry and oil recovery and are of great current interest in the context of carbon sequestration. Flow in partially saturated porous media and the resultant hydrodynamics are important in fields including but not limited to hydrology, chemical, medical, and the petroleum industry. Lastly, Pulsatile and oscillatory flows are prevalent in many biological, industrial, and natural systems.

Displacement propagators were measured at various displacement observation times to quantify the time evolution of dynamics in critical and supercritical fluid flow. In capillary flow, the critical phase transition fluid C_2F_6 showed increased compressibility compared to the near critical gas and supercritical fluid. These flows exhibit large variations in buoyancy arising from large changes in density due to very small changes in temperature.

Ensemble averaged MR measurements were taken to observe the effects on a bead pack partially saturated with air under flowing conditions of water. Air was injected into the bead pack as water flowed simultaneously through the sample. The initial partially saturated state was characterized with MR imaging density maps, free induction decay (FID) experiments, propagators, and velocity maps before the water flow rate was increased. After the maximum flow rate, the MR imaging density maps, FID experiments, propagators, and velocity maps were repeated and compared to the data taken before the maximum flow rate. The work performed here showed that a partially saturated single phase flow had global flow dynamics that returned to characteristic flow statistics once a steady state high flow rate was reached.

A system was constructed to provide a controllable and predictable oscillatory flow in order to gain a better understanding of the impact of oscillatory flow on Newtonian and non-Newtonian fluids, specifically water, xanthan gum (XG), polyacrylamide (PAM) colloidal suspensions. The oscillatory flow system coupled with MR measured the velocity distributions and dynamics of the fluid undergoing oscillatory flow at specific points in the oscillation cycle.

INTRODUCTION

The work presented in this dissertation used magnetic resonance (MR) techniques to characterize the dynamics of fluids in complex systems. The systems explored in this work were critical and supercritical fluids in capillaries and porous media under flow and no flow conditions, partially saturated porous media, and oscillatory flow of simple and complex fluids. The mechanical design and experimental set up is discussed for these complex systems as well as the results obtained from free induction decays (FID), velocity maps, and propagators and the theory of these MR methods used is presented.

Critical and Supercritical Fluid

For the critical and supercritical work, MR techniques [1-4] were used to obtain velocity maps and propagators over a range of pressures and temperatures and MR displacement observation times for flow in either a capillary or a porous media bead pack. Hexafluoroethane, C_2F_6, was chosen for these studies due to its favorable combination of critical temperature $T_c = 19.88\ ^oC$, critical pressure $P_c = 30.48$ bar and MR relaxation times in the pressure range of 10 – 75 bar ($T_1 \sim 80 – 1240$ ms, $T_2 \sim 80 – 1020$ ms) as well as the high natural abundance and strong MR signal for ^{19}F [5-8]. Observations were first made on stationary fluid, then flow characteristics of the supercritical C_2F_6 were studied by obtaining velocity maps, propagators and diffusion coefficients using MR techniques.

Hexafluoroethane, C_2F_6, was pumped through a system specifically designed for high pressure (> 10 bar) driven volumetric flow control within a MR magnet. From the supply tank, the gas was pumped at a range of pressures from the gas phase at 10 bar to SCF at 45 bar using an Isco 500D syringe pump. The Isco 500D provided a constant volumetric flow rate between .001 – 204 mL/min. C_2F_6 flowed through the MR system at a flow rate of 0.5mL/min through PEEK tubing of 1.524 mm and stainless steel tubing outside of the MR equipment. The flow rates for all data presented correspond to Reynolds numbers $\boldsymbol{Re} = \frac{\boldsymbol{\rho \langle v \rangle D_{tube}}}{\boldsymbol{\mu}}$ of 50 - 200. Back pressure for the flow system was maintained by a Thar back pressure regulator APBR-20-1. The porous media bead pack was constructed from d_p = 55 μm ± 8.8 μm diameter copolymer microspheres (Thermo Scientific, 7550A) at porosity $\phi \sim 0.44$ corresponding to a pore length scale $l_p = \frac{\phi d_p}{(1-\phi)} = 43.2$ μm. The packed bed length was 200 mm in PEEK 1.524 mm ID tubing (corresponding to about 28 bead diameters). No flow conditions were also tested in this bead pack to compare the results of the flowing data. Tests on a stationary fluid were also performed in a bead pack of 230 μm Zirconium Silicate Microspheres (Corpuscular) in a sample holder with an ID of 5mm. This sample holder was not designed for flow through experiments as it only had one entrance port. Various pressure transducers and thermocouples monitored the pressure and temperatures throughout the systems. MR data was collected using a 5 or 25 mm RF birdcage coil, an AVANCE III 300 MHz Spectrometer, and a Bruker Micro 2.5 three dimensional gradient probe capable of 1.48 T/m. The temperature of the air surrounding the capillary tube T_{surr} was controlled by the

gradient cooling water and the fluid temperature T_{fluid} was controlled at the gas storage cylinder and temperatures were monitored by thermocouples.

In capillary flow, the critical phase transition fluid C_2F_6 showed increased compressibility compared to the near critical gas and supercritical fluid. The dynamics of the fluids demonstrated tunable properties near the critical point. The velocity profile of the near critical fluid was "M" shaped due to the extreme sensitivity of density to very low amounts of heat transfer, but the velocity profiles below or above the critical point were Poiseuille as expected for normal fluids.

In summary, MR Velocity maps and propagators of supercritical flow in capillaries and porous media have been measured for the first time. Hexafluoroethane was the fluid chosen due to its below room temperature critical temperature, its critical pressure, and the strong signal of ^{19}F. The flow loop has been designed to accurately control the pressure and flow rate of the fluid both of which can alter the properties and intensity of the MR signal. Non-invasive MR has been demonstrated as a useful method in revealing the flow dynamics of fluids in the supercritical region. Experimental velocity data of buoyancy effects in near critical fluids is presented here and has been previously lacking in the literature. Supercritical C_2F_6 was shown to be very sensitive to a small temperature gradient caused by a slightly warmer tube wall ($< 1\ ^{o}C$). This sensitivity caused the fluid near the walls to flow faster than that in the center of the tube causing an "M" shape profile demonstrating control of hydrodynamics via thermodynamics. Flow of supercritical fluid in a homogenous porous media has been

shown to be inconsistent with hydrodynamic dispersion models for normal fluids in porous media.

Partially Saturated Porous Media

For the partially saturated porous media, a 50 mm long porous media was constructed from 100 μm borosilicate glass beads in a 10 mm ID diameter glass tube. The beads were wet loaded with deionized water and compacted in the tube to achieve a porosity of approximately 44 %. The partially saturated state was created by setting the water flow rate to 25 ml/hr and varying the simultaneous flow rate of the air. Two Pharmacia P-500 HPLC pumps were used to deliver the air and deionized water phases against gravity which combined at a tee junction just below the entrance of the bead pack. This flow resulted in an alternating flow of water and then air bubbles up through the bead pack. The dual air/water flow was continued for 8 hours. The air flow was then shut off and the water flow continued at 25 ml/hr until a steady state MR signal indicated a steady state of partial saturation had been achieved (approximately 4 hours). The volumetric rate of the initial air flow was varied between 25 and 100 ml/hr, but there was no difference observed in the final partially saturated state as evidenced by the MR results.

After the partially saturated state had been established, magnetic resonance experiments were performed as the water flow was increased from 0 ml/hr to 500 ml/hr and then decreased to 25 ml/hr to repeat the velocity map before increasing to 50 ml/hr and eventually shutting off flow. The intention was to monitor the degree of partial

saturation as the flow rate was increased from 0 to 500 ml/hr, and to characterize the bead pack before and after the fast flow rate challenge with a density map, propagator and velocity map. The hold time for each flow rate was the time required for completion of all MR experiments at each respective flow rate. At flow rates 25 ml/hr and 50 ml/hr this was about 20 minutes and at all other flow rates it was 5 minutes.

The work performed on the partially saturated porous media showed that a partially saturated single phase flow has global flow dynamics that return to characteristic flow statistics once a steady state high flow rate has been reached. This high flow rate pushed out a significant amount of the air in the bead pack and caused a return of a preferential flow pattern. Velocity maps indicated that local flow statistics were not the same for the before and after blow out conditions.

Data on the saturation of porous media during partially saturated flow are limited and the unique ability of MR to provide this data is demonstrated. The ability of MR to measure the propagator of motion yields the stationary dynamics and connections with the structure of the porous media and percolation models of the flow can be made. In demonstrating these measurements and interpretation the basis for further studies of steady state partially saturated flows for a range of *Ca* numbers, fluids, saturation levels and MR parameters such as displacement observation time has been established.

Oscillatory Flow

For the oscillatory flow project, the flow was generated by a double acting cylinder (Bimba Manufacturing: HL-013-DPY) connected via an adjustable arm to a

rotating pump motor shaft (Cole-Parmer: Model No. 7553-80). In order to trigger the spectrometer at the same point in the cycle, an inductive sensor (A47-18ADSO-2KT21-Single Ch-Target Tracker Gear Tooth Sensor) was used to sense the rotation of the arm. Collectively this creates an approximately sinusoidal oscillatory flow with no net flow rate. The tubing was run through the magnet and connected to the piston cylinder. PVC tubing of internal radius 5.37 mm was used for all the experiments.

A single pulsed gradient spin echo (PGSE) inserted in a basic MR imaging sequence was used to obtain the velocity maps [3]. Rather than obtaining an average over the entire cycle, the LabVIEW program and the delay in the trigger function of ParaVision Version 5.0, allowed velocity maps to be collected at specific intervals in the oscillation cycle. The pulse duration,δ, was 1ms and the gradient pulse spacing, Δ, was 10ms. The PGSE gradient values were set based on the maximum expected velocity. The T_R for frequencies of 0.31 rad/s, 1.26 rad/s, 2.09 rad/s, and 12.57 rad/s were 19.5 s, 4.9s, 2.7 s, and 0.55 s respectively. The bulk fluid was doped with Magnevist to lower the T_1 to 0.2 s ensuring $T_1 < T_R$ for all of the experiments. The velocity maps had a field of view of 15 mm x 15 mm and a resolution of 117.2 μm x 468.7 μm over a slice thickness of 20 mm. A LabVIEW program was developed to convert the voltage signal sent from the inductive sensor to a voltage signal that triggers the AVANCE III Spectrometer. A data acquisition device (NI USB-6009 14-bit multifunction DAQ) was used with LabVIEW 2009 to control the experiment timing and monitor fluid pressure.

In order to observe a range of Womersley numbers, α, the oscillating flow frequency, ω, and fluid viscosity, υ were varied. The fluids tested included both

Newtonian and non-Newtonian fluids. The four fluids were: water, xanthan gum (XG), polyacrylamide (PAM), and hexadecane colloidal particles. Each fluid was oscillated at four frequencies, ω=0.31 rad/s, ω=1.26 rad/s, ω=2.09 rad/s, and ω=12.57 rad/s.

Water: Water is a Newtonian, non-compressible fluid and its properties are well known. The relationship between stress and strain is linear, thus water has a constant viscosity at a constant temperature.

Xanthan gum: XG is a power law fluid and will react differently under shear forces. The xanthan gum molecule is a long chain molecule with pentasaccharide repeat unit [9]. A 0.025% by weight solution is mixed using xanthan gum produced by fermentation of dextrose with Xanthomonas campestris.

Polyacrylamide: The 2000 ppm PAM solution acts as a viscoelastic shear thinning fluid. It is made by dissolving high molecular weight polyacrylamide in water.

Colloidal suspension: The core-shell oil particles were constructed using the method of Loxley and Vincent [10]. An oil phase containing 3.0 g of poly(methyl-methacrylate) (PMMA) MW 350,000, 60 mL dicloromethane, 3.9 mL acetone and 5 mL of hexadecane was added drop-wise to 80 mL of a 2% wt. polyvinyl alcohol (PVA) solution while being stirred with a Heidolph Silent Crusher M homogenizer. To obtain the desired particle sizes, a constant shear rate of 12,000 rpm was applied for a period of one hour following the oil phase addition. The resulting emulsion was then added to 120 mL of a 2% wt. PVA solution and the volatile solvent was allowed to evaporate overnight resulting in a PMMA shell encasing the oil, thus separating the oil and water phases. The microspheres are short range repulsive due to short chain PVA molecules which adhere to the surface

and exhibit hard sphere behavior [11]. The resulting particle size had a range of radii distributed around approximately 1μm (1μm ± 0.46 μm).

Oscillatory flows can be characterized with the Womersley number [12, 13]. Non-parabolic velocity profiles (blunted and split) have been observed with oscillatory flows [12] and these flows have now been studied with MRI. MRI allows the study of velocities in both transparent and opaque (i.e. colloids, porous media) fluid systems. Blunted and split profiles are seen as expected as the unsteady forces begin to dominate over the viscous forces for higher α. Particle migration can occur in low shear regions in the flow, important in plaque buildup [14]. In Newtonian, laminar, unidirectional flow, the particles tend to move to the center. In oscillatory flows, the particles can migrate to several locations and systems could be designed to take advantage of such phenomena for advantageous particle entrapment (i.e. drug delivery) or to avoid plaque buildup. In addition to characterization of flow and transport in oscillatory flows this apparatus could potentially be used in Rheo-NMR [15] applications to generate oscillatory flows for characterization of the shear modulus of complex fluids. The following chapters expand on the results discussed in this introduction. The work has been published (or submitted for publication) as follows: [16], [17], and [18].

BACKGROUND OF NUCLEAR MAGNETIC RESONANCE AND MAGNETIC RESONANCE IMAGING

Larmor Frequency and Net Magnetization

Magnetic Resonance Microscopy (MRM) works on the principle of Nuclear Magnetic Resonance (NMR) in combination with applied linear magnetic field gradients. More details on the discussion in the next several sections can be found in the cornerstone references in the field of NMR [3, 19-21]. The topics and theories necessary to develop a basis for the following chapters that present the groundbreaking work that used the unique method of NMR.

The nuclei of atoms have a magnetic moment (magnetic dipole) and angular momentum, commonly called the spin, $\hat{m}$. In the presence of an external magnetic field, $\boldsymbol{B}_o$, the spin precesses about $\boldsymbol{B}_o$ at a frequency governed by the Larmor frequency (Eqn. 2.1).

$$\omega_o = \gamma \boldsymbol{B}_o \tag{2.1}$$

The Larmor frequency, ω_o, and consequently the NMR signal, is a function of the gyro-magnetic ratio, γ, and the magnetic field strength, $\boldsymbol{B}_o$.

When placed in an external magnetic field, the spin magnetic moment aligns parallel or anti-parallel and precesses about the field due to the torque from the field acting on a system with existing angular momentum [3]. This is true for hydrogen, fluorine, and other spins that have two possible energy states (spin ½). The higher energy

state corresponds to the nuclei moments aligning against the applied field and the lower aligning with the field.

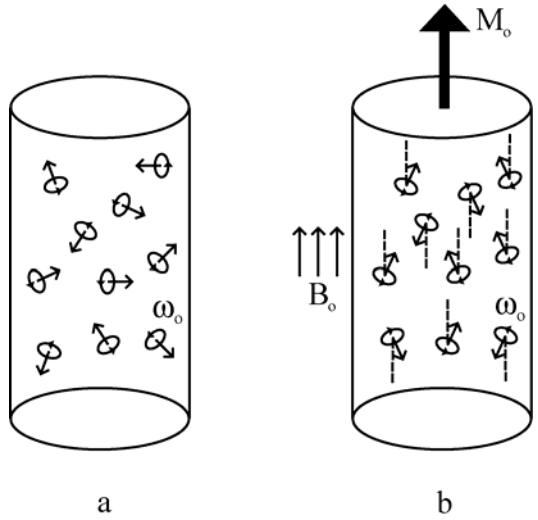

Figure 2.1: Water molecules a) in the absence of a magnetic field b) in the presence of a magnetic field $\boldsymbol{B}_o$ with resultant magnetization vector $\boldsymbol{M}_o$

The lower energy state is of course easier to obtain, therefore, a small majority of nuclei spins orient with the magnetic field and results in a net magnetization vector $\boldsymbol{M}_o$ (Figure 2.1).

Table 2.1: Gyromagnetic ratios for some common isotopes [22]

Isotope	Gyromagnetic Ratio (MHz/T)	Natural Abundance	Isotope	Gyromagnetic Ratio (MHz/T)	Natural Abundance
^{1}H	42.58	99.9885%	^{16}O	0	99.757%
^{2}H	6.54	0.1150%	^{17}O	5.77	0.038%
^{12}C	0	98.93%	^{18}O	0	0.205%
^{13}C	10.71	1.07%	^{19}F	40.08	100%
^{14}N	3.08	99.632%	^{31}P	17.25	100%
^{15}N	4.32	0.368%			

The gyro-magnetic ratio is a constant for a particular isotope and thus the larger the Larmor frequency, the greater is the intensity of the NMR signal. For instance hydrogen ^{1}H has a gyro-magnetic ratio of 26.75 x 10^{-7} rad/s-T (42.58 MHz/T) and fluorine's ^{19}F is 25.15 10^{-7} rad/s-T (40.08 MHz/T).

The NMR signal intensity for ^{1}H and ^{19}F is of the same magnitude. For isotopes such as ^{13}C and ^{17}O the signal intensity is not as good as ^{1}H or ^{19}F. Additionally, the natural abundance of an isotope can also limit the available signal in a naturally occurring sample. For instance in naturally occurring CO_2, ^{12}C makes up 98.93% of the mass and ^{13}C 1.07%. NMR signal can only be gathered from the ^{13}C isotope in CO_2, and therefore, naturally occurring CO_2 as an NMR sample does not provide a good signal. See Table 2.1 for a list of common isotopes and the corresponding gyromagnetic ratios.

Energy, Spin States, and the Rotating Frame

The energy state generated by an excitation field $\boldsymbol{B}_o$ is referred to as the Zeeman interaction and the energy level splitting is (Eqn. 2.2):

$$\Delta E = \gamma \hbar \boldsymbol{B}_o \tag{2.2}$$

where $\Delta\hbar$ is Plank's constant/2π. This equation is derived from the Zeeman Hamiltonian operating in the z-direction (Eqn. 2.3).

$$H = -\gamma \hbar B_o I_z \tag{2.3}$$

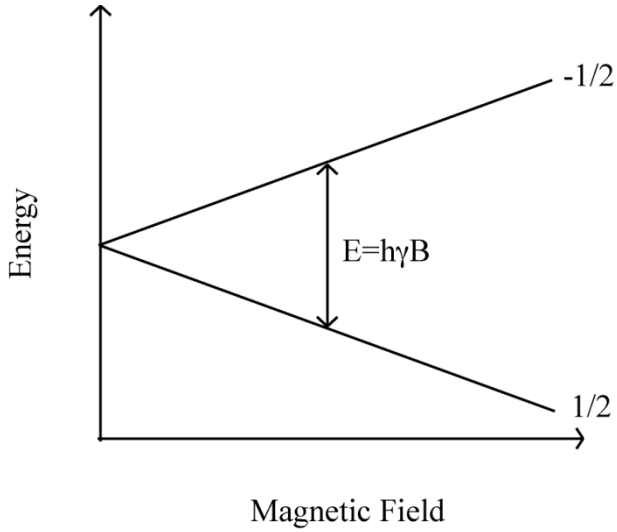

Figure 2.2: Two energy states for spin ½

As shown in Eqn. 2.2, the energy required to switch between the two states is a function of the magnetic field strength. Thus, the energy required to switch between the two states for a system of spin ½ increases as the magnetic field strength increases (Figure 2.2). To change or detect the energy level distribution of a system corresponds to excitation or detection of energy in the radio frequency spectrum for high magnetic fields (1-9 Tesla).

In superconducting laboratory NMR spectrometers (1-9 Tesla), the Larmor frequencies of the proton spins are in the radio frequency (RF) spectrum. All of the spins in one homogenous magnetic field are approximately precessing at the same frequency and therefore interact with each other at this frequency. When an external radio frequency source is applied to the spins at the Larmor frequency, the spins change energy levels coherently. For NMR application, an RF coil is used for this specific purpose. An RF coil can take on several design arrangements such as saddle, bird cage, and others.

All of the RF coil configurations are designed to resonate specifically at the Larmor frequency of a particular nuclei: *i.e.*, ^{19}F, ^{1}H, and etc. The RF coil generates a rotating magnetic field $\boldsymbol{B}_1$ perpendicular to the initial $\boldsymbol{B}_o$ vector at a frequency of, ω_o, and thus manipulates the orientation of the magnetization vector of the sample, $\boldsymbol{M}_o$. The RF energy can rotate the magnetization into the transverse plan, where it precesses about the longitudinal axis. It is convenient to work in a rotating frame of reference that rotates about the longitudinal axis at the Larmor frequency. With a transverse magnetic field applied, the Hamiltonian operator without the rotating frame can be written:

$$H_{lab} = -\gamma \boldsymbol{B}_o I_z - 2\gamma \boldsymbol{B}_1 cos\omega t I_x \tag{2.4}$$

However, in the rotating frame, the Hamiltonian is:

$$H_{rot} = -\gamma \left(\boldsymbol{B}_o - \frac{\omega}{\gamma}\right) I_z - \gamma \boldsymbol{B}_1 I_x \tag{2.5}$$

Conveniently, when the rotating frame is set to oscillate at the Larmor frequency of $\omega = \omega_o$, the first term drops out therefore eliminating the Zeeman interaction from Eqn. 2.5 and the resulting mathematical analysis is hence simplified.

Excitation and Relaxation

If the correct power amplitude and duration pulse is applied through the RF coil the magnetization can be tipped to the transverse plane, orthogonal to $\boldsymbol{B}_o$. This process is termed a 90^o excitation and forms the initiation for many NMR pulse sequences (Figure 2.3).

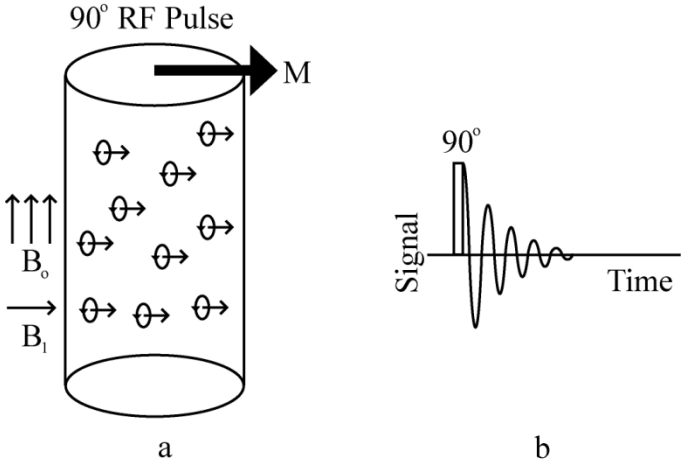

Figure 2.3: a) Affect of a 90° RF Pulse on the magnetization ***M*** and b) the FID resulting from the 90° RF Pulse

$\boldsymbol{M}_z$ is the magnetization in the z-direction parallel with $\boldsymbol{M}_o$. $\boldsymbol{M}_{x,y}$ is the transverse magnetization in the orthogonal plane of $\boldsymbol{M}_o$. Additionally, the RF coil serves as a receiver for any changes in magnetization that may occur only in the transverse plane. This change of $\boldsymbol{M}_{xy}$ induces a current in the RF coil and this is how signal detection is gathered using NMR equipment. After the 90° pulse excitation, the spins begin to relax in two ways. One component of relaxation is a return to the initial magnetization of $\boldsymbol{M}_o$. This is defined as T_1 relaxation and is also commonly called spin-lattice relaxation. The second component is the decaying of the magnetization in the transverse plane and is defined as T_2 relaxation.

Consider a system composed of many molecules with randomly tumbling molecular spins in a spin ½ system. T_1 relaxation in this system is the relaxation of the spins relative to the surrounding thermal equilibrium environment. This change in longitudinal magnetization that causes T_1 relaxation is due to the transition of energy between the two spin states. The energy transitions are caused by the interaction of the

spins with each other and the environment, and the resultant magnetic field fluctuations seen by the spins. There are three primary sources that affect the individual magnetic fields: paramagnetic, which is a molecule having an unbalanced electron, quadrupole, which only occurs in spin systems greater than ½, and nuclear dipole-dipole, which is another nuclear magnetic moment from another spin. T_2 relaxation is attributed solely to the spin-spin interaction and hence the decay of the transverse magnetization.

It is clear that the magnetization is a function of time in both the excitation and relaxation formulations. The purpose here is to derive the equations for magnetization based off of the nuclear magnetic moment and nuclear angular momentum. Beginning with the classical torque equation, torque from a magnetic moment is the magnetization cross multiplied with the magnetic field (Eqn. 2.6).

$$\tau = \boldsymbol{M} \times \boldsymbol{B} \tag{2.6}$$

Torque also equals the angular momentum rate change (Eqn. 2.7):

$$\tau = \frac{d\frac{\boldsymbol{M}}{\gamma}}{dt} \tag{2.7}$$

By equating the two torque equations and dividing both sides by a constant gyromagnetic ratio, γ (Eqn. 2.8):

$$\frac{d\boldsymbol{M}}{dt} = \gamma \boldsymbol{M} \times \boldsymbol{B} \tag{2.8}$$

For the previous conditions discussed, the magnetization of $\boldsymbol{B}_o$ is applied in the *z*-directions and an excitation of a precessing magnetic field of $\boldsymbol{B}_1$ is applied so that $\boldsymbol{B}_1$ precesses in the *x* and *y* plane according to (Eqn. 2.9).

$$\boldsymbol{B}_1(t) = \boldsymbol{B}_1 \cos(\omega_o t) i - \boldsymbol{B}_1 \sin(\omega_o t) j \tag{2.9}$$

Plugging in the magnetic fields into Eqn. 2.8 gives (Eqn. 2.10):

$$\frac{d\boldsymbol{M}}{dt} = \begin{vmatrix} i & j & k \\ \gamma \boldsymbol{M}_x & \gamma \boldsymbol{M}_y & \gamma \boldsymbol{M}_z \\ \boldsymbol{B}_1 \cos(\omega_o t) & -\boldsymbol{B}_1 \sin(\omega_o t) & \boldsymbol{B}_o \end{vmatrix} \tag{2.10}$$

Performing the cross product on Eqn. 2.10 gives the equations for excitation (Eqn. 2.11):

$$\frac{d\boldsymbol{M}_x}{dt} = \gamma\left[\boldsymbol{M}_y \boldsymbol{B}_o + \boldsymbol{M}_z \boldsymbol{B}_1 \sin(\omega_o t)\right]$$

$$\frac{d\boldsymbol{M}_y}{dt} = \gamma[\boldsymbol{M}_z \boldsymbol{B}_1 \cos(\omega_o t) - \boldsymbol{M}_x \boldsymbol{B}_o] \tag{2.11}$$

$$\frac{d\boldsymbol{M}_z}{dt} = \gamma\left[-\boldsymbol{M}_x \boldsymbol{B}_1 \sin(\omega_o t) - \boldsymbol{M}_y \boldsymbol{B}_1 \cos(\omega_o t)\right]$$

Plugging in the initial conditions of $\boldsymbol{M}(t) = \boldsymbol{M}_o k$, which is the initial magnetization of $\boldsymbol{M}_o$ in the z-direction, the magnetization for all three Cartesian coordinates can be determined as a function of time (Eqn. 2.12).

$$\boldsymbol{M}_x = \boldsymbol{M}_o \sin(\omega_1 t) \sin(\omega_o t)$$

$$\boldsymbol{M}_y = \boldsymbol{M}_o \sin(\omega_1 t) \cos(\omega_o t) \tag{2.12}$$

$$\boldsymbol{M}_z = \boldsymbol{M}_o \cos(\omega_1 t)$$

Therefore, the magnetization will oscillate in the transverse plane perpendicular to the z-direction because of $\boldsymbol{B}_1$.

After excitation, the spins begin to relax according the previously discussed phenomena. For relaxation, the equations that model T_1 (longitudinal) and T_2 (transverse) are as follows:

$$\frac{d\boldsymbol{M}_z}{dt} = -\frac{(\boldsymbol{M}_z - \boldsymbol{M}_o)}{T_1}$$

$$\frac{d\boldsymbol{M}_{x,y}}{dt} = -\frac{(\boldsymbol{M}_{x,y})}{T_2} \tag{2.13}$$

The Solution to T_1 and T_2 are shown, respectively:

$$\boldsymbol{M}_z(t) = \boldsymbol{M}_z(0)\exp\left(-\frac{t}{T_1}\right) + \boldsymbol{M}_0\left(1 - exp\left(-\frac{t}{T_1}\right)\right) \tag{2.14}$$

$$\boldsymbol{M}_{x,y}(t) = \boldsymbol{M}_{x,y}(0)\exp\left(-\frac{t}{T_2}\right) \tag{2.15}$$

In the rotating frame, addition of the equations for excitation (Eqn. 2.11) and relaxation (Eqn. 2.13) and accounting for magnetization due to off resonance behavior ($\boldsymbol{B}_o - \omega/\gamma$) give the Bloch equations. These allow calculation of the magnetization in the three Cartesian coordinates due to excitation and relaxation combined (Eqn. 2.16).

$$\frac{d\boldsymbol{M}_x}{dt} = \gamma \boldsymbol{M}_y\left(\boldsymbol{B}_o - \frac{\omega}{\gamma}\right) - \frac{\boldsymbol{M}_x}{T_2}$$

$$\frac{d\boldsymbol{M}_y}{dt} = \gamma \boldsymbol{M}_z \boldsymbol{B}_1 - \gamma \boldsymbol{M}_x\left(\boldsymbol{B}_o - \frac{\omega}{\gamma}\right) - \frac{\boldsymbol{M}_y}{T_2}$$

$$\frac{d\boldsymbol{M}_z}{dt} = -\gamma \boldsymbol{M}_y \boldsymbol{B}_1 - \frac{(\boldsymbol{M}_z - \boldsymbol{M}_o)}{T_1} \tag{2.16}$$

The inherent nature of dual phase detection RF receiver coils independently detect the transverse components of magnetization, $\boldsymbol{M}_{x'}$ and $\boldsymbol{M}_{y'}$. The two components can easily be represented with complex numbers where the *x*-direction is represented by the real portion and the *y*-direction is represented by the imaginary part. Therefore Fourier

transforms can be easily utilized to transform the signal collected in the time domain to the frequency domain and vice versa. This provides the foundation for NMR signal collection and processing that will be discussed in a later section.

Spectral Density and Correlation Time

When two spins are in the vicinity of each other there exists an associated energy with this distance of separation. A translational or rotational change in position of one spin about the other will change the associated energy (Figure 2.4). This energy can change depending on the frequency and time of interactions. The spectral density is therefore a measurement of the energy rate change (power) as a function of frequency of interactions.

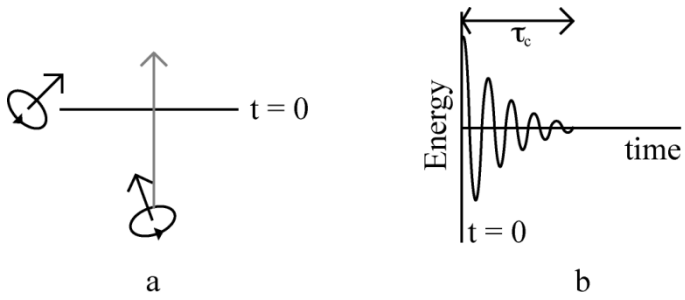

Figure 2.4: Two spins interacting by method of a) translational motion and the resultant b) energy of interaction as a function of time.

In Figure2.4, the concept of correlation time, τ_c, is presented. It is a method to quantify the time scale of the molecular interactions. The model for correlation time is thus contingent on truly random fluctuation of molecular interactions. Additionally, at a given temperature and pressure in a simple fluid, there is only one correlation time. In

such systems, spectral density can be defined as a function of the correlation time and nuclear frequency (Eqn. 2.17).

$$J(\omega) = \frac{\tau_c}{1+\omega^2{\tau_c}^2} \tag{2.17}$$

Figure 2.5 shows the spectral density as a function of ω and for increasing temperature. At a low temperature, the spectral density remains level at low frequencies suggesting that a majority of molecular motion occurs in this range, but not much energy is available at higher frequencies. As the temperature increases, however, more energy exists at the higher frequencies. The area underneath each line in the normalized spectral density curve must be equivalent, therefore as more molecules interact at the higher frequencies, the percentage of the spectral density for the lower frequencies must go down. The significance in the position of ω_0 in Figure 2.5 will be discussed later.

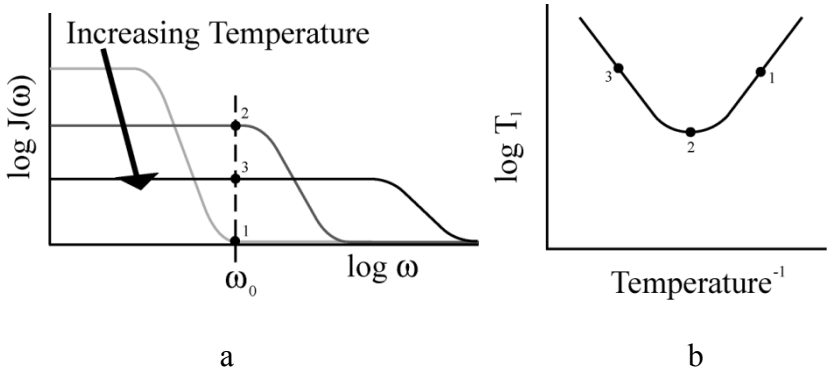

Figure 2.5: a) Spectral density plot as a function of frequency for increasing temperature. b) T_1 relaxation as a function of 1/Temperature. The three temperatures correspond to the ω_0 in Figure a.

The spectral density is important because it leads to the model for T_1 and T_2 relaxation as a function of temperature. There are three terms for spectral density: $J^{(0)}$, $J^{(1)}$, and $J^{(2)}$ (Eqn. 2.18).

$$J^{(0)} = \left(\frac{24}{15R^6}\right)\left[\frac{\tau_c}{1+\omega^2{\tau_c}^2}\right]$$

$$J^{(1)} = \left(\frac{1}{6}\right)\left[J^{(0)}\right] \tag{2.18}$$

$$J^{(2)} = \left(\frac{2}{3}\right)\left[J^{(0)}\right]$$

R in the previous equations is the radius of separation for the interacting molecules. Where two spins are considered, the $J^{(0)}$ term is concerned with both spins simultaneously flipping in relation to one another and resulting in no net energy change. Therefore the relaxation associated with this spin interaction factors only into T_2 relaxation. The next two J terms are associated with both relaxations, T_1 and T_2. The $J^{(1)}$ term is associated with one spin flipping. For $J^{(2)}$, both spins flip, but an energy transition exists. For instance, if both spins are spin up and then both flip to spin down. As stated previously, the T_1 and T_2 relaxation equations are based on these J terms (Eqn. 2.19).

$$\frac{1}{T_1} = \left(\frac{\mu_0}{4\pi}\right)^2 \gamma^4\hbar^2\frac{3}{2}I(I+1)\left[J^{(1)}(\omega_0) + J^{(2)}(2\omega_0)\right]$$

$$\frac{1}{T_2} = \left(\frac{\mu_0}{4\pi}\right)^2 \gamma^4\hbar^2\frac{3}{2}I(I+1)\left[\frac{1}{4}J^{(0)}(0) + \frac{5}{2}J^{(1)}(\omega_0) + \frac{1}{4}J^{(2)}(2\omega_0)\right] \tag{2.19}$$

As can be seen the equation 2.19, T_1 and T_2 are inversely proportional to the $J^{(1)}$ term which is a function of ω_0 and hence $\boldsymbol{B}_o$. The amplitude of $J^{(1)}(\omega_o)$ depends on the system temperature (Figure 2.5a). Therefore T_1 and T_2 are also temperature dependent. A plot of T_1 (Figure 2.5b) shows that the T_1 can have a minimum at a specific temperature as shown in Figure 2.5a. T_2 relaxation, however, has a continual increase for increasing temperature due to the presence of the $J^{(0)}(\omega_o)$ term (Figure 2.6).

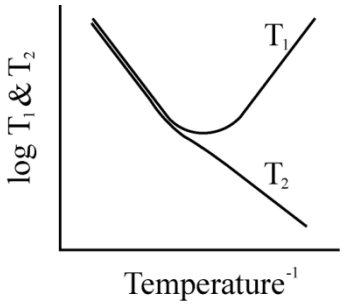

Figure 2.6: T_1 and T_2 relaxation as a function of 1/Temperature.

Inversion Recovery and Measurement of T_1 Relaxation

Although the magnetization can only be detected in the transverse plane by the coil, the longitudinal relaxation of T_1 can still be measured. This can be performed by manipulation techniques that can flip the longitudinal magnetization into the transverse plane. To measure the T_1 of a sample, an inversion recovery technique can be used. The inversion recovery pulse sequence is laid out in Figure 2.7.

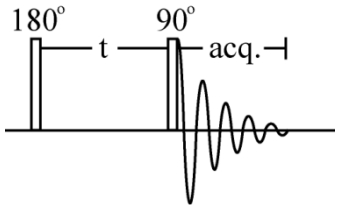

Figure 2.7: Inversion Recovery Pulse Sequence

The first pulse of 180° flips the net spin magnetic moment vector, $\boldsymbol{M}_o$, into negative z-direction to a value of $-\boldsymbol{M}_o$. After the first excitation pulse, the spins begin to relax and return toward the initial magnetization of $\boldsymbol{M}_o$ along the z-direction (Figure 2.9). However, at some time, τ_{inv}, a 90^o_x flips the longitudinal magnetization into the transverse plane and the magnetization is detected. The sequence is repeated at a range of t values;

the T_1 relaxation can then be calculated from an exponential fit to the data. It is important that the sequence repetition time, $T_R > 5T_1$.

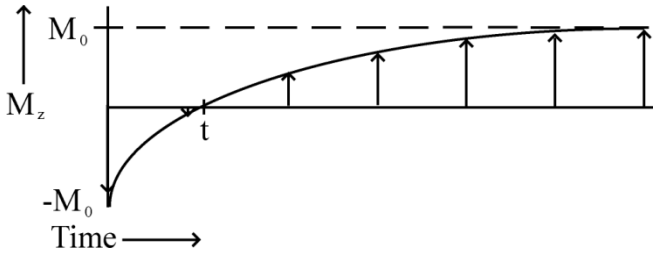

Figure 2.8: Longitudinal magnetization as a function of time for an inversion recovery pulse sequence.

The equation for this magnetization is:

$$\boldsymbol{M}(t) = \boldsymbol{M}_o\left[1 - 2\exp\left(-\frac{\tau_{inv}}{T_1}\right)\right] \tag{2.20}$$

The time τ_{inv} for the magnetization to equal 0 is desired. For $\boldsymbol{M}(t) = 0$, Equation 2.20 reduces to:

$$T_1 = 1.443\tau_{inv} \tag{2.21}$$

Therefore, the time between the two excitation pulses that causes 0 magnetization is 0.6931 of the T_1 relaxation. This is represented in Figure 2.8. The use of a 180° preparation pulse spaced τ_{inv} before the first 90° pulse of a sequence will eliminate any signal from spins with a $T_1 = 1.443\tau_{inv}$. This can be used to obtain a contrast image in which the signal from spins with a $T_1 = 1.443\tau_{inv}$ will be nulled, but signal can be obtained from spins with other T_1 times.

k-space Spatial Resolution, Signal, 1D and 2D Imaging, Slice Selection

In the presence of an externally linearly varying magnetic field gradient, the precession frequency becomes a function of position, ***r***. NMR spectrometers with imaging capabilities can create magnetic field gradients in all three spatial Cartesian coordinate directions: *x*, *y*, and *z*. Take for example a constant field strength $\boldsymbol{B}_o$. If a linearly increasing gradient of strength ***G*** is also applied in the *z*-direction, the resultant field strength as a function of *z* is $\boldsymbol{B}_{eff}$ (Figure 2.9). Consequently, the Larmor frequency will be a function of the position *z*. Equation 2.22 shows the Larmor frequency as a function of position. The addition of magnetic field gradients gives the possibility to spatially resolve the signal from the spins contained in a sample and also enables displacement and velocity encoding.

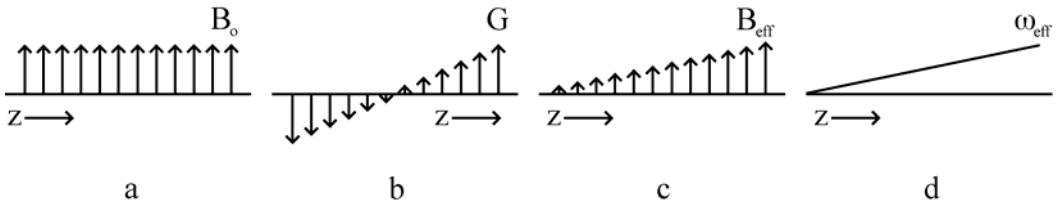

Figure 2.9: A gradient's effect on the magnetic field strength a) $\boldsymbol{B}_o$ as a function of *z* – direction without a gradient b) gradient ***G*** applied in the z-direction c) addition of $\boldsymbol{B}_o$ with the gradient ***G*** to produce a magnetic field strength of $\boldsymbol{B}_{eff}$ and d) resultant effective frequency. Typically $\boldsymbol{B}_o \gg \boldsymbol{G\Delta r}$

$$\omega(\vec{r}) = \gamma \boldsymbol{B}_o + \gamma \boldsymbol{G} \cdot \boldsymbol{r} \tag{2.22}$$

The magnetic field gradients can be applied in any or all of the three Cartesian coordinates. In NMR imaging, a voxel is a volume element and is uniformly discretized to complete the full spectrograph, i.e. in MR imaging many voxels are collected to make

a complete image. The voxels are typically not isotropic. A voxel therefore contains a density of spins and thus, the resolution of the NMR data is based off of the size of the unit voxels. A voxel that is too small won't contain enough spins to measure a signal and hence defines the lower end of the resolution range. For NMR this lower end is on the order of 10 μm.

For one dimensional imaging, a gradient is applied in one direction and the density of spins is detected across the entire sample. For instance, an image in which a gradient is applied in the *z*-direction, $\boldsymbol{G}_z$, will spatially resolve the spins in the *z*-direction, but will intrinsically include the signal from the density of spins in the *x* and *y*-directions. In this case there is no resolution of signal for the *x* and *y*-directions and therefore the voxel size in these dimensions includes the full length in these two directions. Essentially, all signal information is collapsed into one dimension. Figure 2.10a shows a tube of water inside of the coil with an applied gradient.

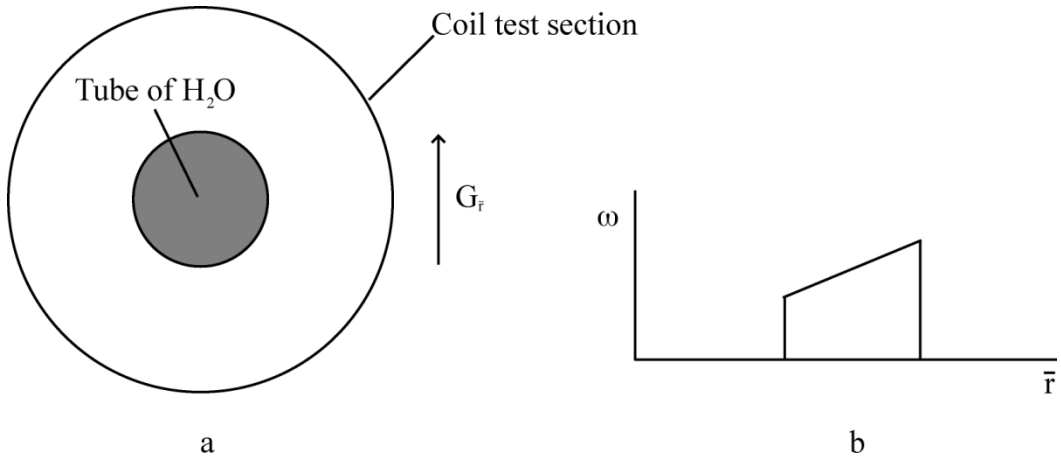

Figure 2.10: a) Tube of H_20 inside a coil with a gradient applied in one dimension, b) Resultant Larmor frequency as a function of position across the tube of water.

The Larmor frequency of the spins is slower from the lower side of the tube where the gradient is small and increases in frequency at the higher side of the tube where the gradient is larger (Figure 2.10b). In the transverse direction, no gradient is applied therefore all spins on one line in the horizontal direction have the same frequency. The result is a voxel representing a slice with a relatively large width and depth, but a small thickness (Figure 2.11a). The signal intensity comes from the density of spins in this thin rectangular box (Figure 2.11b). The full sample is then segmented into many of these thin elements spanning the dimension in which the gradient is applied. Decreasing the voxel thickness in the r-direction increases the resolution of the image. Figure 2.11c shows this increased resolution which results in the signal smoothing as a function of the frequency. The slice thickness can then be controlled by implementing a slice gradient in combination with an excitation pulse that will excite a desired bandwidth of signal.

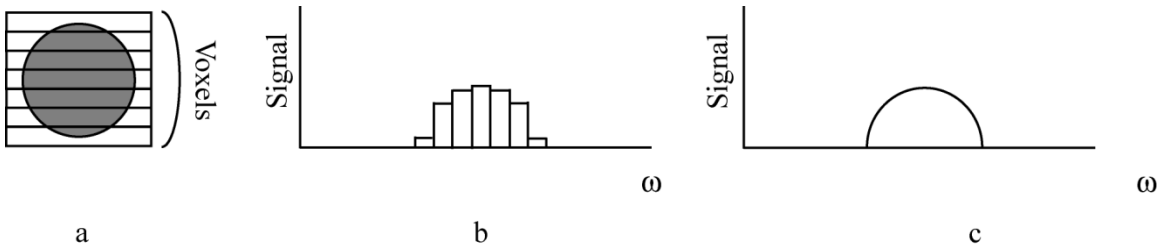

Figure 2.11: a)Voxels discretized through the sample, b) signal intensity as a function of frequency for low resolution large voxel sizes, and c) signal intensity as a function of frequency for high resolution small voxel sizes.

The spectrometer collects signal in real time so that the signal $S(t)$ is a function of time. Through the data processing, the signal is Fourier transformed to get the frequency domain. The gradient amplitude used correlates the frequency to the position. In the

presence of the gradient $\boldsymbol{G}$, the NMR signal $S(t)$ acquired is thus an integration of the signal from all the spins (Eqn. 2.23).

$$S(t) = \iiint \rho(\boldsymbol{r})\, exp[i\gamma \boldsymbol{G} \cdot \boldsymbol{r}t]d\boldsymbol{r} \tag{2.23}$$

If we define a vector $\boldsymbol{k}$ such that:

$$\boldsymbol{k} = \frac{\gamma \boldsymbol{G}t}{2\pi} \tag{2.24}$$

Then it is clear there is a Fourier relationship between the signal and the density or 1D image profile [23].

$$S(\boldsymbol{k}) = \iiint \rho(\boldsymbol{r})\, exp[i2\pi \boldsymbol{k} \cdot \boldsymbol{r}]d\boldsymbol{r} \tag{2.25}$$

$$\rho(\boldsymbol{r}) = \iiint S(\boldsymbol{k})\, exp[-i2\pi \boldsymbol{k} \cdot \boldsymbol{r}]d\boldsymbol{k} \tag{2.26}$$

Imaging using Magnetic Resonance has a resolution threshold due to the diffusion. Decreasing the voxel size in an MR image will increase the resolution of the image, however, a limit exists. If the voxel size is too small therefore allowing a water molecule initially contained inside the voxel to diffuse out of the voxel during the imaging process, signal will be lost. In ***k***-space imaging, the signal is collected while a read gradient is on and the diffusion of spins causes spectral spreading (range of detectable frequencies), thus the resolution is a function of spectral spreading. For ***k***-space imaging motion of the spins is not desired and causes signal loss and resolution limits.

Suppose a ***k***-space image is done without a read gradient. N steps exist in the phase gradient direction and a second phase gradient is used in place of the read gradient to traverse ***k***-space in the second dimension. This means that a total of N^2 steps are

necessary to fully traverse ***k***-space (Figure 2.12a). For each pixel the optimal bandwidth becomes $1/T_2$ (Figure 2.12b).

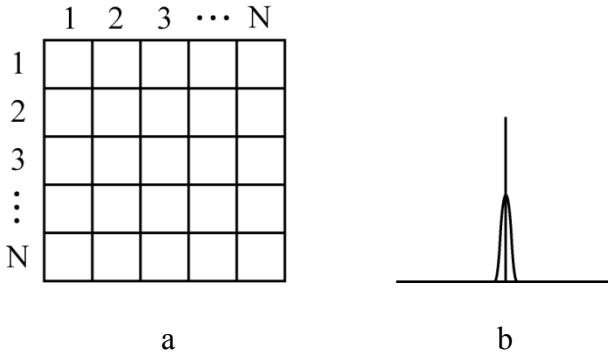

Figure 2.12: a) N^2 steps for a ***k***-space image without a read gradient and b) the optimal bandwidth per pixel.

Noise, σ^2, associated with the spectrum is simply the variance in the spectrum about the mean frequency and the noise power per pixel is proportional to σ^2/T_2. The total noise power is proportional to the noise power per pixel multiplied by the number of steps: $N^2\sigma^2/T_2$. The signal is proportional to the amplitude of the signal, S_o, and so the signal per pixel is proportional to S_o/N^2. On a per pixel basis, the resultant signal to noise ratio is $S_o T_2^{1/2}/\sigma N^2$.

Typically, ***k***-space imaging is performed with a read gradient on not a second phase gradient. The affect of this is to reduce the time required to traverse ***k***-space compared to using a second read gradient. Similar to the previous example, N steps exist in the phase gradient direction, but no extra steps are required to traverse ***k***-space in the read direction. In order to compare on an equivalent time basis to the previous example however, the test is run for N averages. In other words, the signal from each pixel is averaged over N number of experiments and the resultant number of steps is again N^2.

The steps required to fully traverse ***k***-space are shown in Figure 2.13a. For each effective pixel, the spectrum is spread out due to the read gradient and is shown in Figure 2.13b.

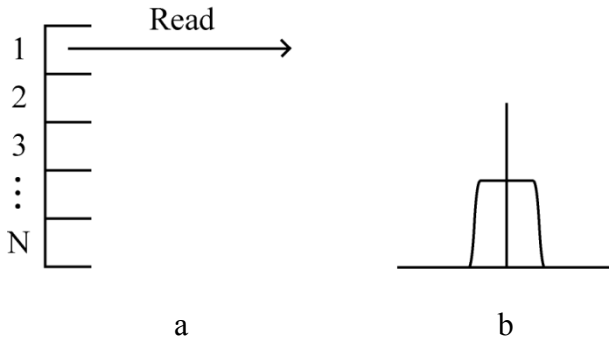

Figure 2.13: a) N steps for a ***k***-space image with a read gradient and b) the optimal bandwidth per pixel.

The optimal bandwidth per pixel is now N/T_2. Noise is again σ^2, but the noise power per pixel is proportional to $N^2\sigma^2/T_2$. Multiplying the noise power per pixel by the number of steps gives the noise proportional to $N^4\sigma^2/T_2$. Signal is proportional to the signal amplitude, S_o, multiplied by the number of averages, N. Per pixel signal is proportional to S_o. On a per pixel basis, the resultant signal to noise ratio is again $S_o T_2^{1/2}/\sigma N^2$ and the signal to noise ratios of both types of ***k***-space imaging is equivalent.

For both forms of ***k***-space imaging, the signal is proportional to the total width of the image squared times the image slice thickness:

$$S_o \propto r_o^2 \Delta z \tag{2.27}$$

The resolution, Δr, is of the same relative magnitude to r_o/N. The variables, r_o, N, and Δz are defined in Figure 2.14.

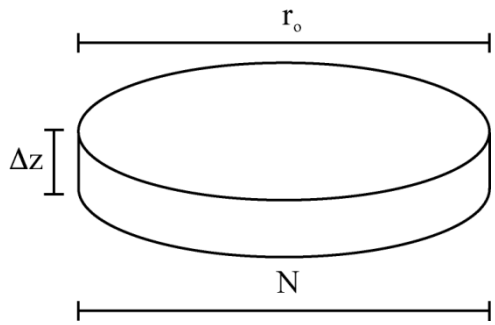

Figure 2.14: Image slice showing thickness, Δz, number of pixels, N, and total image width, r_o [3].

Rearranging the signal to noise ratio in terms of the signal amplitude gives (2.28):

$$S_o = \left(\frac{Signal}{Noise}\right)\sigma N^2 T_2^{-\frac{1}{2}} \tag{2.28}$$

Combining (2.27) with (2.28) and substituting the result for r_o into the order of magnitude resolution result gives [3]:

$$\Delta r \sim \left(\frac{Signal}{Noise}\right)^{\frac{1}{2}} \sigma^{\frac{1}{2}} \Delta z^{-\frac{1}{2}} T_2^{-\frac{1}{4}} \tag{2.29}$$

Equation (2.29) is the resolution for ***k*-**space imaging.

In order to obtain the full signal for each test N, the magnetization of the excited spins needs to fully relax back into the longitudinal direction before the next test can begin, i.e. $T_R > 5T_1$ [3]. The time between each successive experiments is termed the repetition time T_R. If $T_R < T_1$ for some spins in the system and $T_R > T_1$ for other spins then T_1 contrast in an image is achieved.

TRANSLATIONAL DYNAMICS IN NUCLEAR MAGNETIC RESONANCE

Propagators

To measure motion in a sample, NMR can be used to detect an ensemble average of molecular dynamic displacements [2]. Beginning with one particle and using statistics, molecular displacements can be described by probabilities [24, 25]. The probability that one particle starting at position $\boldsymbol{r}$ and moving to $\boldsymbol{r}'$ (total displacement $\boldsymbol{R}$, Figure 3.1) over a time t averaged over all starting position densities $\rho(\boldsymbol{r})$ is called the average propagator (Eqn. 3.1).

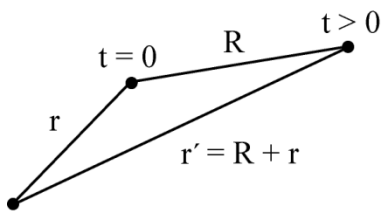

Figure 3.1: Dynamic displacement of a single particle.

$$\overline{P_s}(\boldsymbol{R}, t) = \int P_s(\boldsymbol{r}|\boldsymbol{r}+\boldsymbol{R}, t)\rho(\boldsymbol{r})\, d\boldsymbol{r} \tag{3.1}$$

Motion is detected in the direction of the applied magnetic field gradient. A diffusing particle randomly moves in a direction either negative or positive to its previous position and the magnitude of displacement is also random. In a random walk model of diffusion the random steps n have a mean time of τ_s and a Root Mean Square displacement of ξ. The total observation time of the diffusing particle is t (3.2)

$$t = n\tau_s \tag{3.2}$$

The total displacement Z as a function of time is a sum of individual displacements ξ.

$$Z(t) = \sum_{i=1}^{n} \xi a_i \tag{3.3}$$

where a accounts for the random positive or negative displacement of individual steps, I [3]. Z and ξ are taken with respect to the origin and therefore statistically, the mean displacement or first moment of an ensemble average of particles undergoing Brownian motion is 0. The second moment however, called the variance, reveals the deviation from the mean [24]. For Brownian motion, this is not 0 and characterizes the diffusion of the sample. The variance of equation 3.3 is:

$$\overline{Z^2(t)} = \sum_{i=1}^{n} \xi^2 \overline{a_i^2} \tag{3.4}$$

The individual displacements, ξ, do not depend on i and therefore equation 3.4 reduces to:

$$\overline{Z^2(t)} = \xi^2 \sum_{i=1}^{n} 1 = n\xi^2 \tag{3.5}$$

A diffusion coefficient, D, is defined as:

$$D = \frac{\xi^2}{2\tau_s} \tag{3.6}$$

Substitution of the diffusion definition into the variance of the displacement (3.5) gives the variance as a function of D [3].

$$\overline{Z^2(t)} = 2Dt \tag{3.7}$$

For the normally distributed stochastic Brownian motion, the propagator curve would be a Gaussian distribution centered on zero displacement (Figure 3.2). As stated, the probability of positive or negative displacements is equal and thus the Gaussian curve is centered about zero displacement for a no flow condition. The Full Width at Half

Maximum of the Gaussian is twice the variance and therefore the diffusion coefficient can be calculated from the propagator curve.

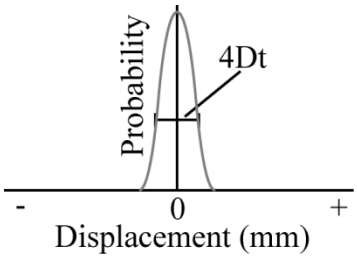

Figure 3.2: Propagator for Brownian motion

With increasing observation time *t*, the Gaussian propagator curve increases in width and decreases in height. This is because a relatively longer observation time will enable molecules to displace greater distances. For observations on molecular displacements other than self-diffusivity experiments, such as flowing conditions, the propagator curve will take on a different shape. For these experiments, sweeping through a variety of observation times will reveal a spectrum of dynamic molecular displacements [25].

Pulsed Field Gradient NMR

To detect particle motion, a pulsed gradient spin echo (PGSE, Figure 3.3) or a pulsed gradient stimulated echo (PGSTE, Figure 3.5) sequence can be used. The sequences are similar, but differ by the excitation pulses used and are discussed in detail in the next sections.

PGSE NMR

The PGSE sequence uses one 90° and one 180° radio frequency pulse and two pulsed magnetic field gradients separated by an observation time to determine translational motion (Figure 3.3).

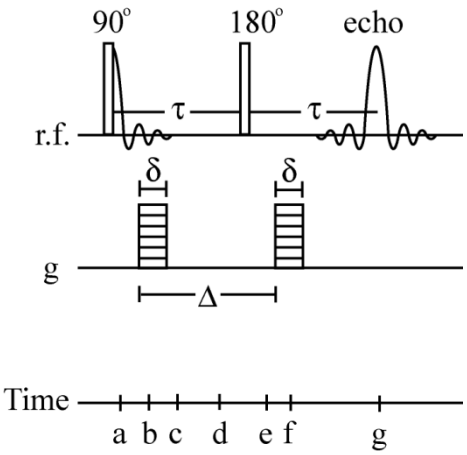

Figure 3.3: PGSE sequence

The time axis in Figure 3.3 corresponds to the alphabetical references in Figure 3.4. Figure 3.4 is a schematic representation of three spins (1-3) at three positions in a hypothetical sample. In Figure 3.4, the phase and frequency of the spins is represented by the circle with the arrow and the curved arrow, respectively. The magnitude and direction of the frequency is indicated by the length and the rotational direction of the curved arrow, respectively. The first 90° pulse puts the magnetization into the transverse plane. At time "a" after the 90° pulse all spins have the same frequency and phase due to the magnetic field $\boldsymbol{B}_o$. The equivalent frequency is indicated by equivalent lengths of the curved arrows and equivalent phase is indicated by the equivalent orientation of the arrow inside the circle.

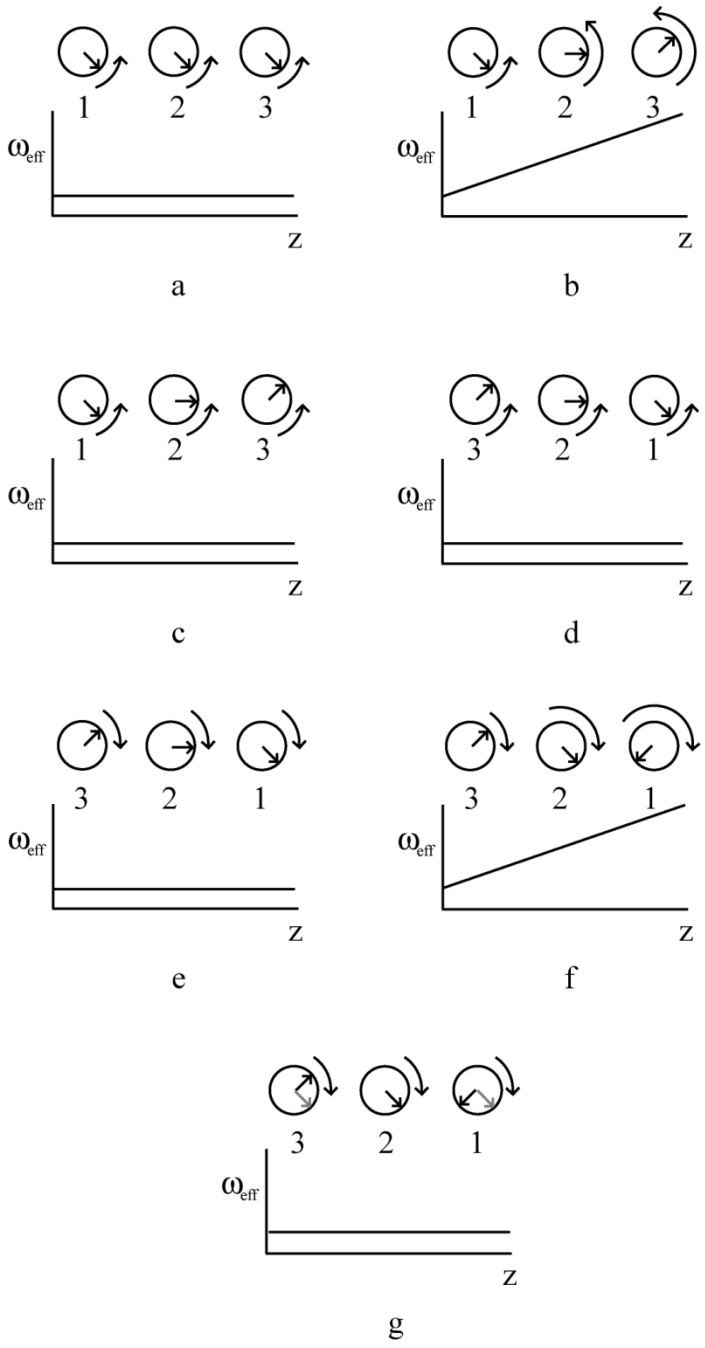

Figure 3.4: Condition of spins in PGSE sequence at times a-g in Figure 3.3

At time "b" while the gradient ***G*** is being applied in the *z*-direction, the frequency of the spins is now a function of the position. In Figure 3.4, the frequency of the spins increases

with increasing *z*. A change in frequency causes the phase of the spins to evolve as a function of the z-direction and continues to evolve for the length of the applied gradient, δ. Once the gradient is turned off (time "c"), the frequency of all the spins returns to that caused by the field $\boldsymbol{B}_o$, but the phase shift remains. At time "d" the spins can displace. As indicated in Figure 3.4d spins 1 and 3 have diffused and swapped positions.

For a time, τ, after the first 90° pulse, a 180° pulse flips the spins so that the frequency is reversed (time "e"). For a time, Δ, after the first gradient pulse, a second gradient pulse is applied which will refocus the spins at a time 2τ from the first 90° pulse (time "f"). At time "g", an echo will form. This echo contains the information regarding the final phase shift of any spins that displaced (spins 1 and 3 in Figure 3.4). The echo comparison to the FID from the first 90° pulse reveals the signal attenuation due to diffusion. For spins that did not displace (2 in Figure 3.4) all phase information that was induced in the first pulsed gradient was undone by the second pulsed gradient. Undisplaced spins cause no attenuation in the echo.

PGSTE NMR

The first 90° pulse in the PGSTE sequence puts the spins and resultant magnetization into the transverse plane. Immediately after, T_2 and T_1 relaxation begin. A gradient, $\boldsymbol{G}$, in the *z*-direction is applied for time δ to begin encoding for spin positions. The second 90° pulse puts the magnetization back into the longitudinal plane thus pausing and storing the transverse relaxation, T_2. T_1 relaxation, however, continues.

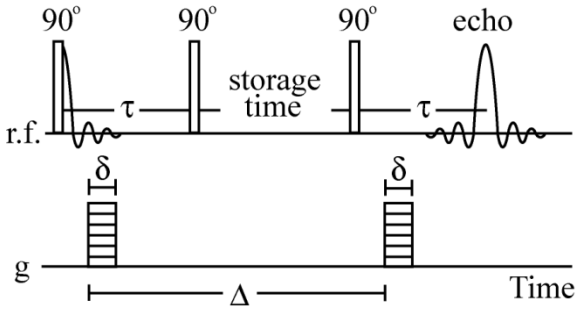

Figure 3.5: The pulsed gradient stimulated echo sequence.

A third 90° pulse is then applied putting the magnetization back into the transverse plane and continuing the T_2 relaxation. The T_1 relaxation has continued and remains undisturbed since the first 90° pulse. A gradient, $\boldsymbol{G}$, is again applied after a time spacing of Δ from the start of the first gradient. This gradient again encodes for position of the spins and as a result, any changes in frequency (phase change) can be observed between the two gradient pulses. The change in phase corresponds to position change of the molecules and therefore probability of displacements can be obtained for the entire sample. Changing Δ, called the observation time, will reveal displacement time scales of the sample [2, 3, 26, 27].

Correlation Functions

A correlation function gives the probability that a particle starting at position $\boldsymbol{r}$ moves to $\boldsymbol{r}'$ over time t (3.8), but this measures change of position of particles relative to each other and not absolute motion (Figure 3.6).

$$P(\boldsymbol{r}|\boldsymbol{r}', t) \tag{3.8}$$

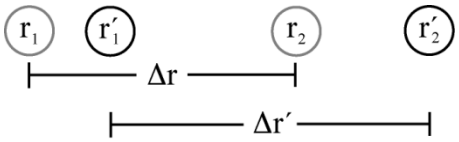

Figure 3.6: Particle representation of a motional correlation function

A self correlation function on the other hand measures absolute motion or self displacement and not relative motion (3.9) [3].

$$P_s(\boldsymbol{r}|\boldsymbol{r}', t) \tag{3.9}$$

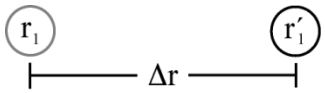

Figure 3.7: Particle representation of a motional self-correlation function

Conveniently, it is the self motion of particles that PGSE NMR detects because the change in position of the nuclei (particle displacement) causes a phase shift [3]. The probability, or propagator of the motion, in (3.9) is for a single particle. To find the probability of displacements for all particles in a system at time *t*, the probability is multiplied by the initial particle density (3.1).

By observing Fick's law for self-diffusion for spatial coordinates of which r is the vector containing the Cartesian coordinates, the probability for unrestricted self-diffusion can be obtained [3].

$$P_s(\boldsymbol{r}|\boldsymbol{r}', t) = (4\pi Dt)^{-\frac{3}{2}} exp\{-(\boldsymbol{r}' - \boldsymbol{r})^2/4Dt\} \tag{3.10}$$

This is the probability of self motion for pure diffusive motion that is detected by PGSE NMR. Equation (3.10) is for addition of displacement by velocity to the molecular diffusion yields for the average propagator:

$$P_s(\boldsymbol{R}, t) = (4\pi Dt)^{-\frac{3}{2}} exp\{-(\boldsymbol{R} - vt)^2/4Dt\} \tag{3.11}$$

For only the *z*-direction the self-correlation becomes:

$$P_s(\boldsymbol{Z}, t) = (4\pi Dt)^{-\frac{1}{2}} exp\{-(\boldsymbol{Z} - v_z t)^2/4Dt\} \tag{3.12}$$

Equation (3.10 - 16) shows that the propagators are Gaussian for diffusion and constant velocity as plotted against displacement.

The auto correlation function is a self correlation function. On the molecular level the auto correlation function shows how a molecular quantity is correlated with itself (3.13).

$$G(t) = \int_0^\infty A(t')A(t' + t)dt \tag{3.13}$$

$A(t')$ is any molecular quantity, velocity for example [3]. When that quantity is integrated over for all possible times it can be determined how the molecular quantity is correlated. If the physical process measured is stationary, the autocorrelation function is independent of the initial starting time. It is therefore the time increment that matters and not the start time, because of this (3.13) is now:

$$G(\tau) = \int_0^\infty A(0)A(\tau)d\tau \tag{3.14}$$

Observation of one particle for $G(\tau)$ over a long time $\tau = t' - t$ will represent the full dynamics of all the particles. Therefore, an ensemble average over all particles will represent $G(\tau)$ as well (3.15).

$$G(\tau) = \overline{A(0)A(\tau)} \tag{3.15}$$

For instance, the velocity correlations can be determined by appropriately substituting velocity functions in place of $A(t)$. It can then be determined how v_z at a specific

observation time, τ, correlates to the initial velocity $v_z(0)$. Additional information is gathered from the correlation time scale τ_c which is

$$\tau_c = \frac{\overline{v_z(0)v_z(\tau)}}{\overline{(v_z(0))^2}} \tag{3.16}$$

where $\overline{v_z(0)^2}$ is the velocity correlation intensity. Using the Wiener-Khintchine theorem, $G(\tau)$, has a Fourier relationship with the power spectrum of the diffusion coefficient (3.17) [24].

$$G(\tau) = \int_{-\infty}^{\infty} D_{\alpha\beta}(\omega) exp^{i\omega\tau} d\omega$$

$$D_{\alpha\beta}(\omega) = \frac{1}{2\pi}\int_{-\infty}^{\infty} G(\tau) exp^{-i\omega\tau} d\tau \tag{3.17}$$

where $D_{\alpha\beta}(\omega)$ is the diffusion tensor. If the velocities are substituted in place of $G(\tau)$ and we are only concerned with isotropic diffusion of the long time limit zero-frequency component (ω = 0), (3.17) becomes [24]:

$$D_{zz}(0) = \int_0^{\infty} \overline{v_z(0)v_z(t)} dt \tag{3.18}$$

and

$$D_{zz}(0) = \overline{v_z{}^2}\tau_c \tag{3.19}$$

Echo Signal of Narrow-Pulse Self-Diffusion and Flow

The following will address the collection of the NMR signal and how it relates to the previous discussion of probabilities of translational motion. The collected signal is the echo that results from a PGSE experiment. In discussing the echo signal it is convenient to define a reciprocal space to displacement, ***q***-space (3.20) [3].

$$\boldsymbol{q} = \frac{\gamma \delta \boldsymbol{g}}{2\pi} \tag{3.20}$$

Traversing $\boldsymbol{q}$-space by incrementing the gradient amplitude, $\boldsymbol{g}$, or modulating the time the gradient is applied δ will give the full spectrum of phase modulations related to the translational motion of the sample. The echo signal as a function of $\boldsymbol{q}$-space is [3]

$$E_{\Delta}(\boldsymbol{q}) = \int \overline{P_s}(\boldsymbol{R}, \Delta) exp(i2\pi \boldsymbol{q} \cdot \boldsymbol{R})\, d\boldsymbol{R} \tag{3.21}$$

The signal is acquired in $\boldsymbol{q}$-space. A Fourier transform will transform (3.21) to get the propagator $\overline{P_s}(R, \Delta)$ as a function of time and dynamic displacement in terms of the signal. Using equation (3.12) for molecular self-diffusion and constant velocity and substituting into (3.21), the signal becomes

$$E_{\Delta}(\boldsymbol{q}) = \int_{-\infty}^{\infty} (4\pi D t)^{-\frac{1}{2}} exp\{-(\boldsymbol{Z} - \boldsymbol{v_z t})^2 / 4Dt\} exp(i2\pi \boldsymbol{q Z})\, d\boldsymbol{Z} \tag{3.22}$$

The Fourier transform of equation (3.22) is simply

$$E_{\Delta}(\boldsymbol{q}) = \exp\left(-4\pi^2 \boldsymbol{q^2} D\Delta + i2\pi \boldsymbol{q} v_z \Delta\right) \tag{3.23}$$

It is clear that the signal has two components. The first term is signal attenuation that comes from diffusive (incoherent motion) and the second is the phase shift that comes from the velocity (coherent motion). This simple relation between the signal from diffusion and signal from velocity allows for both types of translational motion to be resolved simultaneously. For gradient pulses of finite length in δ, equation (3.23) has an effective displacement time (Δ-δ/3) substituted in place of Δ in the diffusion term [2, 3].

Resolution of $\boldsymbol{q}$-space and Comparison to $\boldsymbol{k}$-space

The resolution of $\boldsymbol{k}$-space has been previously discussed in Chapter 2. The resolution of $\boldsymbol{q}$-space and the comparison to $\boldsymbol{k}$-space is discussed here. For $\boldsymbol{q}$-space

imaging motion sensitivity is measurable. Here ***q***-space imaging is defined as using diffusion sampling of the structure to generate diffraction effects in the spin echo signal thus giving information on the spatial characterization of the structure [3, 28]. Therefore ***q***-space imaging uses motion to image the sample whereas motion during ***k***-space imaging limits resolution. For ***q***-space imaging, no read gradient is on during the signal collection in a standard PGSE experiment and therefore spectral spreading does not occur. The theoretical resolution limit of ***q***-space imaging is of finer resolution than ***k***-space imaging as is shown below.

For ***q***-space determination of the resolution ΔR is on the order of $\Delta R_o/N$. The total range of dynamic displacements is ΔR_o. Substitution of the ***q***-space resolution into the ***k***-space resolution for the number of pixels N gives [3]:

$$\Delta R \sim \left(\frac{\Delta R_o}{r_o}\right) \Delta r \tag{3.24}$$

The resolution for ***k***-space imaging, Δr, is given in equation (2.29) and substitution of this into (3.24) gives the order of the resolution for ***q***-space imaging (3.25) [3]

$$\Delta R \sim \left(\frac{\Delta R_o}{r_o}\right) \left(\frac{Signal}{Noise}\right)^{\frac{1}{2}} \sigma^{\frac{1}{2}} \Delta z^{-\frac{1}{2}} T_2^{-\frac{1}{4}} \tag{3.25}.$$

Therefore the resolution of ***q***-space is a factor of the ***k***-space resolution. The factor, $\Delta R_o/r_o$ is most often a reducing factor because the total range of dynamic displacements ΔR_o typically is smaller than total width of the image slice r_o. This means that the resolution of ***q***-space is much better than ***k***-space and can be infinitely better as indicated by the reducing factor. A limit does exist, however, because of hardware limitations in the NMR spectrometer [3].

Restricted Diffusion

The techniques of ***q***-space imaging can be used to probe very small scale regions of restricted diffusion such as those in porous media. NMR techniques continue to be developed to better probe the complex nature of porous media [29-44]. The theory is developed beginning with diffusion in a box and later discussed in a sphere. It is desired to determine the long displacement time limit $\left(\Delta \gg \frac{a^2}{D}\right)$ of diffusion in the box of dimensions as shown in Figure 3.8.

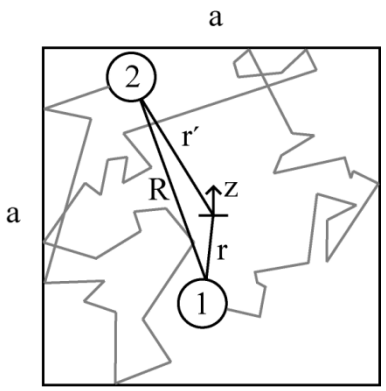

Figure 3.8: Long time limit restricted diffusion in a square box of dimension a

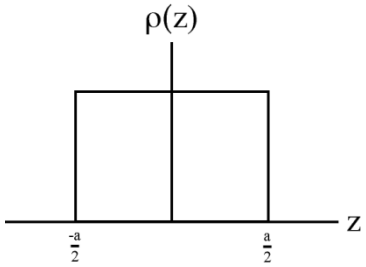

Figure 3.9: Spin density as a function of the *z* coordinate after figure 7.4 of [3].

In the long time limit the molecules can displace throughout the entire box having sampled the walls many times. Additionally, the density of spins as a function of the z coordinate in a square box is constant as shown in Figure 3.9.

Enough time has evolved that displacement vector $\boldsymbol{r}'$ is no longer correlated to the initial position vector $\boldsymbol{r}$. In other words, all memory of the initial position has been lost in the final position. As a result, the probability of motion from $\boldsymbol{r}$ to $\boldsymbol{r}'$ is equivalent to the density at the position $\boldsymbol{r}'$ (3.26).

$$P_s(\boldsymbol{r}|\boldsymbol{r}', \infty) = \boldsymbol{\rho}(\boldsymbol{r}') \tag{3.26}$$

The result of equation (3.26) is then plugged into the average propagator of equation (3.1) and adapted to for the single coordinate dimensions of the box.

$$\overline{P_s}(\boldsymbol{Z}, \infty) = \int_{a-z}^{a+z} \rho(\boldsymbol{r}')\rho(\boldsymbol{r})\, d\boldsymbol{r} \tag{3.27}$$

It is noted that equation (3.27) is the autocorrelation function of the density and the long time limits are the basis of the terminology $\boldsymbol{q}$-space imaging [3, 28]. In the long time limit the autocorrelation of the density is 1 and equation (3.27) integrates to [3]:

$$\overline{P_s}(\boldsymbol{Z}, \infty) = \begin{cases} \frac{a+\boldsymbol{Z}}{a^2}, & -a \leq \boldsymbol{Z} \leq 0 \\ \frac{a-\boldsymbol{Z}}{a^2}, & 0 \leq \boldsymbol{Z} \leq a \end{cases} \tag{3.28}$$

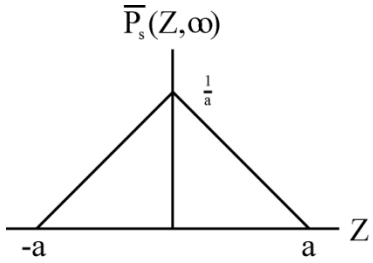

Figure 3.10: Average propagator of a square box as a function of $\boldsymbol{Z}$ after figure 7.4 of [3].

Equation (3.28) is normalized by the area of the box, a^2. This results in zero probability of displacement near the walls and the highest probability in the center of the box at $\boldsymbol{Z} = 0$ (Figure 3.10). The mean square displacement of molecules inside the box can be determined from (3.7) which results in equation (3.29) for a free diffusion Gaussian distributed process.

$$\overline{\overline{\boldsymbol{Z}^2}} = \int_{-\infty}^{\infty} \boldsymbol{Z}^2 \overline{P}_s(\boldsymbol{Z}, \infty)\, d\boldsymbol{Z} \tag{3.29}$$

Here however diffusion is restricted by the dimensions of the box and so the corresponding limits are inserted. The results of (3.28) are also substituted into (3.29) and the mean square displacement becomes one sixth of the area of the box (3.30).

$$\overline{\overline{\boldsymbol{Z}^2}} = \int_{-a}^{0} \boldsymbol{Z}^2 \frac{a+\boldsymbol{Z}}{a^2} d\boldsymbol{Z} + \int_{0}^{a} \boldsymbol{Z}^2 \frac{a-\boldsymbol{Z}}{a^2} d\boldsymbol{Z} = \frac{1}{6} a^2 \tag{3.30}$$

The signal from the NMR experiment as determined by equation (3.21) is:

$$E_\infty(\boldsymbol{q}) = \iint \rho(\boldsymbol{r}')\rho(\boldsymbol{r}) exp\big(i2\pi \boldsymbol{q} \cdot (\boldsymbol{r}' - \boldsymbol{r})\big)\, d\boldsymbol{r}' d\boldsymbol{r} \tag{3.31}$$

The components of $\boldsymbol{r}$ and $\boldsymbol{r}'$ can be separated where each integral relates to one signal amplitude in reciprocal space, $S(\boldsymbol{q})$, at a different phase shift [3].

$$E_\infty(\boldsymbol{q}) = \int \rho(\boldsymbol{r})\, exp\big(-i2\pi \boldsymbol{q} \cdot (\boldsymbol{r})\big) d\boldsymbol{r} \int \rho(\boldsymbol{r}')\, exp\big(i2\pi \boldsymbol{q} \cdot (\boldsymbol{r}')\big) d\boldsymbol{r}'$$

$$E_\infty(\boldsymbol{q}) = S^*(\boldsymbol{q}) S(\boldsymbol{q}) = |S(\boldsymbol{q})|^2 \tag{3.32}$$

$|S(\boldsymbol{q})|^2$ is the intensity. By squaring the amplitude signal and only observing the intensity, phase information is lost. Phase information would allow spatial imaging. However, a dynamic measurement of the dimensions such as the absolute size of the box by Fourier transforming the signal intensity is still possible. This is useful in probing dimensions of structures in systems such as porous media. The Fourier transform of the signal intensity from the box example would result in Figure 3.10. A Fourier transform

of the non-squared signal would result in the spin density, Figure 3.9. Because the signal is squared this causes a loss of information for this ***q***-space imaging process, however the resolution is theoretically infinite subject to hardware gradient amplitude limits, as previously discussed.

Two examples, restricted diffusion in a box and a sphere are discussed [3]. The echo signal for a restricted diffusion in a box is

———— (3.33).

For a sphere, the echo signal is:

– (3.34)

Equating (3.34) to the attenuation result from a Stejskal-Tanner PGSE diffusion process gives:

– (3.35)

The apparent diffusion can then be calculated from (3.35).

— (3.36)

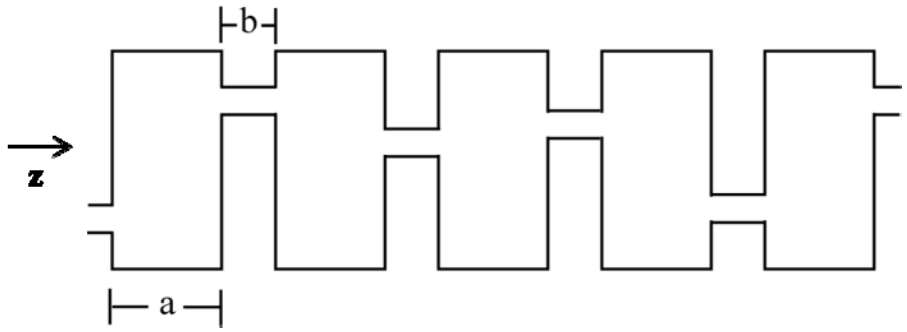

Figure 3.11: Connected network of square boxes aligned with the *z*-direction after figure 7.8 of [3]

The theory can be expanded from a single pore of restricted diffusion to a connected network of pores [3, 31]. For a model of connected boxes, the throat length connecting the boxes is *b* and the network is conveniently lined up with the magnetic field gradient. All pores and connecting throats align with the *z*-direction (Figure 3.11).

The function for the spin density, $\rho_o(\boldsymbol{z})$, for the box network is a convolution of two functions. The first function represents the pore density for one pore of dimension *a* plus the pore density of half the throat added to both sides of the pore. The second function is a delta function that turns on at every pore spacing, *b* (Figure 3.12) [3].

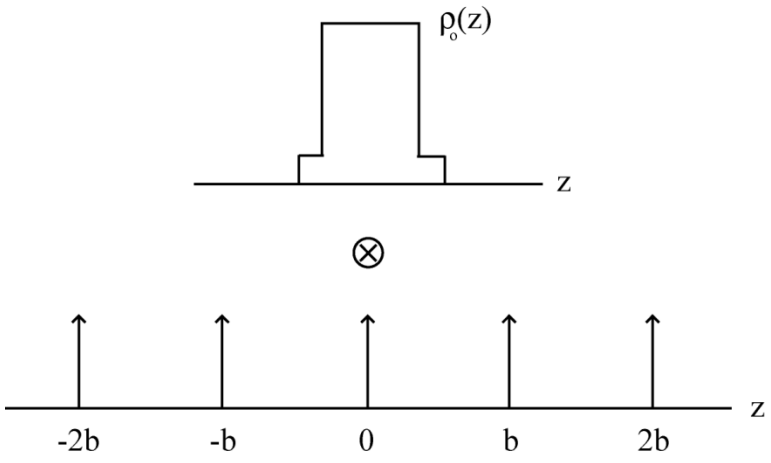

Figure 3.12: The convoluted functions that represent the box connected network after figure 7.8 of [3].

In the connecting throats there is a high probability that the molecules originating in the channels will move the channel length, *b*. This is due to the low volume or limited space to travel inside the throat. The channels act as one dimensional pathways for molecular motion. Therefore, in the long time limit, $\Delta \gg \frac{a^2}{D_o}$, the probability is high that a molecule will cause a phase shift due to a relatively large displacement. In the pore

space, motion is far less restricted because there is a larger volume in the pore than in the connecting channels. The motion can be more random and of smaller total displacement than in the channels. Therefore motion in the box will not have as high of a probability of causing a significant phase shift and resulting signal intensity variation. As in the single box the signal intensity $|S(\boldsymbol{q})|^2$ shows the box dimensions. The box dimensions *a* are larger than the spacing between the pore *b* but both signatures show up in the signal. The resulting echo signal showing both dimensions *a* and *b* is shown in Figure 3.13. The measured echo signal is

$$E_\infty(\boldsymbol{q}) = |S_o(\boldsymbol{q})|^2 \left\{ sinc^2(\pi \boldsymbol{q} N b) \otimes \sum_{n=0}^{\infty} \delta\left(\boldsymbol{q} - \frac{n}{\boldsymbol{b}}\right) \right\} \qquad (3.37).$$

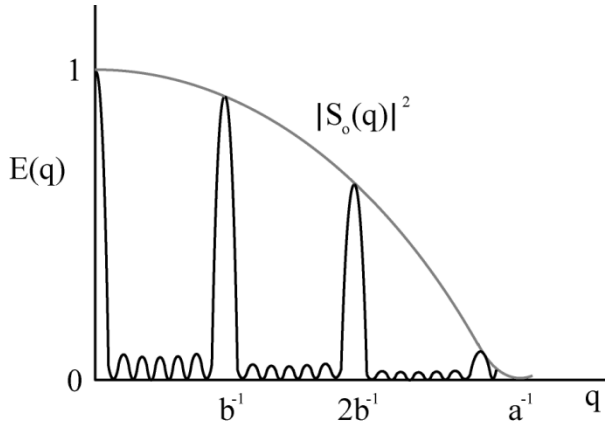

Figure 3.13: Echo signal from the connected box network after figure 7.9 of [3].

Partially Connected Structures

Diverging from the connected network model where all pores are connected in series, the discussion turns to a partially connected structure where pores can have

multiple connections (Figure 3.14). Each pore has an associated density, $\rho_{oi}(\boldsymbol{r}-\boldsymbol{r}_{oi})$. The total density of all the pores *N* is

$$\rho(\boldsymbol{r}) = \frac{1}{N}\sum_{i=1}^{n}\rho_{oi}(\boldsymbol{r}-\boldsymbol{r}_{oi}) \quad (3.38).$$

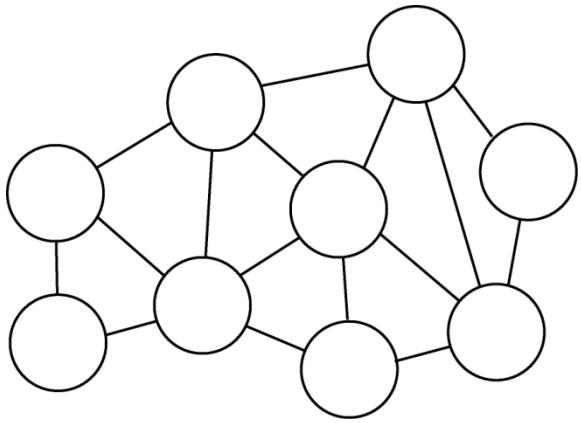

Figure 3.14: Partially connected pore network after figure 7.10 of [3].

The echo signal is then

$$E_{\infty}(\boldsymbol{q}) = \frac{1}{N^2}\sum_{i=1}^{N}\sum_{j=1}^{N}\iint \rho_{oi}(\boldsymbol{r}-\boldsymbol{r}_{oi})\rho_{oi}(\boldsymbol{r}'-\boldsymbol{r}_{oj})exp\big(-i2\pi\boldsymbol{q}\cdot(\boldsymbol{r}'-\boldsymbol{r})\big)d\boldsymbol{r}'d\boldsymbol{r} \quad (3.39).$$

The above echo signal represents a pore matrix in which all of the pores are connected to each other. This is not realitic, so a connection matrix C_{ij} is defined. The connection matrix is zero for pores *i* and *j* that are not connected, but is equal to 1 when *i* and *j* are connected in the pore structure. Additionally, the probability for molecules in pore *i* moving to pore *j* is:

$$P_{si}(r|r',\Delta) = \sum_{j=1}^{n} C_{ij}\rho_{oi}(\boldsymbol{r}-\boldsymbol{r}_{oi}) \quad (3.39)$$

Inserting this result into the echo signal gives:

$$E_\infty(\boldsymbol{q}) = \frac{1}{N}\iint \rho(\boldsymbol{r}) C \rho^T(\boldsymbol{r}') exp\big(-i2\pi \boldsymbol{q}\cdot(\boldsymbol{r}'-\boldsymbol{r})\big) d\boldsymbol{r}' d\boldsymbol{r} \tag{3.40}$$

To test this approach and determine if the results match with previous theory, the connection matrix is set to a diagonal matrix [3]. Physically, this represents a structure in which no pores are connected and only the terms $i = j$ are 1 meaning that a pore is connected to itself. $C_{ii} = N$and the density ρ_{oi} has no correlation to ρ_{oj}. Substituting into (3.40) and reducing gives the echo signal as the addition of signal from N boxes. This aligns with the results from the approach using restricted diffusion in a single box

$$E_\infty(\boldsymbol{q}) = \frac{1}{N}\sum_{i=1}^{N} |S_{oi}(\boldsymbol{q})|^2 \tag{3.41}.$$

An important component of diffusion in porous media is the time scale for which a molecule samples the structure. For a single pore the correlation time is associated with the time it takes for a molecule to sample the entire length scale *a*. Dividing the length scale squared by the molecular diffusion coefficient D_o gives the correlation time, $\tau \sim \frac{a^2}{D_o}$.

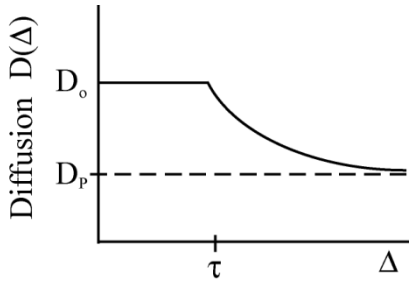

Figure 3.15: Diffusion coefficient in a porous media

For a structure with connected pores the mean squared displacement and its corresponding effective diffusion coefficient $D(\Delta)$ changes as the molecule samples the throats and other pores. This occurs at times $\Delta >> \tau$ and a new diffusion coefficient is

defined as D_p. For times much greater than τ, the coefficient $D(\Delta)$ will asymptotically approach a constant D_p and effectively measure the permeability of the porous media (Figure 3.15). If the porous media has no connected pores, the diffusion coefficient would approach zero, but for a connected network will D_p approach some value. For pores conveniently aligned with the applied gradient, the connection matrix can be approximated by:

$$C_{ij} = b(4\pi D_P \Delta)^{\frac{1}{2}} exp[-(j-i)^2 b^2 / 4 D_P \Delta] \tag{3.42}$$

The echo will then be:

$$E_\Delta(\boldsymbol{q}) = \frac{1}{N}\sum_{i=1}^{N}\sum_{j=1}^{N} C_{ij} exp\left[i2\pi \boldsymbol{q}\cdot\left(\boldsymbol{z_{oj}} - \boldsymbol{z_{oi}}\right)\right] S_{oi}^{*}(\boldsymbol{q}) S_{oj}(\boldsymbol{q}) \tag{3.43}$$

If pores are equivalent in size and shape then the signal as a function of $\boldsymbol{q}$ in the later part of (3.43) reduces to $|S_{oi}(\boldsymbol{q})|^2$. If the pores are not congruent then an average pore structure factor can be defined as $\overline{|S_{oi}(\boldsymbol{q})|^2}$. Making the appropriate substitutions and reworking (3.43) gives the echo in the form of a convolution of a diffusive envelope $\left(d(\boldsymbol{Z},\Delta)\right)$ with a lattice correlation function $\left(L(\boldsymbol{Z})\right)$ all multiplied by the form factor $\left(\overline{|S_{oi}(\boldsymbol{q})|^2}\right)$ [3]

$$E_\Delta(\boldsymbol{q}) = \overline{|S_{oi}(\boldsymbol{q})|^2}[\mathcal{F}\{d(\boldsymbol{Z},\Delta)\} \otimes \mathcal{F}\{L(\boldsymbol{Z})\}] \tag{3.44}.$$

The echo signal is of the form of Figure 3.16. At high $\boldsymbol{q}$ values the echo reveals the shortest range of motions correspond to the pore dimensions. The low $\boldsymbol{q}$ values reveal the longest range motions that are found in throats. The width of the individual peaks also give information corresponding to $(D_P\Delta)^{-1}$.

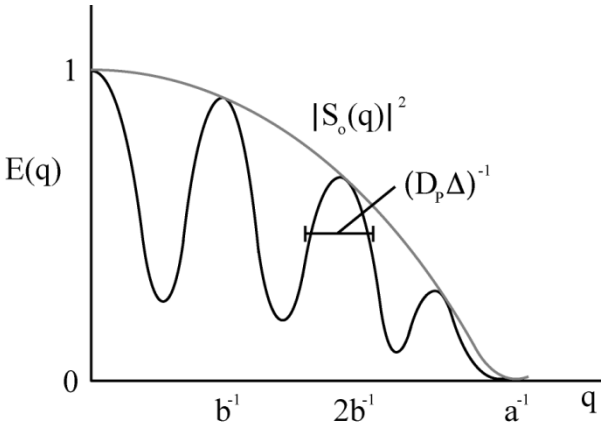

Figure 3.16: Echo signal from the connected box network after figure 7.11 of [3]

Consider two molecules contained in a structure composed of two connected pores (Figure 3.17). If the first molecule at position 1 labeled 1_1 took an equal amount of time to get to position 2 (1_2) as did 2_1 to 2_2, then molecule 1 has moved a greater distance than molecule 2. A lower ***q*** value is needed to encode for a phase change due to the larger translational motion of molecule 1. Molecule 2 did not translate as far and thus a larger ***q*** value is needed to encode a phase shift that can be resolved.

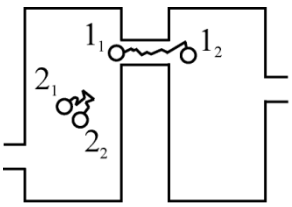

Figure 3.17: Diffusion of 2 molecules to show low and high ***q*** encoding

Susceptibility Inhomogeneities

This section discusses the magnetic susceptibility differences within a heterogeneous porous media. The solid-liquid (fluid) interfaces generate local magnetic

fields which diphase magnetization as molecules diffuse through the structure. Use of this model or the surface sink model depends on the structure, but can also be determined by observations in T_1 and T_2. Indication of susceptibility effects is seen if $T_2 << T_1$. Additionally, by separately observing T_1 and T_2 the influences of surface sinks or susceptibilities inhomogeneities can be independently determined.

Small changes to the magnetic field $\boldsymbol{B}_o$ cause frequency offsets corresponding to the local inhomogeneity of the magnetic field. The change in frequency, $\Delta\omega_o$, becomes a function of the time molecules diffuse within the inhomogeneous field and also dependent on the local field fluctuation $\Delta\boldsymbol{B}_o$

$$\Delta\omega_o(t) = \gamma\Delta\boldsymbol{B}_o(t) \tag{3.45}$$

The rate of the frequency fluctuations is characterized by a correlation time:

$$\tau_c = \int_0^\infty \frac{\overline{\Delta\omega_o(t)\Delta\omega_o(t-\tau)d\tau}}{\overline{\Delta\omega_o{}^2}} \tag{3.46}$$

For a porous media, the correlation time is on the order of l_g^2/D where l_g is the correlation length for $\Delta\boldsymbol{B}_o$ which is on the order of the pore size. Two regimes are defined in relation to the correlation time. The first corresponds to rapid fluctuations and the second is the slow fluctuation regime[3]. The rapid regime is defined as

$$\frac{1}{\tau_c} \gg \left(\overline{\Delta\omega_o{}^2}\right)^{\frac{1}{2}} \tag{3.47},$$

while the slow regime is

$$\frac{1}{\tau_c} \ll \left(\overline{\Delta\omega_o{}^2}\right)^{\frac{1}{2}} \tag{3.48}.$$

If $\Delta\omega_o$ changes slowly due to slow diffusion, then in a PGSE experiment there is a good chance that it hasn't fluctuated between the two pulses. Thus the effects of the

inhomogeneity can be refocused. The additional $\Delta \boldsymbol{B}_o$, however, causes broadening in the frequency signal and is termed inhomogeneous broadening. For fast diffusion and correspondingly rapid fluctuations of $\Delta\omega_o$, there is a good chance that a phase shift has occurred during the PGSE experiment because of $\Delta\omega_o$. This randomly fluctuated phase shift cannot be refocused and leaves a residual phase shift. The resulting FID and Echo for the rapid fluctuations are:

$$G(t) = exp\left(-t\overline{\Delta\omega_o{}^2}\tau_c\right) \tag{3.49}$$

$$E(2\tau) = exp\left(-2\tau\overline{\Delta\omega_o{}^2}\tau_c\right) \tag{3.50}$$

The resulting FID and Echo for the slow fluctuations are:

$$G(t) = exp\left(-\frac{1}{2}\overline{\Delta\omega_o{}^2}t^2\right) \tag{3.51}$$

$$E(2\tau) = exp\left(-\frac{2}{3}\overline{\Delta\omega_o{}^2}\frac{1}{\tau_c}\tau^3\right) \tag{3.52}$$

where the τ^3 time dependence of the diffusive attenuation in the susceptibility fields is shown in (3.61).

Velocity Maps

Velocity measurements take only the phase information of the signal and not the signal attenuation which is due to diffusion. For the work in this dissertation, velocity maps were made using a pulse sequence that combined imaging (discussed in Chapter 2) and PGSE. The velocity mapping acquired two *q*-space planes of phase information. For each point in the plane a difference of phase information resulted in velocity information for the respective pixel. The differences for all pixels resulted in a velocity map. More

details of the velocity map pulse sequence are shown in later chapters as well as a diagram of the pulse sequence.

FLUID DYNAMICS IN COMPLEX SYSTEMS

Introduction to Critical and Supercritical Fluids

A supercritical fluid (SCF) is a fluid above its critical temperature, pressure, and density [45]. A fluid in this state has properties simultaneously similar to that of gases and liquids. A SCF has transport properties such as diffusivities and viscosities similar to that of the gas phase while densities resemble those similar to the liquid phase. These qualities, make SCF's a novel environmentally safe solvent with beneficial transport properties [46].

Many SCF solvents, such as CO_2, have less environmental impact than current petroleum based solvents [47]. Although a greenhouse gas, CO_2 is naturally occurring and often an unavoidable byproduct of some processes. Its abundance and lower environmental toxicity makes CO_2 a viable option for use as a SCF for processing, including food processing [48]. Enhanced Oil Recovery (EOR) utilizes supercritical CO_2 to force out oil that has saturated porous rock [49-51], and many other supercritical fluid extraction (SFE) and chromatography (SFC) processes which employ the transport and solubility advantages of supercritical fluids [52, 53]. Storage of CO_2 in a supercritical state in earth formations is currently being implemented and assessed as a means to reduce atmospheric CO_2 to combat global climate change [49, 54-56].

The properties of a SCF are tunable by adjusting the pressure or temperature of the fluid in a range encasing the critical values. Thermophysical properties such as specific heat, density, viscosity, and heat transfer coefficients of CO_2 are shown for a

range of temperature including the critical temperature at a pressure of 8.5MPa which is above the critical pressure in [57]. Experimentally, the effects of the thermophysical properties of a supercritical fluid under flowing conditions against and with gravity have been well studied [58-61]. At a threshold, buoyancy in the fluid begins to impact the heat transfer and mass transport. Much work has been performed to numerically or theoretically [62-71] predict and validate the thermophysical behavior of near critical fluids including buoyancy effects [72-76]. Recently some focus has shifted from larger scale experiments to mini-tubes [77] and porous tubes [57, 78, 79]. The work thus far has validated numerical and theoretical models with thermophysical experimental data, but hydrodynamic data is very limited. Spatial velocity distributions of a flowing fluid near the critical point have been theoretically or numerically modeled for turbulent or laminar entrance flows [57, 64, 65, 80-83], but only a few studies provided experimental data [84, 85]. Previously published velocity data used Pitot tubes inserted invasively along a radial line at incremental points of a 22.7 mm ID tube. The experimental velocity maps presented in this paper were taken using non-invasive magnetic resonance MR and provide a full axial slice of spatially and velocity encoded data, not simply a radial line of incremental points.

It has been previously shown using MR that in porous media the critical point occurred at lower temperatures in the pore spaces than compared to the critical temperature of the bulk fluid and the shifted critical temperature inside the pores was directly related to the void size [86, 87]. The previous MR work discussing SCF in porous media was for non-flowing conditions. Little work has been performed using MR

with to study flow of SCF's. One recent exception was the application of MR to obtain signal intensity and relaxation components in the porous media [88]. Spatial velocity information was not obtained. The need exists to quantifiably analyze SCF fluid transport due to the wide and projected use of flowing SCF for applications other than heat transfer. MR has been used in supercritical applications to detect ^{1}H solute spectra in supercritical CO_2 solvent using supercritical fluid chromatography (SFC) equipment [47, 52, 53, 89]. The first application of MR to flowing supercritical fluids in a capillary and model porous media with the purpose of obtaining transport properties and flow dynamics has recently been reported [16] and here the detailed analysis of capillary flow is undertaken.

Equations and Modeling of Critical Fluids

The Navier-Stokes equations for continuity, momentum, and energy are used for compressible flow of a supercritical fluid in a cylindrical tube of two dimensions. This system of Navier-Stokes equations works well for laminar flow, but can also be time and Favre (density weighted average) averaged to model compressible flow [64] and account for temperature and buoyancy dependent material properties. The equations of continuity (4.1), momentum (4.2), and energy (4.3):

$$\frac{\partial(r\rho u)}{\partial x} + \frac{\partial(r\rho v)}{\partial r} = \mathbf{0} \tag{4.1}$$

$$\rho u\frac{\partial u}{\partial x} + \rho v\frac{\partial u}{\partial r} = \frac{1}{r}\frac{\partial}{\partial r}\left(r\mu\frac{\partial u}{\partial r}\right) - \rho g - \frac{dp}{dx} \tag{4.2}$$

$$\rho u\frac{\partial h}{\partial x} + \rho v\frac{\partial h}{\partial r} = \frac{1}{r}\frac{\partial}{\partial r}\left(r\frac{\lambda}{C_p}\frac{\partial h}{\partial r}\right) + u\frac{dp}{dx} + \mu\left(\frac{\partial u}{\partial r}\right)^2 \tag{4.3}$$

where ρ is density, u and v are the longitudinal and radial velocity components, respectfully, the specific enthalpy is h, λ is the thermal conductivity, and C_p is the specific heat. The time averaging of Eqns. 3.1 - 3.3 results in mass flux fluctuation terms $\overline{\rho' u'}$ and $\overline{\rho' v'}$ as well as the heat flux fluctuation $\overline{\rho' h'}$ which account for buoyancy induced fluctuations in the time averaged equations [90].

Mixed convection for these supercritical flows deal with forced convection due to a pump causing a pressure gradient across a sample and free convection as a result of buoyancy. The Richardson number Ri (4.4) is a dimensionless parameter which compares the natural convection (buoyancy forces) and the forced convection (inertial forces) using the Grashof number $Gr = \frac{buoyancy\ forces}{viscous\ forces}$ (4.6) and the Reynolds number $Re = \frac{inertial\ forces}{viscous\ forces}$ (4.7). The substitution of Gr (4.6) and the square of Re (4.7) into (4.4) and subsequent reduction results in the Ri number representing the ratio of potential energy to kinetic energy. An empirical correction of $Re^{2.7}$ has been determined for supercritical flow of carbon dioxide (4.5) [91].

$$\boldsymbol{Ri} = \frac{\boldsymbol{Gr}}{\boldsymbol{Re^2}} \tag{4.4}$$

$$\boldsymbol{Ri} = \frac{\boldsymbol{Gr}}{\boldsymbol{Re^{2.7}}} \tag{4.5}$$

where [64, 91]:

$$\boldsymbol{Gr} = \frac{(\boldsymbol{\rho_b - \bar{\rho}})\boldsymbol{\rho_b} \boldsymbol{g} \boldsymbol{D^3}}{\boldsymbol{\mu_b^2}} \tag{4.6}$$

$$\boldsymbol{Re} = \frac{\boldsymbol{\rho_b} \boldsymbol{u} \boldsymbol{D}}{\boldsymbol{\mu_b}} \tag{4.7}$$

$$\overline{\boldsymbol{\rho}} \approx \begin{cases} \frac{(\boldsymbol{\rho_w + \rho_b})}{\boldsymbol{2}}, & \boldsymbol{T_w > T_{pc}\ or\ T_b < T_{pc}} \\ \frac{[\boldsymbol{\rho_b}(\boldsymbol{T_b - T_{pc}}) + \boldsymbol{\rho_w}(\boldsymbol{T_{pc} - T_w})]}{\boldsymbol{T_b - T_w}}, & \boldsymbol{T_w < T_{pc} < T_b} \end{cases} \tag{4.8}$$

At high mass flow rates, forced convection dominates the dynamics of the flowing system. At low mass flow rates, free convection dominates. A threshold therefore separates the two influencing regimes and has been empirically determined for carbon dioxide (4.9) [91]. Richardson numbers above 10^{-5} for carbon dioxide indicate buoyancy influenced dynamics. For other fluids, the threshold will be different.

$$\boldsymbol{Ri} = \frac{\boldsymbol{Gr}}{\boldsymbol{Re^{2.7}}} > \boldsymbol{10^{-5}} \tag{4.9}$$

Bae *et al.* used the Navier-Stokes equations and solved them numerically in a computational fluid dynamics code [64]. Eight *Ri* numbers were tested by varying the tube diameter and the flow direction (up or down) or convection type (forced or mixed) was also altered. For each case density, viscosity, temperature, friction coefficient, and velocity profiles as a function of the radial coordinate were observed. Of relevance to the work presented here is the velocity profile and density as a function of radius in the fully developed flow region far from the tube entrance $\left(\frac{L}{D_v} = 27.52\right)$. This case was for mixed upward convection of CO_2 with heating at the wall of a 2 mm diameter tube and the following conditions: P = 8 MPa, T = 301.15 K, Re = 5400, and $Pr = \frac{v}{\alpha} = \frac{kinematic\ viscosity}{coeff.\ of\ thermal\ expansion} =$ 3.08 [64].

The time averaged density as a function of radial position showed that the heating of the walls clearly decreases the density near the walls and causes a gradient in the density leading to an evolution of buoyancy. For laminar flow a decrease in *Re* number causes the density gradient as a function of the radial position to shift. The drop in density near the pseudocritical point shifts toward the tube center for decreasing *Re* number [83].

It is the region spanning the pseudocritical point that can have the greatest fluctuations in density caused by temperature or pressure fluctuations. Small changes in pressure can cause large fluctuations in density near the critical point, *i.e*. the slope of the critical isotherm on a pressure vs. density phase diagram becomes 0 ($dP/d\rho = 0$) [92]. This states that at the critical pressure and the critical temperature large fluctuations of density are present. Bae *et al.* numerically observed the fluctuating density ρ' for upward flow in a tube near the wall [64]**.** The rms density fluctuations divided by the mean density show that there is little density fluctuation at the center of the pipe. At the wall however where the temperature and pressure is nearest the pseudocritical point, the density fluctuates up to ~55% of the mean density.

The density fluctuations in the critical range can be modeled stochastically using concepts of critical phase transition dynamics. Nonlinear Langevin equations arise for the evolution of an order parameter, *e.g.* density fluctuation [76, 93]. For a binary fluid such as CO_2 or C_2F_6 in the gas-liquid states a conserved order parameter model, termed Model H is proposed [76]. Model H equations define all pertinent variables such as density, diffusive flux, viscosity, and etc. under dynamic conditions. The group of equations (4.10) shown are a portion of the complex system of equations composing Model H.

$$\frac{\partial \psi}{\partial t} = \boldsymbol{L_o \nabla^2 \frac{\delta \beta \mathcal{H}}{\delta \psi} - \nabla \cdot (\psi v) + \theta} \tag{4.10}$$

$$\rho \frac{\partial v}{\partial t} = \eta_o \nabla^2 v - \left(\psi \nabla \frac{\delta \mathcal{H}}{\delta \psi}\right)_{\perp} + (\zeta)_{\perp}$$

$$\langle \theta(r,t), \theta(r',t') \rangle = -2L_o \nabla^2 \delta(r-r')\delta(t-t')$$

$$\langle \zeta_i(r,t), \zeta_j(r',t') \rangle = -2T\eta_o \delta_{ij} \nabla^2 \delta(r-r')\delta(t-t')$$

$$\psi = \rho_B - \rho_A$$

where t is time, v is velocity, ρ is density, L_o and $\boldsymbol{\beta}$ are transport coefficients, $\mathcal{H}$ is the Hamiltonian energy of the system, and η_o is the viscosity. The last terms in the first two equations of (4.10), θ and $(\zeta)_\perp$ are delta correlated noise terms that account for the stochastic fluctuations of density and concentration flux, respectively. The order parameter,ψ, approaches 0 near the critical point where the strongest fluctuations in density occur. These fluctuations in fact occur over some length scale increasing in size as the critical temperature is approached from below. This length scale of fluctuations is defined by the correlation length (4.11). The correlation length is a characteristic length separating two points in a system at which a molecular quantity between the two points no longer has memory of the previous state. In binary fluid systems far below the critical point, *i.e* gas-liquid equilibrium, the correlation length is of the molecular scale. In a near critical fluid, as the temperature of the system nears the critical temperature, the correlation length diverges (4.11) [76].

$$\boldsymbol{\xi} \propto (\mathbf{T} - \mathbf{T_c})^{-\boldsymbol{\nu}} \tag{4.11}$$

The divergence of the correlation length scale will impact MR measurements of translational dynamics [16] and magnetic relaxation [94]. A typical value for the critical exponent is $\nu = 0.62$ [76]. A striking example of this divergence in length scale of fluctuations in density is critical opalescence in a near critical fluid when this length scale becomes greater than the wavelength of light (> 500 nm) [92]. The impact of the fluctuating density on the hydrodynamics has not been analyzed in detail.

Several fluids near their critical points have been experimentally studied to map out the thermodynamic dependence of correlation lengths [95-98]. The divergence of the correlation length scale corresponds to the "critical slowing down" as observed in near critical fluids [97]. It is at this point that the diffusion of molecules slows and the distance traveled increases. An autocorrelation function for CHF_3 showed the decreased "memory loss" of molecular correlations near the critical temperature [97]. The "critical slowing down" is observed in the increased time for the correlation to decay as the temperature ratio T/T_c approached the critical temperature ratio of $T/T_c = 1$[97]. For further discourse as well as reviews on supercritical fluids and/or Model H, the reader is referred to more complete sources [45, 72, 73, 75, 76, 93, 95-97, 99, 100].

Shown in the numerical simulation of spatial velocity distributions of [64], the velocity is strongly dependent on density fluctuations near the critical point and inducing buoyancy effects. For upward flow against and downward flow aligned with the direction of the gravitational force previous work [57, 60, 61, 64, 67, 69, 70, 77-82, 90, 101] is discussed as a reference to the work presented in this dissertation. At a sufficient length along a tube so that the velocity is fully developed, the spatial velocity distribution develops an "M" shape that maintains mass conservation and energy. Experimentally Kurganov and Kaptil'ny [85] have studied this and numerically simulations have been conducted [57, 60, 65, 77-79, 90, 101].

Flow against and with gravity near the critical point has been compared reverse the effects of buoyancy relative to the pressure driven flow direction [60]. Numerical studies performed for a tube with wall cooling illustrate the differences [60]. For wall

cooling and upward flow against gravity, the velocity near the wall "slows" and shows an inflection point in the velocity profile corresponding to a more dense fluid near the walls than compared to the fluid in the center of the pipe [60]. The buoyancy force is largest in the center of the tube because of the lower density and acceleration is seen in this region. For the downward flow with gravity, the more dense fluid near the walls is impacted by gravity and shows an increase in velocity [60]. In the center of the tube, the fluid is not as dense and is more buoyant. The buoyancy force is upward against the downward flow direction and shows exactly the opposite results of what has been observed for wall heating.

Partially Saturated Porous Media Theory

The modeling of imbibition and drainage of fluids in porous media has led to development of the theory of invasion percolation [102, 103]. The invading fluid generates clusters and structures that exhibit power law size scaling [104]. Much of the theoretical development has focused on transient fluid invasion processes and is reviewed in Chap 12 of the book by Sahimi [105]. The balance of capillary and viscous forces, described by the capillary number [106] $Ca = \frac{\mu v_w}{\sigma}$, provides a characterization of the flow in terms of the physical properties of viscosity μ and surface tension σ and velocity v_w of the wetting fluid. Transient imbibitions and drainage studies have been conducted for liquid-liquid systems such as oil and water [104, 105, 107] and gas-liquid systems such as air and water [108-110]. A primary result of invasion percolation studies is the scaling of the invading fluid saturation $S \propto L^{(D_f-2)}$ where L is the lattice size and D_f is the fractal dimension. The subsequent scaling of cluster size is $N \propto L^{D_f}$ where D_f~1.89

for 2D models and D_f~2.52 for 3D models [103, 104]. Other transient models deal with the scaling of interface thickness with capillary number [108] and power law noise scaling of interface fluctuations [109].

The less studied steady state flow regime represents a continuous interaction between imbibitions and drainage [111]. In this case cluster size distributions exhibit a power law probability distribution with an exponential cutoff $p(l) \sim l^{-2} \exp\left(-{}^{l}/_{l^*}\right)$ where l is the cluster size and l^* is the cutoff cluster size [111-113]. The cutoff cluster length has been shown to scale as a power law with Ca as $l^* \sim Ca^{-\zeta}$ with $\zeta \sim 0.98$ in 2D [113]. The non-wetting fluid saturation has been observed experimentally to decrease with increasing *Ca* and a theoretical explanation is lacking [113]. The dynamics in these experimental studies have been characterized in terms of the dissipation of energy by the fluctuating interfacial area between the wetting and non wetting phases at steady state [112]. This analysis leads to the scaling of pressure drop in the bead pack with capillary number as $|\nabla P| \propto Ca^{\beta}$ with $\beta \sim 0.5$ in 2D experiments [112]. This result is consistent with a physical model in which the wetting fluid flows subject to an effective permeability which varies as $\kappa_{\text{eff}} \sim \sqrt{Ca}$ assuming D'Arcy's law $v_\omega \sim \frac{\kappa_{\text{eff}}}{\mu_\omega} |\nabla P|$ holds [112]. The *Ca* scaling results are related to the idea that the cutoff cluster size l^* represents an extension length for cluster mobility [112]. This is important since in the work of Tallakstad *et al.* [113] it is assumed that the energy dissipation is localized in a dissipative wetting fluid volume $V_d = \frac{dV_{total}}{l^*}$ where d is the grain size of the porous media and l^*, the cutoff length, gives the spacing between the flowing channels of

wetting fluid in channels of width d [112]. In discussion of the dynamics measured by PGSE NMR we will examine the role of the pore size in this context.

While the scaling theory of cluster size distribution and mean field pressure drop have been recently studied experimentally in steady-state partially saturated flows, hydrodynamic dispersion has not been similarly analyzed. De Gennes [114] has presented the detailed theory of hydrodynamic dispersion, the interaction of random diffusive dynamics and coherent advection [115], in partially saturated porous media. The wetting fluid is treated as a percolation cluster with a backbone and dead ends [114]. The theory provides a detailed discussion of the scaling of the dispersion during external steady pressure driven D'Arcy flow in terms of a critical pressure P_c to form an infinite cluster and hence generate fluid flow through the porous medium. The scaling is found to depend on the average fluid velocity of all fluid particles $\bar{v} = \frac{v_S}{s_w}$ where v_S is the superficial velocity $\frac{Q_w}{A}$ and s_w is the wetting fluid saturation level. The dependence on $\bar{v}$ rather than the backbone average velocity $\bar{v}_B = \frac{v_S}{s_B}$ where s_B is the probability of a fluid particle being on the backbone and is an important feature of this model of partially saturated flow [114]. As a result De Gennes [114] finds the longitudinal dispersion scales as $D_{\|} \propto \frac{(\bar{u}\xi)^2}{D_a}$ where $D_a = D_0 \left(\frac{\Delta P}{P_c}\right)^{\bar{t}-\epsilon}$ is the ant in a labyrinth diffusivity, dependent on $\Delta P = P - P_c$, the molecular diffusivity D_0 with scaling exponents $\bar{t}$ - $\epsilon \sim 1.31$, and ξ is the correlation length, or "mesh size of a cluster". The correlation length scales as $\xi \propto d \left(\frac{\Delta P}{P_c}\right)^{-\nu}$ with d the pore size diameter and $\nu \sim 0.9$ [114]. The fact that the scaling of the dispersion $D_{\|}$ is with the average fluid velocity $\bar{v}$ is important since

in NMR measurements of the propagator of motion all fluid particles contribute to the measurement. In this model the correlation length ξ is associated with the maximum size of the dead ends. As a side note it is often missed in the literature that this paper by DeGennes [114] is one of the first to apply nonequilibrium statistical mechanics in the context of the power law waiting time distributions of Montroll and Scher [116] and memory functions to hydrodynamic dispersion. This presages the large body of work in application of nonequilibrium statistical mechanics [117] to porous media transport in the context of continuous time random walks [118] in the last 20 years.

Oscillatory Flow Phenomena in Simple and Complex Fluids

Oscillatory flow occurs in many biomedical and environmental situations and of specific interest are the impacts of pulsatile blood flow. Specific velocity profiles are expected for different fluids under oscillatory flow conditions. In a pipe, Newtonian fluids, such as water, display Poiseuille flow under laminar steady pressure conditions; the Reynolds (*Re*) number is the dimensionless number that characterizes the flow regime. For oscillatory pipe flow, velocity profiles are characterized by the Womersley number, α, which is the ratio of the unsteady forces to the viscous forces [12]:

$$\alpha = R\sqrt{\frac{\omega}{\nu}} \tag{4.12}$$

where R is the tube radius, ω is the oscillatory flow frequency, and ν is the kinematic viscosity of the fluid [12]. In most fluids, a low α will result in a parabolic shaped

velocity profile. Whereas, for a high α the velocity profile is flat and sometimes split as the unsteady forces begin to dominate [13].

The velocity profile of an oscillatory flow can be modeled beginning with the equation of motion in cylindrical coordinates:

$$\rho \frac{\partial v}{\partial t} = -\frac{\partial p}{\partial z} - \frac{1}{r}\frac{\partial}{\partial r}(r\tau) \tag{4.13}$$

where v is the velocity as a function of time, *t,* and radius, *r*, the $\frac{\partial p}{\partial z}$ pressure gradient is applied in the *z*-direction, ρ is the density of the fluid and τ is the shear stress. For a Newtonian fluid, the shear stress can be modeled using a periodic function. The pressure gradient and the velocity profile as a function of the radius can also be modeled using a periodic function. This system of equations has been solved and the results can be found elsewhere [119-121]. The velocity profile is repeatable and stable for relatively low Womersley numbers [120]. At very low Womersley numbers, the velocity profile for the fastest flow rate in the cycle has a nearly parabolic velocity profile with the maximum velocity in the center of the pipe ($r = 0$) [120]. With increasing Womersley numbers or increasing frequency of oscillations, the maximum velocity profile begins to flatten out in the center of the flow and the maximum velocity occurs closer to the pipe walls [119]. The velocity in the center of the tube mimics that of plug like flow and is called an inviscid core. With an increasing Womersley number, this inviscid core grows.

The viscosity of the fluid is an important factor in the Womersley number and can therefore impact the velocity profile. Increasing the dynamic viscosity has a similar affect to decreasing the oscillatory flow frequency. The result is that the maximum

velocity peaks in the profile will be more towards the center of the tube compared to a less viscous fluid in which the maximum velocity peaks are closer to the cylinder walls [122]. A fluid that has visco-elastic or other non-Newtonian behavior can also alter the velocity profile and the results are discussed in greater detail elsewhere [122, 123]. The velocity profiles of complex as well as Newtonian fluids are presented here and were obtained using NMR. The ease with which NMR non-invasively measures these velocity profiles reveals that the method is a convenient way to determine the rheological properties of simple, complex, and physiological fluids under oscillatory flow.

MR VELOCITY MAPS AND PROPAGATORS OF A SUB, CRITICAL, AND SUPERCRITICAL FLUORINATED GAS, C_2F_6, IN A CAPILLARY

Methods

Magnetic resonance microscopy techniques [1-4, 6, 19] were used to obtain velocity maps and propagators over a range of pressures and observation times for flowing and non-flowing fluid. Hexafluoroethane, C_2F_6, was chosen for these studies due to its favorable combination of physical properties, critical temperature T_c = 19.88 ^oC, critical pressure P_c = 30.48 bar (1 bar = .1 MPa) (Figure 5.1) and MR properties of relaxation time, high natural abundance and strong MR signal comparable to proton signal for ^{19}F [5-8].

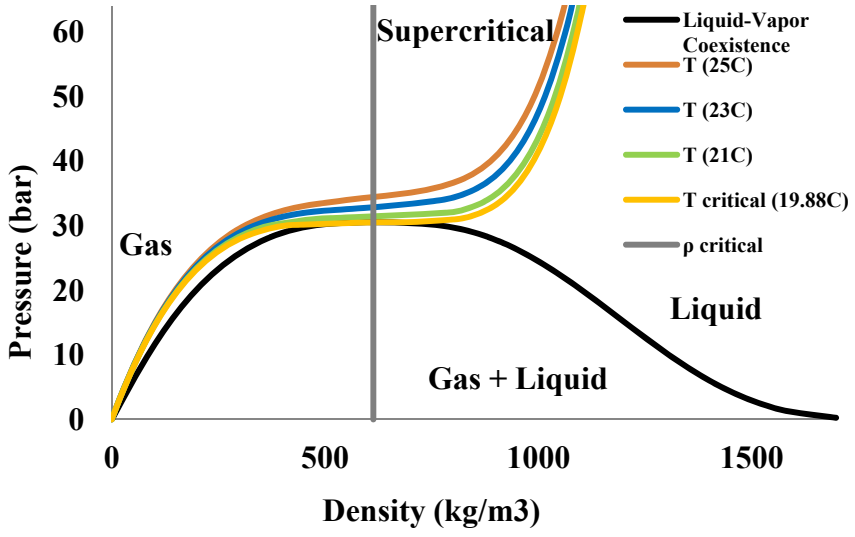

Figure 5.1: Pressure vs. Density Diagram for C_2F_6 [7]

Table 5.1 shows a comparison of C_2F_6 to other fluids of potential use as model systems or of interest for applications. Observations were first made on stagnant fluid to confirm the critical point via MR and to determine the impact of density fluctuations near the critical point on dynamics in the fluid due to buoyancy.

Table 5.1: Fluids considered for supercritical study.

Fluid Name	Chemical Formula	T_C (^oC)	P_C (bar)
Hexafluoroethane	**C_2F_6**	**19.88**	**29.8**
Carbon Tetrafluoride	**CF_4**	**-45.65**	**37.4**
Octafluorocyclobutane	**C_4F_8**	**115.3**	**27.8**
Sulfur Hexafluoride	**SF_6**	**45.5**	**37.6**
Trifluoromethane	**CHF_3**	**25.6**	**48.4**
Octafluoropropane	**C_3F_8**	**71.9**	**26.8**
Carbon Dioxide	**CO_2**	**31.04**	**73.8**

The fluid dynamics and transport behavior of C_2F_6 over a range of conditions above, below, and at the critical point was studied. Scale dependent velocity maps, propagators and diffusion coefficients were measured using magnetic resonance techniques.

Hexafluoroethane C_2F_6 was pumped through a system designed for the Bruker Avance 300 MR imaging spectrometer. Gas was compressed to a range of pressures below, near, and above the critical pressure using an Isco 500D syringe pump. The Isco 500D allows for volumetric flow rate control. C_2F_6 flowed through the MR system at a flow rate of 0.5 mL/min through PEEK tubing of 1.524 mm ID and through stainless steel tubing outside of the NMR equipment. Back pressure of the system was maintained by a Thar back pressure regulator APBR-20-1. After exiting the back pressure regulator, the depressurized C_2F_6 was collected in a gas cylinder and reused. Various pressure

transducers and thermocouples monitored the pressure and temperatures throughout the system at predetermined regions. Several temperature configurations were tested at various pressures. See Figure 5.2 for a layout of the supercritical flow loop. Details of the MR methods will be given in presenting results of the measurements.

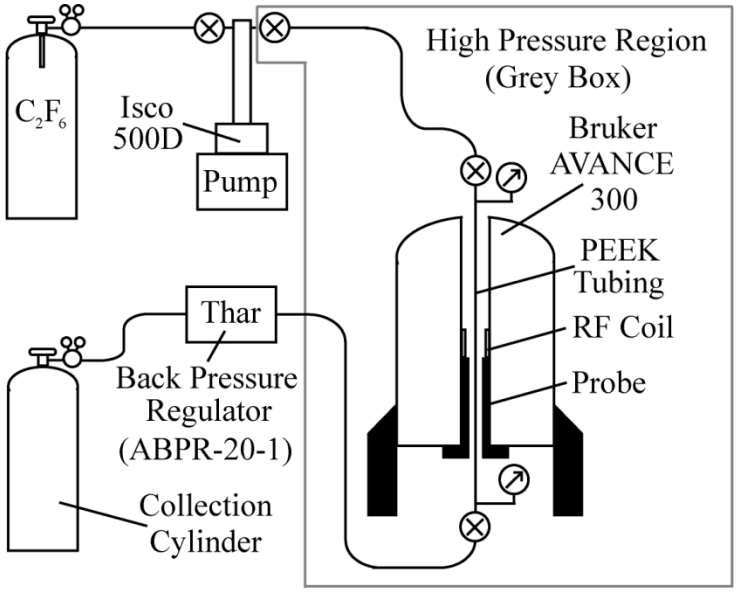

Figure 5.2: Supercritical flow loop schematic

Results

Under no flow conditions the diffusion coefficient of C_2F_6 was measured as a function of pressure in the range of 20 to 65 bar and at two fluid temperatures, 15 and 25 ^{o}C (Figure 5.3). The diffusion coefficient was determined using a double pulsed gradient spin echo (d-PGSE) sequence to refocus natural convection [124, 125]. A displacement observation time of Δ = 100 ms was used. At temperatures and pressures below the critical pressure, the self-diffusivity decreased with increasing pressure toward the critical pressure, as expected for a gas. However, near the critical pressure the diffusion

coefficient continued to steadily drop for the test above the critical temperature (25 ^{o}C) but rapidly decreased in a discontinuous jump for the experiments below the critical temperature (15 ^{o}C). This jump in diffusivity for temperatures and pressures below the critical values is indicative of the gas-liquid first-order phase transition [92]. The smooth decrease in diffusivity above the critical temperature is consistent with a second-order continuous phase transition [92]. The jump occurred near 29 bar and corresponds to a 3% error from the published pressure [7]. Additional no flow data for a larger inner diameter sample holder containing the bulk fluid is contained in Appendix A.

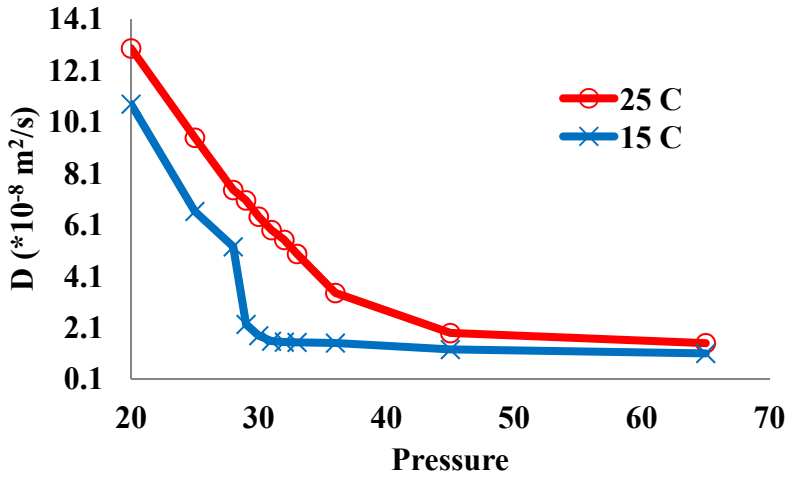

Figure 5.3: Diffusion coefficient as a function of pressure for C_2F_6

Axial velocity maps of the capillary cross section were taken at pressures P = 25 to 65 bar at fluid temperatures T_f = 20, 21, or 23 ^{o}C. External capillary wall temperatures T_s = 15, 21, or 25 ^{o}C were used to vary buoyancy effect during upward flow against gravity (Figure 5.4, Figure 5.6a, Figure 5.7, and Figure 5.8). To study dynamics with the gravitational force in the direction of the pressure driven flow of the supercritical fluid

downward flow experiments were also performed. The same range of pressures P = 25 - 65 bar were used for fluid temperatures T_f = 21 ^oC with a surrounding wall temperature T_s = 25 ^oC (Figure 5.5 and Figure 5.6b). The velocity map MR pulse sequence used had a displacement observation time Δ = 7.41 ms, a pulse duration δ = 0.5 ms and a radio frequency (RF) excitation pulse length of 1 ms. The in plane spatial resolution with a field of view of 4 mm x 2 mm was 62.5 µm x 62.5 µm over 64 x 32 points and a 20 mm slice. The experiments had 32 averages for a total test time of 70 minutes. The data was analyzed in Prospa (Magritek, NZ) filtered using a mask from the spatial image and a profile of the velocity field across the diameter of the tube was generated for each pressure. For an in depth discussion on processing the data using Prospa, see Appendix B.

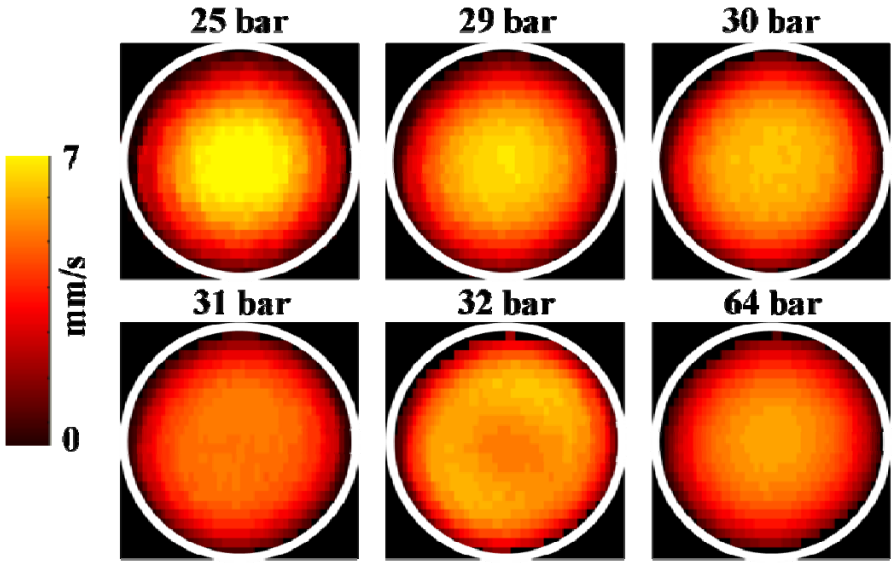

Figure 5.4: Velocity maps of C_2F_6 at P = 25, 29, 30, 31, 32, and 64 bar with T_f = 23 ^oC and T_s = 25 ^oC for upward flow against gravity.

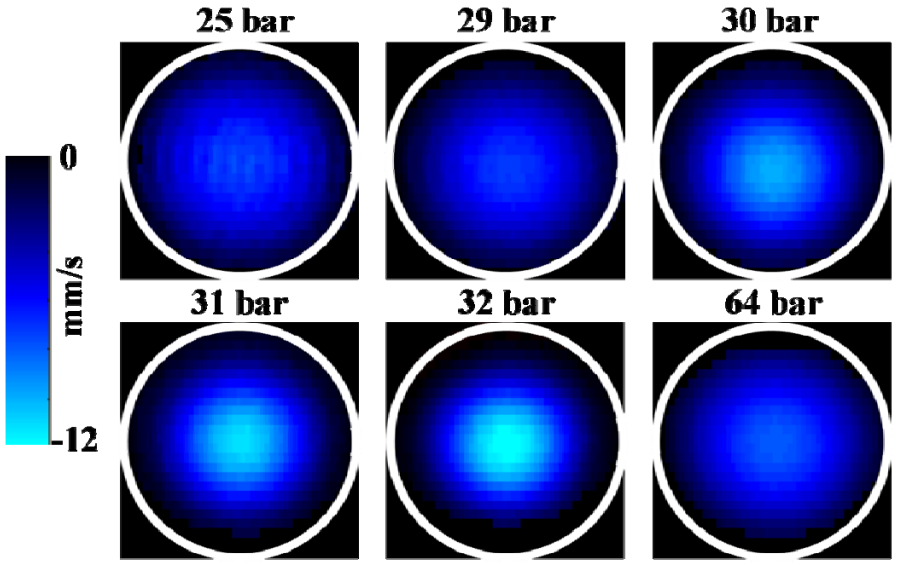

Figure 5.5: Velocity maps of C_2F_6 at P = 25, 29, 30, 31, 32, and 64 bar with T_f = 23 °C and T_s = 25 °C for downward flow with gravity.

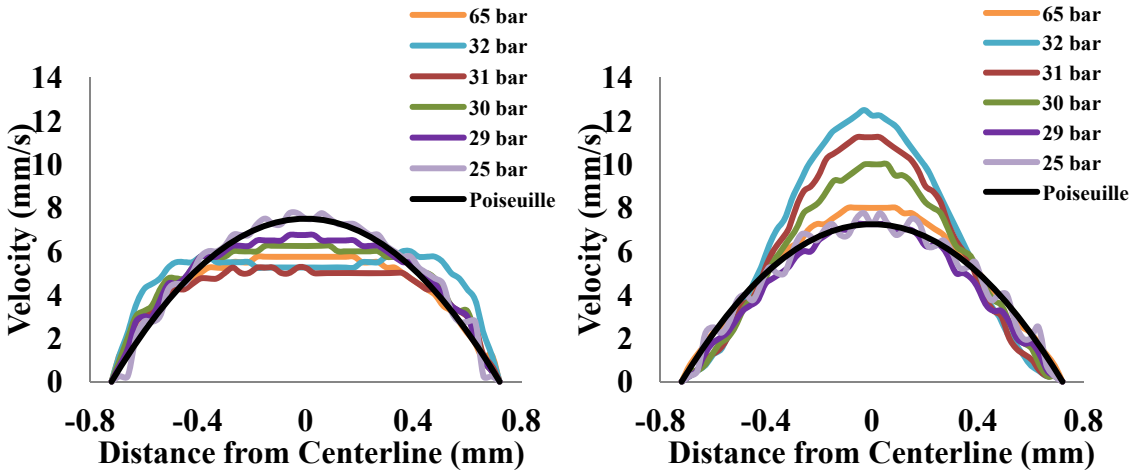

Figure 5.6: Velocity profiles of C_2F_6 below, near, and above the critical pressure at a fluid temperature of 23 °C and a surrounding temperature of 25 °C for a) upward flow and b) downward flow.

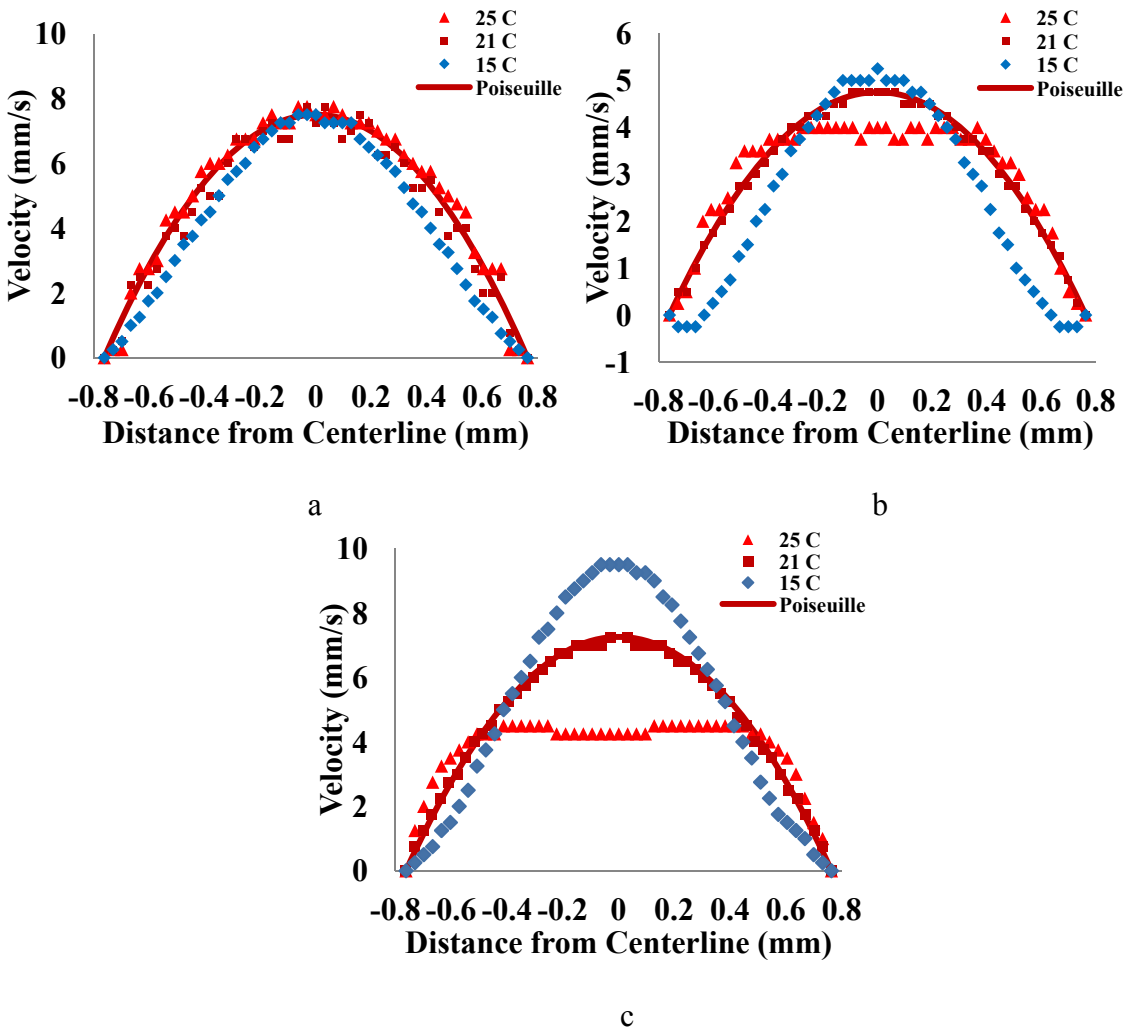

Figure 5.7: Velocity profiles of C_2F_6 at a fluid temperature of 21 ^oC and varied surrounding temperatures for upward flow at a) 25 bar, b) 29 bar, and c) 45 bar.

The experimental data indicates the impact of the interplay between the fluid dynamics and the thermodynamic density variation as pressure and temperature vary. At a fluid temperature of 21 ^oC and a surrounding temperature of 21 ^oC no temperature gradient should exist across the PEEK capillary wall. Surrounding temperatures that did not match the fluid temperature generated a temperature gradient across the PEEK wall generating energy flux causing warmer or cooler inside wall temperature. Figure 5.7 is

the velocity profile data displayed for each pressure and shows the effects of temperature, while Figure 5.8 is the data displayed for each temperature configuration and shows the effects of pressure.

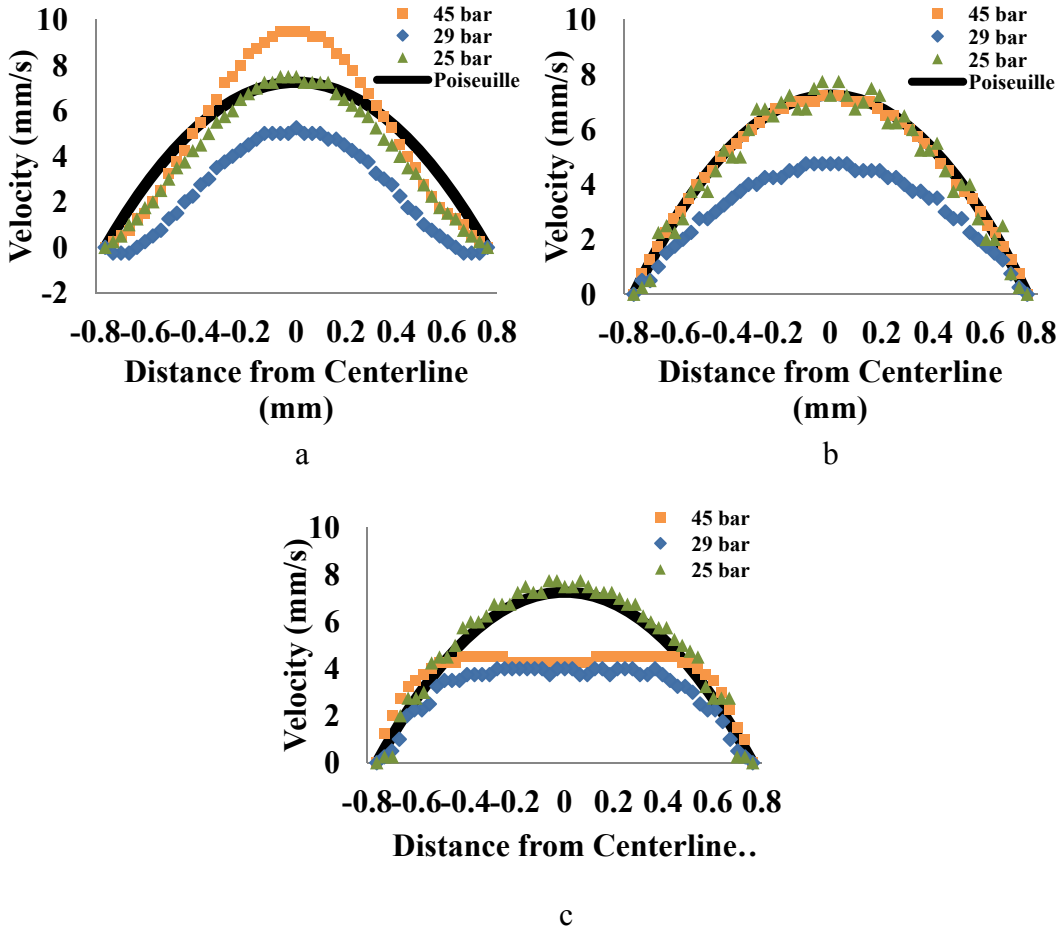

Figure 5.8: Velocity profiles of C_2F_6 at a fluid temperature of 21 ^oC and varied pressures for upward flow with a surrounding temperature of a) 15 ^oC, b) 21 ^oC, and c) 25 ^oC.

Velocity maps were acquired near the critical point P = 29 bar at fluid temperature T_f = 20 ^oC, and surrounding temperature T_s = 18 to 21 ^oC (Figure 5.9a-b). Figure 5.9a shows the susceptibility of buoyancy near the critical temperature for small temperature differences between T_s and T_f. The "M" shaped profile has the greatest

difference between maximum and minimum velocities for a temperature difference of 1 °C. The velocity in the center of the pipe for T_f = 20 °C and T_s = 21 °C is near 0 mm/s.

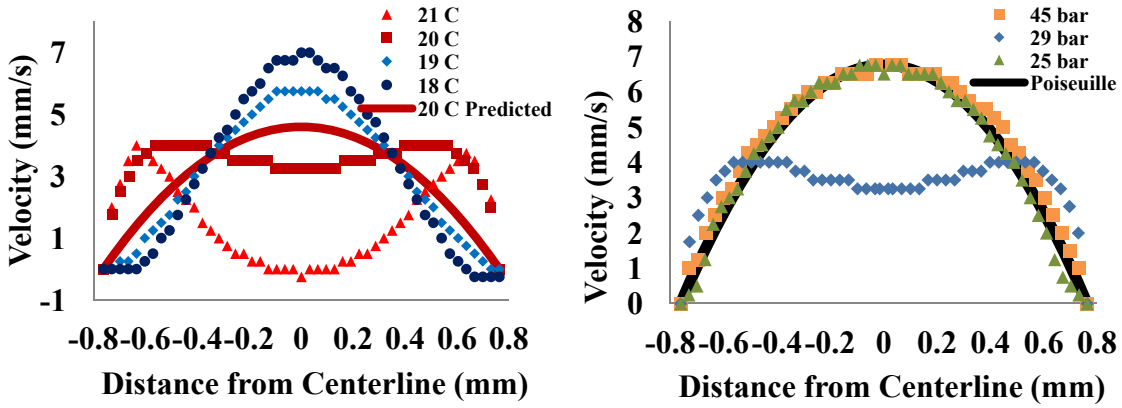

a b

Figure 5.9: Velocity profiles for upward flow of C_2F_6 near the critical point at a) 29 bar fluid temperatures of 20 °C and surrounding temperatures of 18 to 21 °C and b) fluid and surrounding temperatures of 20 °C at varied pressures.

For Laminar flow of an incompressible Newtonian fluid in a capillary, the velocity profile is Poiseuille and is given as a function of capillary radial position r by equation (5.1)$\boldsymbol{V(r) = V_{max}\ 1 - \left(\frac{r}{R}\right)^2}$ (5.1) with a maximum velocity $V_{max} = \frac{\Delta P R^2}{4\eta_o L}$ in the center of the tubing dependent of the pressure drop per unit length $\frac{\Delta P}{L}$, capillary radius R and fluid viscosity η_o

$$\boldsymbol{V(r) = V_{max}\left(1 - \left(\frac{r}{R}\right)^2\right)} \quad (5.1).$$

The flow rate 0.5 mL/min studied in this work should produce a laminar flow regime as long as the Reynolds Re number remains low (Re < 2300). For example, at 25 °C and a pressure of 65 bar, C_2F_6 is supercritical and the density is similar to the liquid state, therefore, the Re = 80.9. In fact, for all of the pressures the Re number was far below the

turbulent transition threshold of 2300 (Table 5.2). The density ρ and dynamic viscosity η_o values for C_2F_6 were taken from the National Institute for Standards and Technology thermophysical properties data base [7].

Table 5.2: *Re* numbers for various pressures and temperatures of flowing C_2F_6

Temp. (^{o}C)	Pressure (bar)	Re_o	Temp. (^{o}C)	Pressure (bar)	Re_o
23	**25**	**92.6**	**25**	**25**	**90.0**
23	**29**	**111.5**	**25**	**29**	**107.9**
23	**30**	**116.4**	**25**	**30**	**112.3**
23	**31**	**121.2**	**25**	**31**	**116.7**
23	**32**	**125.2**	**25**	**32**	**120.9**
23	**65**	**79.2**	**25**	**65**	**80.9**

Re is based on the diameter of the pipe D = 1.524 mm and the mean velocity v = 4.625 mm/s was calculated from the 0.5 mL/min flow rate assuming incompressible flow. Flow of C_2F_6 near the critical point is compressible due to the density fluctuations the viscosity decreases so the actual *Re* number will fluctuate. A reference Reynolds number Re_o is therefore defined using the inlet parameters (Table 5.2). The related Grashof *Gr* and Richardson *Ri* numbers were also calculated (Table 5.3).

Table 5.3 *Gr* and *Ri* numbers
for flowing C_2F_6 at T_s = 25 ^{o}C and T_{fluid} = 21 ^{o}C

Pressure	Gr	Ri
25	**85912.8**	**10.6**
29	**230090.5**	**19.8**
30	**318617.8**	**25.3**
31	**477266.4**	**35.0**
32	**840598.5**	**57.5**
65	**35553.1**	**5.4**

It is clear that near the critical pressure of 32 bar, the buoyancy forces are dominant as indicated by the *Ri* number. The two lowest *Ri* numbers are at the pressures farthest from the critical point. These experiments will have the lowest buoyancy effects as is seen in the MR velocity map data. The velocity data presented above was for temperatures above the critical isotherm. At temperatures below the critical isotherm and pressures below, but near critical, the fluid is in the two phase fluid regime under the coexistence curve.

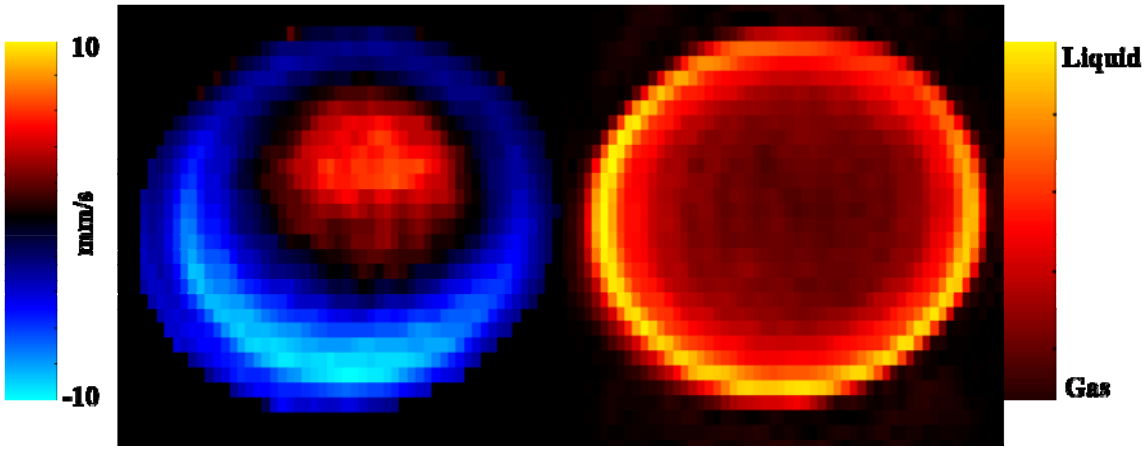

Figure 5.10: a) Velocity map and b) density map of two-phase C_2F_6 at 29 bar, 19 ^oC fluid temperature, and 15 ^oC surrounding temperature.

Velocity data acquired at P = 29 bar, T_f = 19 ^oC, and T_s = 15 ^oC resulted in flow of a two phase fluid in which the denser liquid phase had negative velocities near the wall and the less dense gas phase flowed in the center of the tube (Figure 5.10). The density map of Figure 5.10 shows the molecular spin density. Due to the colder wall temperature, the fluid condensed near the walls and was in the liquid state while the warmer fluid in the center of the tube was in the gaseous state. For all of the experiments above the critical isotherm, Figure 5.4 through 5.9 in which the fluid was either gas, near critical,

supercritical, or liquid the density maps were homogenous and showed no variation across the capillary indicating a single phase.

Propagators at the same flow conditions as the velocity maps were taken to observe the transport dynamics for below (Figure 5.11), near (Figure 5.12), and above (Figure 5.13) critical pressures. The propagators were acquired for displacement observation times in the range Δ = 10 - 100 ms (Figure 5.14), with gradient pulse duration δ = 1 ms, and a maximum gradient value g = 0.945 T/m. Propagators for P = 25, 29, and 45 bar upward flow at a fluid temperature T_f =21 °C and a surrounding temperature T_s =15, 21, 25 °C are reported. The propagator curves are plotted as probability of velocity $P(v)$ vs. velocity $v = \frac{z}{\Delta}$ and they are an ensemble average of the flow statistics through the cross section of the tubing with a slice thickness of 15 mm.

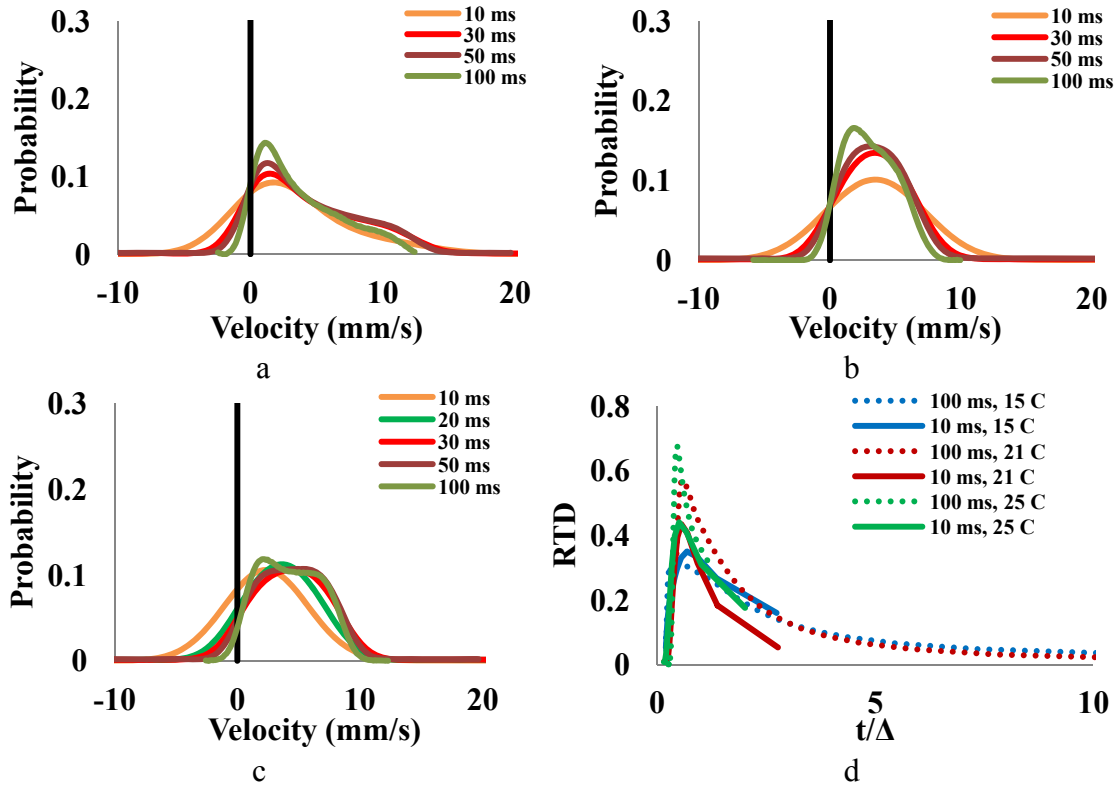

figure continued…

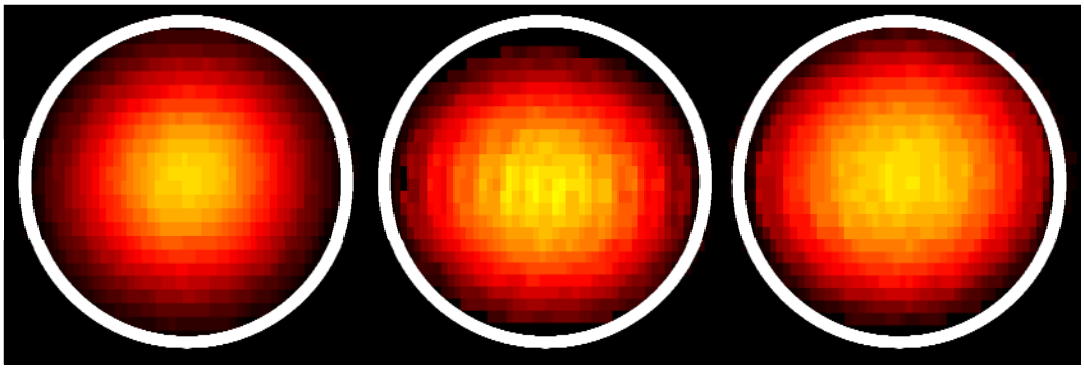

e

Figure 5.11: Upward flow propagators plotted as probability $P(v)$ of velocity – for varying displacement observation time Δ of C_2F_6 at P = 25 bar, fluid temperature T_f = 21 °C, and a surrounding temperature T_s = a) 15 °C, b) 21 °C, and c) 25 °C. d) RTD at Δ = 10 and 100 ms e) Velocity maps that correspond to a), b), and c) with Δ = 7.41 ms.

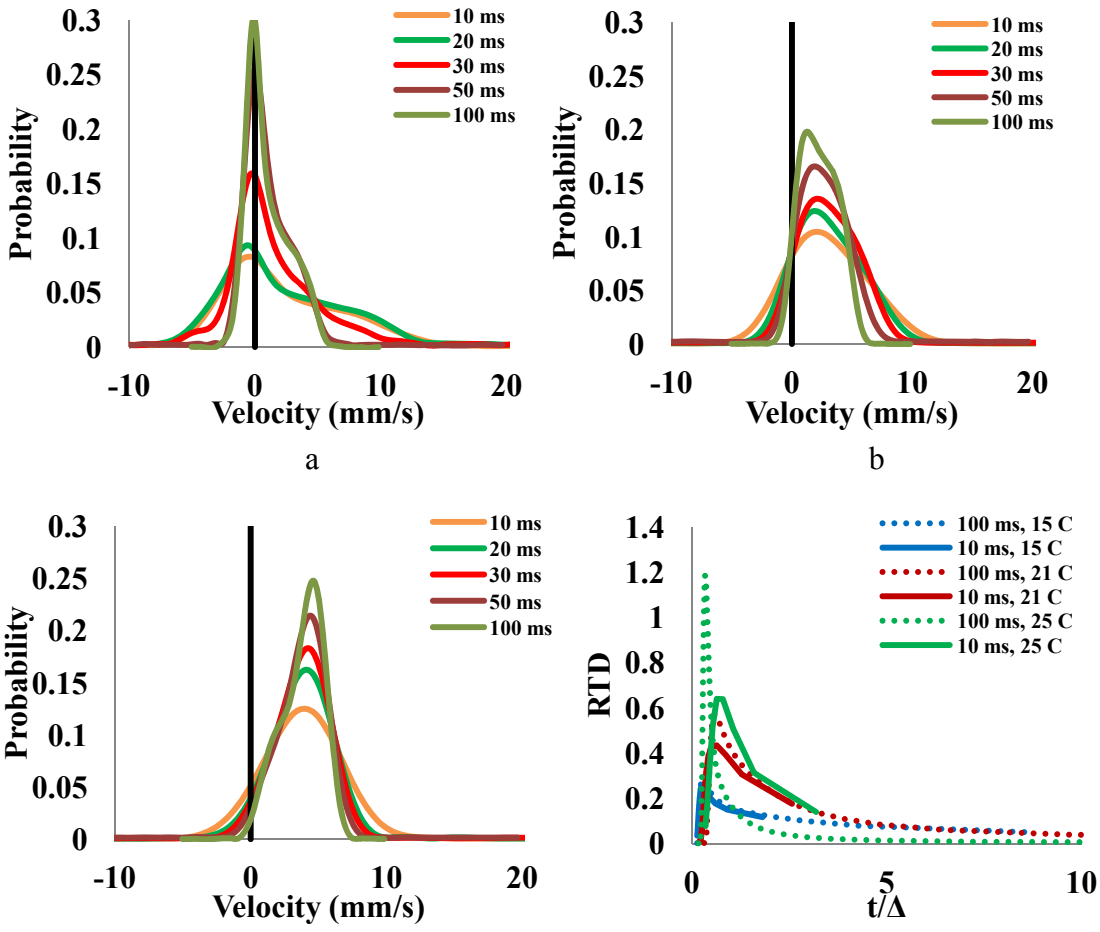

figure continued…

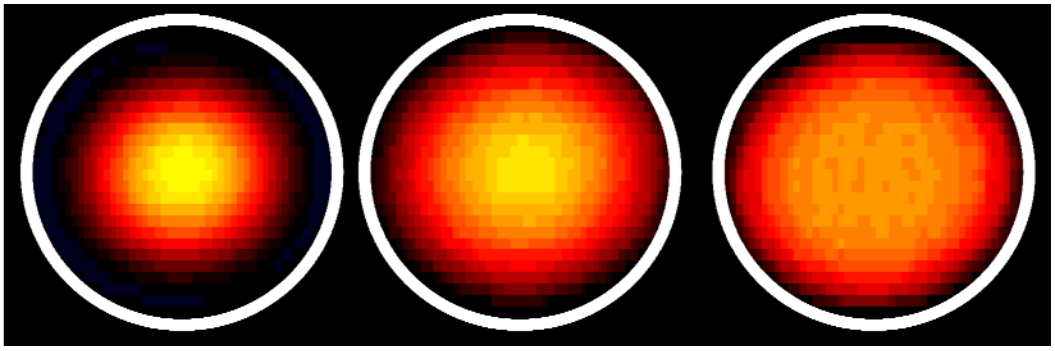

e

Figure 5.12: Upward flow propagators plotted as probability $P(v)$ of velocity – for varying displacement observation time Δ of C_2F_6 at P = 29 bar, fluid temperature T_f = 21 °C, and a surrounding temperature T_s = a) 15 °C, b) 21 °C, and c) 25 °C. d) RTD at Δ = 10 and 100 ms e) Velocity maps that correspond to a), b), and c) with Δ = 7.41 ms.

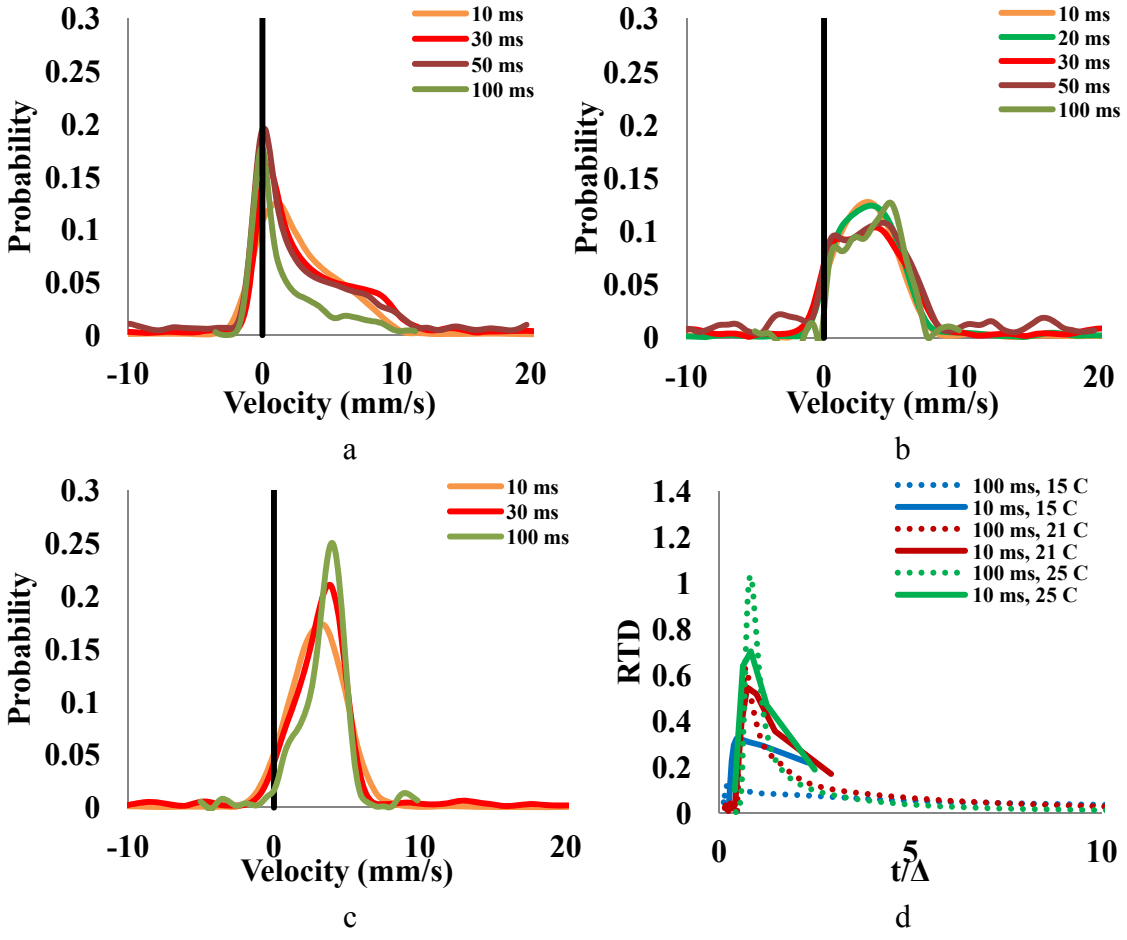

figure continued…

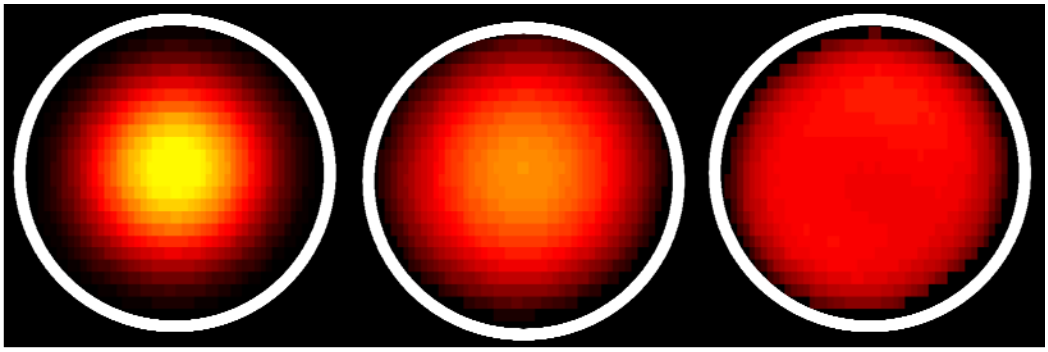

e

Figure 5.13: Upward flow propagators plotted as probability $P(v)$ of velocity – for varying displacement observation time Δ of C_2F_6 at P = 45 bar, fluid temperature T_f = 21 °C, and a surrounding temperature T_s = a) 15 °C, b) 21 °C, and c) 25 °C. d) RTD at Δ = 10 and 100 ms e) Velocity maps that correspond to a), b), and c) with Δ = 7.41 ms.

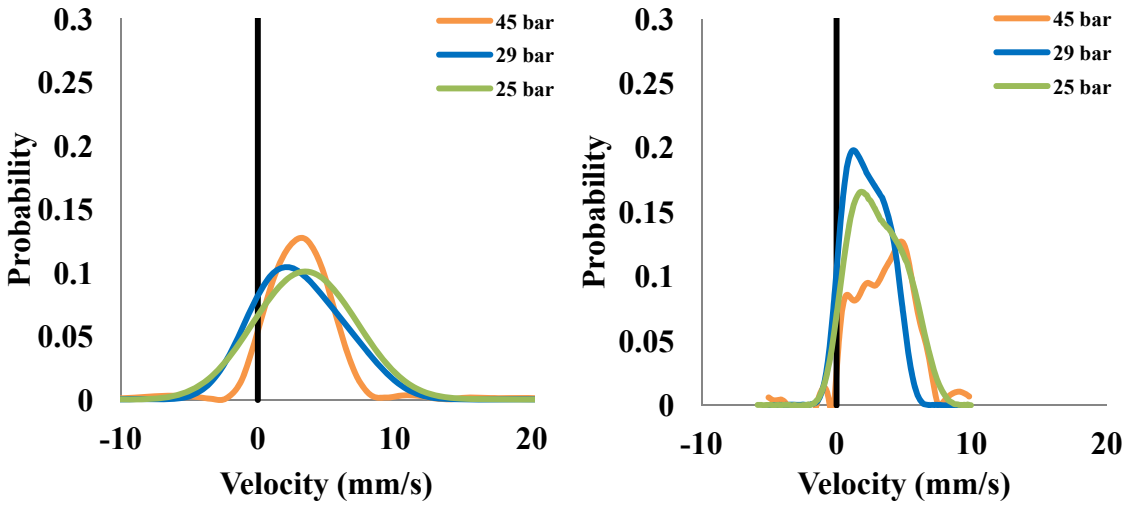

a b

Figure 5.14: Upward flow propagators of C_2F_6 at 25, 29, and 45 bar with a fluid temperature of 21 °C, a surrounding temperature of 21 °C, and at an observation time of a) 10 ms and b) 100 ms.

Near the critical point the flow needed about 210 min. to reach steady state flow. At pressures and temperatures away from the critical point, times on the order of 5 minutes were required for the flow to reach steady state. At P = 29 bar, velocity maps

(Figure 5.15) and propagators using Δ = 50 ms (Figure 5.16) were taken to observe the evolution of the flow to steady state. A second test run under the same pressure and temperature conditions was performed to check if the steady state equilibrium was reproducible or if the flow was unstable and would set up differently for different runs. The flow was considered converged to steady state if two sequential propagators showed equivalent flow dynamics and separate runs showed equivalent results in the final state indicating stability.

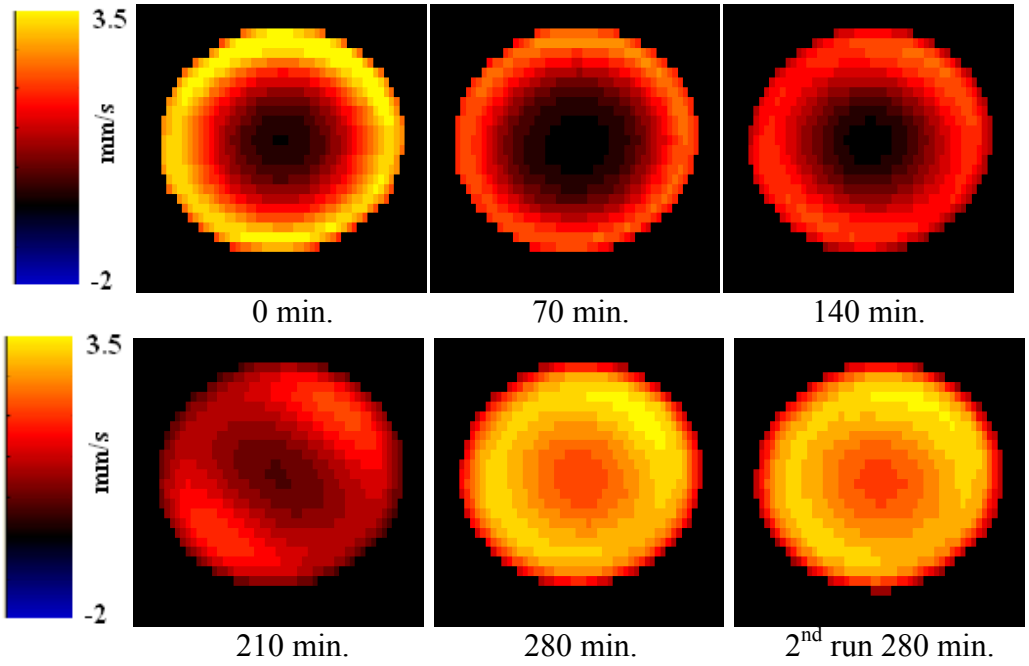

Figure 5.15: Velocity maps showing the time to steady state near the critical point at 29 bar, T_{fluid} = 20 °C, and T_s = 20 °C.

Velocity maps and propagators were observed during a temperature drop to observe the shift in dynamics of C_2F_6 at P = 29 bar with a temperature starting at T_{fluid} = 22 °C and T_s = 21 °C transitioning to T_f = 20 °C and T_s = 21 °C.

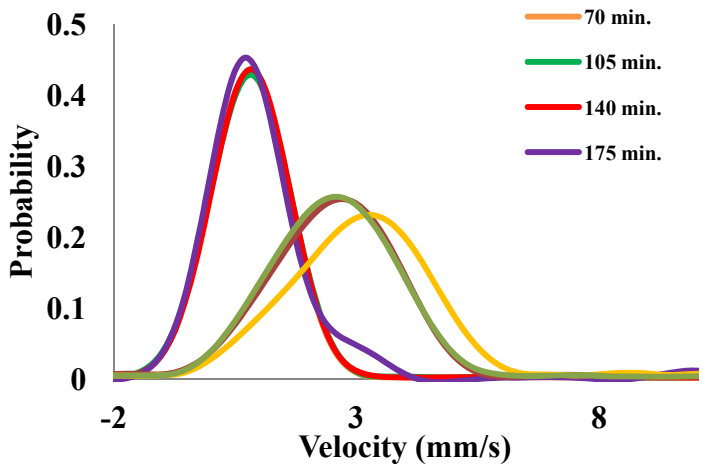

Figure 5.16: Velocity Propagators at 50 ms observation time showing the time to steady state equilibrium near the critical point at 29 bar, $T_f = 20\ ^oC$, and $T_s = 20\ ^oC$.

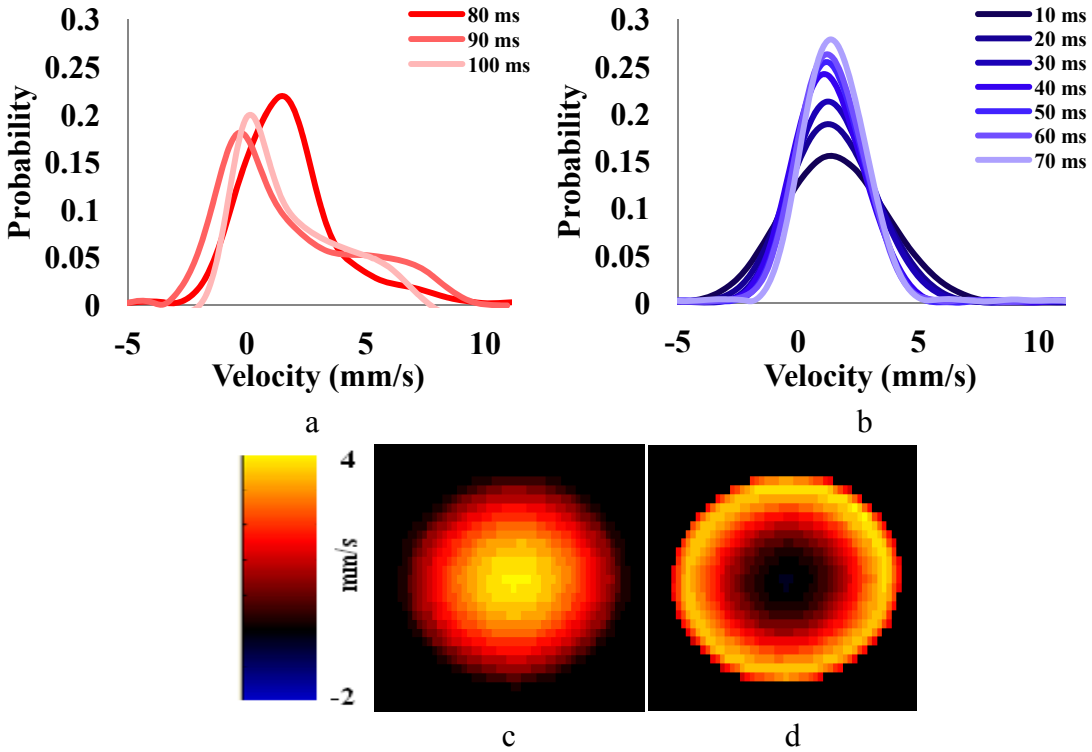

Figure 5.17: Shift in Dynamics of C_2F_6 at 29 bar with a temperature starting at $T_f = 22\ ^oC$ and $T_s = 21\ ^oC$ transitioning to $T_f = 20\ ^oC$ and $T_s = 21\ ^oC$. Propagators correspond to a) the beginning of the run where the temperature was at $T_f = 22\ ^oC$ and $T_s = 21\ ^oC$. b) correspond to the post shift dynamics where the temperature at the end of the run was $T_f = 20\ ^oC$ and $T_s = 21\ ^oC$. Velocity map c) corresponds to $T_f = 22\ ^oC$ and $T_s = 21\ ^oC$ at the beginning of the run and d) $T_f = 20\ ^oC$ and $T_s = 21\ ^oC$ at the end of the run.

Propagators acquired with incremented displacement time from Δ = 100 ms to 10 ms during which the temperature change occurred indicate the dynamics shift due to the temperature change. Propagators in Figure 5.17a correspond to the beginning of the run where the temperature was T_f = 22 °C and T_s = 21 °C. A shift in the dynamics occurred at Δ = 70 and 80 ms observation time and the propagators in Figure 5.17b correspond to the post shift dynamics where the temperature at the end of the run was T_f = 20 °C and T_s = 21 °C. The velocity map in Figure 5.17c corresponds to temperatures of T_f = 22 °C and T_s = 21 °C at the beginning of the run and the velocity map in Figure 5.17d corresponds to temperatures of T_f = 20 °C and T_s = 21 °C at the end of the run.

Diffusion measurements were performed at both non-flowing and flowing (0.5 mL/min) conditions by observing the signal attenuation over many gradient steps, *G*. The experiments were performed in Topspin using a d-PGSE sequence to refocus spin dephasing due to coherent motion in the sample.

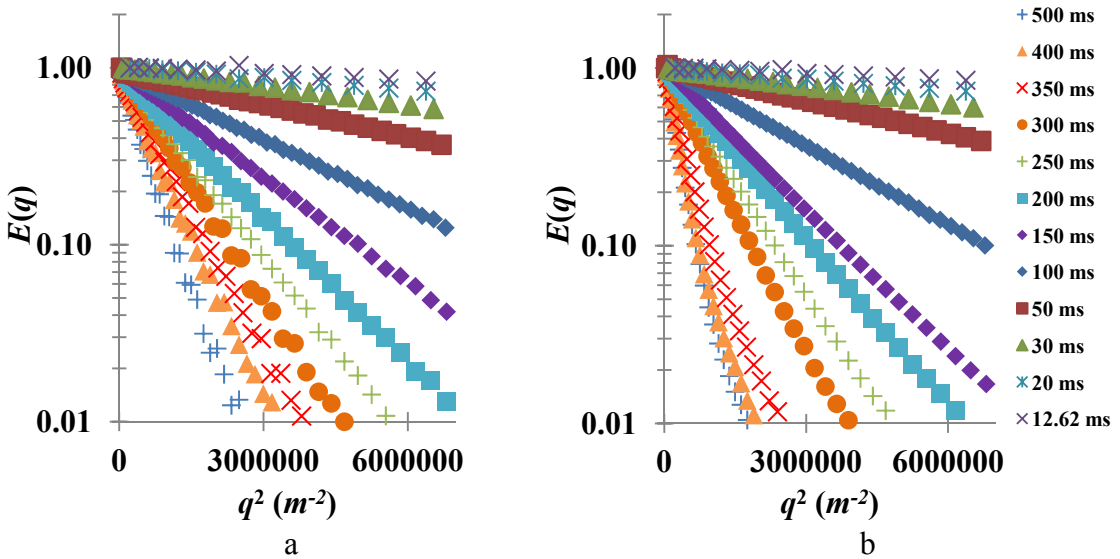

Figure 5.18: 25 bar dPGSE signal attenuation plots of C_2F_6 at T_f = 20 °C and T_s = 20 °C for a) non-flowing and b) 0.5 mL/min conditions.

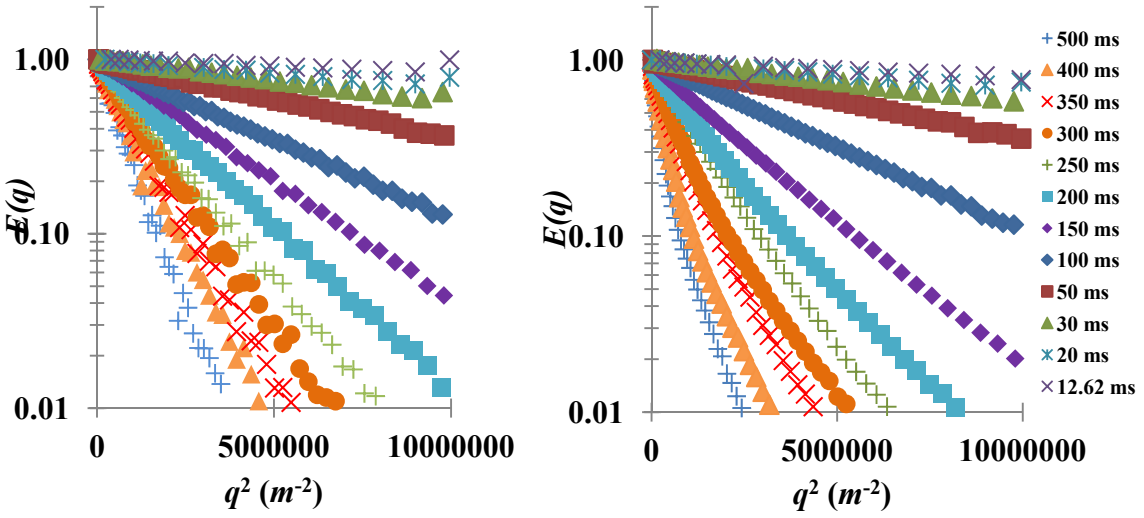

Figure 5.19: 29 bar dPGSE signal attenuation plots of C_2F_6 at T_f = 20 °C and T_s = 20 °C for a) non-flowing and b) 0.5 mL/min conditions.

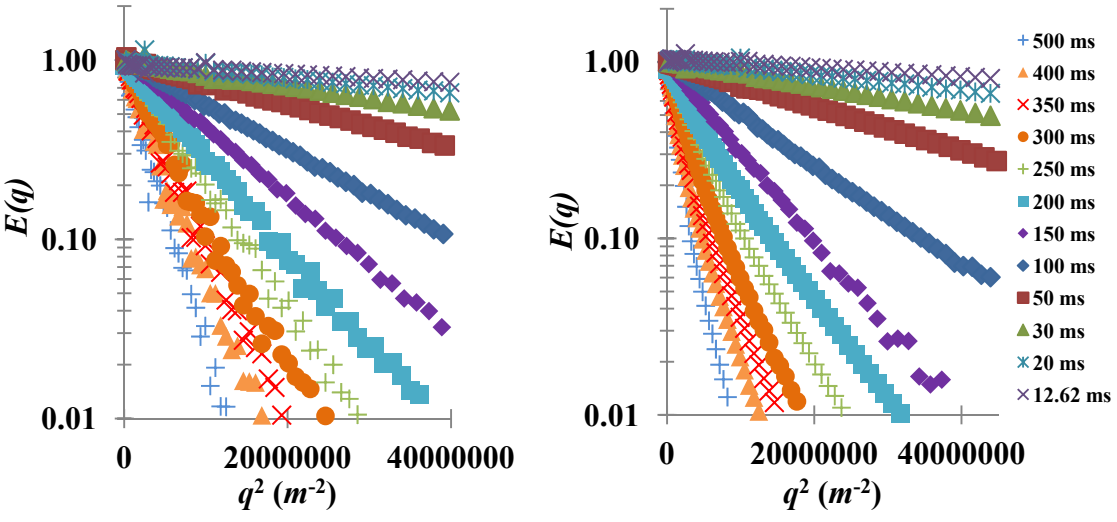

Figure 5.20: 45 bar dPGSE signal attenuation plots of C_2F_6 at T_f = 20 °C and T_s = 20 °C for a) non-flowing and b) 0.5 mL/min conditions.

The pressures measured were P = 25 (Figure 5.18), 29 (Figure 5.19), and 45 bar (Figure 5.20) with T_f = 20 °C and T_s = 20 °C. Displacement observation times measured

ranged from Δ = 12.62 to 500 ms, using 128 gradient steps with 8 averages for Δ = 12.62 to 100 ms and 64 gradient steps with 16 averages for Δ = 150 to 500 ms. All experiments used δ = 1 ms and maximum gradient from 0.50 T/m for Δ = 12.62 ms to 0.08 T/m for Δ = 500 ms.

A diffusion (no flow) or dispersion (flow) coefficient was calculated from each of the signal attenuation curves and plotted in Figure 5.21. The graph is plotted as diffusion, D, or dispersion, D^*, vs. displacement observation time Δ for P = 25, 29, and 45 bar. The flowing experiments had two components of diffusion (slow and fast) visible also in the nonlinearity of the attenuation plots (Figure 5.18, 19, and 20).

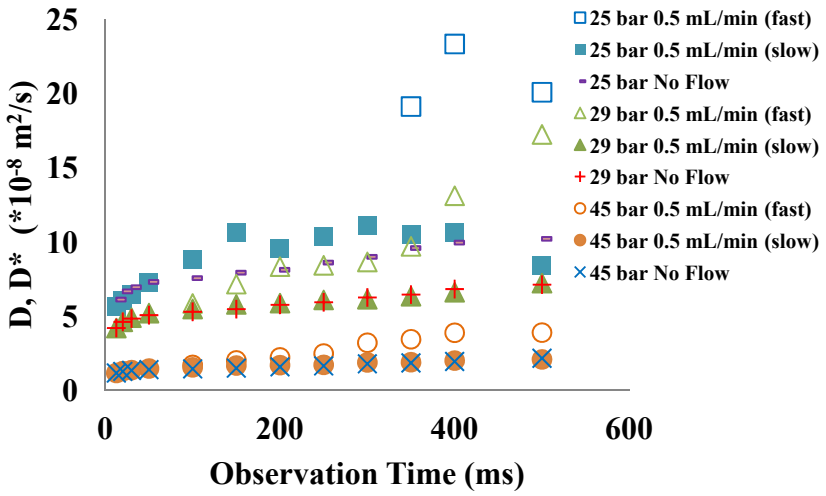

Figure 5.21: Diffusion and dispersion coefficients from 25, 29, and 45 under non-flowing and flowing (0.5 mL/min) conditions.

Relaxation measurements were made to determine T_1 and T_2 relaxation at three pressures P = 25, 29, and 45 bar for both flowing and non-flowing conditions at temperatures T_f = 20 °C and T_s = 20 °C. In Figure 5.22 the relaxation measurements are plotted on a log-log scale with T_1 on the vertical axis and T_2 on the horizontal axis.

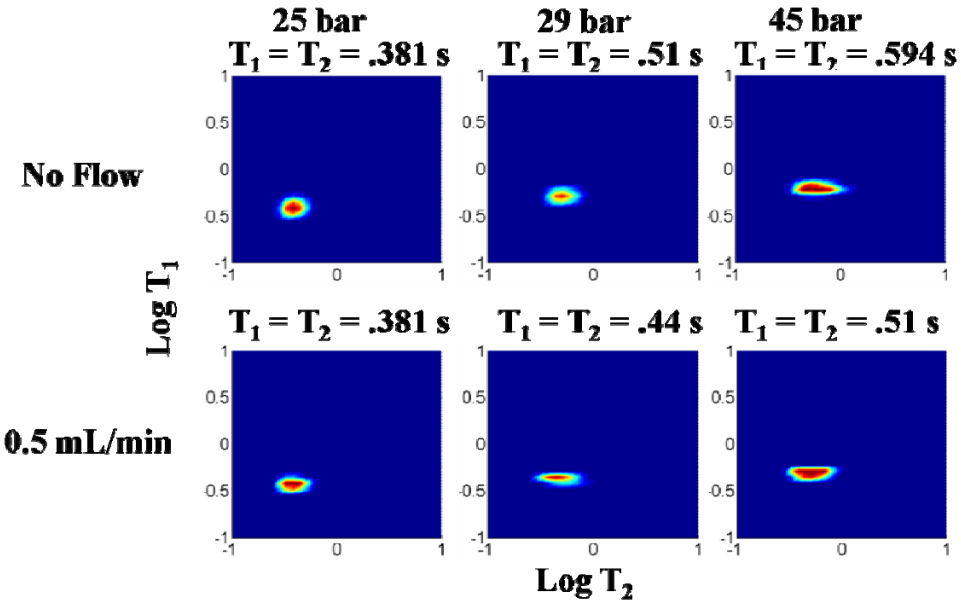

Figure 5.22: T_1-T_2 plots for non-flowing and flowing (0.5 mL/min) C_2F_6 at P = 25, 29, and 45 bar T_f = 20 °C and T_s = 20 °C.

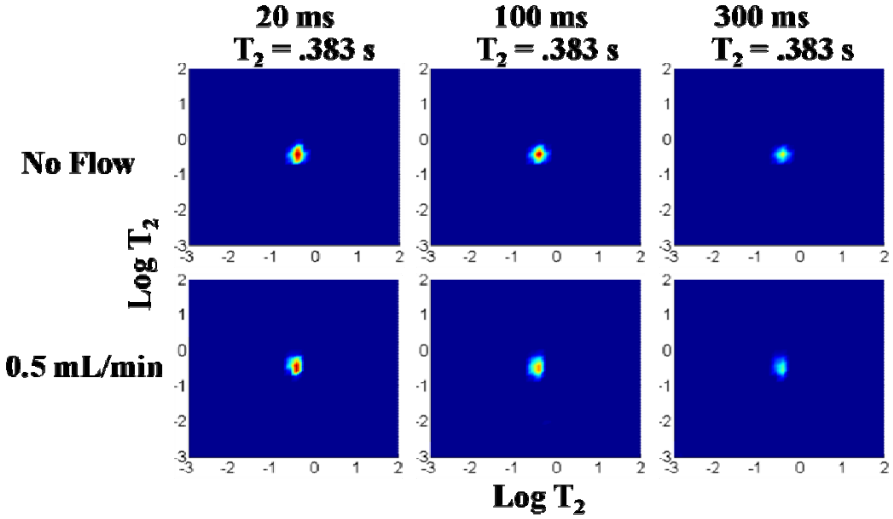

Figure 5.23: T_2-T_2 plots for non-flowing and flowing (0.5 mL/min) C_2F_6 at 25 bar. Temperatures were T_f = 20 °C and T_s = 20 °C. For mixing times of τ_m = 20 ms, 100 ms, and 300 ms the mean T_2 is given above each column.

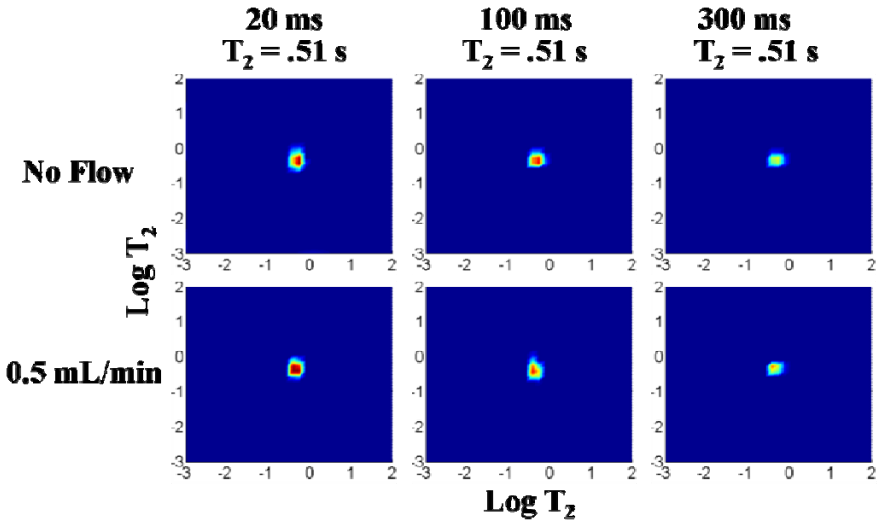

Figure 5.24: T_2-T_2 plots for non-flowing and flowing (0.5 mL/min) C_2F_6 at 29 bar. Temperatures were $T_f = 20\ ^oC$ and $T_s = 20\ ^oC$. For mixing times of $\tau_m = 20$ ms, 100 ms, and 300 ms the mean T_2 is given above each column.

Additional relaxation experiments were run to determine T_2- T_2 relaxation at the two lower pressures P = 25 (Figure 5.23) and 29 bar (Figure 5.24) for flowing and non-flowing conditions. These experiments were made at three mixing times $\tau_m = 20$, 100, and 300 ms to determine if any exchange occurred between potential multiple populations of T_2 relaxation.

Discussion

At a constant $T = 15\ ^oC$, the pressure range P = 20 to 65 bar traverses the pressure vs. density phase diagram across the constant isotherm slightly below the critical isotherm from the gas phase through the two phase gas-liquid region to the liquid phase. A jump in the diffusivity is expected at this temperature for an increase in pressure corresponding to the transition across the two-phase region as shown in Figure 5.3. For

the higher temperature isotherm T = 25 ^{o}C the transition from gas to liquid phase is first order and crosses the smooth transition region of the supercritical fluid and a jump in diffusivity is not expected, as expected in Figure 5.3. The observed difference in diffusivity pressure dependence for temperatures above and below the critical isotherm confirms the experimental system generates a critical phase transition.

Temperature of the fluid was controlled by room heaters and air conditioning devices to ±0.5 ^{o}C. The temperature inside the rf coil within the magnet where the fluid passes during observation, was controlled by the cooling water used to maintain magnetic gradient coil temperature. The temperature inside the rf coil was monitored by a thermocouple and corresponded to the external wall temperature of the flow capillary. The surrounding temperature of the rf coil air as controlled by the coil cooling water either caused positive, negative, or no heat transfer to the system.

The MR velocity maps presented are the first non-invasive measurement of flow of a near critical or supercritical fluid and give supporting evidence to numerical results. For fluid at T_f = 21 ^{o}C, surrounding temperature at T_s = 15 ^{o}C caused cooling at the wall of the cylindrical tube (Figure 5.7 and Figure 5.8). A surrounding temperature T_s = 25 ^{o}C caused heating at the wall, while T_s = 21 ^{o}C showed no heat transfer to the fluid (Figure 5.7 and Figure 5.8). At conditions above the critical isotherm and near a fluid's critical pressure, the MR velocity data show the impact of heat transfer on the fluid dynamics. A system that should otherwise exhibit a laminar Poiseuille flow profile in fact shows speeding up or slowing down due to temperature gradients caused by heat transfer into or out of the fluid at the pipe walls.

For the P = 25 bar near critical gas regime the temperature variations had minimal impact on the velocity profile (Figure 5.7a). All three surrounding temperatures corresponding to heating, cooling, or no temperature gradient, the velocity profile was Poiseuille or nearly Poiseuille. Increased pressure for all three surrounding temperatures exhibit breakdown of the Poiseuille velocity profile near the critical point. The Poiseuille profile begins to reemerge at pressures P = 45 bar well above the critical pressure at the same temperature conditions Figure 5.6a. The highest pressure tested here was P = 65 bar Figure 5.6a and the data suggest that for higher pressures the velocity profile returns to the parabolic Poiseuille profile for all surrounding temperature variations. It is therefore only near the critical point where the fluid dynamics are significantly altered by heat transfer. This showed that supercritical and near critical fluids are strongly impacted by buoyancy forces due to heat transfer.

Although the Reynolds numbers using inlet conditions for pressures near the pseudocritical or critical point P = 29, 30, 31, and 32 bar suggest that the flow should be laminar, the velocity profiles suggest otherwise for experiments with heat transfer at the walls T_s = 25 ^oC. For pressures closest to the critical point and upward flow, the profiles have an increased or decreased flow near the pipe walls due to wall heating T_s = 25 ^oC or cooling T_s = 15 ^oC, respectively (Figure 5.4, Figure 5.6, Figure 5.8, and Figure 5.9). The velocity profiles suggest that buoyancy forces are significant in the flow because of heat transfer at the wall boundary. Additionally, the reduction of viscosity characteristic of near critical fluids [75] is manifested as a change in shear rate $\frac{dv_z}{dr}$ near the walls. For heating and upward flow at several critical conditions, the reduction of viscosity and

density has caused the fluid near the walls to flow faster due to the upward buoyancy forces, than that in the center of the tube, generating an "M" shape velocity profile (Figure 5.9) [90]. The more dense and viscous fluid in the center of the pipe flows slower due to the buoyancy force. Velocity data nearest the critical point shows a drastic reduction in viscosity and shear rate (Figure 5.9). In contrast, for a cooling wall boundary T_s = 15 ^{o}C, the more dense fluid is near the wall and the less dense fluid is in the center of the capillary. The velocity profiles show the more dense fluid has slowed down due to the buoyancy force acting against the pressure driven flow and in some cases reverses directions (Figure 5.8a). The less dense fluid in the center of the pipe has sped up due to the buoyancy force enhancing the pressure driven flow.

When the temperatures were balanced, T_s = 21 ^{o}C and T_f = 21 ^{o}C there was no heat transfer to the fluid. The velocity maps indicated a Poiseuille profile for all pressures including near critical pressures. This agreed with the Reynolds number calculation of laminar flow. At P = 25 and 45 bar pressure, the Poiseuille profile indicated equivalent velocities of the fluid and in neargreement with the volumetric flow Q = 0.5 mL/min. The near critical pressure of 29 bar shows an overall slowdown in the Poiseuille profile (Figure 5.8b) indicating a change in volumetric flow rate due to compressibility. Mass is conserved not volume. Hence the volumetric flow rate in the test region is lower than that maintained upstream by the pump. The Poiseuille profiles measured at the individual pressures served as a template velocity profile relative to which the heating or cooling cases are compared (Figure 5.7a-c).

For the downward flow, viscous and buoyancy effects are pronounced (Figure 5.5). The downward flow dynamics show the impact of the buoyancy force acting in the opposite direction to the pressure driven velocity. Near the critical pressure, the higher density fluid is at the center of the capillary because of heating at the walls. The higher density results in the fluid falling faster with gravity compared to the Poiseuille profile. The buoyancy and reduction of viscosity are apparent near the walls showing decreased resistance to the bulk motion. It is evident by the prolonged near zero velocity showing a trend toward the lower velocity at streamlines near but increasingly farther away from the wall. It disrupts what would otherwise seem to be a parabolic profile.

Propagators near critical point at 29 bar reflect the dynamics indicated by the spatial velocity distributions while providing characterization of the Lagrangian transport in the system (Figure 5.12). The propagators for P = 25, 29, and 45 bar at surrounding temperatures of T_s = 15 have higher velocity probabilities of lower velocities due to heat removal near the walls increasing fluid density and decreasing buoyancy forces slowing the fluid (Figure 5.11 - Figure 5.13). Heat flux into the fluid for T_s = 25 ^{o}C shifts the probability of velocity towards larger velocity values due to the buoyancy force on the less dense fluid near the walls, generating faster velocity for all pressures. Propagators at all pressures with no heat transfer T_s = 21 ^{o}C trend toward a hat function, the velocity probability for the parabolic spatial velocity distribution, with diffusive effects of the Poiseuille profile. Diffusive effects are most evident at P = 25 bar in the near critical gas where the diffusion coefficient is largest. This is indicated by the “roundedness” of the hat function edges. The P = 45 bar propagators have sharper sides indicative of less

diffusion. The propagators reveal the transport effects of heating or cooling on a near critical gas, critical and supercritical fluid.

The propagator data show information the velocity maps cannot reveal. The velocity maps have lower signal to noise compared to the propagator measurements due to the impact of spatial resolution of the magnetization. The propagators can measure dynamics over a range of displacement observation times Δ that are longer than for the velocity maps as shown in Figure 5.11 to 5.13. Figure 5.14 compares the displacement observation times Δ = 10 and 100 ms for P = 25, 29, and 45 bar for $T_s = T_f = 21$ °C. . In contrast to the behavior seen in normal liquids in capillary flow in which $P(v)$ varies from a hat function at short times due to the equal probability of velocity in the parabolic velocity distribution to a Gaussian at long $\left(\Delta \gg \frac{R^2}{D_o}\right)$ times [4, 126], the propagators are near Gaussian at 10 ms and transition to non Gaussian. At 10 ms the diffusion length scale is $l_D \sim \sqrt{2D_o\Delta}$ = 49.6, 31.7, and 18.4 μm for P = 25, 29, and 45 bar, based on the NMR measured molecular diffusivity D_o = 1.23 x 10^{-7}, 5.02 x 10^{-8}, and 1.7 x 10^{-8} m^2/s at each pressure, respectively. This is of the same order of magnitude as the advection length scale $l_v = \langle v \rangle \Delta$= 34.8, 29.2, and 34.4 μm. Transport processes in capillary flow of supercritical and critical fluids is strongly dominated by random diffusive motions at displacement timescales on the order of 10 ms in contrast to ordinary liquids. At longer displacement time Δ = 100 ms the system is still far from the Taylor hydrodynamic dispersion regime for which $\frac{R^2}{D_o} \sim$4.5, 7.6, and 26.4 s for P = 25, 29, and 45 bar, respectively. The propagators at 100 ms reflect the advection dynamics of the C_2F_6 molecules since now $l_D \sim$ 161.2, 123.3, and 66.3 μm and $l_v \sim$290, 227, and 354 μm. The

near critical gas at P = 25 bar and the critical fluid P = 29 bar have a probability peaked toward slower velocity while the supercritical fluid P = 45 bar has higher probability of maximum velocity. The fluid compressibility due to the critical phase transition dynamics at P = 29 bar narrows the propagator generating less axial spreading as occurs in Taylor dispersion where the hydrodynamic dispersion scales as $D^* = \frac{\langle v \rangle^2 R^2}{48 D_o}$ and D_o is larger, narrowing $\bar{P}(Z, \Delta)$ due to the phase transition fluctuations.

The propagators contain equivalent information to a timescale dependent residence time distribution (RTD) a classic characterization of transport in reactor systems [127, 128]. The propagator data indicates how small variation in energy flux to a flowing near or supercritical fluid can tune the dynamics through the impact of the buoyancy force. The T_s = 15 ^oC and T_f = 21 ^oC data indicate longer residence time in Figure 5.11d), 5.12d) and 5.13d) for all 3 pressures, relative to the T_s = 25 ^oC dynamics which are Poiseuille like in the near critical gas at P = 25 bar and become more slug flow like as pressure increases through the critical point. The small displacements in the propagators generate the long tails in the RTD and indicate the ability to control dynamics relevant to microfluidic sensor design [129].

Near the critical point, the flow takes about 210 minutes to reach steady state from start-up. At conditions away from the critical point, minimal time of the order of 10 minutes is required to reach steady state flow. Both velocity maps (Figure 5.15) and propagators (Figure 5.16) measure the time required to reach steady state flow conditions at T_f = 20 ^oC, T_f = 20 ^oC and P = 29 bar at the critical point. The flow started out with an average velocity of ~0.9 mm/s and the highest velocities nearest the walls as shown in

Figure 5.15 in the 0 minute velocity map. Away from the walls, the velocity drops drastically and was 0 mm/s in the center of the pipe. The flow field changed as time progressed between 70 – 210 min. with the wall velocity dropping and velocity in the center increasing. Although the velocity map showed the spatial velocity field changing, the average velocity and velocity probability distributions remained constant throughout the time interval 140-175 min as seen in the propagators (Figure 5.16). The propagator taken starting at 175 min. showed the initial shift to the final velocity state. The final velocity map and propagators revealed that the average velocity shifted to about 2.8 mm/s at steady state conditions. Additional velocity map and propagator data taken after the 210 minute threshold during separate runs starting from no flow conditions showed that the final steady state flow dynamics were repeatable for the given temperature and pressure.

The observed changes in flow dynamics due to a temperature shift during a run in which propagators with varying displacement time and velocity maps were being acquired is shown in Figure 5.17. The experiment began with a fluid temperature of T_f = 22 ^oC and T_s = 21 ^oC and transitioned to T_f = 20^oC and T_s = 21 ^oC. The flow at T_f = 22 ^oC and T_s = 21 ^oC at the start of the run appeared to be operating under steady state conditions and did so up until the propagator at an observation time of 80 ms, the third acquired in a sequence for Δ = 100 ms to 10 ms in 10 ms increments. The velocity map (Figure 5.17c) and the initial propagators at 100 and 90 ms showed a higher probability for slower flows near the walls. Similar results were discussed above for P = 29 bar and T_f = 23 ^oC T_s = 21 ^oC and in those experiments steady state was reached instantaneously.

At Δ = 80 ms, the impact of the temperature change due to a change in the buoyancy force is evident. At Δ = 70 ms, the flow dynamics have transitioned analogous to the P = 29 bar data when the buoyancy force is reversed in Figure 5.12. The decreasing observation time propagators show similar dynamics as those observed in 70 ms Figure 5.17b and the velocity map of Figure 5.17d has been presented in Figure 5.15. The fluid temperature drop from T_f = 22 to 20 ^oC, and all other conditions stable, the flow dynamics suddenly shift, indicating the extreme sensitivity of the transport dynamics of flowing fluids near the critical point.

The diffusion measurements taken at 0.5 mL/min flow conditions show the hydrodynamic dispersion due to interaction between advection and diffusion [4, 126], dynamics not seen in the non-flowing experiments. Diffusion and hydrodynamic dispersion data exist for supercritical carbon dioxide [130-135], but the literature does not contain information on diffusion and dispersion for supercritical C_2F_6. The dPGSE signal attenuation plots for the flowing conditions for all pressures P = 25 (Figure 5.18), 29 (Figure 5.19), and 45 bar (Figure 5.20), became nonlinear at displacement observation times above Δ = 100 ms. For P = 25 bar measurements at flowing conditions became nonlinear at Δ = 250 ms, while for P = 29 and 45 bar the data exhibit nonlinear behavior at Δ = 150 ms. Linear signal attenuation plots, a diffusion or effective diffusion coefficient was determined from a curve fit to all of the data points. For the nonlinear signal attenuation plots, a biexponential model was fit to the fast diffusion component (low q-values) and to the slow diffusion component (high q-values). The diffusion (no flow) or dispersion (flow) coefficients were plotted in Figure 5.21. The slow component

of dispersion for the flowing experiments matched the diffusion coefficient of the non-flowing experiments. The fast dispersion component emerged only during flow. This suggested that a two diffusion population existed in the sample for flow conditions. The observation time at which the second component emerged could provide insight into the correlation length of near critical fluids. For instance, at P = 25 bar the diffusion coefficient was roughly $D_o = 8.5 \times 10^{-8}$ m^2/s. Multiplication of the diffusion coefficient by the displacement observation time Δ = 250 ms and taking the square root gives $l_D \sim \sqrt{2D_o\Delta} =$ 145 μm. This same calculation for P = 29 and P = 45 bar yields $l_D \sim$ 90 and 47 μm, respectively. Two populations as seen in the diffusion data were not observed in the magnetic relaxation time as discussed later. The data do no exhibit any q-space diffraction peaks as have been observed in porous media [124, 126, 136]. It was hypothesized that the correlation length of the density fluctuations might induce diffraction like effects yielding a length scale of dynamics variation in q^{-1}, but it was not observed.

T_1-T_2 magnetic relaxation correlation experiments were run on C_2F_6 at P = 25, 29, and 45 bar under non-flowing and flowing (0.5 mL/min) $T_f = 20^oC$ and $T_s = 20\ ^oC$ conditions (Figure 5.22). This was done to quantify the magnetic relaxation times as a function of pressure and to determine if two populations of relaxation times existed which correspond to two modes of diffusion. Only one peak in the T_1-T_2 at all pressures was found. For both flowing and non-flowing conditions, T_1 and T_2 increased with increasing pressure. Magnetic relaxation time for P = 25 bar were $T_1 = T_2 = 0.38$ s, P = 29 bar $T_1 = T_2 = 0.51$ s, and P = 45 bar $T_1 = T_2 = 0.59$ s for non-flowing conditions. The

relaxation times for P = 25 bar under the flowing condition were the same as in the non-flowing $T_1 = T_2 = 0.38$ s. For P = 29 and 45 bar, however, the relaxation values decreased to $T_1 = T_2 = 0.44$ and 0.51 s, respectively. The relaxation values reported here were taken from the maximum intensity of the peak on the T_1-T_2 graphs. Although the maximum of the peaks shifted slightly between the non-flowing and flowing T_1-T_2 plots, the range of relaxation values has overlap. The addition of flow to the C_2F_6 system did not significantly change T_1-T_2 relaxation. However an interesting aspect of the data is the broader distribution of T_2 as P increases for the no flow fluid. Measurement of exchange in Figure 5.23 and Figure 5.24 showed no additional information as a result of mixing time. These plots confirmed that for P = 25 and 29 bar T_2 =0.38 and 0.51 s, respectively. These plots indicate that only one component of relaxation exists for P = 25 and 29 bar.

Conclusions

MR velocity maps have non-invasively measured the spatial distribution of velocity in critical and supercritical fluids for the first time. Hexafluoroethane was chosen for the fluid because its critical temperature is below room temperature, its critical pressure is relatively easy to maintain inside of the restrictive environment of an MR magnet, and the signal intensity of ^{19}F is comparable to ^{1}H. The flow loop has been designed to accurately control the pressure and flow rate of the fluid both of which can alter the material and magnetic resonance properties of the MR fluid. Non-invasive MR has shown itself a useful method in revealing the fluid dynamics and transport dynamics of the supercritical region.

MR VELOCITY MAPS AND PROPAGATORS OF A SUB, CRITICAL, AND SUPERCRITICAL FLUORINATED GAS, C_2F_6, IN A POROUS MEDIA

Introduction

A supercritical fluid (SCF) is a fluid that is above its critical temperature, pressure, and density [45]. A fluid in this state has properties simultaneously similar to that of gases and liquids. For instance, a SCF has transport properties such as diffusivities and viscosities similar to that of the gas phase while densities resemble those similar to the liquid phase. With these qualities, a SCF makes for a novel and environmentally safe solvent with beneficial transport properties [46].

Many SCF solvents have less environmental impact than current petroleum based solvents. One such solvent is CO_2 [47]. Although a greenhouse gas, CO_2 is naturally occurring and often an unavoidable byproduct of some processes. Its abundance and relatively lower environmental impact makes CO_2 a viable option for use as a SCF for processing. Supercritical CO_2 has been utilized in various porous media applications, one of which is Enhanced Oil Recovery (EOR). EOR is a process utilizing supercritical CO_2 to force out oil that has saturated porous rock [49-51]. Additionally, supercritical CO_2 is used in chromatography (SFC) which employs the transport and solubility advantages of supercritical fluids [52, 53] in porous media. Storage of CO_2 in a supercritical state in earth formations including porous rock is currently being implemented as means to reduce CO_2 in the atmosphere and hence combat global climate change [49, 54-56].

The properties of a SCF are tunable by adjusting the pressure or temperature of the fluid in the critical range. Thermophysical properties such as specific heat, density, viscosity, and heat transfer coefficients of CO_2 can be tailored near the critical point [57]. Experimentally, the effects of the thermophysical properties of a supercritical fluid under flowing conditions in non-porous samples against and with gravity have been well studied [58-61]. Near the critical point buoyancy in the fluid begins to impact the heat transfer and mass transport. Several numerical or theoretical studies have [62-68] predictd and validated the experimentally observed thermophysical behavior including buoyancy effects of near critical fluids including buoyancy effects [72-76]. Recently some focus has shifted from larger scale experiments to mini-tubes [77] and porous tubes [57, 78, 79]. In regards to velocity distributions of a flowing fluid near the critical point in non-porous media, several groups offer reliable theoretical or numerical models for turbulent or laminar entrance flows [57, 64, 65, 80-83, 137], but only a few appear to provide experimental data [84, 85]. So far no experimental studies have observed flow dynamics of SCF's in porous media. The experimental velocity maps and propagators presented in this paper were taken using non-invasive MR. MR velocity maps were used to observe flow at P = 45 bar using a repetition time of T_R = 2 s and 32 averages. MR propagators were used to observe fluid dynamics at three pressures P = 25, 29, and 45 bar over a time evolution of displacement observation times Δ = 30 – 500 ms. The sequence used was a stimulated echo to store the T_2 magnetization due to a short T_2* because of the pores.

MR has previously shown that for non-flowing SCF in porous media the phenomenon of tunable properties occurred at lower temperatures in the pore spaces relative to the bulk fluid. Additionally the shifted critical temperature inside the pores was directly affected by the void size [86, 87]. An MR study of flowing SCF [88] used MR imaging to obtain signal intensity and relaxation components in a porous media, but no in depth MR studies of SCF fluid dynamics in porous media have been published. Despite the lack of experimental data, the need exists to study SCF flow dynamics in porous media due to the wide current and projected use of flowing SCF for applications other than heat transfer. MR has been used in several applications which use supercritical CO_2 as a solvent [47, 52, 53, 89]. However, the first application of MR to flowing supercritical fluids in porous media with the purpose of obtaining transport properties and flow dynamics is presented here.

Methods

Magnetic resonance microscopy techniques [1-4, 6, 19] were used to obtain velocity maps and propagators over a range of pressures and observation times for the respective flowing or non-flowing regimes in porous media. Hexafluoroethane, C_2F_6, was chosen for these studies due to its favorable combination of physical properties, (critical temperature T_c = 19.88 ^oC and critical pressure P_c = 30.48 bar) and MR relaxation times as well as the high natural abundance and high MR signal (comparable to proton signal) for ^{19}F [5-8]. Observations were first made on stagnant fluid to provide a basis for comparison. Then the flow characteristics of the supercritical C_2F_6 was

studied by obtaining scale dependent velocity maps, propagators and diffusion coefficients using magnetic resonance techniques.

Hexafluoroethane, C_2F_6, was pumped through a system designed for the Bruker Avance 300 MR imaging spectrometer. From the supply tank, the gas was pumped to a range of pressures below, near, and above the critical pressure using an Isco 500D syringe pump. The Isco 500D is a single cylinder syringe pump that provides a constant volumetric flow rate from the cylinder. C_2F_6 exited the syringe pump at a flow rate of 0.5mL/min and traveled through PEEK tubing of 1.524 mm ID (inside the MR magnet) and stainless steel tubing (outside of the MR magnet). The 200 mm bead pack was constructed from 55 μm copolymer microspheres (Thermo Scientific, 7550A) packed directly into the PEEK 1.524 mm ID tubing and constrained by 10 μm filters placed at either end inside tubing connectors. The porosity was $\phi \sim 0.44$ corresponding to a pore length scale $l_p = \frac{\phi d_p}{(1-\phi)} = 43.2$ μm. Back pressure was maintained by a Thar back pressure regulator APBR-20-1. The depressurized C_2F_6 was collected in a gas cylinder and used to refill the syringe pump for subsequent experiments. Pressure transducers monitored the pressure of the fluid upstream and downstream of the MR magnet. The room temperature was also monitored and controlled with a precision of ±0.5 ^{o}C. The fluid temperature was equilibrated with room temperature for 1 hour before experiments were run.

Measurements were made under no flow conditions for comparison with the flow conditions. In addition to the 55 μm copolymer microspheres, no-flow experiments were carried out on 230 μm and 550 μm (MR images only) Zirconium Silicate Microspheres

(Corpuscular) beadpacks. The sample holder had an ID of 5mm and only one entrance port, so it was not designed for flow through experiments. A velocity map of C_2F_6 flowing at 0.5 mL/min through the 55 μm bead pack contained in a 1.524 mm ID PEEK capillary at supercritical pressure P = 45 bar was measured The velocity map pulse sequence had a displacement observation time Δ = 2.239 ms and gradient pulse duration δ = 0.25 ms. The stimulated echo was used due to the shorter T_2* of the fluid in the porous media. No slice selection was used so the image is of the entire excitation region of the rf coil (length = 20 mm). The repetition time was T_R = 2 s and 32 signal averages were used for a total experiment time of 68 minutes. The spatial resolution with a field of view of 4 mm x 2 mm [64 x 32] was 62.5 μm x 62.5 μm. The maximum and minimum gradient value for the velocity maps were ±.1942 T/m.

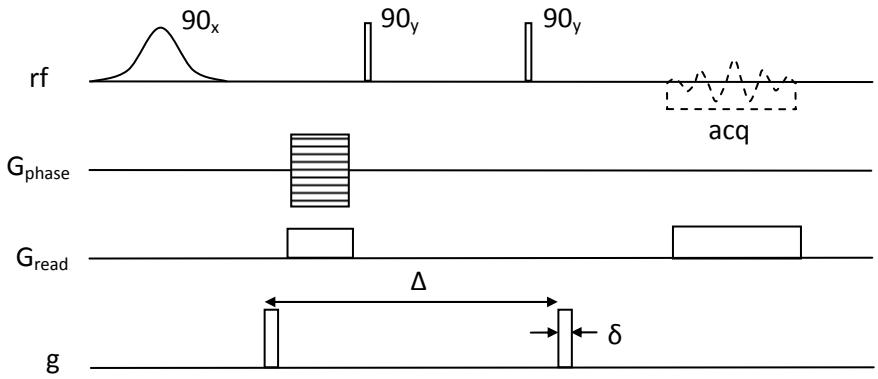

Figure 6.1: Velocity map pulse sequence using a stimulated echo.

Single PGSE (Figure 6.2) and double PGSE (Figure 6.3) propagators characterize the hydrodynamic dispersion in porous media [44, 138] and were measured for flowing C_2F_6 at 0.5 mL/min in the 55 μm beads at three pressures P = 25 bar, 29 bar, and 45 bar (Figure 7). The propagator sequence used a stimulated echo PGSE with displacement

observation times in the range Δ = 50 – 500 ms and gradient pulse duration δ = 0.25 or 0.5 ms, depending on the maximum gradient requirements for shorter displacement observation times. No slice selection was used, exciting the entire excitation region of the rf coil (approx. 20 mm length). The repetition time T_R = 2 s and 16 signal averages were taken for each pressure resulting in a data acquisition time of 67 minutes.

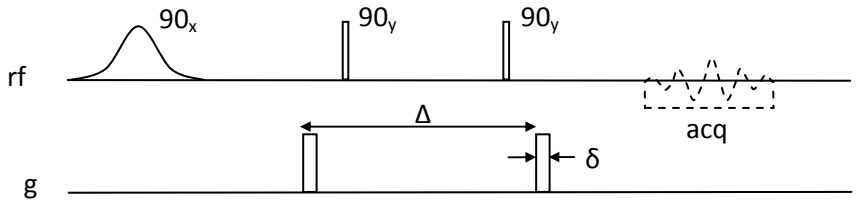

Figure 6.2: Single pulsed gradient stimulated echo pulse sequence.

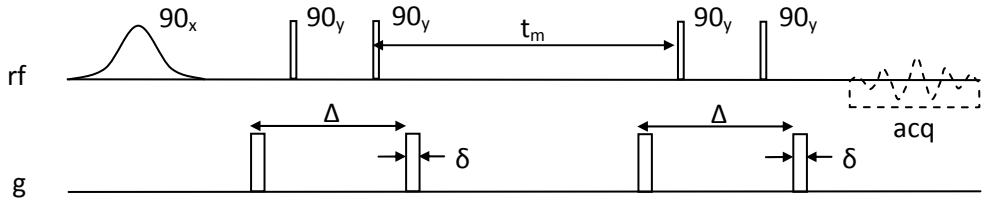

Figure 6.3: Double pulsed gradient stimulated echo pulse sequence.

MR images (Figure 6.4) were obtained of the supercritical fluid in the porous media for 230 and 550 μm beads. For all the MR images a resolution of 109.4 x 109.4 μm with a field of view of 7 mm x 7 mm was used. For the 550 μm beadpack at 45 bar the experimental parameters were; T_E = 3 ms, T_R = 3000 ms, 52 averages, total test time of 3 hours and a slice thickness of .5 mm. For the 230 μm beads at 70 bar, the experimental parameters were; T_E = 3 ms, T_R = 1500 ms, 176 averages (5 hours), 8 averages (13

minutes), and 8 averages (13 minutes) for the .2 mm, 1 mm, and 20 mm slice thicknesses, respectively.

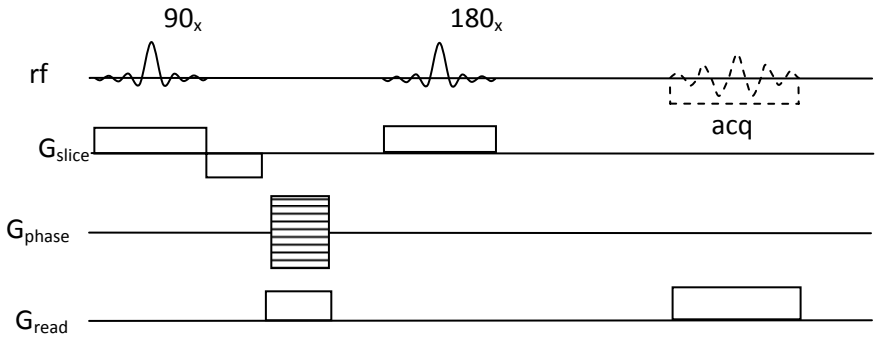

Figure 6.4: Pulse sequence for MRI density maps.

Results

Non-flowing results were obtained for 55 μm beads in a 1.5 mm ID capillary tube as well as 230 μm beads in a 5 mm ID sample holder. Flowing results were obtained for 55 μm beads in a 1.5 mm ID capillary tube.

No Flow Results

Non-flowing sPGSE propagators were taken at three pressures, 25 bar, 29 bar, and 45 bar (Figure 6.5) in the 55 μm beadpack. The temperature of the fluid $T_f = 21\ ^oC$ and surrounding temperature $T_s = 21\ ^oC$. The propagators used observation times Δ in the range of 10 – 500 ms. For all of the pressures, an observation time of 500 ms was the cut off time due to signal noise. Longer observation times were accessible given the long MR relaxation times, but were not possible because the experimental time required for the necessary signal averaging would have been greater than a single pass of the single

cylinder syringe pump. Displayed are the displacement propagators for all three pressures.

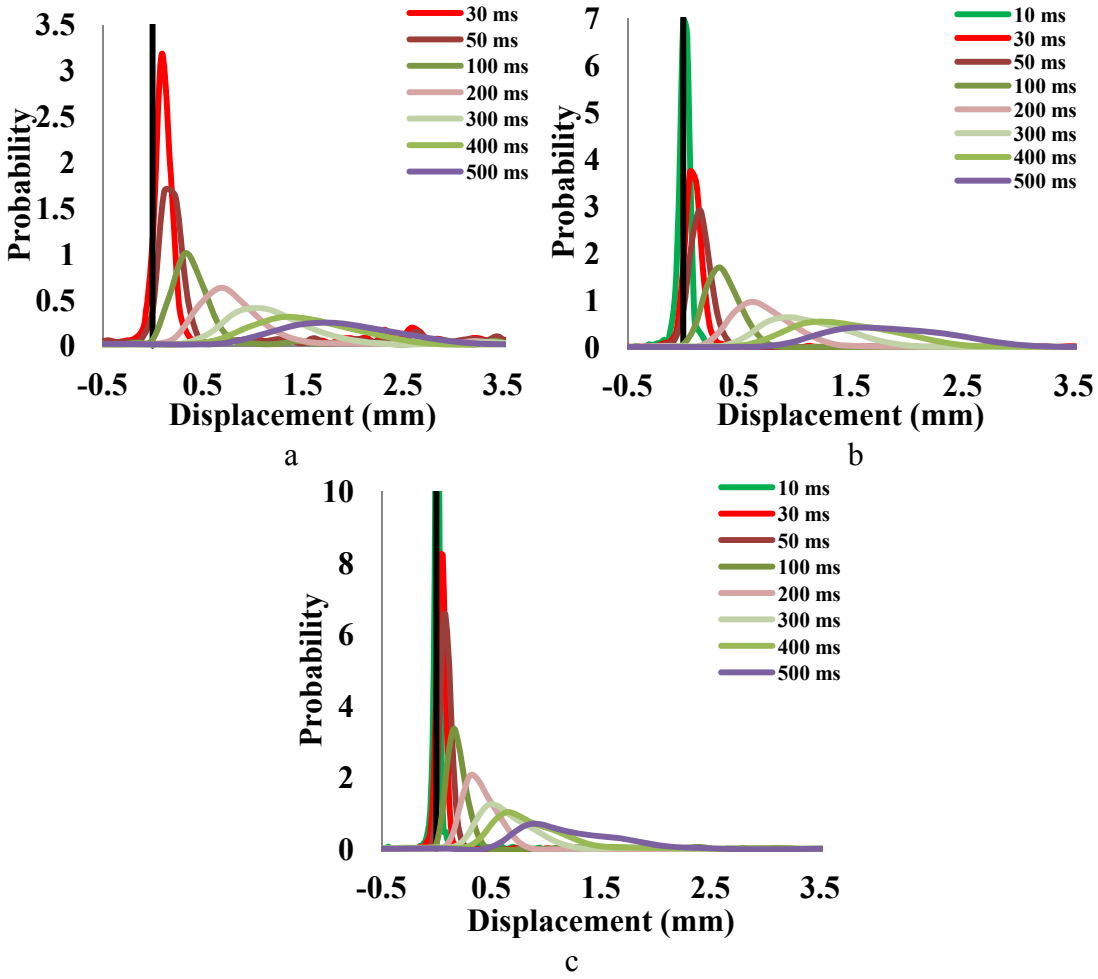

Figure 6.5: No flow sPGSE propagators of C_2F_6 in 55 µm beads contained in 1.5 mm ID capillary at a) 25 bar, b) 29 bar, and c) 45 bar for T_f = 21 °C and T_s = 21 °C.

Although the experiments were for no flow conditions, a minor flow was observed in the propagators at all three pressures. This small flow was most likely due to a small leak in the system. Several attempts to tighten fittings and all attempts at leak detection failed. As verification that a leak was the cause of the observed net displacement, the volume of the system as displayed on the pump was recorded before

and after the experiments. The results confirmed a loss of fluid. Due to the minor flow caused by the uncontrollable leak in the 1.5 mm diameter capillary system containing the porous media, the data cannot be used to accurately describe no flow conditions in porous media.

A second system was built that accurately tested for no flow conditions. The set-up was designed as a dead end system with 230 μm Zirconium Silicate Microspheres packed inside a 5 mm diameter and 200 mm long cylinder.

Non-flowing sPGSE and dPGSE propagators were taken at three pressures, 25 bar (Figure 6.6), 29 bar (Figure 6.8), and 45 bar (Figure 6.9). The temperature of the fluid T_f = 22 ^oC and the surrounding temperature T_s = 21 ^oC. The propagators used displacement observation times Δ in the range of 10 – 500 ms. These propagators have a mean of zero and hence no mean flow.

The dPGSE propagators are a measure of the incoherent motion or diffusion of the fluid. The sPGSE experiments on the other hand contain both incoherent and coherent motion. Although there is no apparent mean unidirectional flow, the differences between the dPGSE and sPGSE is a measure of the coherent motion in the sample. This coherent flow is due to convective motion from temperature gradients in the sample.

For 25 bar, the dPGSE propagators (Figure 6.6b) showed a symmetric curve about zero displacement. The corresponding sPGSE propagators (Figure 6.6a) were not symmetric and can be interpreted as the superposition of two Gaussian curves as demonstrated in Figure 6.9.

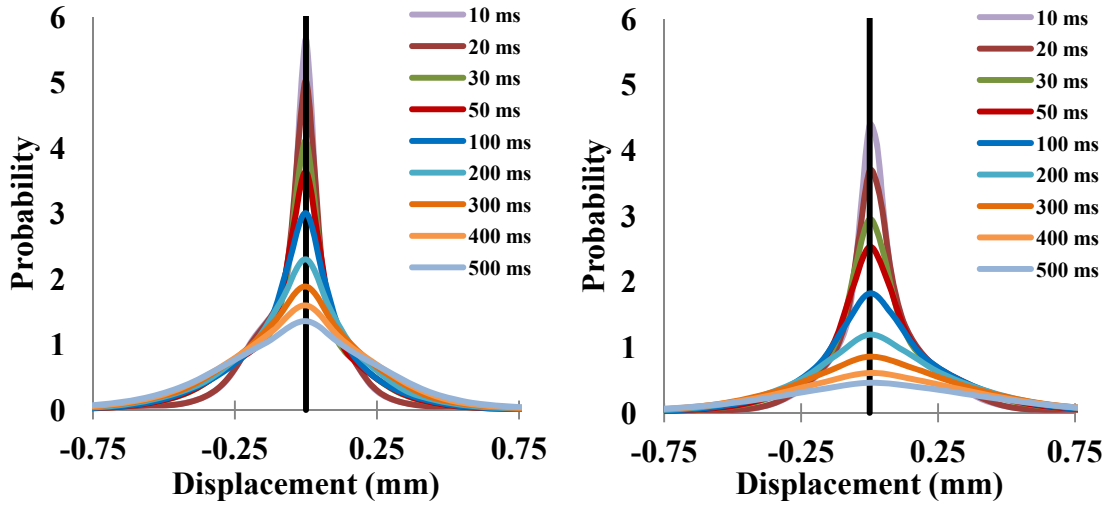

Figure 6.6: No flow a) sPGSE and b) dPGSE propagators of C_2F_6 in 230 µm beads contained in 5 mm ID sample holder at 25 bar.

The two Gaussian curves indicated two populations were present in the sample at each observation time. The broader Gaussian shifted to the left corresponds to the faster downward convection current and the narrower Gaussian shifted to the right corresponds to the slower upwards moving spins.

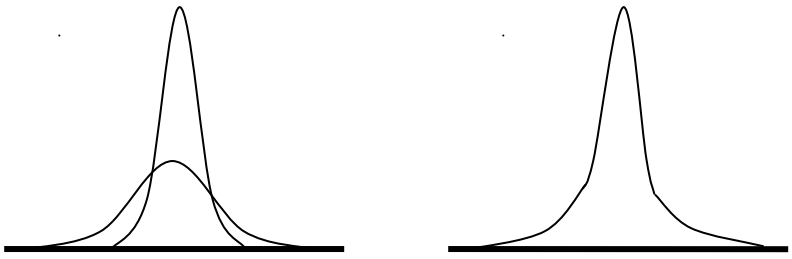

Figure 6.7: a) Superposition of two Gaussian Curves b) merged into one as observed in the sPGSE experiments.

In the sPGSE propagators for 25 bar a length scale of ~180 μm is apparent. This corresponds to the approximate pore size as determined by $l_d = (\varphi/1\text{-}\varphi)d_p = 181$ μm where $\varphi \approx 0.44$ and $d_p = 230$ μm.

One population of motion is shown in the dPGSE propagators and the dPGSE propagator measures the incoherent motion (diffusion) and can be modeled with a single Gaussian that is similar to the broader (faster) component of the sPGSE propagator.

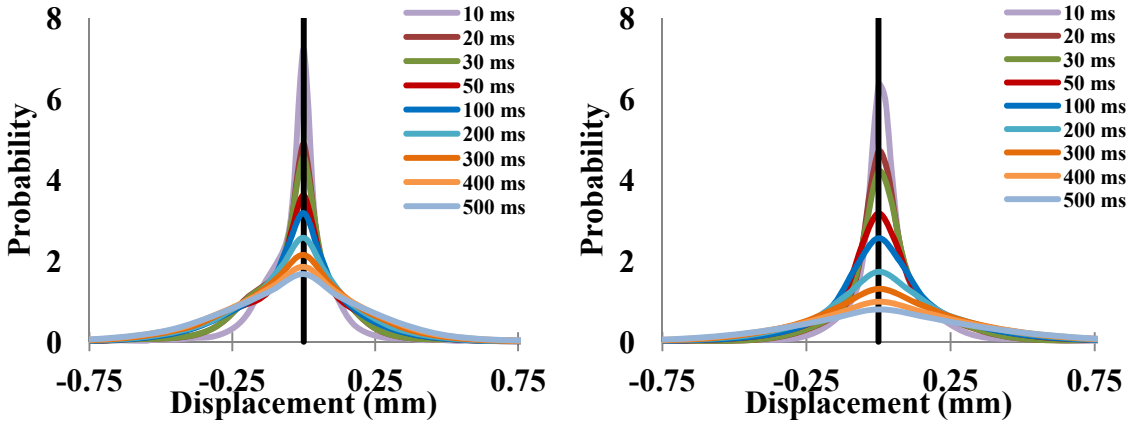

Figure 6.8: No flow a) sPGSE and b) dPGSE propagators of C_2F_6 in 230 μm beads contained in 5 mm ID sample holder at 29 bar.

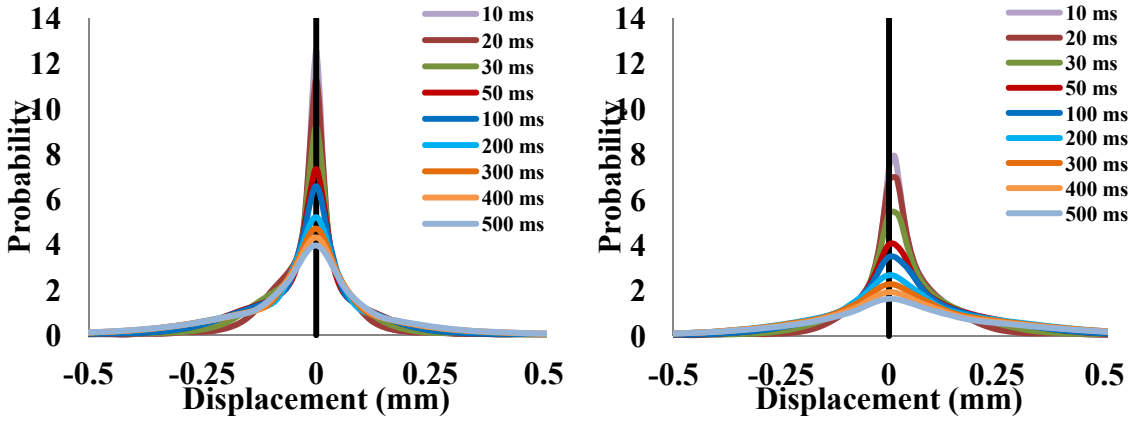

Figure 6.9: No flow a) sPGSE and b) dPGSE propagators of C_2F_6 in 230 μm beads contained in 5 mm ID sample holder at 45 bar.

The thermally convective currents sample larger displacements for a given observation time Δ and allow structure features such as pore size to be clearly identified. The range of displacement at the longest observation times in the dPGSE should also show the pore structure, but does not because of the low signal to noise ratio.

An alternative way to view the data is in the reciprocal *q* domain, this is the domain in which the data is collected. Stejskal-Tanner plots for each pressure are shown in Figure 6.10 – Figure 6.12. The slope of these plots provides a measure of the diffusion or effective diffusion coefficient. The lower the pressure for C_2F_6 the faster the self-diffusion and thus the steeper the attenuation on a Stejskal-Tanner plot. For the sPGSE experiments two slopes are visible, but only one primary slope is visible for the dPGSE experiments, in a direct reflection of the single or double Gaussian model discussed with the propagator data. The dPGSE plots do show 5% of the signal is from a faster diffusing population that was not clearly visible in the propagator data. In the sPGSE experiments approximately 50% of signal is in a faster diffusion population.

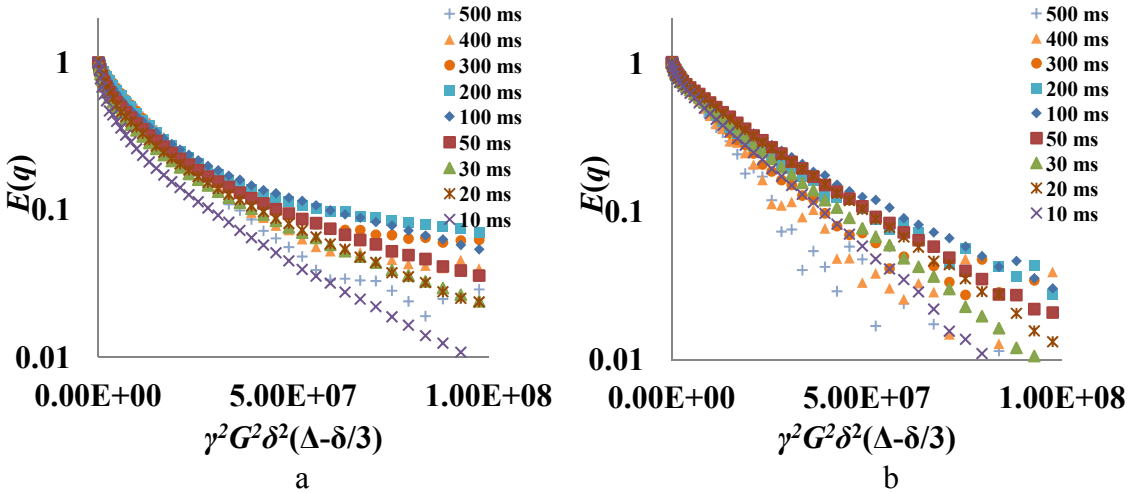

Figure 6.10: No flow a) sPGSE and b) dPGSE Stejskal-Tanner signal attenuation of C_2F_6 in 230 µm beads contained in 5 mm ID sample holder at 25 bar.

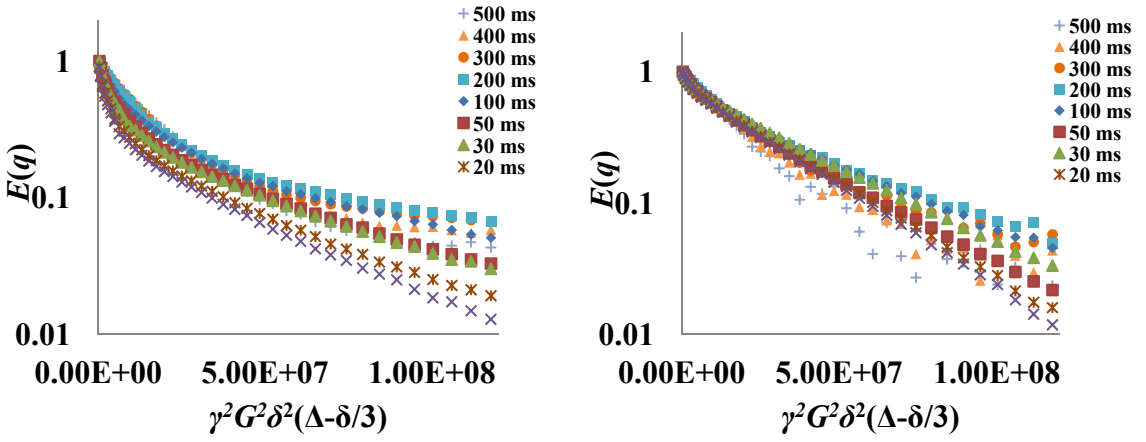

Figure 6.11: No flow a) sPGSE and b) dPGSE Stejskal-Tanner signal attenuation of C_2F_6 in 230 µm beads contained in 5 mm ID sample holder at 29 bar.

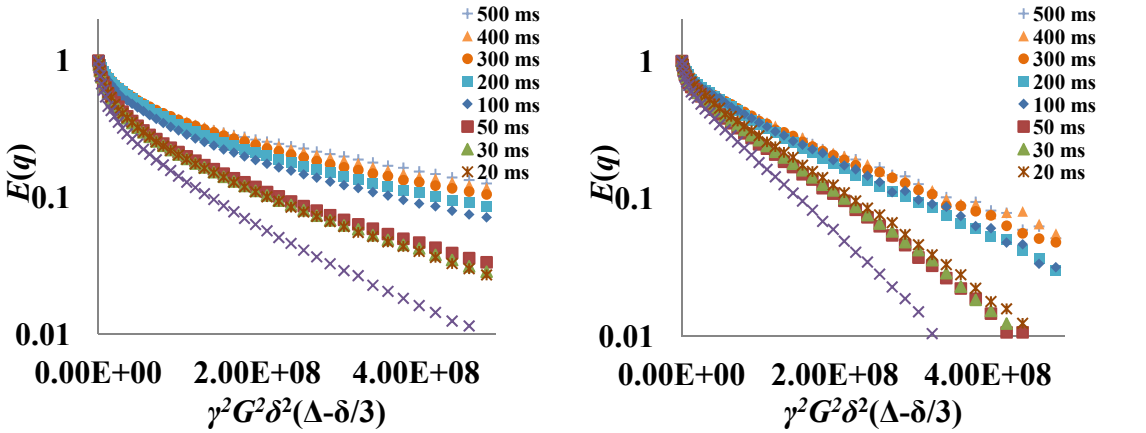

Figure 6.12: No flow a) sPGSE and b) dPGSE Stejskal-Tanner signal attenuation of C_2F_6 in 230 µm beads contained in 5 mm ID sample holder at 45 bar.

The sPGSE and dPGSE attenuation plots are shown for the three pressures of $P = 25$ bar (Figure 6.13), $P = 29$ bar (Figure 6.14), and $P = 45$ bar (Figure 6.15). Of the three pressures tested, fluid at $P = 25$ bar has the fastest self diffusion and convection and will sample a confining structure more quickly than at $P = 45$ bar. The feature only becomes apparent at longer observation times, because it takes the moving particles nearly 300 ms

at P = 25 bar (400 ms for P = 29 bar and an unknown time for P = 45 bar) to sample the confining pore structure of l_d = 181 µm $\left(q = \frac{1}{2}\frac{1}{2800}m^{-1}\right)$. The enhanced transport of the C_2F_6 fluid due to thermal convection allows faster pore structure sampling in the sPGSE but this sampling was refocused in the dPGSE experiments. The pore structure could have been sampled by diffusion in the dPGSE experiments by improving the signal to noise ratio using a larger number of test averages.

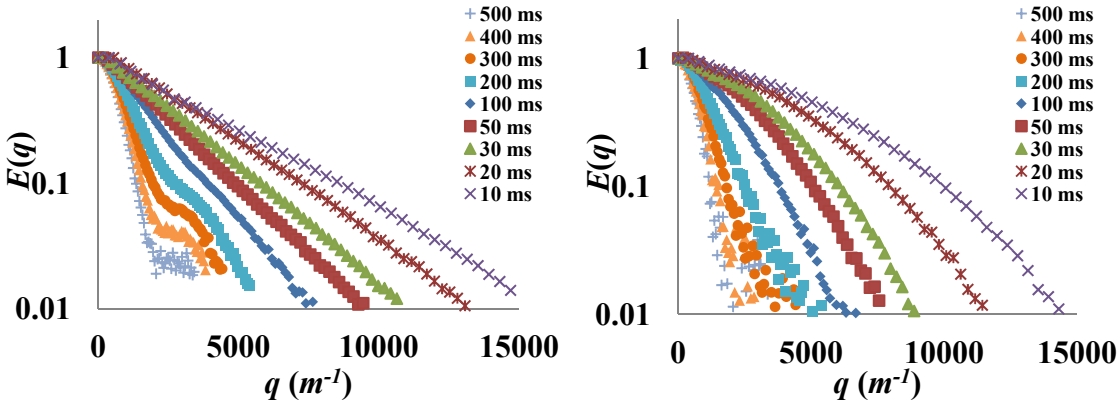

a b

Figure 6.13: No flow a) sPGSE and b) dPGSE q-space signal attenuation of C_2F_6 in 230 µm beads contained in 5 mm ID sample holder at 25 bar.

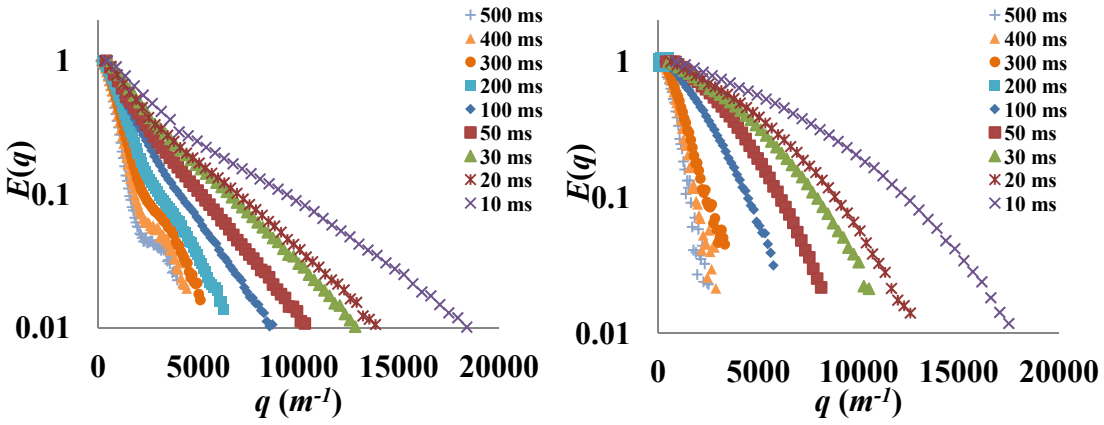

a b

Figure 6.14: No flow a) sPGSE and b) dPGSE q-space signal attenuation of C_2F_6 in 230 µm beads contained in 5 mm ID sample holder at 29 bar.

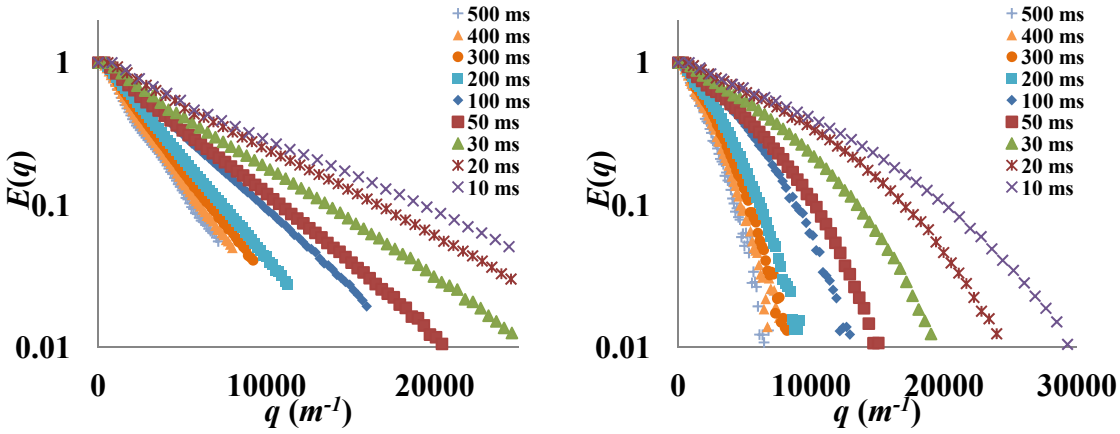

Figure 6.15: No flow a) sPGSE and b) dPGSE *q*-space signal attenuation of C_2F_6 in 230 µm beads contained in 5 mm ID sample holder at 45 bar.

The MR images presented in Figure 6.16 and Figure 6.17 are the first images of supercritical fluid in a bead pack. The images revealed that the fluid can penetrate the void spaces between 230 µm beads homogenously. MR images of the supercritical fluids can reveal the heterogeneity of the pore structure, but the low resolution means sPGSE and dPGSE are a better tool to probe smaller pore size because the diffusion of C_2F_6 for instance has a faster diffusion by an order of magnitude compared to water.

The ordered bead pack structure can be seen in the images. The .2 mm slice (Figure 6.16a), which is slightly smaller than one bead diameter, is very heterogeneous. However, for an increasing slice thickness, the ordering becomes apparent. At 1 mm, about 4 bead diameters (Figure 6.16b), the packing near the walls is visible. For a 20 mm slice, the ordering is visible in 3 or 4 layers of beads around the wall. This ordering around the walls is likely to create less tortuous channels around the perimeter of the bead pack (indicated by the bright spots on Figure 6.16c). The image of Figure 6.17 was taken to observe 550 µm beads in the same sample holder. The larger beads were more

ordered because the number of bead diameters across the diameter of the sample holder was smaller (9 for the 550 μm beads vs. 21 for the 230 μm beads).

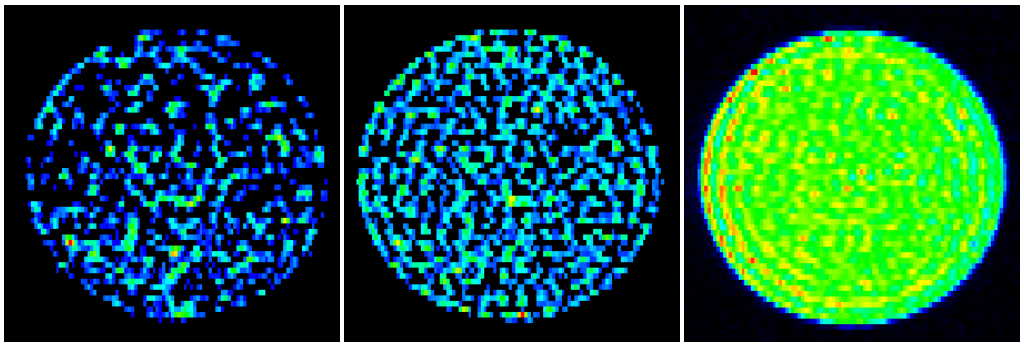

a b c

Figure 6.16: MR images of C_2F_6 in 230 μm beads contained in 5 mm ID sample holder at 70 bar for a slice thickness of a) .2 mm, b) 1 mm, and c) 20 mm.

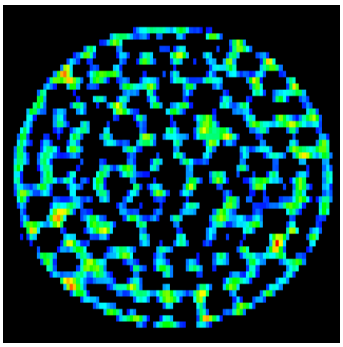

Figure 6.17: MR image of C_2F_6 in 550 μm beads contained in 5 mm ID sample holder at 45 bar for a slice thickness of .5 mm.

Non-flowing velocity maps at an observation time of 2.239 ms were taken of C_2F_6 in 230 μm beads contained in a 5 mm ID sample holder with a slice thickness of 20 mm at pressures of 25 bar (Figure 6.18a), 29 bar (Figure 6.18b), and 45 bar (Figure 6.18c). The no flow velocity maps showed that the fluctuation of velocity (not to be confused with diffusion) increases with decreasing pressure.

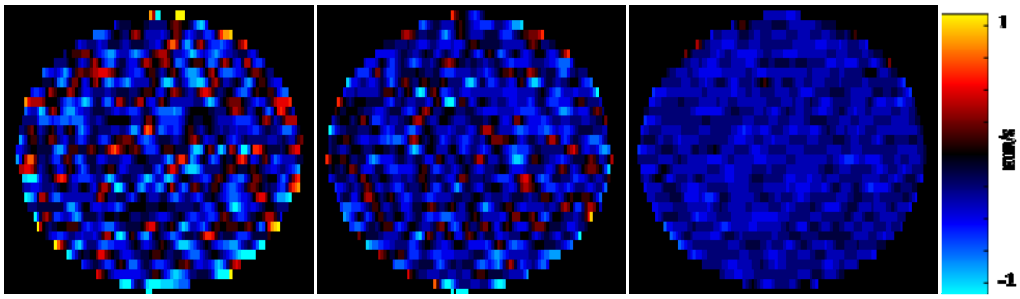

a b c

Figure 6.18: Non-flowing velocity maps, at an observation time of 2.239 ms, for C_2F_6 in 230 µm beads contained in 5 mm ID sample holder with a slice thickness of 20 mm at pressures of a) 25 bar, b) 29 bar, and c) 45 bar.

At the highest pressure P = 45 bar, the randomness of the no flow velocity field became more homogenous. This randomness in the velocity is caused by the convection in the pores due to thermal gradients and was also observed in the propagators.

Flow Results

Velocity maps were taken for C_2F_6 flowing at 0.5 mL/min through the 55 µm bead pack described earlier. The beads were contained in a 1.55 mm ID PEEK capillary with a fluid temperature T_f = 21 ^oC and a surrounding temperature T_s = 21 ^oC. Data was only obtained for P = 45 bar (Figure 6.19). The velocity map sequence used an observation time Δ = 2.239 ms and a pulse duration δ = 0.25 ms. The stimulated echo sequence was used due to the short T_2* of C_2F_6 in the porous media. No slice selection was used. The repetition time was T_R = 5 s and 32 signal averages were used giving a total experiment time of 68 minutes. The resolution with a field of view of 4 mm x 2 mm was 62.5 µm x 62.5 µm. These are the first full field velocity maps of supercritical fluid flowing in porous media.

The velocity map at P = 45 bar had fluctuations in the range ±11.1 mm/s and a volume averaged velocity of 4.97 mm/s.

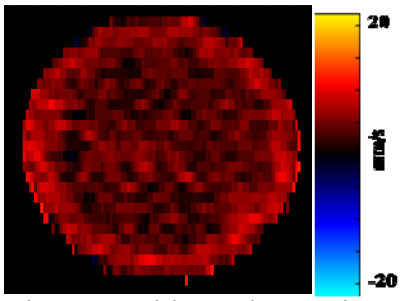

Figure 6.19: 0.5 mL/min velocity map with an observation time of 2.239 ms of C_2F_6 in 55 µm beads contained in 1.5 mm ID capillary at 45 bar at T_f = 21 °C and T_s = 21 °C.

Velocity maps were also obtained for a fluid temperature T_f = 21 °C and a varied surrounding temperature T_s =15 and 25 °C. (Figure 6.20). These experiments were performed to determine if a temperature gradient across the sample would manifest itself in an altered velocity profile as observed for bulk fluid flow in a capillary (See Chapter 5). The test showed that the velocity profile remained similar for all coil temperatures tested and revealed that flow in the porous media was not as sensitive to temperature gradients. The beads damp out the impact of thermal gradients.

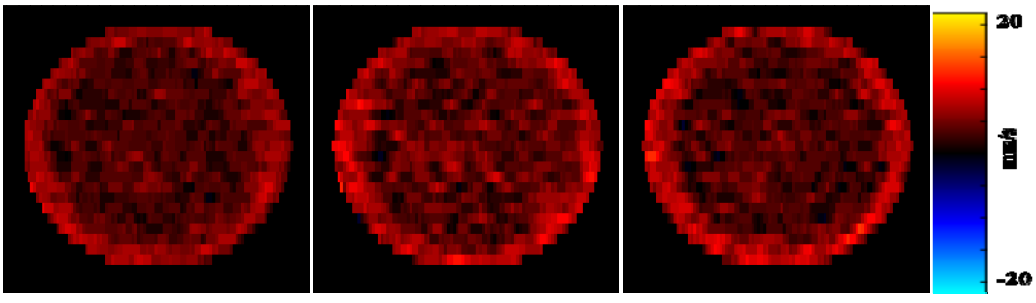

a b c

Figure 6.20: 0.5 mL/min of C_2F_6 velocity maps at 45 bar in 55 µm beads with T_f = 21 °C and at a surrounding temperature T_s = a) 15 °C, b) 21 °C, and c) 25 °C.

Flowing sPGSE propagators were taken at three pressures, 25 bar, 29 bar, and 45 bar (Figure 6.21) in the 55 µm bead pack. The volumetric flow rate programmed at the pump was 0.5 mL/min. The temperature of the fluid was T_f = 21 °C and the surrounding temperature was also T_s = 21 °C. The propagators used observation times in the range of 10 – 500 ms. For all of the pressures, an observation time of 500 ms was the cut off time due to signal noise. This was a similar requirement for the no flow. Displayed are the displacement propagators for all three pressures.

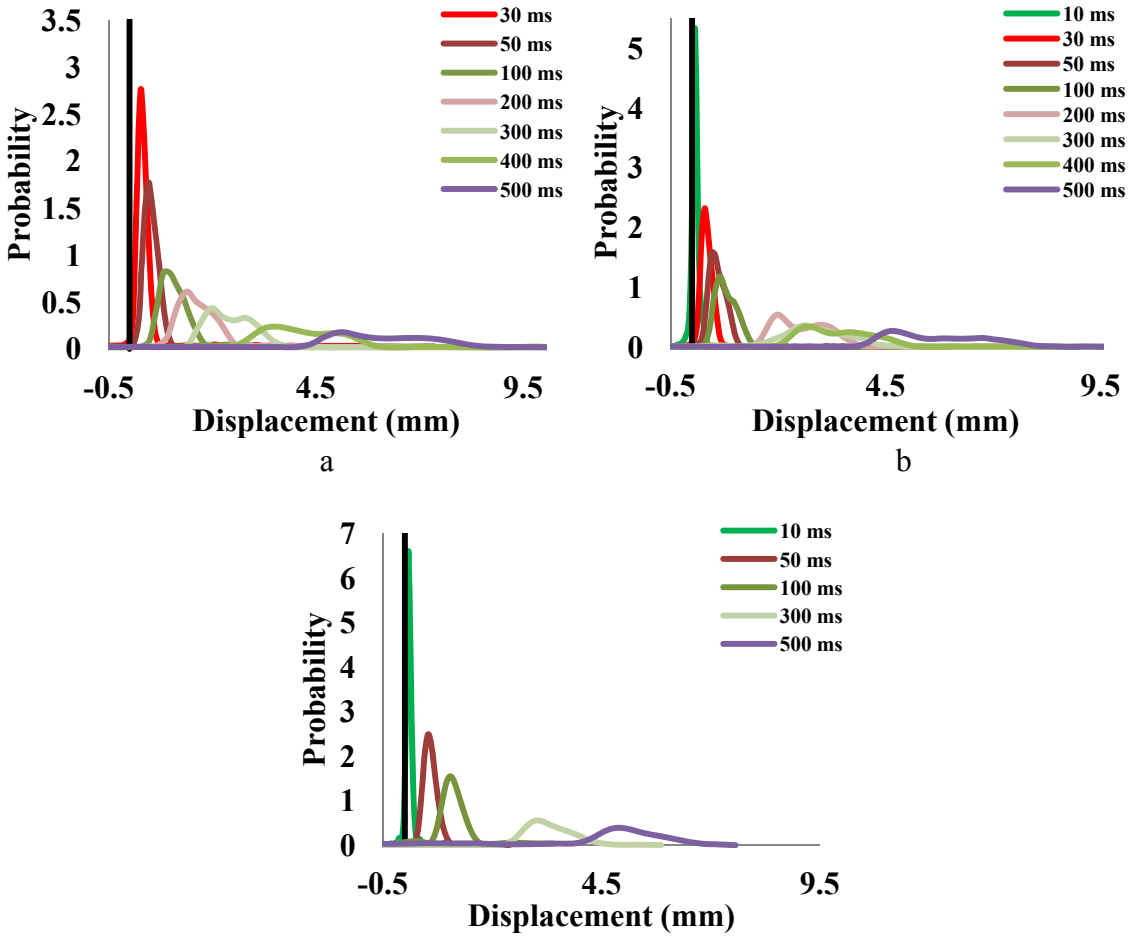

Figure 6.21: 0.5 mL/min flow sPGSE propagators of C_2F_6 in 55 µm beads contained in 1.5 mm ID capillary at a) 25 bar, b) 29 bar, and c) 45 bar.

In normal fluids the propagators from bead packs undergo an evolution with displacement time Δ from a near Cauchy like distribution at short Δ relative to the time to traverse a pore by translational motion, $i.e. \tau_v = \frac{l_p}{v_s}$ the ratio of the effective pore length scale l_p and $v_s = \frac{\langle v \rangle}{\phi}$, to a Gaussian distribution of displacements after multiple pores are traversed and hydrodynamic dispersion dominates [26, 44, 138]. The propagators for the near critical gas P = 25 bar and the supercritical fluid P = 45 bar follow a similar displacement time evolution to one another but drastically differ than normal fluids. A distinct bimodal distribution is present at longer displacement times. The superficial velocity v_s = 8.2 mm/s for both of these fluids so $\tau_v \sim 5$ ms and multiple pores of the structure of the porous media are sampled for all displacement times in Figure 7. The critical phase transition fluid P = 29 bar exhibits different behavior than the other pressures. Strikingly the impact of compressibility, which caused slower mean displacement in the capillary is not evident as the mean displacement in the porous media is of similar magnitude to the near critical gas and supercritical fluid. The P = 29 bar propagator undergoes a transition with displacement time from a distribution with more skew towards higher displacement than the other fluids at Δ = 50 ms. At Δ = 300 ms P = 25 and 45 bar are clearly bimodal by this time and P = 29 bar becomes bimodal at Δ = 500 ms similar to the other pressures.

For 29 bar, testing did not begin until the stead state had been reached after 4.5 hours. A series of propagators at the same observation time of 100 ms were used to watch the flow develop into steady state flow (Figure 6.22). The 136 and 204 minute

propagators in Figure 6.22 show repeatable flow dynamics, although Figure 6.21b suggest that the velocity can still fluctuate after reaching a steady state flow.

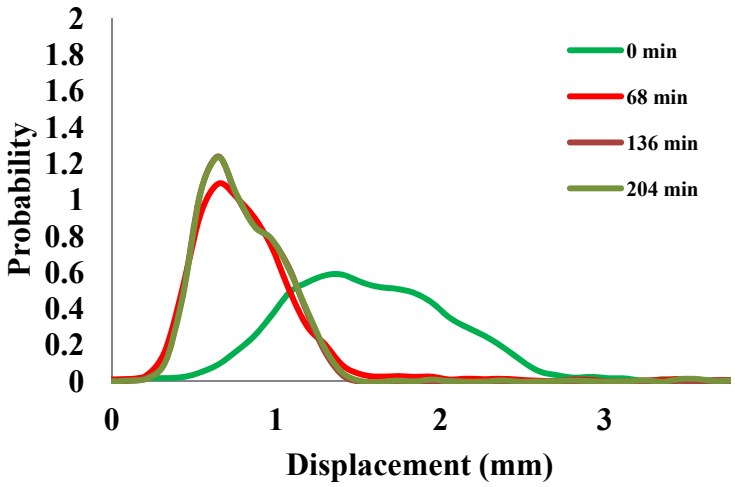

Figure 6.22: Series of 100 ms observation time propagators to determine steady state flow. Times stated are when the test began, *i.e.* the test labeled "68 min" began at 68 minutes from the start of the flow.

The propagator experiments for Δ = 10 – 500 ms observation times, were started well after the flow was stabilized (272 minutes into the flow). At 29 bar, velocity fluctuations are due to a phenomenon called dynamic equilibrium which arises in near critical fluid flow because the fluid density, compressibility, and viscosity can change drastically with small changes in temperature and pressure.

The sPGSE Stejskal-Tanner plots for all three pressures under flowing conditions are shown in Figure 6.23. The plots come from the positive *q*-space of the propagators in Figure 6.5. Under flowing conditions these plots can show the dynamic structure of the bead pack in the manifestation of coherence peaks. These coherence peaks arise from non-Gaussian features in the propagators. A propagator with a width of x will show a

coherence minimum at $q = \frac{1}{x}$. The 25 and 29 bar experiments exhibit coherence features for $\Delta \geq 50$ ms, but the 45 bar only exhibit coherence features at the longest observation times $\Delta \geq 300$ ms. This indicates the Δ at which the average convective flow through the pore structure becomes apparent.

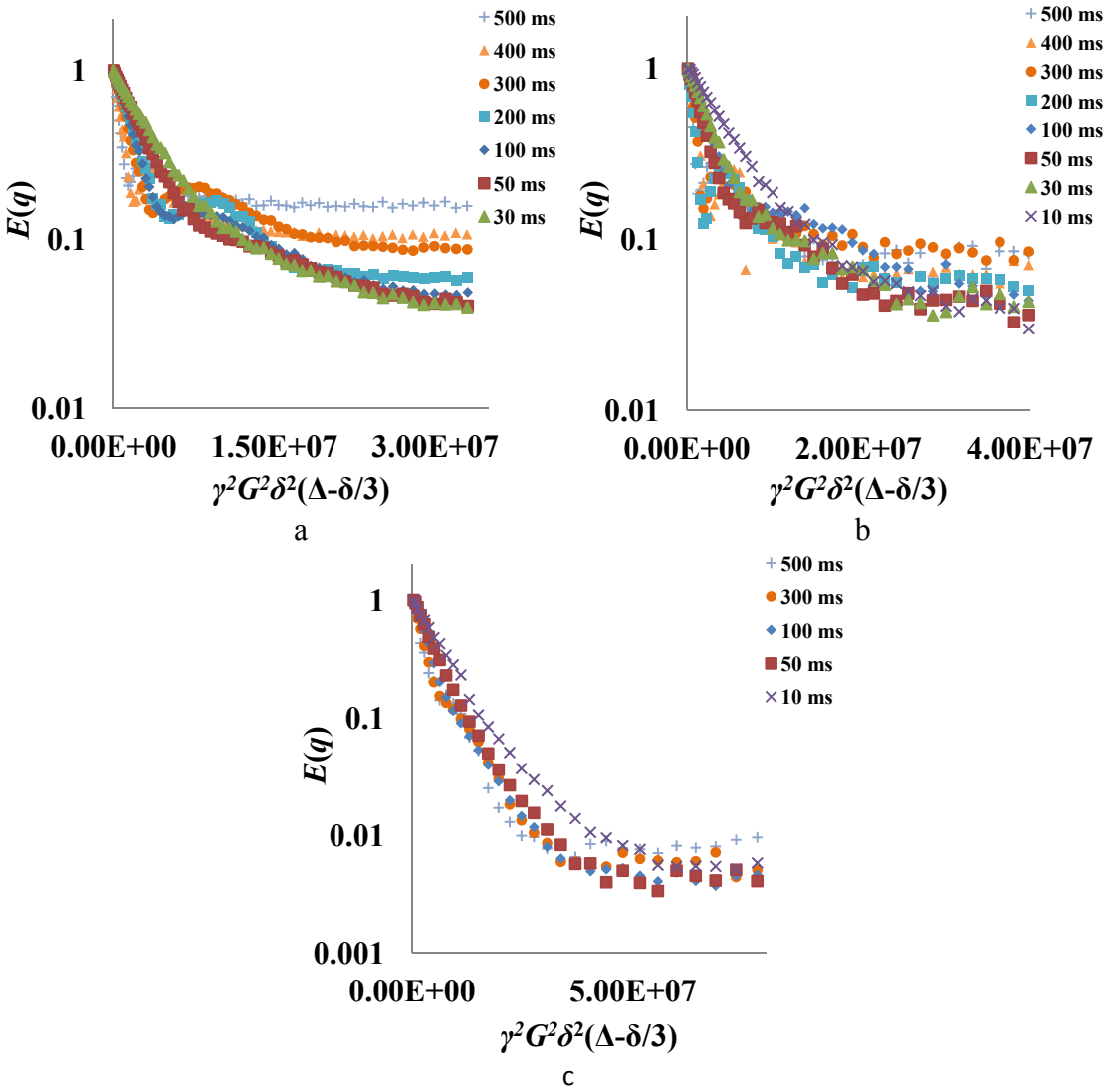

Figure 6.23: 0.5 mL/min flow sPGSE Stejskal-Tanner signal attenuation of C_2F_6 in 55 µm beads contained in 1.5 mm ID capillary at a) 25 bar, b) 29 bar, and c) 45 bar.

The coherence peaks are best quantified by observing the sPGSE signal attenuation vs. the q-vector (Figure 6.24). For Δ = 100 ms at P = 25 bar, the first minimum occurs at q = 1190 m^{-1}. This corresponds to a width of 804 µm as seen in the corresponding propagator in Figure 6.21a.

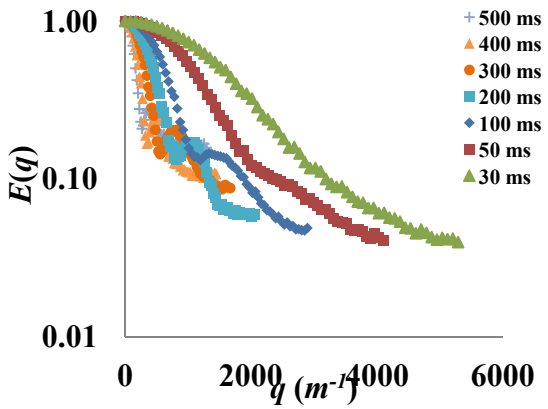

Figure 6.24: sPGSE signal attenuation E(q) vs. q-vector for 0.5 mL/min flow of C_2F_6 in 55 µm beads contained in 1.5 mm ID capillary at 25 bar.

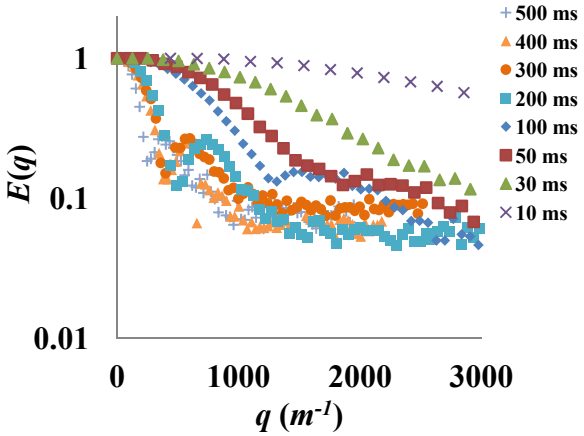

Figure 6.25 sPGSE signal attenuation E(q) vs. q-vector for 0.5 mL/min flow of C_2F_6 in 55 µm beads contained in 1.5 mm ID capillary at 29 bar.

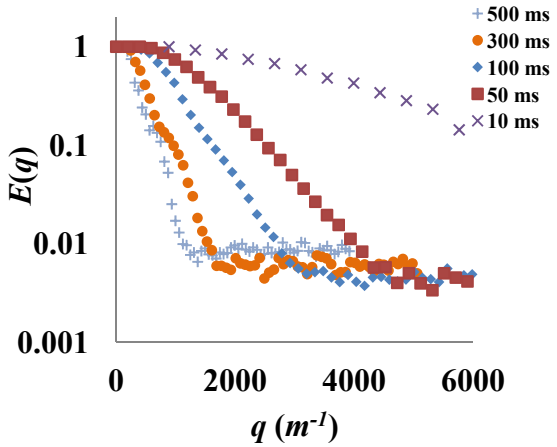

Figure 6.26: sPGSE signal attenuation E(q) vs. q-vector for 0.5 mL/min flow of C_2F_6 in 55 µm beads contained in 1.5 mm ID capillary at 45 bar.

Following the same procedure for the remaining observation times: 200, 300, 400, and 500 ms resulted in widths of 6.2, 6.0, 7.3, and 7.5 µm/s, respectively. These also correspond to the related propagators in Figure 6.21a. Similarly for the P = 29 bar and 45 bar experiments, any coherence feature visible in the q space plots (Figures 6.25 and 6.26) reflect non-Gaussian features in the corresponding propagators in Figure 6.21.

Conclusions

MR Propagators, Velocity maps, and images were used to determine the diffusion, dispersion, and pore structure of non-flowing and flowing critical point or supercritical C_2F_6 in porous media. Two systems were designed. The non-flowing experiments used a 5 mm ID PEEK dead end sample holder and 230 µm beads and the flowing experiments used a 1.524 mm ID PEEK tubing containing 55 µm beads. The sPGSE and dPGSE propagators at P = 25, 29, and 45 bar in the 230 µm beads showed that both coherent (convection) and incoherent (diffusion) motion were present even

without a mean volumetric flow due to the sensitivity to small temperature gradients. These convection currents sampled the pore structure on a shorter time scale compared to the diffusion.

A volumetric flow rate imposed on the bead pack by a pump accurately controlled the flow rate. For the flowing experiments the flow rate of 0.5 mL/min produced propagators that showed a second population of motion emerging at longer displacement observation times. This was because the fast flow rate allowed the molecules to sample the wall structure. The fluid flow at the critical point $P = 29$ bar fluctuated more than $P =$ 25 and 45 bar because of the increased compressibility near the critical point and a steady flow was hard to achieve at $P = 29$ bar.

MR CHARACTERIZATION OF THE STATIONARY DYNAMICS OF PARTIALLY SATURATED MEDIA DURING STEADY STATE INFILTRATION FLOW

Introduction

A porous medium is characterized as a structural material composed of void spaces. In many situations, the pores exist in a connected network. In nature, porous materials can harbor water, organisms, or offer a means to a lightweight yet rigid structure. Porous media can be utilized in industry for chemical reactions, filtering processes, chromatography and many other uses. The physics of liquid and gas infiltration in porous media is of relevance to biological, geophysical and industrial systems. In many systems of interest cyclic saturation and partial saturation events control the transport processes in the porous structure. A particular example is the seasonal hydrologic cycling of contaminant radionuclide transport in the earth's subsurface [139-141]. An intricate interplay of surface tension, advection, diffusion and buoyancy forces render the quantitative modeling of partially saturated flow difficult. Cyclic infiltration of liquid into partially saturated porous media results in a redistribution of flow paths due to a redistribution of clusters of saturated pores which form a backbone of advective transport [114, 142].

Nuclear magnetic resonance (NMR) has proven effective in determining transport phenomena of porous media [32, 33, 38, 41]. It has been used to characterize hydrodynamic dispersion, fluid phase interactions, and other transport phenomena in porous media for both saturated [35, 37, 44, 143-145] and two-phase flows [146, 147].

Saturated single phase flows of water in a bead pack have been well studied, but partially saturated flows have been less studied and are not thoroughly understood. NMR methods have been applied to determine dynamics of combined liquid and gas flows in porous media [43, 148]. Rapid NMR velocimetry methods [43, 149, 150] provide details on the complex temporal variation of dynamics within the porous structure on the timescale of 100 ms. Two-phase flow has been shown to exhibit hysteresis between imbibition and drainage by using MR imaging [43], by recording the pressure drop vs. flow rate [151], and by X-ray radiography [152]. MR imaging experiments [43, 44, 153] have shown that single phase flow does not have hysteresis if the bead pack is fully saturated. However, if air is present in the pack, then hysteresis effects in regards to pressure drops across the porous media can occur if the beads are randomly packed and there is not a great deal of order [153]. The work performed here shows that a partially saturated single phase flow has global flow dynamics that return to characteristic flow statistics once a steady state high flow rate has been reached. This high flow rate pushed out a significant amount of the air in the bead pack and caused a return of a preferential flow pattern. Velocity maps indicated that local flow statistics were not the same for the before and after blow out conditions. It has been suggested and shown previously that a flow pattern can return to similar statistics if the previous flow history is similar [154].

In this work we analyze the stationary dynamics of the transport during spatially and temporally variable processes. Of particular interest is the observation that the ensemble averaged system dynamics are structurally, *i.e*. pore size, dependent and globally reproducible over a fixed range of displacement scales despite local spatial and

temporal variations after cycling of gas and liquid flow rates. A particular model of partially saturated flow in porous media that is consistent with this result is a percolation network. In percolation models the transport or flux is independent of exact spatial location of connected pores, rather it depends on the probabilistic percentage of occupied pores [105]. While not a direct quantitative confirmation of this idea, our data presented here indicates this conceptual model is correct. The immiscible displacements of gas and liquid phases in porous media have provided a rich example for physics theories of percolation [103, 104] and fractal interfacial structure and dynamics [107-110] scaling [105]. Fluid invasion flows are most studied in the context of these theories and are transient imbibition and drainage type flows [105]. Steady-state flows have received far less experimental and theoretical attention [112, 113, 155]. These steady-state flows are of great interest since they represent the stationary stochastic states of a non-equilibrium system with external energy input balancing irreversible energy dissipation processes [112, 113, 155]. This makes this system of relevance to understanding non-equilibrium thermodynamics [114, 156]. In this section we present NMR measurements of the liquid and gas phase fractions and stationary dynamics for the steady-state flow of water over a range of volumetric rates through a homogenous porous media of packed spheres in a partially saturated state.

Methods

The NMR experiments were conducted on a Bruker super-wide bore 300MHz magnet with a Micro2.5 magnetic field gradient probe containing a 10 mm birdcage rf

coil and networked to a Bruker Avance III spectrometer with gradient controls. The gradient set is capable of producing orthogonal magnetic field gradients up to 1.5T/m in three orthogonal directions.

All experiments were performed on the same porous media bead pack sample. NMR and MRI techniques are inherently non-invasive and therefore the sample did not have to be disturbed in any way to obtain the experimental results presented here.

The 50 mm long porous media was constructed from 100 μm borosilicate glass beads in a 10 mm ID diameter glass tube. The beads were wet filled with deionized water and compacted in the tube to achieve a porosity of approximately 44 %. The partially saturated state was created by setting the water flow rate to 25 ml/hr and varying the simultaneous flow rate of the air. Two Pharmacia P-500 HPLC pumps were used to deliver the air and deionized water phases against gravity which combined at a tee junction just below the entrance of the bead pack. This flow resulted in an alternating flow of water and then air bubbles up through the bead pack. The dual air/water flow was continued for 8 hours. The air flow was then shut off and the water flow continued at 25 ml/hr until a steady state NMR signal indicated a steady state of partial saturation had been achieved (approximately 4 hours). The volumetric rate of the initial air flow was varied between 25 and 100 ml/hr, but there was no difference observed in the final partially saturated state as observed by the NMR results.

After the partially saturated state had been established, magnetic resonance experiments were performed as the water flow was increased from 0 ml/hr to 500 ml/hr and then decreased to 25 ml/hr to repeat the velocity map before increasing to 50 ml/hr

and eventually shutting off flow. In Table 7.1 flow rates are listed in the order they were used and the table indicates the experiments that were run at each flow rate. The intention was to monitor the degree of partial saturation as the flow rate was increased from 0 to 500 ml/hr, and to characterize the bead pack before and after the fast flow rate challenge with a density map, propagator and velocity map. The hold time for each flow rate was the time required for completion of all NMR experiments at each respective flow rate. At flow rates 25 ml/hr and 50 ml/hr this was about 20 minutes and at all other flow rates it was 5 minutes.

Table 7.1: Experimental flow rate and NMR experiments run at each flow rate.

Water flow rate	MR Experiments Performed
0 ml/hr	NMR FID Signal; MRI Density Map
25 ml/hr	NMR FID Signal; Propagator (Δ = 400 ms)
50 ml/hr	NMR FID Signal; Velocity Map (Δ = 9 ms)
100, 150, 200…. 500 ml/hr	NMR FID Signal
25 ml/hr	NMR FID Signal; Velocity Map (Δ = 9 ms)
50 ml/hr	NMR FID Signal; Propagator (Δ = 400 ms)
0 ml/hr	NMR FID Signal; MRI Density Map

The pulse sequences for the various NMR testing methods are shown in Figure 7.1. For the MR imaging density maps, which indicate the presence of water (white) and the presence of air or bead (black), at 0 mL/hr a resolution of 78.1 x 43.0 μm and a slice thickness of 1.5 mm was used. The slice was excited in the center of the bead pack. The echo and repetition times were T_E = 16.42 and T_R = 1000 ms, respectively and four averages resulted in an experiment time of about 17 minutes for a single data set.

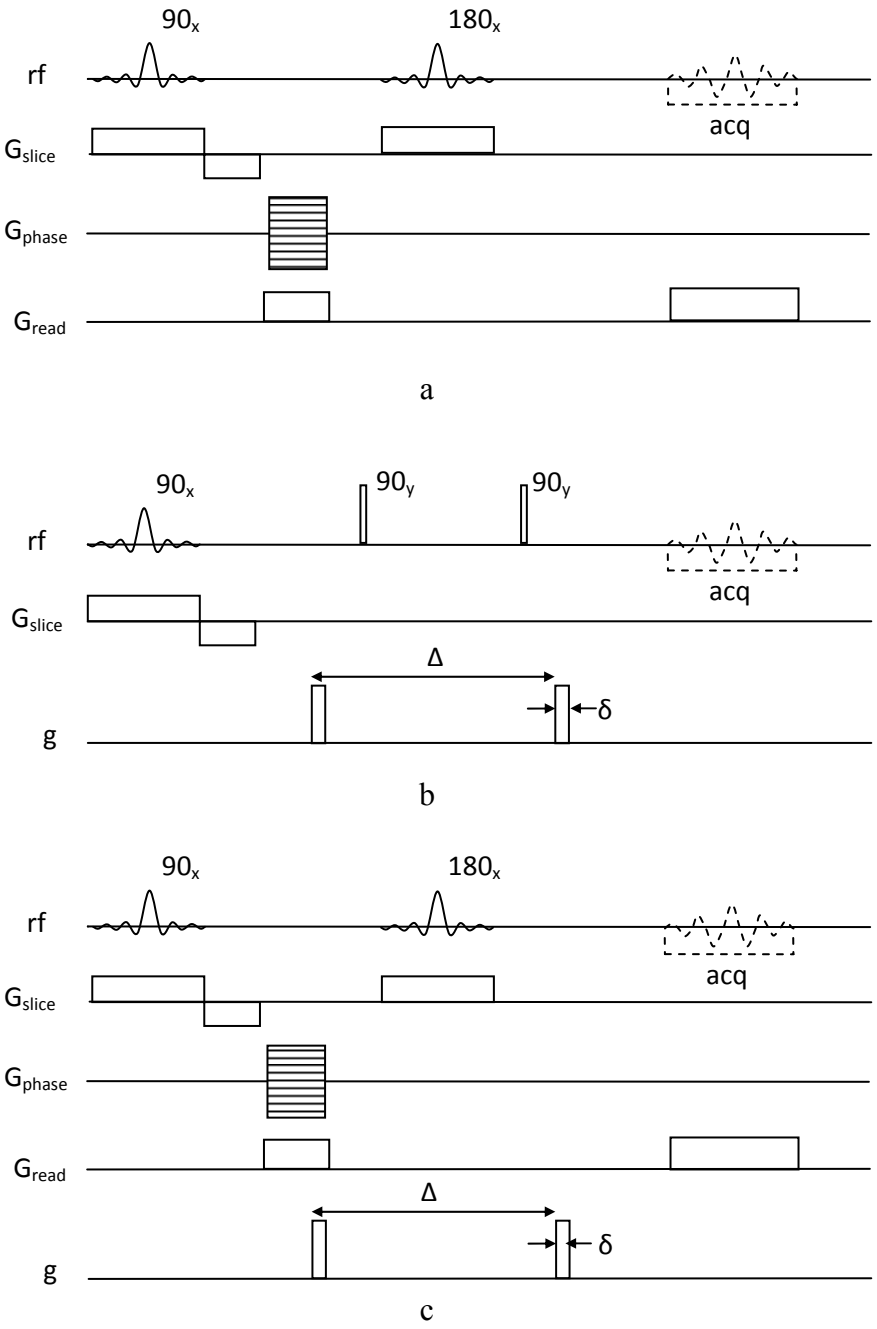

Figure 7.1: Pulse sequences for a) MRI density maps, b) propagators, and c) velocity map experiments.

For the propagator measurements at 25 mL/hr, a slice thickness of 10 mm was used. The slice was excited in the center of the bead pack. The echo and repetition times

were T_E = 5 ms and T_R = 1000 ms, respectively and eight averages resulted in an experiment time of about 17 minutes for a single data set. Displacement observation time was Δ = 400 ms, pulse gradient length was δ = 1 ms and 128 gradient steps were used with a gradient strength increment of 18 mT/mm resulting in a min/max gradient strength of +/-1.134 T/m.

For the velocity maps measured at 50 mL/hr, a resolution of 156.2 x 156.2 μm and a slice thickness of 10 mm was used. The slice was excited in the center of the bead pack. The echo and repetition times were T_E = 13 ms and T_R = 2000 ms, respectively and four averages resulted in an experiment time of 35 mins for a single data set. Displacement observation time was Δ = 9 ms, pulse gradient length was δ = 1025 ms, and the gradient pulses were g = ±1.06 T/m. The free induction decays (FID) measured the total water signal from excitation of the entire sample at each flow rate from 0 – 500 ml/hr, thus providing a method to determine relative water saturation levels or non-wetting saturation levels. For these saturation measurements, a repetition time of 5 seconds and 30 averages resulted in an experiment time of 35 mins for a single data set.

Results and Discussion

The MR imaging density maps, Figure 7.2, and FID signals, Figure 7.3, measured under 0mL/hr no flow conditions before and after the maximum flow rate indicated larger pockets of air were present before, but not after the maximum flow rate. For all repetitions initial partially saturated states show local regions in the MR imaging density maps that have low or no water signal, indicating larger multiple pore size air pockets.

The MR imaging density maps of the same region after the maximum flow rate show a return of the water signal intensity throughout the sample and indicates the larger air pockets are eliminated by the fast flowing water. Although the MR imaging density maps show no evidence of air after the maximum water flow rate of 500 ml/hr (Figure 7.2), the slightly lower FID normalized area (Figure 7.3) indicates that smaller air pockets below the resolution of the MR imaging density maps are present. The FID measurements were repeated at regular intervals as the flow rate was increased from 0 – 500 ml/hr (Figure 7.3) in time steps of 3-5 minutes.

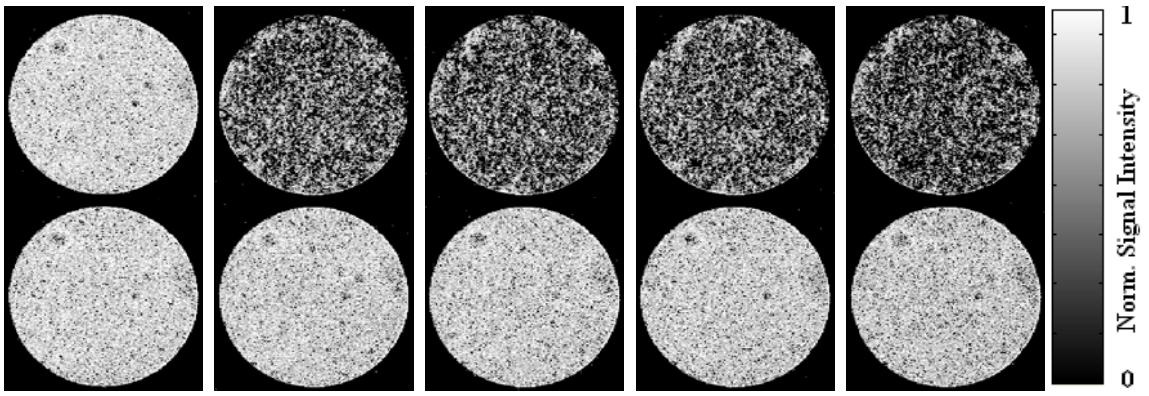

Figure 7.2: MR image density maps for a 1.5 mm slice excited in the center of the 10 mm ID bead pack. Top row: the initial partially saturated state. Signal intensity is proportional to water content in the volume (voxel) centered around the pixel of the image; Bottom row: after a 500ml/hr water flow has pushed out much of the air. Column 1 shows the initial fully saturated sample and the remaining columns show data from four repetitions (I-IV) of the initial partially saturated state and then the saturation after the high flow rate.

The FID signal begins to increase at 250 ml/hr indicating the flow rate at which air begins to leave the bead pack. This corresponds to a capillary number of 7.6×10^{-4}. The data in Figure 7.3a has been plotted against the Capillary number, Ca, (Figure 7.3b)

to be presented in a manner consistent with data previously published for a 2D system [113] to allow direct comparison. For the conversion of the flow rate to Capillary number the definition given in the theory section was used [106]. The non-wetting saturation level S_{nw} is calculated using the ratio of the FID normalized area FID_{NA} of the partially saturated condition, $FID_{NA(ps)}$, to the fully saturated condition, $FID_{NA(fs)}$, as $S_{nw} = 1 - \frac{FID_{NA(ps)}}{FID_{NA(fs)}}$. The inverse proportion of S_{nw} to Ca has been discussed in the context of compressibility of the non wetting gas phase (air) in analysis of the 2D data of Tallakstad *et al* [113] and they conclude compressibility of the air is not the cause of the decrease in S_{nw} with Ca.

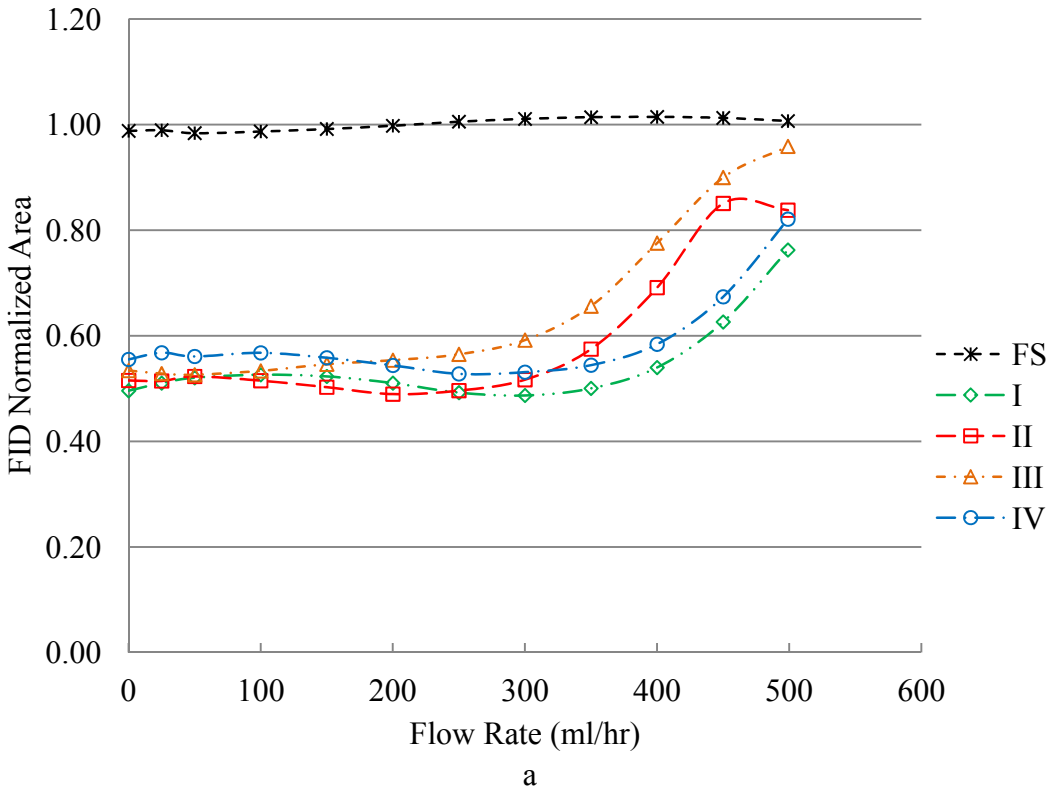

a

figure continued…

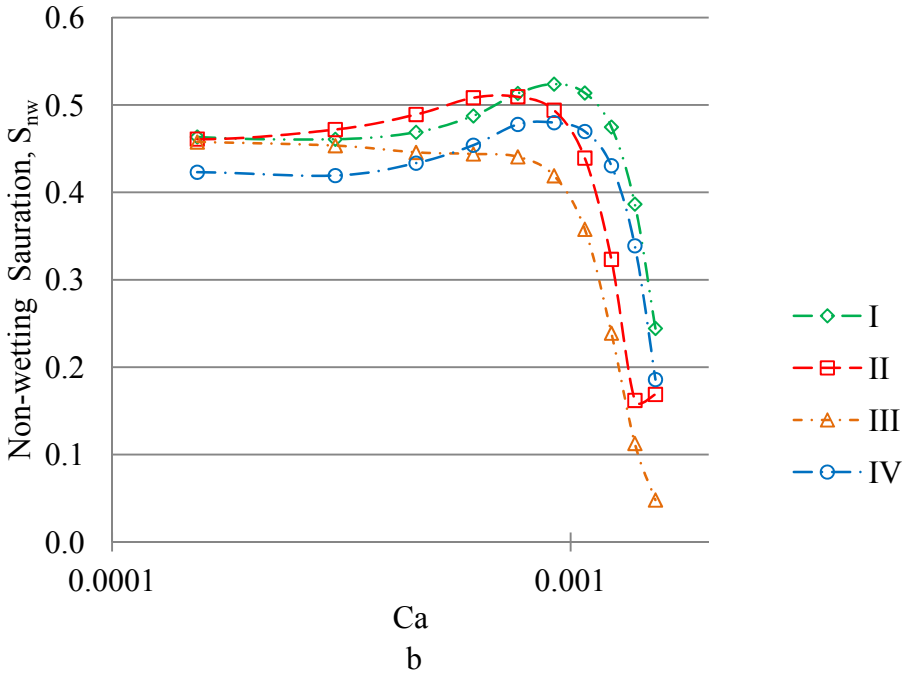

b

Figure 7.3: a) Total FID normalized area vs. flow rate. b) Non-wetting saturation fraction vs. Capillary number for repetitions I-IV.

Tallakstad et al. also note the dearth of data on saturation in steady state. Computer simulations comparing saturation levels and pressure drop in steady partially saturated flows have been undertaken [157] but no theory for S_{nw} scaling with *Ca* exists, and to our knowledge Figure 7.3b is the first to report of this in 3D [111].

The velocity maps measured at 50ml/hr before and after the maximum flow rate of 500 ml/hr are shown in Figure 7.4. These velocity maps provide further evidence that some pores below the resolution of the MR image are filled with air as there are significant regions with no flow and other regions with high backbone flows. Such velocity structures are not visible in the initial homogeneous bead pack, Figure 7.4

(Column 1). However they are present in all the subsequent partially saturated states and most of the states after the maximum flow rate has blown out the large air pockets. Such no flow and high back bone flow structures are expected in a percolation model structure [114]. The variation in the number of spatial regions of no signal, *i.e*. regions of higher dispersion caused by small air pockets, in the velocity maps for each trial after a maximum flow challenge are consistent with the slight saturation variations in Figure 7.3.

Pressure drops across the sample were measured as the flow rate and hence capillary number were increased as shown in Figure 7.5. A power law scaling of approximately .33 was observed which is consistent with the percolation cluster model which predicts $|\Delta P| \propto \mathrm{Ca}^{\gamma}$ constrained by $\gamma \leq 0.5$ [113]. In the limiting case of identical viscosities for the two fluids a scaling of 0.5 is expected and this represents an upper limit to the expected scaling.

The propagators measured at 25mL/hr before and after the maximum flow rate of 500 ml/hr are shown in Figure 7.6. The propagator for the initial fully saturated flow is shown in both Figure 7.6a and Figure 7.6b. This fully saturated homogeneous bead pack propagator has two peaks, one centered around zero displacement representing water that is initially in the no flow regions of the bead pack and the other peak centered around the average water velocity, with the dip in the propagator corresponding to the pore size $d = \frac{d_p \phi}{(1-\phi)}$ and hence nominal bead diameter d_p as has previously been observed and discussed in many detailed MR studies of fully saturated flow in homogeneous bead packs [35, 37, 144, 146].

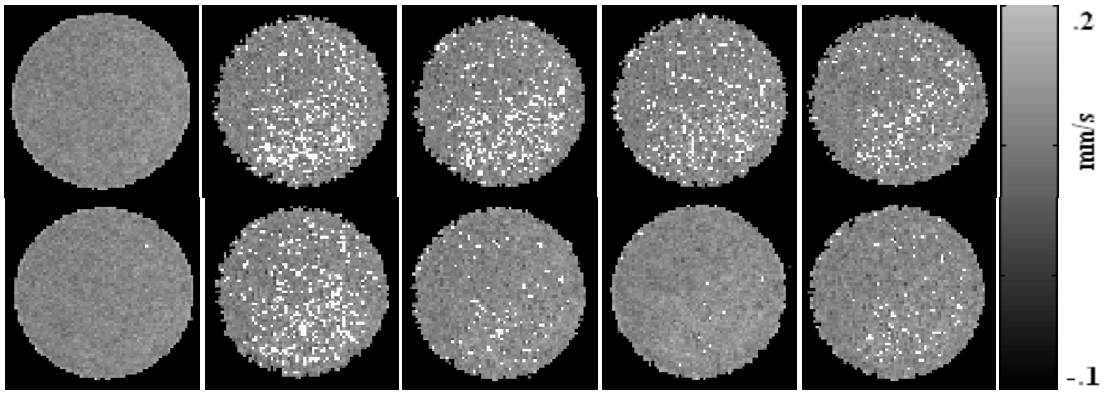

Figure 7.4: Velocity maps from a 10 mm slice excited in the center of the 10 mm ID bead pack. Top row: the velocity maps for the initial partially saturated state. Signal intensity is proportional to the average water veloicty in the volume (voxel) centered around the pixel of the image; Bottom row: the velocity maps after a 500ml/hr water flow has pushed out much of the air. Column 1 shows the initial fully saturated sample and the remaining columns show data from four repetitions (I-IV) of the initial partially saturated state and then the saturation after the high flow rate. The white regions have been falsely colored to indicate when the NMR signal was below the noise level due to regions of higher dispersion.

The propagators for the initial partially saturated states before maximum flow (Figure 7.6a) show a higher probability of zero displacement and a long tail of large displacements indicative of a backbone flow structure resulting from the many large air blockages to the water flow path with regions where the water is trapped and pathways where the water can flow faster [158]. All the propagators taken after the maximum flow rate of 500 ml/hr (Figure 7.6b) look qualitatively similar to each other and to that obtained for the initial fully saturated state. Although FID measurements (Figure 7.3) show that there is still some air present, and velocity maps (Figure 7.4) show that the velocity distribution is no longer spatially homogeneous, these propagator results clearly show that the global flow statistics have returned or nearly returned to the fully saturated flowing condition. This also suggests that the flow returned to some characteristic flow

pattern that closely resembled the dynamics of the saturated bead pack. This pattern was then stable and could not be altered unless air was introduced again.

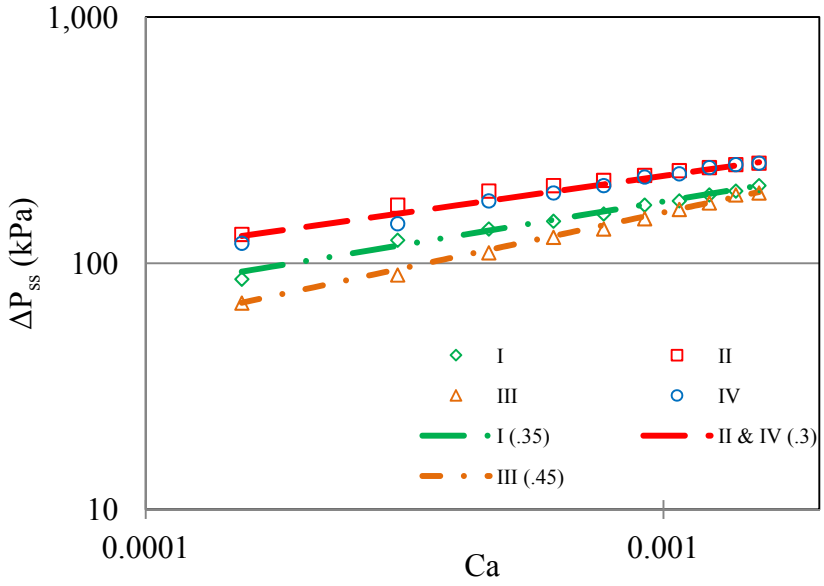

Figure 7.5: Average steady-state pressure drop vs. Capillary number for each repetition I – IV. The straight lines show the power law fits for each repetition: I $\beta = .35$, II $\beta = .3$, III $\beta = .45$, and IV $\beta = .3$.

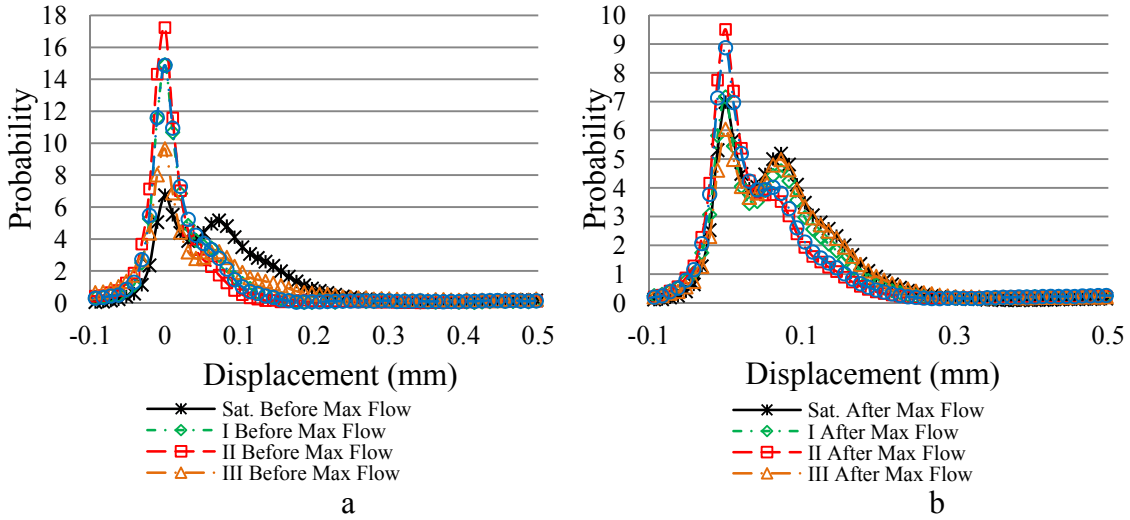

Figure 7.6: Displacement propagators ($\Delta = 400$ ms) for a flow rate of 25 ml/hr a) for the initial fully saturated and subsequent partially saturated states and b) for the initial fully saturated and subsequent partially saturated states after the maximum flow rate of 500 mL/hr.

For clarity and ease of comparison, the propagators from each repetition are compared individually to the propagators for the saturated condition (Figure 7.7). As expected the propagators from before and after maximum flow rate for the initial fully saturated condition show identical inflections at the pore size *d* and similar probabilities of displacements.

This corroborated the results of the initial MR image density maps and FID signals that also showed limited difference after the high flow rate. For the initial partially saturated states it is clear that the flow dynamics converge to the saturated dynamics after the maximum flow rate of water has gone through and removed the large air pockets, even though the FID signal and velocity maps show clearly that more air than in the saturated system is still present.

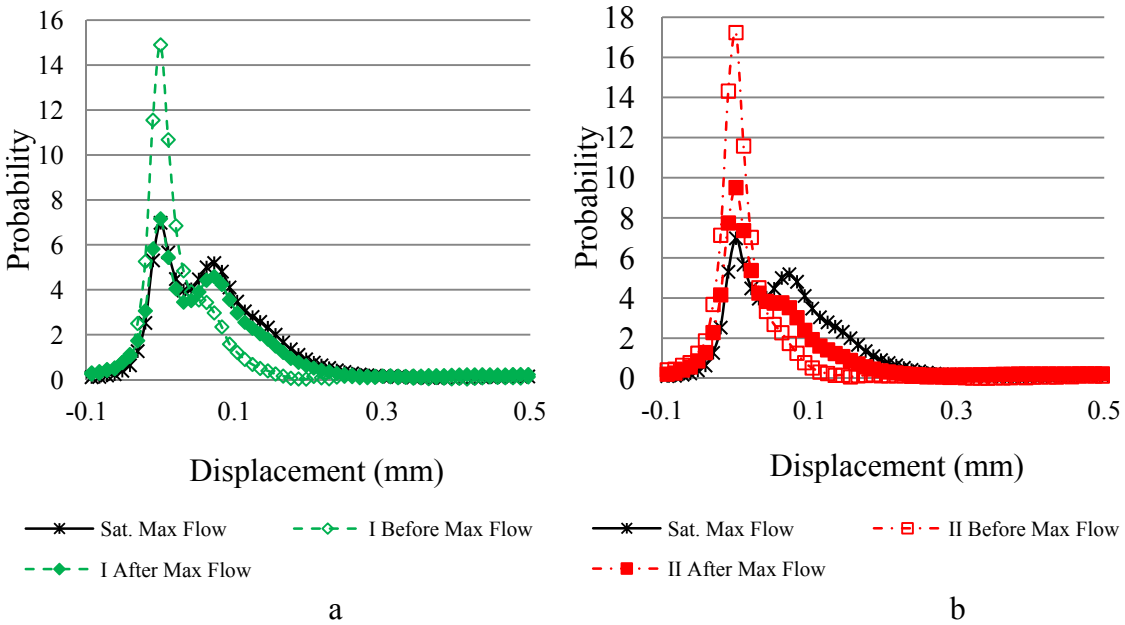

a b

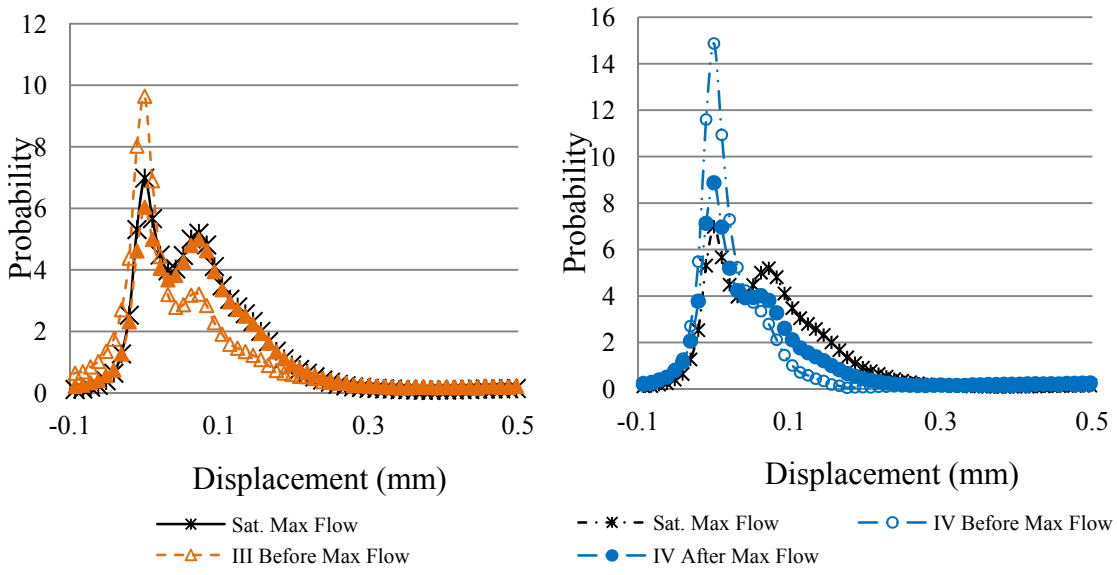

c d

Figure 7.7: Displacement propagators (Δ = 400 ms) comparing before and after max flow to saturated flow dynamics for each repetition a) I, b) II, c) III, and d) IV.

The higher probability of displacement around d~79 µm indicates the impact the underlying pore structure has on the dynamics in the bead pack, consistent with the cutoff length l^* representing a cluster mobility extension length [112]. That is, there is an increased probability of displacements at the pore scale d which then decays away until the cutoff length scale is reached and backbone, long displacement, dynamics dominate. The theory of De Gennes [114] indicates that the mean of the entire distribution of dynamics, including the no flow peak around zero displacement is the appropriate mean displacement for use in the analyzing dispersion dynamics. While the propagators for the fully saturated and partially saturated after maximum flow have many similarities, one aspect that requires further study is that on a log scale the partially saturated after maximum flow propagators consistently have a long displacement tail, *i.e.* higher probability of large displacements.

Conclusions

In this section data on the stationary dynamics and saturation of steady state partially saturated flow in porous media before and after flushing with a high water flow rate to mimic cyclic invasion phenomena have been presented. Data on the saturation of porous media during partially saturated flow are limited and the unique ability of NMR to provide this data is clearly demonstrated. The ability of NMR to measure the propagator of motion yields the stationary dynamics and connections with the structure of the porous media and percolation models of the flow can be made. In demonstrating these measurements and interpretation the basis for further studies of steady state partially saturated flows for a range of *Ca* numbers, fluids, saturation levels and NMR parameters such as displacement observation time has been established.

Acknowledgements

The work in this section was published in the New Journal of Physics **13** (2011) 015007 and can be found online at http://www.njp.org/. The authors would like to thank the members of the Magnetic Resonance Laboratory at Montana State University for assistance and support. SLC and EMR acknowledge funding support from the National Science Foundation (NSF CAREER #0642328). JDS acknowledges funding support from the Department of Energy (DOE-Epscor DE-FG02-08ER46527). Equipment was funded by the National Science Foundation and the Murdock trust.

OSCILLATORY FLOW PHENOMENA IN SIMPLE AND COMPLEX FLUIDS

Introduction

The world depends upon oscillatory or pulsatile flow to sustain itself; more specifically the human body is maintained by pulsing blood throughout the body. Many techniques have been used to measure the velocity profiles of fluids undergoing oscillatory (no net transport of the fluid) or pulsatile (net transfer of fluid) flow in pipes and capillaries. Such techniques include, but are not limited to Laser Doppler Velocimetry (LDV) [159], hot wire anemometry [160], injected dyes [161] or particle dyes, and particle imaging velocimetry (PIV) [162]. However, many of these techniques are invasive and disrupt the flow of the fluid. A few of the techniques that are non-invasive such as LDV are limited to translucent flow cells and the techniques do not work for fluid flow in opaque samples. Nuclear Magnetic Resonance (NMR), however, is a non-invasive method for evaluating fluid mechanics and can be used to obtain spatially resolved velocity maps in complex fluids such as biofilms, blood, and porous media [14, 163, 164]. Additionally, NMR images typically have a resolution of 20-1000 μm, with samples anywhere from microscopic to human scale. NMR therefore is a competitive option for studying pulsatile or oscillatory flow *in situ* and is ideally suited to study pulsatile flow *in vitro.*

J.R Womersley was one of the first to experimentally study oscillating flow and performed his studies on the femoral artery of a dog [13, 161]. In these studies, the velocity profiles, viscous drag, and Reynolds number were calculated from the pressure

gradient. It was the pressure gradient that was used to determine the flow characteristics indirectly. Since then, much work has been performed on the flow stability and transition to turbulence of oscillatory and pulsatile flow both experimentally and numerically [120, 159, 160, 165-168] and oscillatory flows superimposed on advective flow [169, 170]. In addition to physiological fluids, other complex fluids that have visco-elastic and shear-thinning characteristics have also been studied [122, 123, 169]. It is shown here the data rich technique of NMR in studying oscillatory flow phenomena in simple and complex fluids.

Methods

Oscillatory Apparatus

The oscillatory flow is generated by a double acting cylinder (Bimba Manufacturing: HL-013-DPY) shown in Figure 8.1.

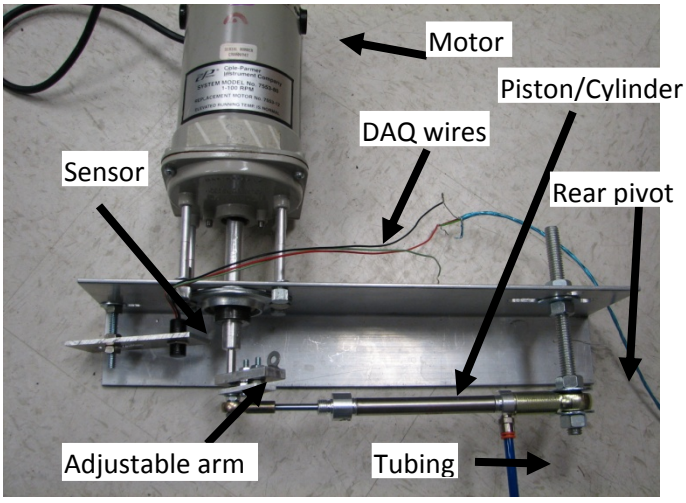

Figure 8.1: Apparatus used to create an oscillatory flow equipped with a sensor to trigger experiments at the same point in the cycle.

It is connected via an adjustable arm to a rotating pump motor shaft (Cole-Parmer: Model No. 7553-80). In order to trigger the spectrometer at the same point in the cycle, an inductive sensor (A47-18ADSO-2KT21-Single Ch-Target Tracker Gear Tooth Sensor) is used to sense the rotation of the arm. Collectively this creates an approximately sinusoidal oscillatory flow with no net flow rate.

MRI Experiments

A single pulsed gradient spin echo (PGSE) was used to obtain the velocity maps inserted in a basic NMR imaging sequence [171]. Rather than obtaining an average over the entire cycle, the LabVIEW program and the delay in the trigger function of ParaVision Version 5.0, velocity maps were able to be collected at specific intervals in the oscillation cycle. The pulse duration,δ, was 1 ms and the gradient pulse spacing, Δ, was 10 ms. The PGSE gradient values were set based on the maximum expected velocity and are shown in Table 8.1. The T_R for frequencies of 0.31 rad/s, 1.26 rad/s, 2.09 rad/s, and 12.57 rad/s were 19.5 s, 4.9 s, 2.7 s, and 0.55 s respectively. The bulk fluid was doped with Magnevist to lower the T_1 to 0.2 s ensuring $T_1 < T_R$ for all of the experiments. The velocity maps had a field of view of 15 mm x 15 mm and a resolution of 117.2 μm x 468.7 um over a slice thickness of 20 mm.

Table 8.1: MRI Experimental parameters

Frequency (rad/s)	**δ (ms)**	**Δ (ms)**	**Gradient value (T/m)**	**T_R (sec)**
0.31	1	10	0.1086	2.17
1.26	1	10	0.0154	0.61
2.09	1	10	0.0073	0.45
12.57	1	10	0.0022	0.25

Trigger

A LabVIEW program was developed to convert the voltage signal sent from the inductive sensor to a voltage signal that triggers the AVANCE III Spectrometer. The data acquisition device (NI USB-6009 14-bit multifunction DAQ) was used with LabVIEW 2009.

Fluids and Flow Frequencies

In order to observe a range of Womersley numbers, α, the oscillating flow frequency, ω, and fluid viscosity, υ were varied. The fluids tested included both Newtonian and non-Newtonian fluids. The four fluids were: water, xanthan gum (XG), polyacrylamide (PAM), and hexadecane colloidal particles. Each fluid was oscillated at four frequencies, ω=0.31 rad/s, ω=1.26 rad/s, ω=2.09 rad/s, and ω=12.57 rad/s. Water is a Newtonian, non-compressible fluid and its properties are well known. The relationship between stress and strain is linear, thus water has a constant viscosity at a constant temperature. Xanthan gum is a power law fluid and will react differently under shear forces. The xanthan gum molecule is a long chain molecule with pentasaccharide repeat unit [9]. A 0.025% by weight solution is mixed using xanthan gum produced by fermentation of dextrose with Xanthomonas campestris. The 2000 ppm Polyacrylamide solution acts as a viscoelastic shear thinning fluid. It is made by dissolving high molecular weight polyacrylamide in water. The Colloidal suspension core-shell oil particles were constructed using the method of Loxley and Vincent [10]. An oil phase containing 3.0g of poly(methyl-methacrylate) (PMMA) MW 350,000, 60 mL dicloromethane, 3.9 mL acetone and 5mL of hexadecane was added drop-wise to 80 mL

of a 2% wt. polyvinyl alcohol (PVA) solution while being stirred with a Heidolph Silent Crusher M homogenizer. To obtain the desired particle sizes, a constant shear rate of 12,000 rpm was applied for a period of one hour following the oil phase addition. The resulting emulsion was then added to 120 mL of a 2% wt. PVA solution and the volatile solvent was allowed to evaporate overnight resulting in a PMMA shell encasing the oil, thus separating the oil and water phases. The microspheres are short range repulsive due to short chain PVA molecules which adhere to the surface and exhibit hard sphere behavior [11]. The resulting particle size had a range of radii distributed around approximately 1 μm.

Setup

The experimental set up is shown in Figure 8.2 The tubing is run through the magnet and connected to the piston cylinder.

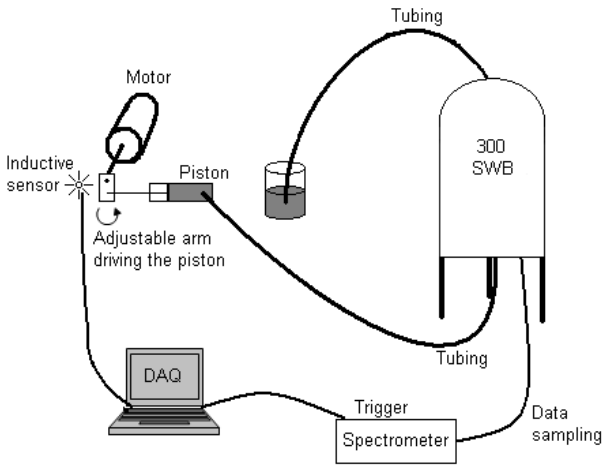

Figure 8.2: Experimental setup: Fluid is oscillated in the tubing via the motor and piston setup. The tubing runs up through the 300 SWB magnet into the fluid reservoir. A DAQ system transfers information from the inductive sensor to the spectrometer's trigger so that experiments start at the same point in the oscillation cycle.

PVC tubing of internal radius 5.37 mm was used for all the experiments. The motor drives the adjustable arm which is detected by the inductive sensor once per rotation. The signal is sent to the DAQ and LabVIEW program which converts it to a 5 V signal triggering the spectrometer. This triggering system ensures the NMR data is collected at the same point in the cycle each time.

Results and Discussion

For each oscillatory frequency, velocity maps were obtained at anywhere between 6-11 evenly spaced intervals after the trigger. The trigger was positioned identically relative to the piston rotation for each fluid. Figure 8.3 shows average velocity measured at each point relative to the time after the trigger. The sinusoidal nature of the driving force is clear for all the frequencies shown in Figure 8.3 Offsets in the overlap for each fluid are due to the formation of air gaps in the tubing and/or piston cylinder which were minimized but not possible to completely eliminate. The bubbles likely caused a capacitative lag between the driving force and the fluid response.

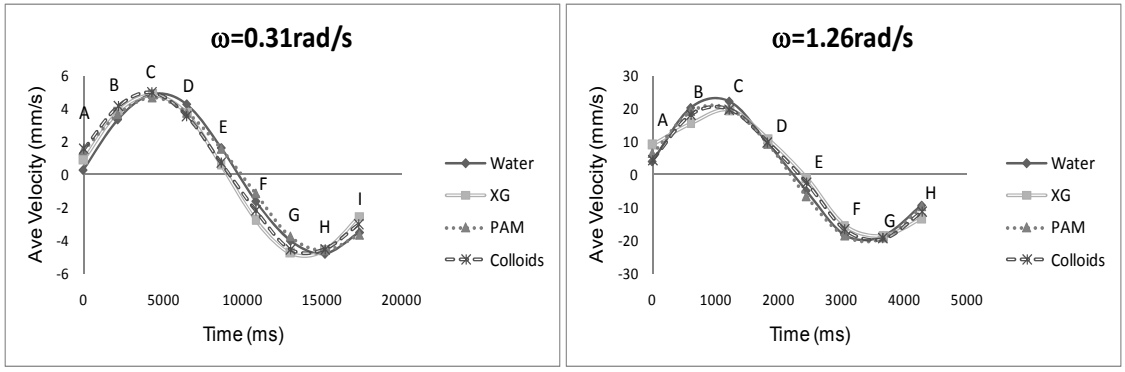

figure continued…

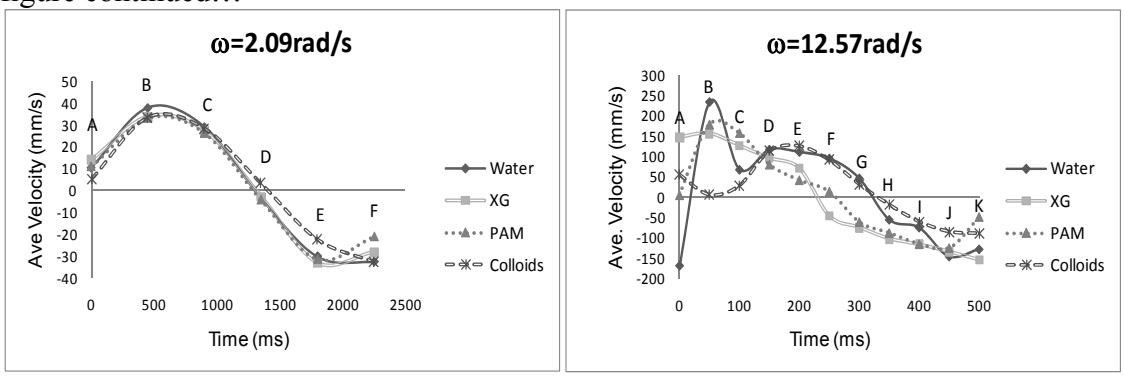

Figure 8.3: Average velocity data for the four rotation rates used to access a range of Womersley numbers. A wave close to the sinusoidal volumetric driving force is seen for lower frequencies, however, at the fastest rotation rate the waves have diverged possibly due to the high Re numbers for several of the fluids and the impact of any air gaps.

At the highest oscillation frequency, ω=12.57 rad/s the fluid response is the most inconsistent as expected due to the higher Re number for several of the fluids (approaching or in the turbulent regime Re>2200) and due to the increased impact of any bubbles. At each point in the cycle for each fluid shown in Figure 8.3, a 2D velocity map was obtained. A velocity profile through the center of the fluid was generated by extracting the center line of each velocity map, Figure 8.4.

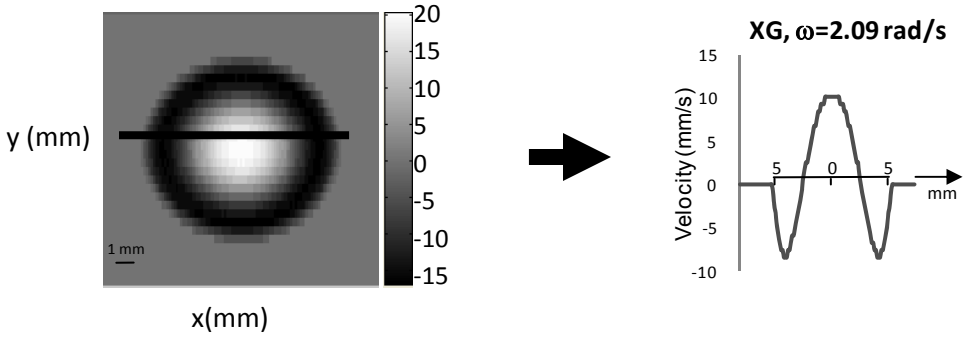

Figure 8.4: Velocity map with the corresponding velocity profile extracted from the center line.

Characterized by the Womersley number, the shape of a velocity profile is dependent on the tube's radius, the fluid's viscosity, and the oscillatory flow frequency. The tubing radius was constant for all the experiments and all other parameters were dependent on the fluid used and the angular frequency at which the piston cylinder was being driven, Table 8.2. The Reynolds number ($Re = \frac{v \times D}{\nu}$) is also included and indicates that only water at ω=12.57 rad/s is likely to be in the turbulent regime (i.e. Re > 2200) for a portion of the cycle.

All profiles for α<3 demonstrated Poiseuille flow Figure 8.3. This includes most of the ω=0.31 rad/s profiles excluding water which has α=3. As the Womersley number increases (≤ 3) the profiles begin to split and are blunted. Ku found profiles began to split and become blunted for α>10 [12].This can clearly be seen in the profiles with ω=1.26 rad/s and higher. The data has been rearranged in Figure 8.5 to display each fluid on the same plot for each point in the cycle.

Table 8.2: Fluid properties for the four fluids and experimental parameters at each of the frequencies tested. Note: water has the highest α at each frequency.

		ω=0.31rad/s	ω=1.26rad/s	ω=2.09rad/s	ω=12.57rad/s
Water	ν (m^2/s)	1.00E-06	1.00E-06	1.00E-06	1.00E-06
	α	2.8	5.59	7.22	17.69
	Re	16 to 49	26 to 154	63 to 241	451 to 2313
XG	ν (m^2/s)	3.00E-06 to	2.43E-06 to	2.18E-06	1.31E-06
	α	0.63 to 1.90	3.15 to 3.59	4.60 to 4.99	13.11 to 15.51
	Re	2 to 3	6 to 73	20 to 118	282 to 1187
PAM	ν (m^2/s)	3.73E-06	3.55E-06	3.46E-06	3.25E-06
	α	1.43 to 1.45	2.94 to 2.98	3.85 to 3.89	9.65 to 9.83
	Re	3 to 12	12 to 54	14 to 80	38 to 384
Colloids	ν (m^2/s)	1.10E-05	0.000011	1.10E-05	1.10E-05
	α	0.68	1.69	2.18	5.34
	Re	.6 to 5	2 to 18	3 to 29	19 to 82

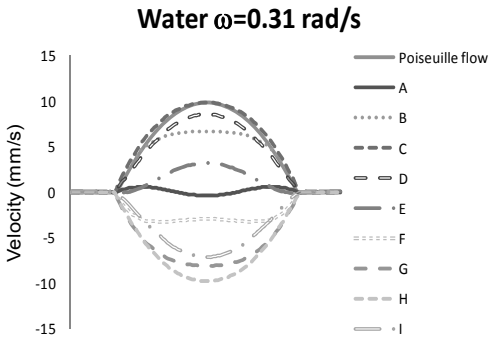
Water ω=0.31 rad/s
Velocity (mm/s)
15
10
5
0
-5
-10
-15
Poiseuille flow
A
B
C
D
E
F
G
H
I

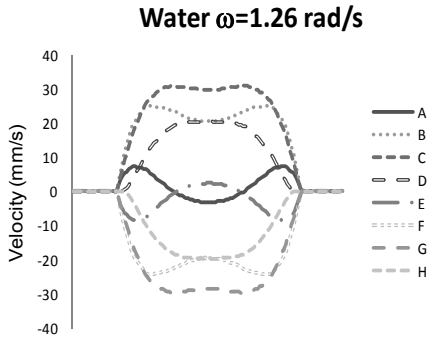
Water ω=1.26 rad/s
Velocity (mm/s)
40
30
20
10
0
-10
-20
-30
-40
A
B
C
D
E
F
G
H

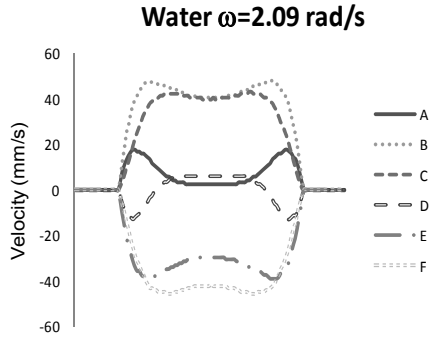
Water ω=2.09 rad/s
Velocity (mm/s)
60
40
20
0
-20
-40
-60
A
B
C
D
E
F

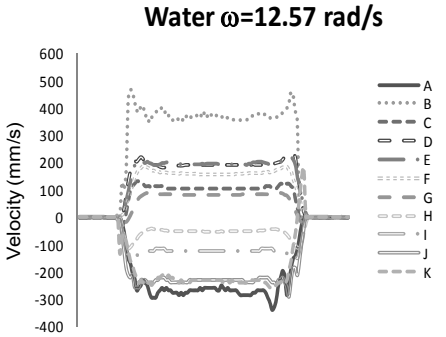
Water ω=12.57 rad/s
Velocity (mm/s)
600
500
400
300
200
100
0
-100
-200
-300
-400
A
B
C
D
E
F
G
H
I
J
K

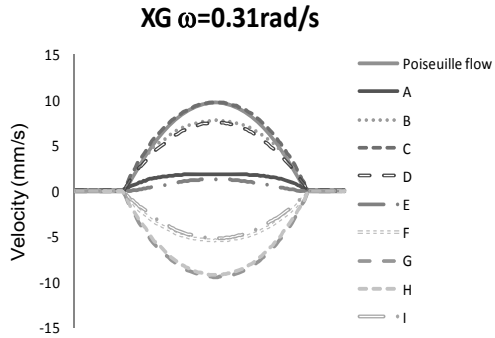
XG ω=0.31rad/s
Velocity (mm/s)
15
10
5
0
-5
-10
-15
Poiseuille flow
A
B
C
D
E
F
G
H
I

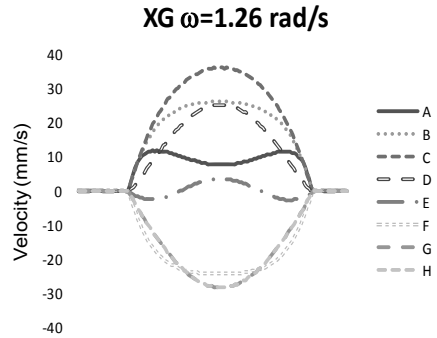
XG ω=1.26 rad/s
Velocity (mm/s)
40
30
20
10
0
-10
-20
-30
-40
A
B
C
D
E
F
G
H

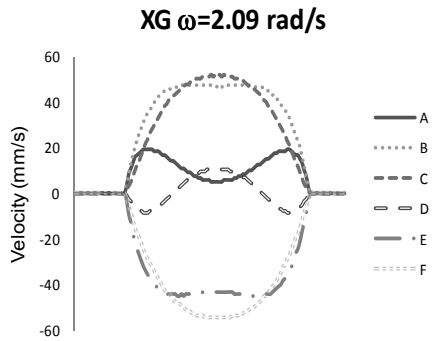
XG ω=2.09 rad/s
Velocity (mm/s)
60
40
20
0
-20
-40
-60
A
B
C
D
E
F

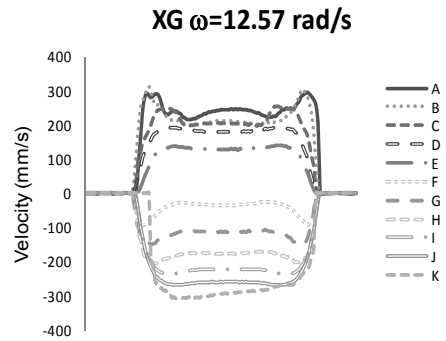
XG ω=12.57 rad/s
Velocity (mm/s)
400
300
200
100
0
-100
-200
-300
-400
A
B
C
D
E
F
G
H
I
J
K

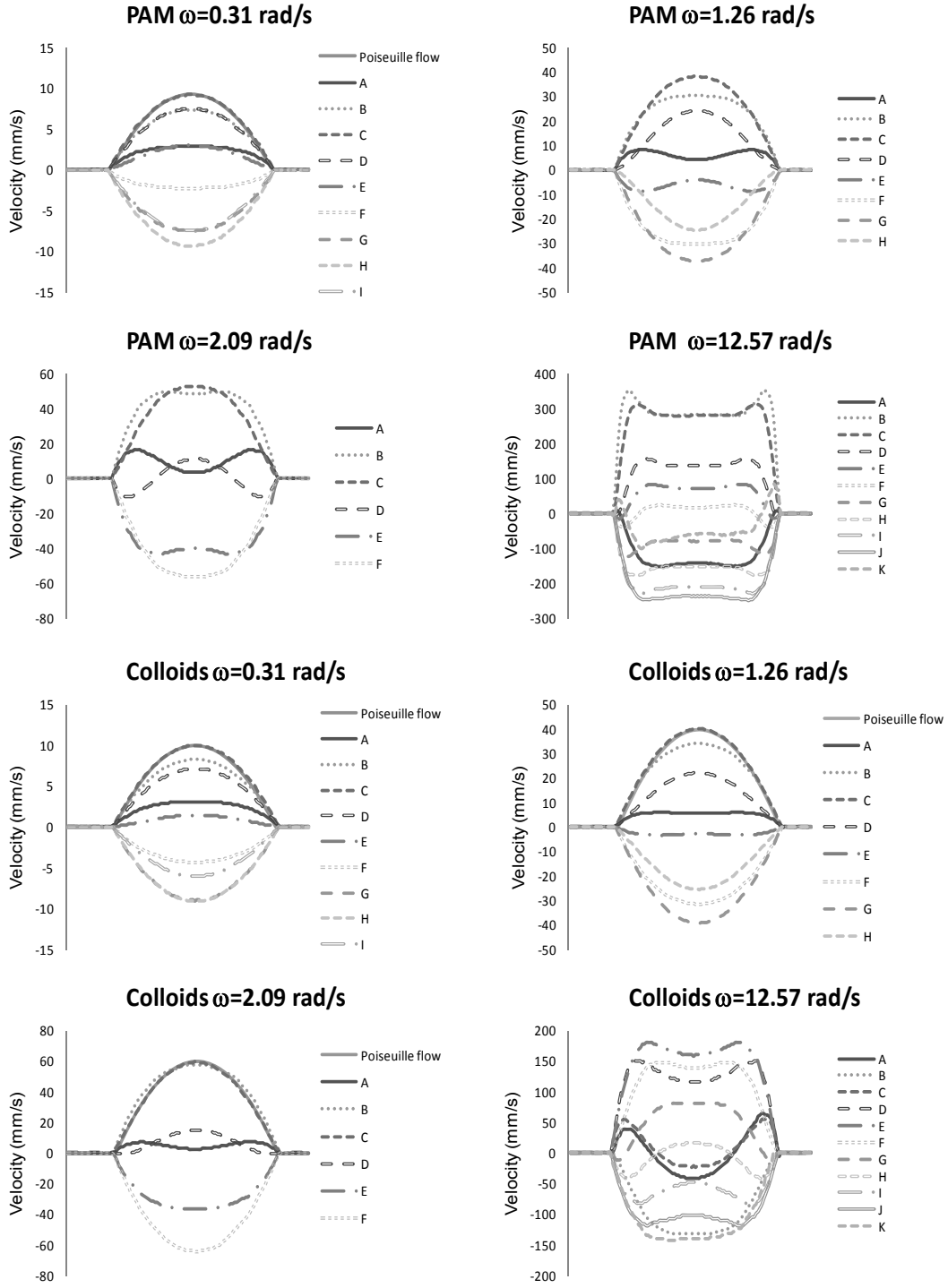

Figure 8.5: By varying the viscosity and rotation rate a range of Womersley numbers were measured. Comparison between a Newtonian fluid (water), a non-Newtonian power-law fluid (XG), viscoelastic shear thinning fluid (PAM) and a colloidal suspension (hexadecane colloids) shows a variety of profiles.

Figure 8.6 displays the normalized velocity profiles that have α closest to three. It can be seen that the profiles are qualitatively very similar. Water has a shape most different than the other fluids due to its lower viscosity. The low viscosity fluid more readily changes direction, thus the fluid in the outer stream that was lagging becomes the leading stream when the piston changes direction and a wide distribution of velocities form. In the fluids with higher viscosity, the viscosity provides resistance and keeps the range of fluid velocities in a narrower range.

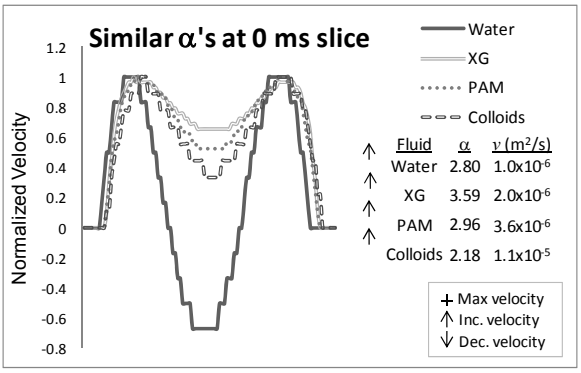

Figure 8.6: Normalized velocity of the four fluids with α close to three. Similarities confirm the fluid dynamics are well characterized by the Womersley number.

Figure 8.7 compares the eight points (A, B, C, D, E, F, G, and H) during the ω=1.26 rad/s cycle for the four fluids. As expected, the two fluids with similar viscosities and thus α, XG and PAM, display similar profiles throughout the cycle. The fluid with a higher viscosity and thus a lower α, colloids, shows a Poiseuille profile at most points in the cycle (all but A). The fluid with a lower viscosity and thus higher α, water, transitions through a point (A) with an exaggerated split profile and large range of velocities to a very blunted profile for the points (D and H) at the other extremes of the cycle.

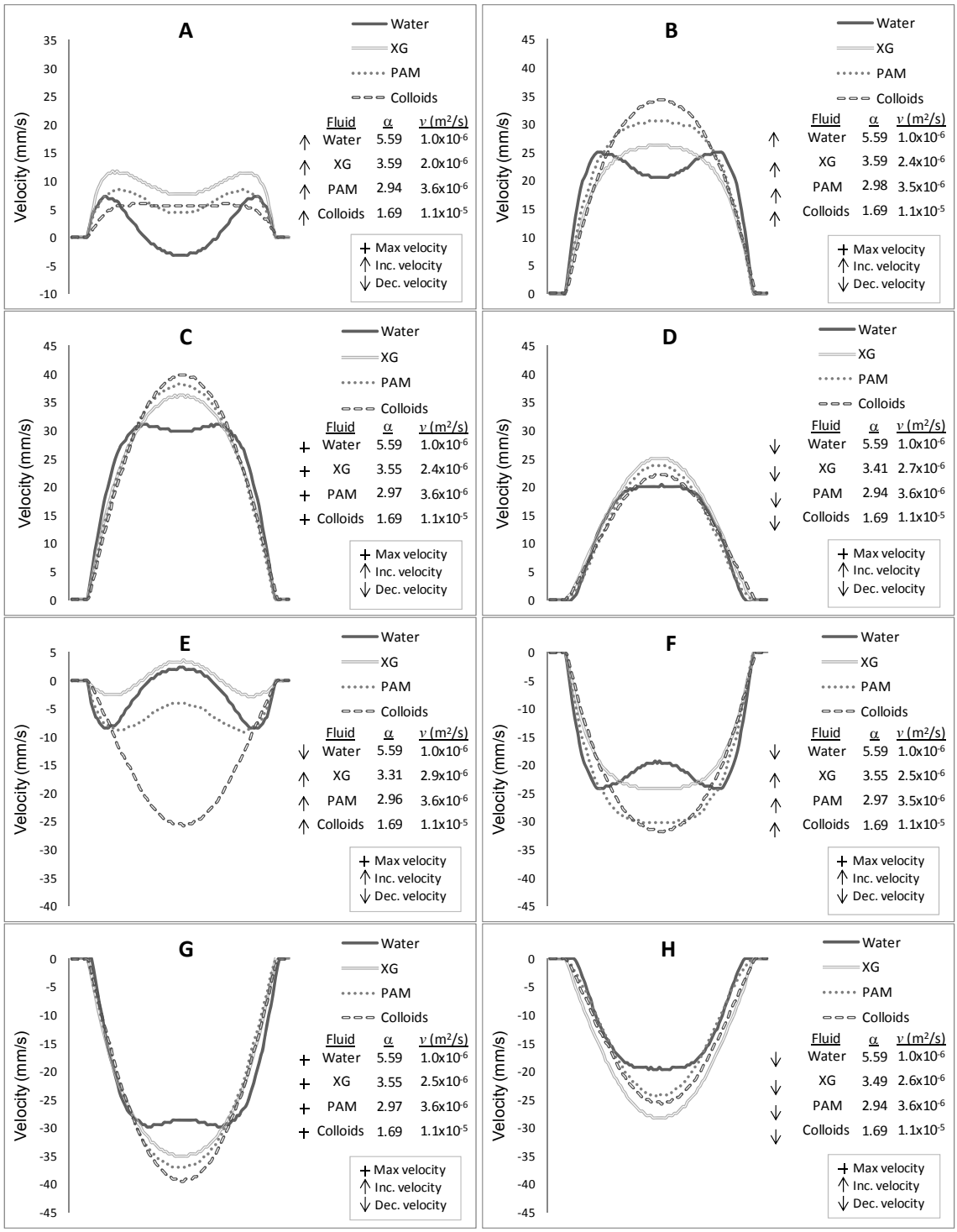

Figure 8.7: Velocity profiles collected at eight points (A, B, C, D, E, F, G, and H) in the oscillation cycle with a rotation of 1.26 rad/s. A comparison between the four fluids clearly presents the impact of varying viscosities and hence α.

Conclusions

Oscillatory flows can be characterized with the Womersley number [12, 13]. Non-parabolic velocity profiles (blunted and split) have been observed with oscillatory flows [12] and these flows have now been studied with MRI. MRI allows the study of velocities in both transparent and opaque (i.e. colloids, porous media) fluid systems. Blunted and split profiles are seen as expected as the unsteady forces begin to dominate over the viscous forces for higher α. Particle migration can occur in low shear regions in the flow, important in plaque buildup [14]. In Newtonian, laminar, unidirectional flow, the particles tend to move to the center. In oscillatory flows, the particles can migrate to several locations and systems could be designed to take advantage of such phenomena for advantageous particle entrapment (i.e. drug delivery) or to avoid plaque buildup. In addition to characterization of flow and transport in oscillatory flows this apparatus could potentially be used in Rheo-NMR [15] applications to generate oscillatory flows for characterization of the shear modulus of complex fluids.

FUTURE WORK

Introduction

The research on critical and supercritical fluids presented in this dissertation used C_2F_6. However, the study of CO_2 in the critical and supercritical state is of more immediate interest due to carbon sequestration efforts and green chemistry applications. C_2F_6 is a good fluid for examining physical phenomena related to supercritical fluid dynamics and transport in porous media because of its low critical pressure and temperature as well as the strong MR signal from ^{19}F. Preliminary work on CO_2 is presented in this chapter.

Although CO_2 is more abundant in nature compared to C_2F_6, using it in the MR laboratory environment is more complicated. MR signal is only obtained from the ^{13}C isotope and the signal is weaker than ^{19}F because the gyromagnetic ratio is about ¼ of ^{19}F. The natural abundance of ^{13}C in CO_2 is roughly 1% [22], limiting MR signal from naturally occurring CO_2. ^{13}C isotropically enhanced CO_2 can provide MR signal enhancement relative to naturally occurring CO_2 and is available from Cambridge Isotope Laboratories (Andover, MA). The product is significantly more expensive per Liter compared to C_2F_6. The pressure and temperature to obtain the critical state of CO_2 is 73.8 bar and 31.04 ^{o}C, roughly 43 bar and 12 ^{o}C higher than C_2F_6. This presents technical issues for duplication of the results of this dissertation with CO_2. The pressure transducers used in the C_2F_6 system had to be upgraded to accommodate the increased pressure requirements. Additionally, a heating system was used to achieve the 31.04 ^{o}C

temperature whereas the temperature of C_2F_6 was more easily maintained with room temperature control.

Methods

Magnetic resonance microscopy techniques [1-4, 6, 19] were used to obtain an image and propagators at 80 bar and 100 ^{o}C over a range of observation times for a non-flowing condition in porous media. Staitionary (no flow) experiments measured the diffusion dynamics in 230 μm Zirconium Silicate Microspheres (Corpuscular). The sample holder containing the beads had an ID of 5 mm, but was not designed for flow through experiments having only one fluid port. An imaging sequence of using a slice thickness of 20 mm, repetition time T_R = 5 sec, echo time T_E, = 6.74 ms, and 768 signal averages was used, resulting in an acquisition time of 68.2 hours.

Single PGSE and double PGSE sequences were used to measure propagators. T_2* (~10 ms) in the pores was short and required the use of a stimulated echo sequence. The PGSE experiments used an observation time in the range of Δ = 12 - 1000 ms and a gradient pulse duration δ = .25 or .5 ms, dependent on the maximum allowable gradient. The maximum gradient value was unique for each observation time and used 128 gradient steps covering negative and positive gradient values for a full sampling of *q*-space for the propagators. No slice selection was used, exciting the entire sample, with repetition time T_R = 5 sec and 32 signal averages were taken for each observation time Δ resulting in an acquisition time of 5 hours 44 minutes.

Preliminary Results and Discussion

The image revealed the time intensiveness of gathering MR data from CO_2. An image at a lower pressure or a thinner slice thickness would have taken much longer to complete. The pressure of 80 bar was chosen because it was several bar above the critical pressure and the slice thickness of 20 mm was the maximum slice thickness possible with the RF coil used. The image was taken as a proof of concept indicating that imaging of critical or supercritical CO_2 is possible, however, to obtain information on packing order or single pore length scale molecular spin densities will be time consuming. The 20 mm slice was 87 times the bead diameter and does not show a packing order.

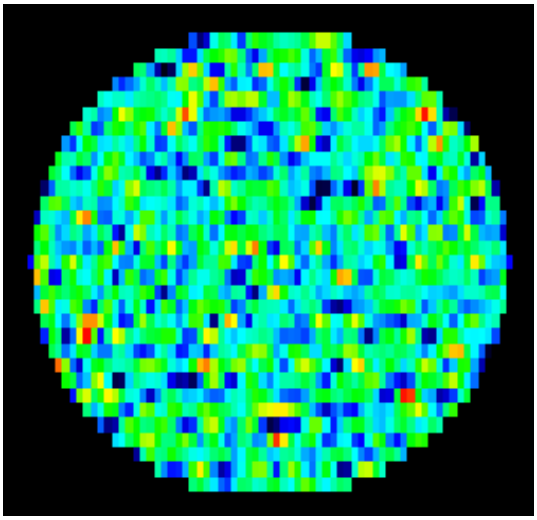

Figure 9.1: Image of Supercritical CO_2 in 230 µm beads at 80 bar. Sample holder had a 5 mm inner diameter and the image had a 20 mm slice thickness.

Preliminary propagator data did not exhibit any significant variation in dynamics as compared to C_2F_6. The sPGSE and dPGSE showed similar molecular displacement for

the dynamics at 80 bar and 100 ^{o}C which was approximately 6 bar above the critical pressure and 70 ^{o}C above the critical temperature. The time evolution for both the dPGSE and sPGSE showed similar displacements indicating that only diffusion motion existed. It was expected that dynamics similar to the critical test for C_2F_6 at 29 bar would have been manifested at 80 bar for CO_2 but this proved untrue in the preliminary experiments. The propagators of C_2F_6 at 29 bar showed a second population of motion at higher displacements. Further experiments may indicate that a change in testing pressure and/or temperature might produce results similar to those seen in the C_2F_6 results. These experiments showed a proof of concept in acquiring translational motion data by MR for CO_2 at the critical and supercritical phases.

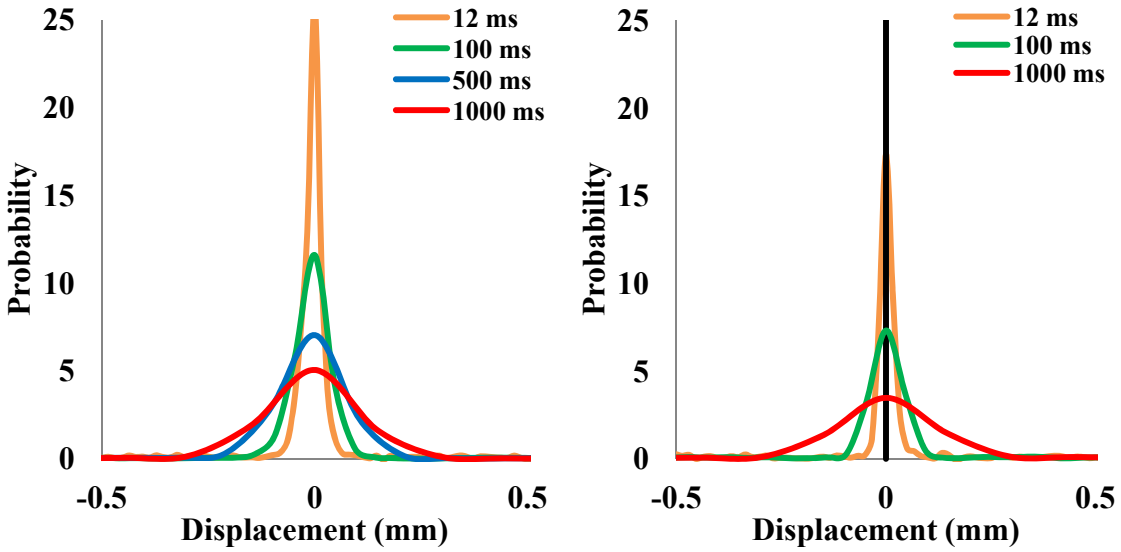

Figure 9.2: a) sPGSE and b) dPGSE propagators of CO_2 at 80 bar 100 ^{o}C.

More experiments are needed on the bulk fluid for CO_2 without the presence of a porous media to establish baseline diffusion values[172] and determine if convection is present in the sample holder as was observed for C_2F_6. The same sample holder was used

for both CO_2 and C_2F_6, but the heating system used on CO_2 was not required for the C_2F_6 work. Tests and modifications need to be made to determine the performance of the heating system (heat loss, convection, heat flow, and etc.) and to determine how well the critical temperature of the CO_2 compares with published values. The experiments on the bulk fluid would indicate dynamics that are present due to the geometry of the sample holder and dynamics that are fluid specific. After completion of the bulk fluid experiments, it would be necessary to retest CO_2 in the porous media and complete the same spectrum of experiments that were performed on C_2F_6 to give the time evolution of dynamics of CO_2 in porous media. Future experiments should observe the dynamics in different bead sizes and a similar range of observation times (12 - 1000 ms) should be obtainable.

Conclusion

The preliminary data measuring the dynamics of CO_2 in porous media provides a foundation for future testing of critical and supercritical CO_2. The results indicated that testing time of CO_2 takes much longer than C_2F_6 due to the lower MR signal and longer T_1 relaxation. The system and sample holder have been tested to above critical pressures and temperatures and allow the expansion of test parameters to include observations in other porous media types as well as mixing brine with CO_2.

REFERENCES CITED

1. Newling, B., *Gas flow measurements by NMR.* Progress in Nuclear Magnetic Resonance Spectroscopy, 2008. **52**: p. 31-48.

2. Stejskal, E.O. and J.E. Tanner, *Spin diffusion measurements: Spin echoes in the presence of a time-dependent field gradient.* Journal of Chemical Physics, 1965. **42**: p. 288.

3. Callaghan, P.T., *Principles of Nuclear Magnetic Resonance Microscopy*. 1991, New York: Oxford University Press.

4. Codd, S.L., et al., *Taylor dispersion and molecular displacements in poiseuille flow.* Physical Review E, 1999. **60**(4): p. R3491-R3494.

5. Saikawa, K., et al., *Determination of the critical-temperature and density of hexafluoroethane.* Journal of Chemical and Engineering Data, 1979. **24**(3): p. 165-167.

6. Kuethe, D.O., T. Pietrass, and V.C. Behr, *Inert fluorinated gas T-1 calculator.* Journal of Magnetic Resonance, 2005. **177**(2): p. 212-220.

7. Lemmon, E.W., McLinden, M. O., & Friend, D. G., *Thermophysical properties of fluid systems in NIST chemistry webbook, NIST standard reference database*, ed. W.G.M. P. J. Linstrom, Eds. Vol. 69, Gaithersburg, MD 20899: National Institute of Standards and Technology.

8. Madani, H., et al., *Vapor-liquid equilibrium data for the (hexafluoroethane + 1,1,1,2-tetrafluoroethane) system at temperatures from 263 to 353 K and pressures up to 4.16 MPa (vol 268, pg 68, 2008).* Fluid Phase Equilibria, 2008. **273**(1-2): p. 92-92.

9. Goycoolea, F.M., et al., *Stoichiometry and conformation of xanthan in synergistic gelation with locust bean gum or konjac glucomannan-evidence for heterotypic binding.* Macromolecules, 1995. **28**(24): p. 8308-8320.

10. Loxley, A. and B. Vincent, *Preparation of Poly(methylmethacrylate) Microcapsules with Liquid Cores.* Journal of Colloid and Interphace Science, 1998. **208**: p. 49-62.

11. Wassenius, H., M. Nyden, and B. Vincent, *NMR diffusion studies of translational properties of oil inside core-shell latex particles.* Journal of Colloid and Interface Science, 2003. **264**(2): p. 538-547.

12. Ku, D.N., *Blood flow in arteries.* Annual Review of Fluid Mechanics, 1997. **29**: p. 399-434.

13. Womersley, J.R., *Method for the calculation of velocity, rate of flow and viscous drag in arteries when the pressure gradient is known.* Journal of Physiology-London, 1955. **127**(3): p. 553-563.

14. Brown, J.R., et al., *Dynamics of the solid and liquid phases in dilute sheared Brownian suspensions: Irreversibility and particle migration.* Physical Review Letters, 2007. **99**(24).

15. Callaghan, P.T., *Rheo-NMR: nuclear magnetic resonance and the rheology of complex fluids.* Reports on Progress in Physics, 1999. **62**(4): p. 599-670.

16. Rassi, E.M., Codd, S.L., and Seymour, J.D., *MR measurement of Critical Phase Transition Dynamics and Supercritical Fluid Dynamics in Capillary and Porous Media Flow.* Manuscript accepted for publication in Journal of Magnetic Resonance, 2011.

17. Rassi, E.M., Codd, S.L., and Seymour, J.D., *Nuclear magnetic resonance characterization of the stationary dynamics of partially saturated media during steady-state infiltration flow* New Journal of Physics, 2011. **13**(1).

18. Evertz, L.Q., Rassi, E.M., Kennedy, J.R.M., Codd, S.L., and Seymour, J.D., *Oscillatory flow phenomena in simple and complex fluids.* Manuscript accepted for publication in Applied Magnetic Resonance, 2011.

19. Fukushima, E. and S.B.W. Roeder, *Experimental Pulse NMR: A nuts and bolts approach*. 1981, Reading, MA: Addison-Wesley.

20. Levitt, M.H., *Spin dynamics: Basics of nuclear magnetic resonance - 2nd Edition*. 2008, West Sussex: Wiley and Sons Ltd.

21. Mansfield, P. and P.K. Grannell, *NMR 'diffraction' in solids?* Journal of Physics C, 1973. **6**: p. L422-L426.

22. Wolfe, R.R., & Chinkles, D. L., *Isotope tracers in metabolic research: Principles and practice of kinetic analysis.* 2005, Hoboken: Wiley-Liss.

23. Sodickson, A. and D.G. Cory, *A generalized k-space formalism for treating the spatial aspects of a variety of NMR experiments.* Progress in Nuclear Magnetic Resonance Spectroscopy, 1998. **33**: p. 77-108.

24. Kubo, R., M. Toda, and N. Hashitsume, *Statistical Physics II: Nonequilibrium Statistical Mechanics*. Springer Series in Solid-State Sciences, ed. P. Fulde. Vol. 31. 1991, Berlin: Springer-Verlag.

25. Karger, J. and W. Heink, *The propagator representation of molecular transport in microporous crystallites.* Journal of Magnetic Resonance, 1983. **51**(1): p. 1-7.
26. Codd, S.L. and S.A. Altobelli, *A PGSE study of propane gas flow through model porous bead packs.* Journal of Magnetic Resonance, 2003. **163**: p. 16-22.

27. Vasenkov, S., & Kärger, J., *NMR diffusion studies of nanoporous materials.* Fluid Trans. in Nanoporous Mat., 2006: p. 375-381.

28. Callaghan, P.T., et al., *Diffraction-like effects in NMR diffusion studies of fluids in porous solids.* Nature, 1991. **351**: p. 467-469.

29. Brownstein, K.R. and C.E. Tarr, *Importance of classical diffusion in NMR-studies of water in biological cells.* Physical Review A, 1979. **19**(6): p. 2446-2453.

30. Song, Y.Q., *Detection of the high eigenmodes of spin diffusion in porous media.* Physical Review Letters, 2000. **85**(18): p. 3878-3881.

31. Callaghan, P.T., et al., *Diffusion in Porous systems and the influence of pore morphology in pulsed gradient spin echo nuclear magnetic resonance studies.* Journal of Chemical Physics, 1992. **97**(1): p. 651-662.

32. Callaghan, P.T., et al., *Diffusion in Porous systems and the Influence of Pore Morphology in Pulsed Gradient Spin-Echo Nuclear Magnetic-Resonance Studies.* Journal of Chemical Physics, 1992. **97**(1): p. 651-662.

33. Callaghan, P.T., et al., *Diffraction-like Effects in NMR Diffusion Studies of Fluids in Porous Solids.* Nature, 1991. **351**(6326): p. 467-469.

34. Cushman, J.H., *Dynamics of Fluids in Hierarchical Porous Media*. 1990, San Diego: Academic Press.

35. Lebon, L., J. Leblond, and J.P. Hulin, *Experimental measurement of dispersion processes at short times using a pulsed field gradient NMR technique.* Physics of Fluids, 1997. **9**(3): p. 481-490.

36. Lebon, L., et al., *Pulsed field gradient NMR measurements of probability distribution of displacement under flow in sphere packings.* Magnetic Resonance Imaging, 1996. **14**(7-8): p. 989-991.

37. Lebon, L., et al., *Pulsed gradient NMR measurements and numerical simulation of flow velocity distribution in sphere packings.* Physics of Fluids, 1996. **8**(2): p. 293-301.

38. Liaw, H.K., et al., *Characterization of fluid distributions in porous media by NMR techniques.* Aiche Journal, 1996. **42**(2): p. 538-546.

39. Mair, R.W., et al., *Tortuosity measurement and the effects of finite pulse widths on xenon gas diffusion NMR studies of porous media.* Magnetic Resonance Imaging, 2001. **19**(3-4): p. 345-351.

40. Manz, B., P. Alexander, and L.F. Gladden, *Correlations between dispersion and structure in porous media probed by nuclear magnetic resonance.* Physics of Fluids, 1999. **11**(2): p. 259-267.

41. Mitra, P.P., P.N. Sen, and L.M. Schwartz, *Short time behavior of the diffusion coefficient as a geometrical probe of porous media.* Physical Review B: Condensed Matter, 1993. **47**(14): p. 8565-8574.

42. Mitra, P.P., et al., *DIFFUSION PROPAGATOR AS A PROBE OF THE STRUCTURE OF POROUS-MEDIA.* Physical Review Letters, 1992. **68**(24): p. 3555-3558.

43. Sankey, M.H., et al., *Magnetic resonance velocity imaging of liquid and gas two-phase flow in packed beds.* J Magn Reson, 2009. **196**(2): p. 142-8.

44. Seymour, J.D. and P.T. Callaghan, *Generalized approach to NMR analysis of flow and dispersion in porous media.* Aiche Journal, 1997. **43**(8): p. 2096-2111.

45. Sonntag, R.E., Borgnakke, C., & van Wylen, G. J., *Fundamentals of thermodynamics*. 1998, New York: John Wiley and Sons.

46. Stanley, H.E., *Introduction to Phase Transitions and Critical Phenomena*. 1971, New York: Oxford University Press.

47. Maiwald, M., et al., *On-line H-1 NMR spectroscopic investigation of hydrogen bonding in supercritical and near critical CO2-methanol up to 35 MPa and 403 K.* Journal of Supercritical Fluids, 2007. **43**: p. 267-275.

48. Brunner, G., *Supercritical fluids: technology and application to food processing.* Journal of Food Engineering, 2005. **67**(1-2): p. 21-33.

49. Klusman, R.W., *Evaluation of leakage potential from a carbon dioxide EOR/sequestration project.* Energy Conversion and Management, 2003. **44**(12): p. 1921-1940.

50. Parker, M.E., Meyer, J. P., & Meadows, S. R., *Carbon dioxide enhanced oil recovery injection technologies.* Energy Procedia, 2009: p. 3141-3148.

51. Orr, F.M. and J.J. Taber, *Use of carbon-dioxide in enhanced oil recovery.* Science, 1984. **224**(4649): p. 563-569.

52. Allen, L.A., T.E. Glass, and H.C. Dorn, *Direct monitoring of supercritical fluids and supercritical chromatographic separations by proton nuclear magnetic-resonance.* Analytical Chemistry, 1988. **60**(5): p. 390-394.

53. Albert, K., et al., *Online coupling of supercritical-fluid chromatography and proton high-field nuclear-magnetic-resonance spectroscopy.* Analytical Chemistry, 1994. **66**(19): p. 3042-3046.

54. Van der Meer, L.G.H., *The CO2 storage efficiency of aquifers.* Energy Conversion and Management, 1995. **36**(6-9): p. 513-518.

55. Ravagnani, A., Ligero, E. L., & Suslick, S. B., *CO2 sequestration through enhanced oil recovery in a mature oil field.* J. of Petro. Sci. and Eng., 2009. **65**: p. 129-138.

56. Okwen, R.T., M.T. Stewart, and J.A. Cunningham, *Analytical solution for estimating storage efficiency of geologic sequestration of CO2.* International Journal of Greenhouse Gas Control. **4**(1): p. 102-107.

57. Jiang, P.X., et al., *Experimental and numerical study of convection heat transfer of CO2 at supercritical pressures in vertical porous tubes.* International Journal of Heat and Mass Transfer, 2008. **51**(25-26): p. 6283-6293.

58. Duffey, R.B. and I.L. Pioro, *Experimental heat transfer of supercritical carbon dioxide flowing inside channels (survey).* Nuclear Engineering and Design, 2005. **235**(8): p. 913-924.

59. Pioro, I.L., H.F. Khartabil, and R.B. Duffey, *Heat transfer to supercritical fluids flowing in channels - empirical correlations (survey).* Nuclear Engineering and Design, 2004. **230**(1-3): p. 69-91.

60. Jiang, P.X., et al., *Experimental and numerical study of convection heat transfer of CO2 at super-critical pressures during cooling in small vertical tube.* International Journal of Heat and Mass Transfer, 2009. **52**(21-22): p. 4748-4756.

61. Liao, S.M. and T.S. Zhao, *An experimental investigation of convection heat transfer to supercritical carbon dioxide in miniature tubes.* International Journal of Heat and Mass Transfer, 2002. **45**(25): p. 5025-5034.

62. Dang, C.B. and E. Hihara, *In-tube cooling heat transfer of supercritical carbon dioxide. Part 2. Comparison of numerical calculation with different turbulence*

models. International Journal of Refrigeration-Revue Internationale Du Froid, 2004. **27**(7): p. 748-760.

63. Jain, P.K. and u. Rizwan, *Numerical analysis of supercritical flow instabilities in a natural circulation loop.* Nuclear Engineering and Design, 2008. **238**(8): p. 1947-1957.

64. Bae, J.H., J.Y. Yoo, and H. Choi, *Direct numerical simulation of turbulent supercritical flows with heat transfer.* Physics of Fluids, 2005. **17**(10).

65. He, S., W.S. Kim, and J.D. Jackson, *A computational study of convective heat transfer to carbon dioxide at a pressure just above the critical value.* Applied Thermal Engineering, 2008. **28**(13): p. 1662-1675.

66. Fard, M.H., *CFD modeling of heat transfer of CO2 at supercritical pressures flowing vertically in porous tubes.* International Communications in Heat and Mass Transfer. **37**(1): p. 98-102.

67. Bae, Y.Y. and H.Y. Kim, *Convective heat transfer to CO2 at a supercritical pressure flowing vertically upward in tubes and an annular channel.* Experimental Thermal and Fluid Science, 2009. **33**(2): p. 329-339.

68. Bruch, A., A. Bontemps, and S. Colasson, *Experimental investigation of heat transfer of supercritical carbon dioxide flowing in a cooled vertical tube.* International Journal of Heat and Mass Transfer, 2009. **52**(11-12): p. 2589-2598.

69. Liao, S.M.a.Z., T. S. , *A numerical investigation of laminar convection of supercritical carbon dioxide in vertical mini/micro tubes.* Progress in Computational Fluid Dynamics, 2002. **2**: p. 144-152.

70. Lee, S.H. and J.R. Howell, *Turbulent developing convective heat transfer in a tube for fluids near the critical point.* International Journal of Heat and Mass Transfer, 1998. **41**(10): p. 1205-1218.

71. He, S., W.S. Kim, and J.H. Bae, *Assessment of performance of turbulence models in predicting supercritical pressure heat transfer in a vertical tube.* International Journal of Heat and Mass Transfer, 2008. **51**(19-20): p. 4659-4675.

72. Barmatz, M., et al., *Critical phenomena in microgravity: Past, present, and future.* Reviews of Modern Physics, 2007. **79**: p. 1-52.

73. Beysens, D.A., *Near-critical point hydrodynamics and microgravity.* Mech. of the 21st Century, 2005: p. 117-130.

74. de Gennes, P.G., ed. *Phase transition and turbulence: An introduction*. Proceedings of the NATO Advanced Study Institute on Fluctuations, Instabilities, and Phase Transitions, ed. T. Riste. 1975, Plenum Press. 1-81.

75. Landau, L.D., & Lifshitz, E. M., *Fluid Mechanics*. Vol. 26. 1959, London: Pergamon Press.

76. Hohenberg, P.C. and B.I. Halperin, *Theory of dynamic critical phenomena.* Reviews of Modern Physics, 1977. **49**(3): p. 435-479.

77. Jiang, P.X., Y. Zhang, and R.F. Shi, *Experimental and numerical investigation of convection heat transfer Of CO2 at supercritical pressures in a vertical mini-tube.* International Journal of Heat and Mass Transfer, 2008. **51**(11-12): p. 3052-3056.

78. Jiang, P.X., et al., *Experimental investigation of flow resistance and convection heat transfer of CO2 at supercritical pressures in a vertical porous tube.* Journal of Supercritical Fluids, 2006. **38**(3): p. 339-346.

79. Jiang, P.X., et al., *Experimental investigation of convection heat transfer of CO2 at super-critical pressures in vertical mini-tubes and in porous media.* Applied Thermal Engineering, 2004. **24**(8-9): p. 1255-1270.

80. Howell, J.R. and S.H. Lee, *Convective heat transfer in the entrance region of a vertical tube for water near the thermodynamic critical point.* International Journal of Heat and Mass Transfer, 1999. **42**(7): p. 1177-1187.

81. Tanaka, H., et al., *Effects of buoyancy and of acceleration owing to thermal-expansion on forced turbulent convection in vertical circular tubes - criteria of effects, velocity and temperature profiles, and reverse transition from turbulent to laminar flow.* International Journal of Heat and Mass Transfer, 1973. **16**(6): p. 1267-1288.

82. Lee, S.H. and J.R. Howell, *Gravitational effects on laminar convection to near-critical water in a vertical tube.* Journal of Thermophysics and Heat Transfer, 1996. **10**(4): p. 627-632.

83. Lee, S.H. and J.R. Howell, *Laminar forced convection at zero gravity to water near the critical region.* Journal of Thermophysics and Heat Transfer, 1996. **10**(3): p. 504-510.

84. Kurganov, V.A. and A.G. Kaptil'ny, *Flow structure and turbulent transport of a supercritical pressure fluid in a vertical heated tube under the conditions of mixed convection - experimental-data.* International Journal of Heat and Mass Transfer, 1993. **36**(13): p. 3383-3392.

85. Kurganov, V.A. and A.G. Kaptil'ny, *Velocity and enthalpy fields and eddy diffusivities in a heated supercritical fluid flow.* Experimental Thermal and Fluid Science, 1992. **5**: p. 465-478.

86. Dvoyashkin, M., R. Valiullin, and J. Karger, *Supercritical fluids in mesopores - new insight using NMR.* Adsorption-Journal of the International Adsorption Society, 2007. **13**(3-4): p. 197-200.

87. Dvoyashkin, M., et al., *Direct assessment of transport properties of supercritical fluids confined to nanopores.* Journal of the American Chemical Society, 2007. **129**(34): p. 10344-+.

88. Suekane, T., et al., *Application of MRI in the Measurement of Two-Phase Flow of Supercritical CO2 and Water in Porous Rocks.* Journal of Porous Media, 2009. **12**(2): p. 143-154.

89. Yonker, C.R. and J.C. Linehan, *The use of supercritical fluids as solvents for NMR spectroscopy.* Progress in Nuclear Magnetic Resonance Spectroscopy, 2005. **47**(1-2): p. 95-109.

90. Jiang, P.X., et al., *Experimental and numerical investigation of convection heat transfer of CO2 at supercritical pressures in a vertical tube at low Reynolds numbers.* International Journal of Thermal Sciences, 2008. **47**(8): p. 998-1011.

91. Jackson, J.D. and W.B. Hall, eds. *Influences of buoyancy on heat transfer to fluids in vertical tubes under turbulent conditions*. Turbulent Forced Convection in Channels and Bundles, ed. S.K.a.D.B. Spalding. 1979, Hemisphere Publishing Corp. 613–640.

92. Stanley, H.E., *Introduction to phase transistions and critical phenomena*. 1971, New York: Oxford University Press.

93. Onuki, A., *Phase Transition Dynamics*. 2002, Cambridge: Cambridge University Press.

94. Krynicki, K., et al., *Nuclear-spin-lattice relaxation due to critical fluctuations in fluids.* Communications on Physics, 1976. **1**(6): p. 183-189.

95. Kajiya, D., K. Nishikawa, and K. Saitow, *Time evolution of density fluctuation in the supercritical region. 2. Comparison of hydrogen- and non-hydrogen-bonded fluids.* Journal of Physical Chemistry A, 2005. **109**(33): p. 7365-7370.

96. Saitow, K.I., D. Kajiya, and K. Nishikawa, *Time evolution of density fluctuation in supercritical region. I. Non-hydrogen-bonded fluids studied by dynamic light scattering.* Journal of Physical Chemistry A, 2005. **109**(1): p. 83-91.

97. Saitow, K., D. Kajiya, and K. Nishikawa, *Dynamics of density fluctuation of supercritical fluid mapped on phase diagram.* Journal of the American Chemical Society, 2004. **126**(2): p. 422-423.

98. Maccabee, B.S. and J.A. White, *Supercritical correlation length of carbon dioxide along critical isochore.* Physical Review Letters, 1971. **27**(8): p. 495-&.

99. Zappoli, B., *Near-critical fluid hydrodynamics.* Comptes Rendus Mecanique, 2003. **331**(10): p. 713-726.

100. Zappoli, B., S. Amiroudine, and S. Gauthier, *Rayleigh-Taylor-like instability in near-critical pure fluids.* International Journal of Thermophysics, 1999. **20**(1): p. 257-265.

101. Jiang, P.X., et al., *Convection heat transfer of CO2 at supercritical pressures in a vertical mini tube at relatively low reynolds numbers.* Experimental Thermal and Fluid Science, 2008. **32**(8): p. 1628-1637.

102. Stauffer, D. and A. Aharony, *Introduction to Percolation Theory*. 1985, London: Taylor and Francis.

103. Wilkinson, D.a.W., J.F., *Invasion percolation: a new form of percolation theory.* J Phys A, 1983. **16**(14): p. 3365-3376.

104. Lenormand, R. and C. Zarcone, *Invasion Percolation in an Etched Network-Measurement of a Fractal Dimension.* Physical Review Letters, 1985. **54**(20): p. 2226-2229.

105. Sahimi, M., *Flow and Transport in Porous Media and Fractured Rock: From Classical methods to Modern Approaches*. 1995, Weinheim: VCH.

106. Bird, R.B., W.E. Stewart, and E.N. Lightfoot, *Transport Phenomena*. 2nd ed. 2002, New York: Wiley & Sons. 780.

107. Stokes, J.P., A.P. Kushnick, and M.O. Robbins, *Interface Dynamics in Porous-Media- a Random Field Descriptio.* Physical Review Letters, 1988. **60**(14): p. 1386-1389.

108. Shaw, T.M., *Drying as an Immiscible Displacement Process with Fluid Counterflow.* Physical Review Letters, 1987. **59**(15): p. 1671-1674.

109. Rubio, M.A., et al., *Self-Affine Fractal Interfaces from Immiscible Displacement in Porous-Media.* Physical Review Letters, 1989. **63**(16): p. 1685-1688.

110. Horvath, V.K., F. Family, and T. Vicsek, *Anomalous Noise Distribution of the Interface in 2-Phase Fluid-Flow.* Physical Review Letters, 1991. **67**(23): p. 3207-3210.

111. Ramstad, T. and A. Hansen, *Cluster evolution in steady-state two-phase flow in porous media.* Physical Review E, 2006. **73**(2).

112. Tallakstad, K.T., et al., *Steady-State Two-Phase Flow in Porous Media: Statistics and Transport Properties.* Physical Review Letters, 2009. **102**(7).

113. Tallakstad, K.T., et al., *Steady-state, simultaneous two-phase flow in porous media: An experimental study.* Physical Review E, 2009. **80**(3).

114. de Gennes, P.-G., *Hydrodynamic dispersion in unsaturated porous media.* Journal of Fluid Mechanics, 1983. **136**: p. 189-200.

115. Saffman, P.G., *Dispersion due to Molecular Diffusion and Macroscopic Mixing in Flow through a Network of Capillaries.* Journal of Fluid Mechanics, 1960. **7**(2): p. 194-208.

116. Scher, H. and E.W. Montroll, *Anomalous Transit-Time Dispersions in Amorphous Solids.* Physical Review B, 1975. **12**(6): p. 2455-2477.

117. Cushman, J.H., B.X. Hu, and T.R. Ginn, *Nonequilibrium statistical mechanics of preasymptotic dispersion.* Journal of Statistical Physics, 1994. **75**: p. 859-878.

118. Berkowitz, B., et al., *Physical pictures of transport in heterogeneous media: Advection-dispersion, randolm-walk and fractional derivative formulations.* Water Resources Research, 2002. **38**(10): p. 1191-12.

119. Harris, J., G. Peev, and Wilkinso.Wl, *Velocity profiles in laminar oscillatory flow in tubes* Journal of Physics E-Scientific Instruments, 1969. **2**(11): p. 913-&.

120. Nebauer, H.M.B.a.J.R.A., *Stability of oscillatory and pulsatile pipe flow*, in *Seventh International Conference on CFD in the Mineral and Process Industries*. 2009, CSIRO: Melbourne, Australia. p. 1-6.

121. Sergeev, S.I., *Fluid oscillations in pipes at moderate Reynolds numbers.* Fluid Dynamics, 1966. **1**(1): p. 121-122.

122. Jones, T.S.W.a.J.R., *Flow of elstico-viscous liquids in channels under the influence of a periodic pressure gradient, part 1.* Rheologica Acta, 1967: p. 240-245.

123. Escudier, M.P., et al., *On the reproducibility of the rheology of shear-thinning liquids.* Journal of Non-Newtonian Fluid Mechanics, 2001. **97**(2-3): p. 99-124.

124. Manz, B., J.D. Seymour, and P.T. Callaghan, *PGSE NMR measurements of convection in a capillary.* Journal of Magnetic Resonance, 1997. **125**: p. 153-158.

125. Jerschow, A., and Müller, N., *Suppression of Convection Artifacts in Stimulated Echo Diffusion Experiments. Double Stimulated Echo Experiments.* J. Magn. Reson. , 1997: p. 372-5.

126. Callaghan, P.T., S.L. Codd, and J.D. Seymour, *Spatial coherence phenomena arising from translational spin motion in gradient spin echo experiments.* Concepts in Magnetic Resonance, 1999. **11**: p. 181-202.

127. Danckwerts, P.V., *Continuous flow systems: Distribution of residence times.* Chemical Engineering Science, 1953. **2**(1): p. 1-13.

128. Codd, S.L., et al., *Magnetic Resonance Microscopy of Biofilm and Bioreactor Transport*, in *NMR Imaging in Chemical Engineering*, S. Stapf and S.-I. Han, Editors. 2006, Wiley-VCH: Weinheim.

129. Squires, T.M., R.J. Messinger, and S.R. Manalis, *Making it stick: convection, reaction and diffusion in surface-based biosensors.* Nature Biotechnology, 2008. **26**(4): p. 417-426.

130. Tan, C.S. and D.C. Liou, *Axial-dispersion of supercritical carbon-dioxide in packed beds.* Industrial & Engineering Chemistry Research, 1989. **28**(8): p. 1246-1250.

131. Ghoreishi, S.M. and A. Akgerman, *Dispersion coefficients of supercritical fluid in fixed beds.* Separation and Purification Technology, 2004. **39**(1-2): p. 39-50.

132. Funazukuri, T., C.Y. Kong, and S. Kagei, *Effective axial dispersion coefficients in packed beds under supercritical conditions.* Journal of Supercritical Fluids, 1998. **13**(1-3): p. 169-175.

133. Yu, D., K. Jackson, and T.C. Harmon, *Dispersion and diffusion in porous media under supercritical conditions.* Chemical Engineering Science, 1999. **54**(3): p. 357-367.

134. Catchpole, O.J., R. Bernig, and M.B. King, *Measurement and correlation of packed-bed axial dispersion coefficients in supercritical carbon dioxide.* Industrial & Engineering Chemistry Research, 1996. **35**(3): p. 824-828.

135. Lin, R.H. and L.L. Tavlarides, *Determination of diffusion coefficients by supercritical fluid chromatography: Effects of mobile phase mean velocity and column orientation.* Journal of Chromatography A. **1217**(26): p. 4454-4462.

136. Mair, R.W., et al., *Applications of controlled-flow laser-polarized xenon gas to porous and granular media study.* Magnetic Resonance Imaging, 2003. **21**(3-4): p. 287-292.

137. Zhou, N.a.K., A. *Laminar and turbulent heat transfer in flow of supercritical CO2*. in *1995 National Heat Transfer Conference*. 1995. Portland, OR: ASME.

138. Seymour, J.D. and P.T. Callaghan, *"Flow-Diffraction" structural characterization and measurement of hydrodynamic dispersion in porous media by PGSE NMR.* Journal of Magnetic Resonance. Series A, 1996. **122**: p. 90-93.

139. Vongunten, H.R., et al., *Seasonal Biogeochemical Cycles in Riverborne Groundwater.* Geochimica Et Cosmochimica Acta, 1991. **55**(12): p. 3597-3609.

140. *Plans and Practices for Groundwater Protection at the Los Alamos National Laboratory*. 2007, Washington, D.C.: The National Academies Press.

141. Goldberg, S., et al., *Adsorption - Desorption processes in subsurface reactive transport modeling.* Vadose Zone Journal, 2007. **6**(3): p. 407-435.

142. Gouet-Kaplan, M., A. Tartakovsky, and B. Berkowitz, *Simulation of the interplay between resident and infiltrating water in partially saturated porous media.* Water Resources Research, 2009. **45**.

143. Scheven, U.M. and P.N. Sen, *Spatial and temporal coarse graining for dispersion in randomly packed spheres.* Physical Review Letters, 2002. **89**(25): p. 254501.

144. Kutsovsky, Y.E., et al., *NMR imaging of velocity profiles and velocity distributions in bead packs.* Physics of Fluids, 1996. **8**(4): p. 863-871.

145. Scheven, U.M., R. Harris, and M.L. Johns, *Intrinsic dispersivity of randomly packed monodisperse spheres.* Phys Rev Lett, 2007. **99**(5): p. 054502.

146. Khrapitchev, A.A., et al., *Spectrally resolved velocity exchange spectroscopy of two-phase flow.* Journal of Magnetic Resonance, 2002. **159**(1): p. 36-45.

147. Tessier, J.J. and K.J. Packer, *The Characterization of multiphase fluid transport in a porous solid by pulsed gadient stimulated echo nuclear magnetic resonance.* Physics of Fluids, 1998. **10**(1): p. 75-85.

148. Sederman, A.J. and L.F. Gladden, *Magnetic resonance imaging as a quantitative probe of gas-liquid distribution and wetting efficiency in trickle-bed reactors.* Chemical Engineering Science, 2001. **56**(8): p. 2615-2628.

149. Anadon, L.D., A.J. Sederman, and L.F. Gladden, *Mechanism of the trickle-to-pulse flow transition in fixed-bed reactors.* Aiche Journal, 2006. **52**(4): p. 1522-1532.

150. Kose, K., *Spatial Mapping of Velocity Power Spectra in Taylor-Couette Flow Using Ultrafast NMR Imaging.* Physical Review Letters, 1994. **72**(10): p. 1467-1470.

151. Wang, R., Z.S. Mao, and J.Y. Chen, *Experimental and Theoretical-Studies of Pressure-Drop Hysteresis in Trickle-Bed Reactors.* Chemical Engineering Science, 1995. **50**(14): p. 2321-2328.

152. van der Merwe, W., W. Nicol, and F. de Beer, *Trickle flow distribution and stability by X-ray radiography.* Chemical Engineering Journal, 2007. **132**(1-3): p. 47-59.

153. Johns, M.L., et al., *Local transitions in flow phenomena through packed beds identified by MRI.* Aiche Journal, 2000. **46**(11): p. 2151-2161.

154. Lutran, P.G., Ng, K. M., Delikat, E. P, *Liquid distribution in tricklebeds. An experimental study using computer-assisted tomography. Ind. Eng. Chem. Res.*, 1991. ***30***(6): p. 1270–1280.

155. Avraam, D.G. and A.C. Payatakes, *Flow Regimes and Relative Permeabilities during Stead-State 2-Phase Flow in Porous-Media.* Journal of Fluid Mechanics, 1995. **293**: p. 207-236.

156. Lebon, G., Jou, D., and Casas-Vazquez, J., *Understanding Non-Equilibrium Thermodynamics*. 2008: Springer.

157. Knudsen, H.A. and A. Hansen, *Relation between pressure and fractional flow in two-phase flow in porous media.* Physical Review E, 2002. **65**(5).

158. Tallarek, U., F.J. Vergeldt, and H. van As, *Stagnant mobile phase mass transfer in chromatographic media: intraparticle diffusion and exchange kinetics.* Journal of Physical Chemistry B, 1999. **103**: p. 7654-7664.

159. Eckmann, D.M. and J.B. Grotberg, *Experiments on transition to turbulence in oscillatory pipe-flow.* Journal of Fluid Mechanics, 1991. **222**: p. 329-350.

160. Hino, M., M. Sawamoto, and S. Takasu, *Experiments on transition to turbulence in an oscillatory pipe-flow* Journal of Fluid Mechanics, 1976. **75**(MAY27): p. 193-207.

161. Hale, J.F., D.A. McDonald, and J.R. Womersley, *Velocity profiles of oscillating arterial flow, with some calculations of viscous drag and the Reynolds number* Journal of Physiology-London, 1955. **128**(3): p. 629-640.

162. Torralba, M., et al., *Instabilities in the oscillatory flow of a complex fluid.* Physical Review E, 2007. **75**.

163. Brosten, T.R., et al., *Dynamic Length-Scale Characterization and Nonequilibrium Statistical Mechanics of Transport in Open-Cell Foams.* Physical Review Letters, 2009. **103**(21).

164. Seymour, J.D., et al., *Anomalous fluid transport in porous media induced by biofilm growth.* Phys Rev Lett, 2004. **93**(19): p. 198103.

165. Akhavan, R., R.D. Kamm, and A.H. Shapiro, *An investigation of transition to turbulence in bounded oscillatory stokes flows .1. Experiments.* Journal of Fluid Mechanics, 1991. **225**: p. 395-422.

166. Akhavan, R., R.D. Kamm, and A.H. Shapiro, *An investigation of transition to turbulence in bounded oscillatory stokes flows .2. Numerical simulations.* Journal of Fluid Mechanics, 1991. **225**: p. 423-444.

167. M. Ohmi, M.I., K. Kakehashi, and T. Masuda, *Transition to turbulence and velocity distribution in an oscillating pipe-flow.* Bulletin of the JSME, 1982. **25**(201): p. 365-371

168. Fishler, L.S. and R.S. Brodkey, *Transition, Turbulence and Oscillating Flow in a Pipe - A Visual Study.* Experiments in Fluids, 1991. **11**(6): p. 388-398.

169. Peev, G., *Problem of oscillatory laminar-flow of elasticoviscous liquids in channels* Rheologica Acta, 1975. **14**(5): p. 450-452.

170. Lodahl, C.R., B.M. Sumer, and J. Fredsoe, *Turbulent combined oscillatory flow and current in a pipe.* Journal of Fluid Mechanics, 1998. **373**: p. 313-348.

171. Callaghan, P.T., *Principles of Nuclear Magnetic Resonance Microscopy*. 1991, Oxford University Press: New York

172. Etesse, P., J.A. Zega, and R. Kobayashi, *High pressure nuclear magnetic resonance measurement of spin-lattice relaxation and self-diffusion in carbon-dioxide.* Journal of Chemical Physics, 1992. **97**(3): p. 2022-2029.

173. Jacob, R.E., Y. V. Chang, C. K. Choong, A. Bierhals, D. Zheng Hu, J. Zheng, D.A. Yablonskiy, J.C. Woods, D.S. Gierada, M.S. Conradi, *19F MR imaging of ventilation and diffusion in excised lungs.* Magnetic Resonance in Medicine, 2005. **54**(3): p. 577-585.

174. Cussler, E.L., *Diffusion: Mass transfer in fluid systems -2nd edition*. 1999, Cambridge: Cambridge University Press.

APPENDICES

APPENDIX A

MR PROPAGATORS OF A NEAR CRITICAL GAS, CRITICAL, AND SUPERCRITICAL FLUORINATED FLUID, C_2F_6, IN A DEAD END SAMPLE HOLDER

Methods

Magnetic resonance microscopy techniques [1-4, 6, 19] were used to obtain propagators over a range of pressures and observation times for Hexafluoroethane, C_2F_6, under no flow conditions. C_2F_6, was pumped to the pressures of 10, 25, 29, 45, and 70 bar with an Isco 500D syringe pump into a dead end sample holder constructed of PEEK (Figure A.1). The dead end sample holder resided in the Bruker Avance 300 NMR imaging spectrometer where it was used to record the propagators at the five pressures.

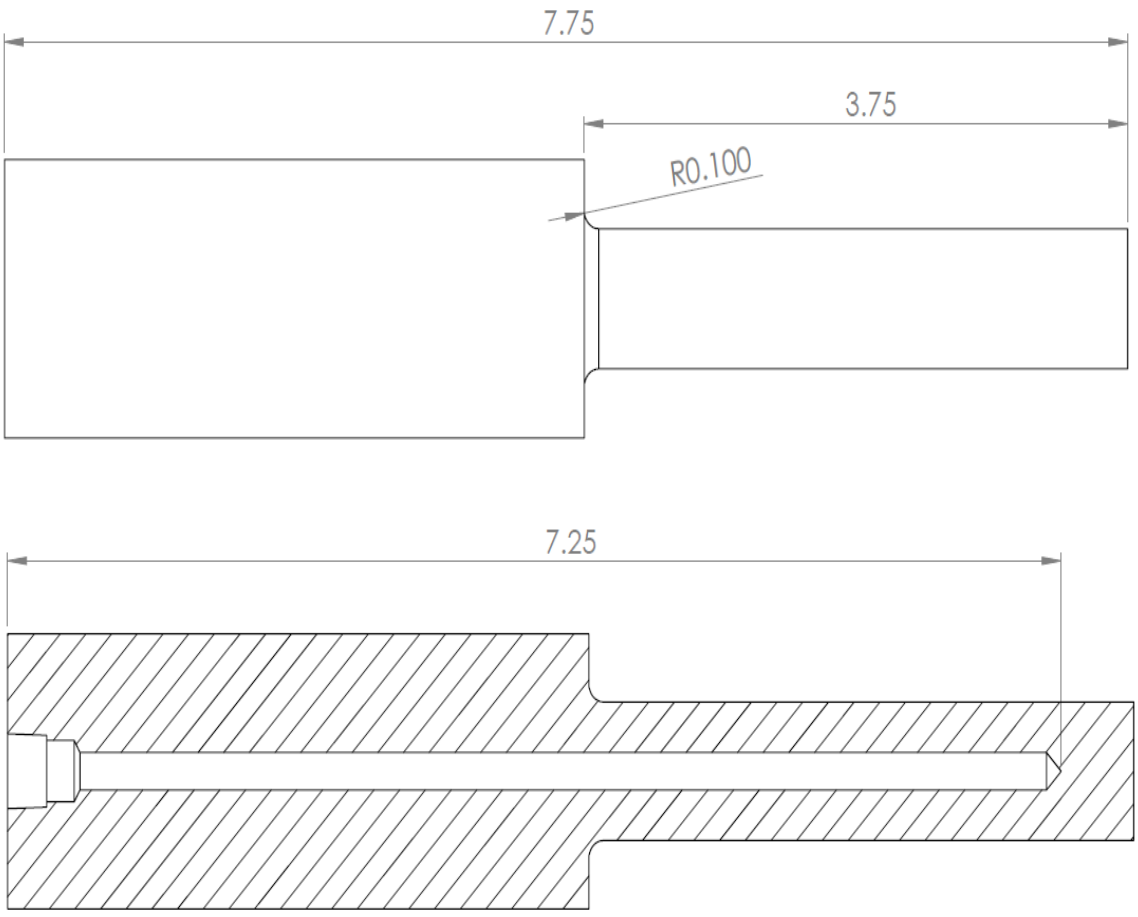

Figure A.1: PEEK dead end sample holder.

The repetition time T_R was determined from T_1-T_2 experiments performed on C_2F_6 as a function of pressure. sPGSE and dPGSE propagators were taken under no flow conditions to determine the diffusion of as a function of observation time.

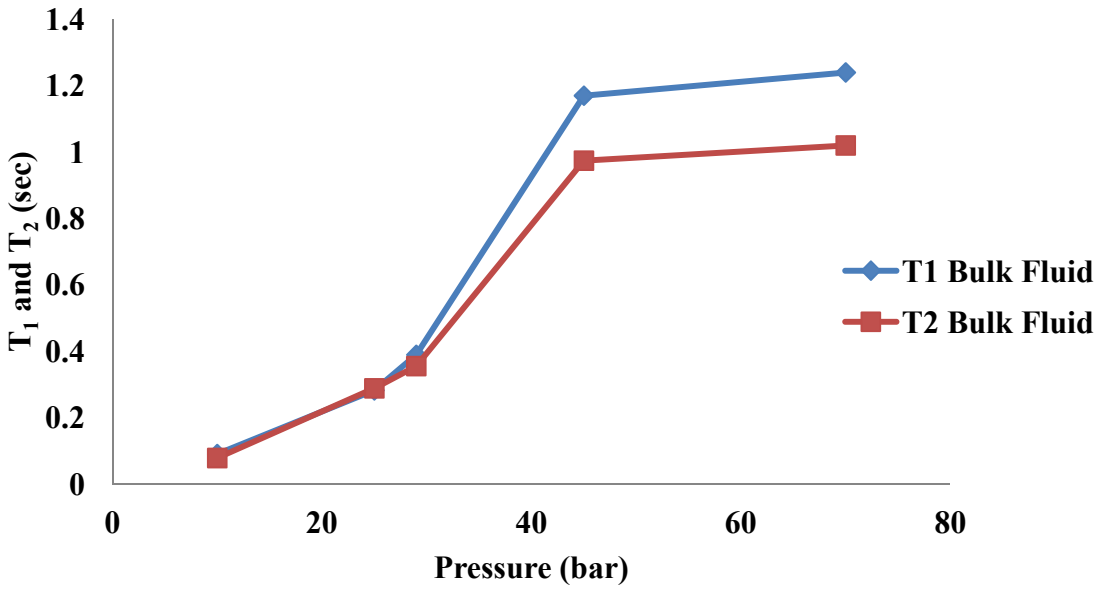

Figure A.2: T_1-T_2 Relaxation for C_2F_6 as a function of pressure.

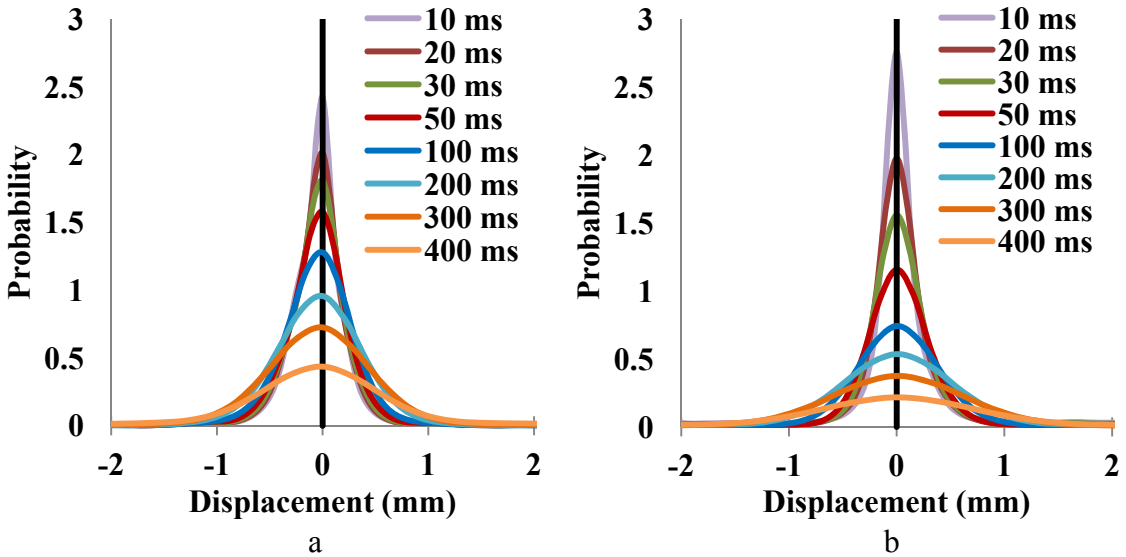

Figure A.3: 10 bar Propagators of C_2F_6 at T_{fluid} = 21 °C and $T_{surr.}$ = 21 °C for a) sPGSE and b) dPGSE.

For 10 bar, the observation times tested were 10 – 400 ms and 10 – 500 ms for all other pressures higher than 10 bar. This was due to lower signal at the lower pressure. The propagators are for the full excitation region of the R.F. coil. For 10 bar, 128 averages were used for each observation time with a $\delta = 0.25$ ms and a $T_R = 2$ s (Figure A.3).

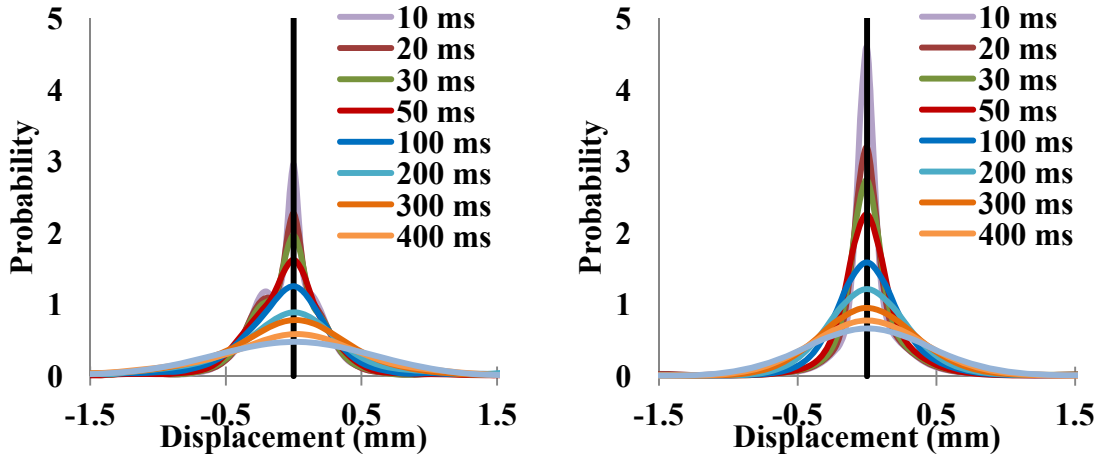

Figure A.4: 25 bar Propagators of C_2F_6 at $T_{fluid} = 21\ ^oC$ and $T_{surr.} = 21\ ^oC$ for a) sPGSE and b) dPGSE.

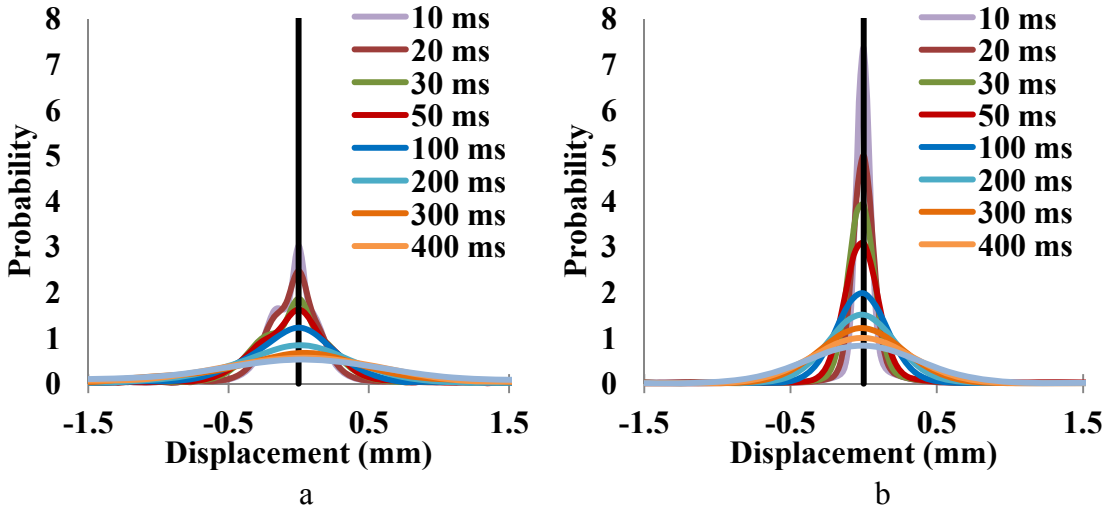

Figure A.5: 29 bar Propagators of C_2F_6 at $T_{fluid} = 21\ ^oC$ and $T_{surr.} = 21\ ^oC$ for a) sPGSE and b) dPGSE.

For all of the other pressures, 16 averages were used for each observation time with a δ = 0.25 ms and a T_R = 2 s for 25 and 29 bar and T_R = 5 s for 45 and 70 bar.

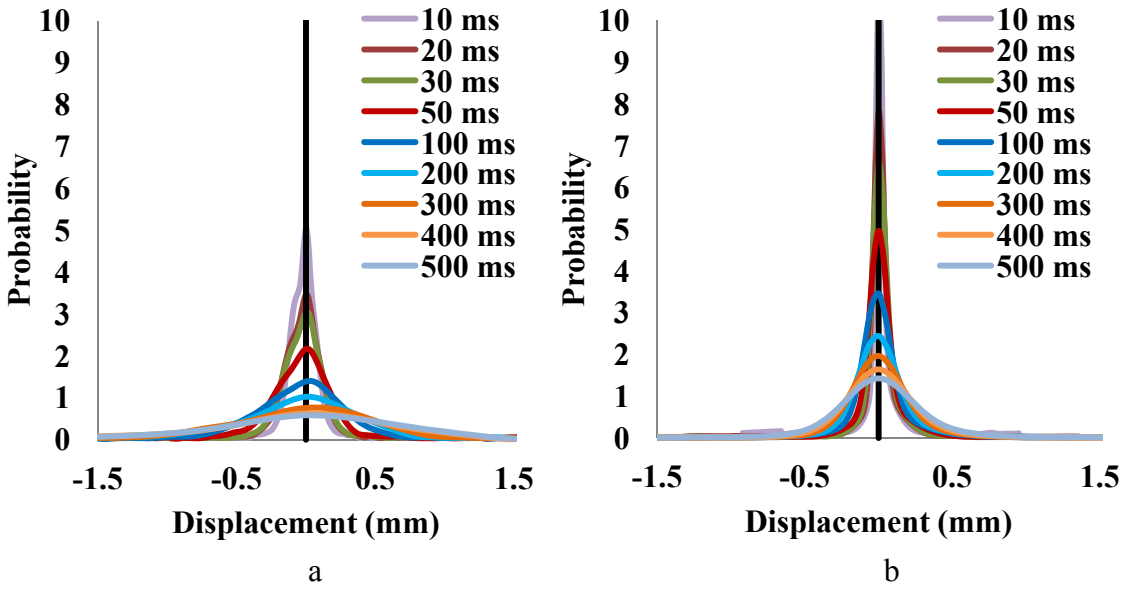

Figure A.6: 45 bar Propagators of C_2F_6 at T_{fluid} = 21 °C and $T_{surr.}$ = 21 °C for a) sPGSE and b) dPGSE.

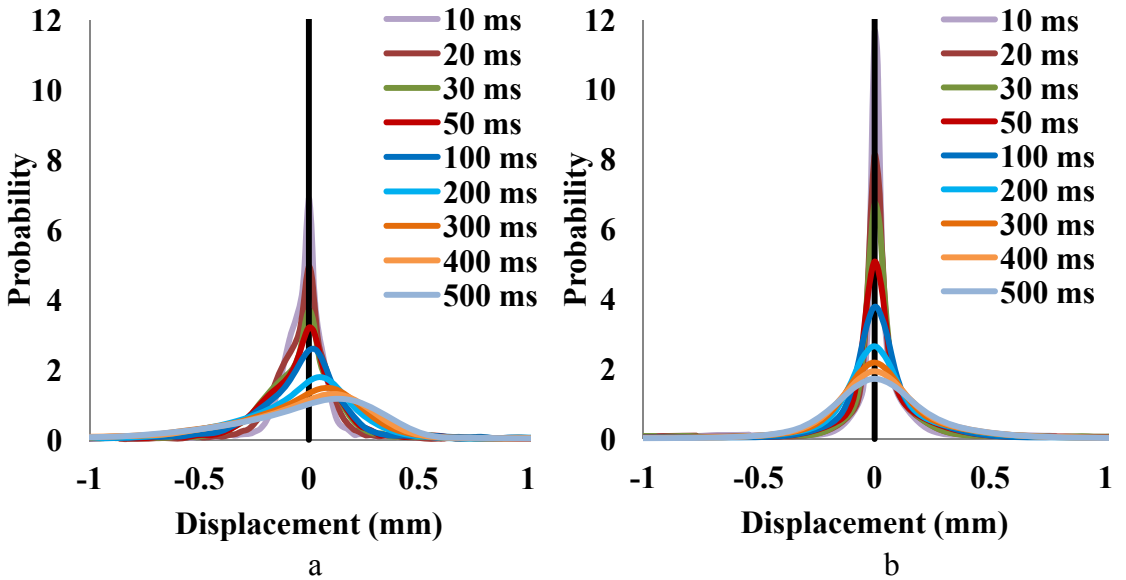

Figure A.7: 70 bar Propagators of C_2F_6 at T_{fluid} = 21 °C and $T_{surr.}$ = 21 °C for a) sPGSE and b) dPGSE.

The data of the propagators for all pressures was reanalyzed and plotted for signal attenuation vs. the Stejskal-Tanner correction for the *q*-vector (Figure A.8 - Figure A.12). This gives a simple formulation to quantitatively show the diffusion of the sample revealed by the slope of the lines plotted for each observation time.

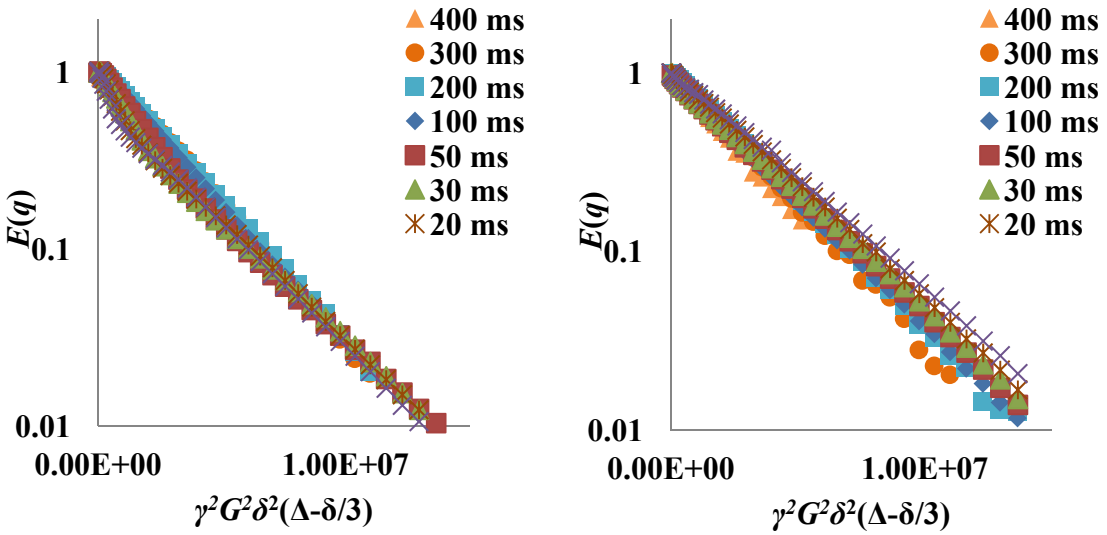

Figure A.8: 10 bar Stejskal-Tanner diffusion plots of C_2F_6 at T_{fluid} = 21 °C and $T_{surr.}$ = 21 °C for a) sPGSE and b) dPGSE.

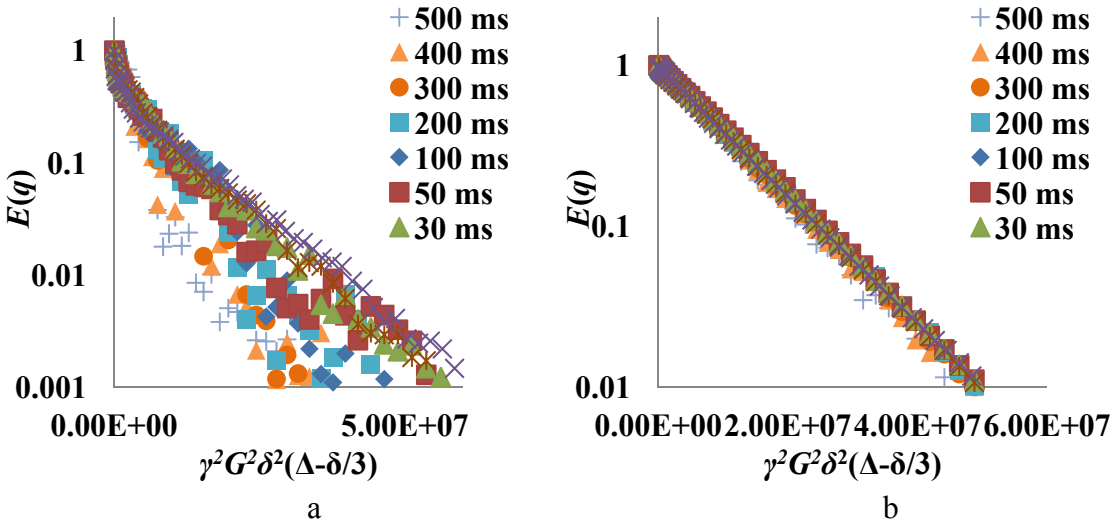

Figure A.9: 25 bar Stejskal-Tanner diffusion plots of C_2F_6 at T_{fluid} = 21 °C and $T_{surr.}$ = 21 °C for a) sPGSE and b) dPGSE.

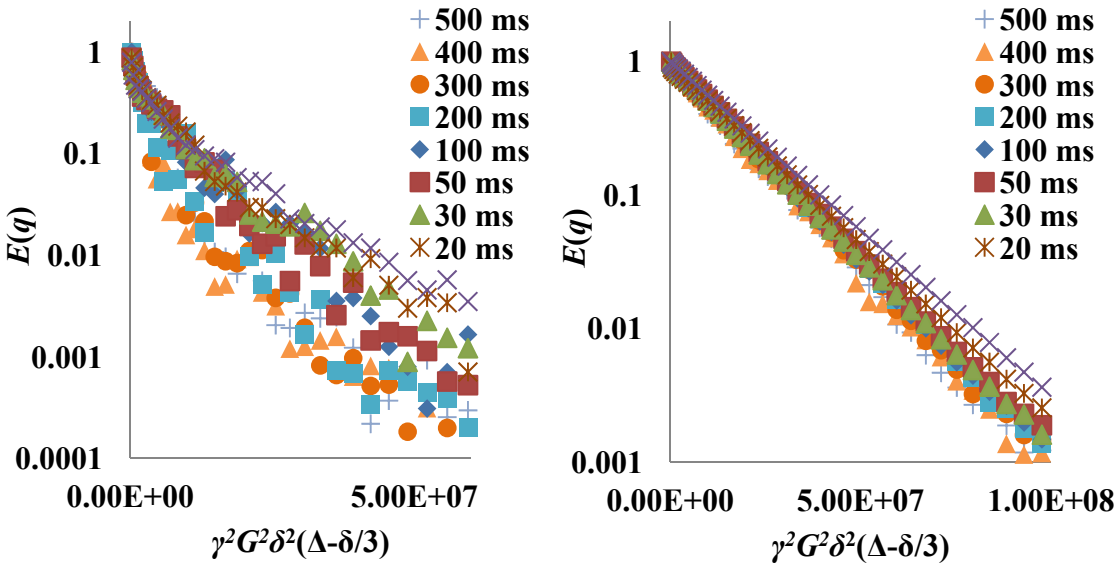

a b

Figure A.10: 29 bar Stejskal-Tanner diffusion plots of C_2F_6 at T_{fluid} = 21 °C and $T_{surr.}$ = 21 °C for a) sPGSE and b) dPGSE.

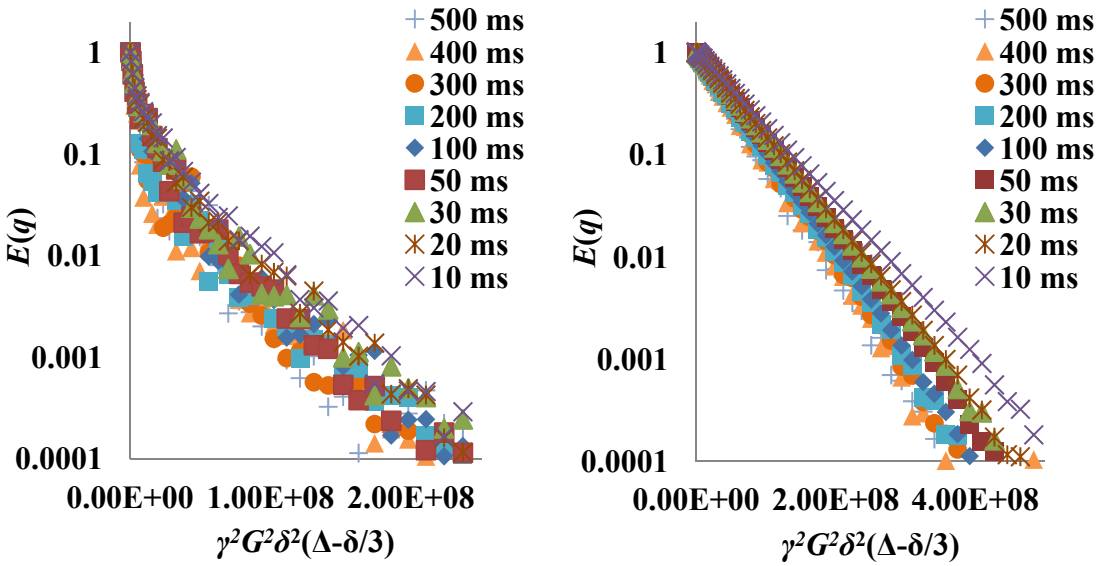

a b

Figure A.11: 45 bar Stejskal-Tanner diffusion plots of C_2F_6 at T_{fluid} = 21 °C and $T_{surr.}$ = 21 °C for a) sPGSE and b) dPGSE.

The diffusion coefficients taken from the slope of the Stejskal-Tanner diffusion plots were then plotted diffusion vs. observation time (Figure A.13 - Figure A.17). This was performed for both sPGSE and dPGSE and plotted against each other. For the sPGSE plots the slow component is labeled 1st and the fast is labeled 2nd.

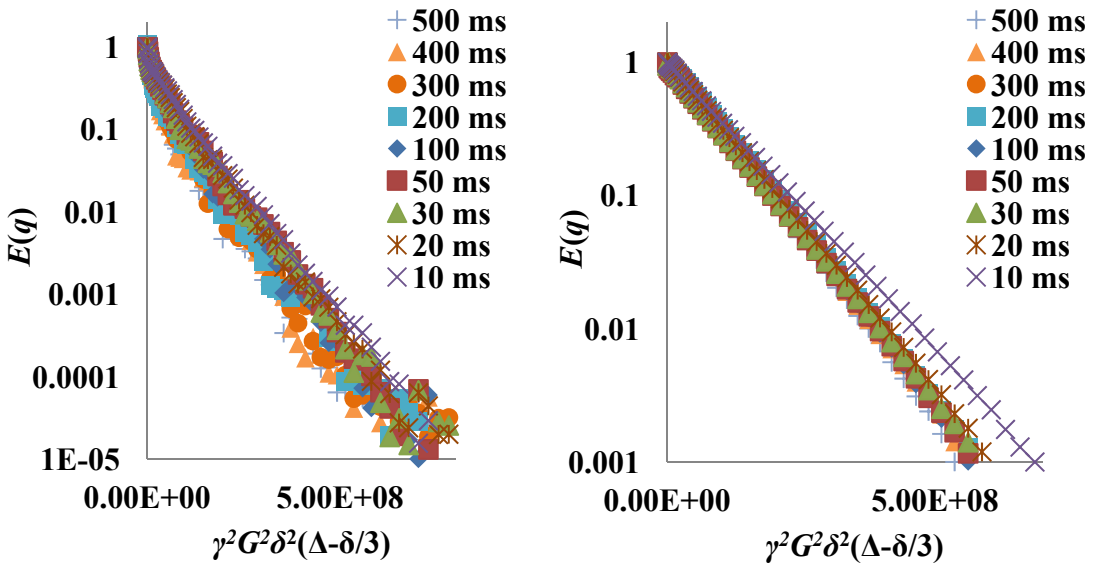

Figure A.12: 70 bar Stejskal-Tanner diffusion plots of C_2F_6 at T_{fluid} = 21 °C and $T_{surr.}$ = 21 °C for a) sPGSE and b) dPGSE.

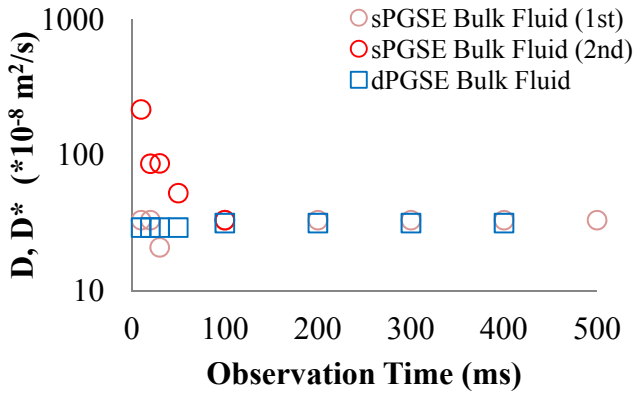

Figure A.13: 10 bar D and D* Coefficient vs. Observation Time

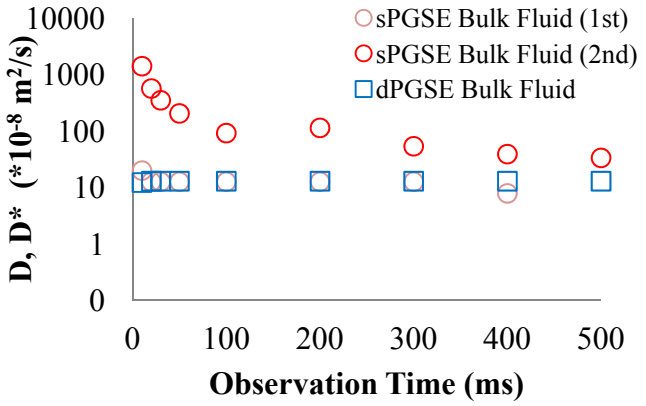

Figure A.14: 25 bar D and D* Coefficient vs. Observation Time

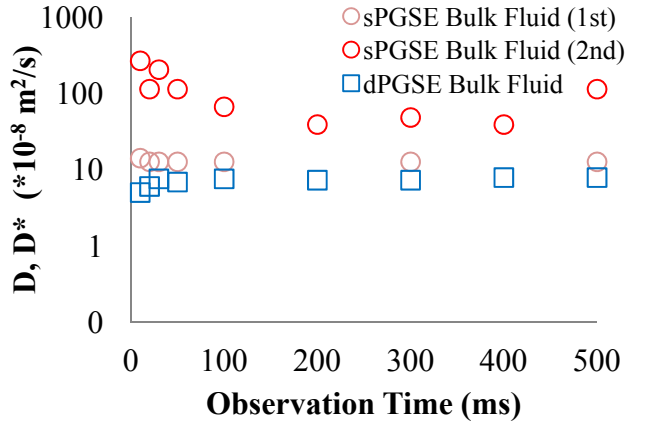

Figure A.15: 29 bar D and D* Coefficient vs. Observation Time

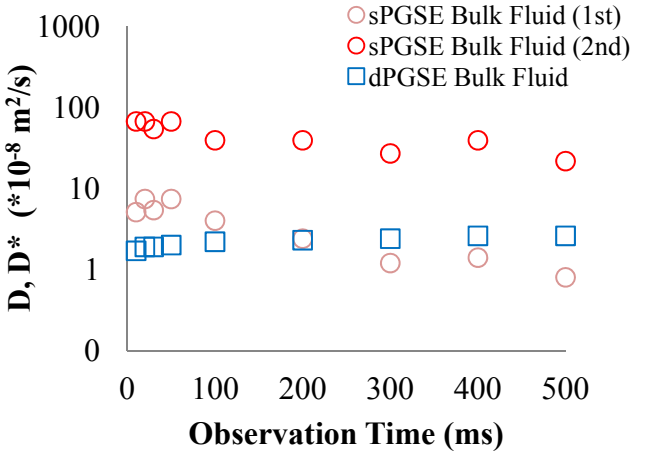

Figure A.16: 45 bar D and D* Coefficient vs. Observation Time

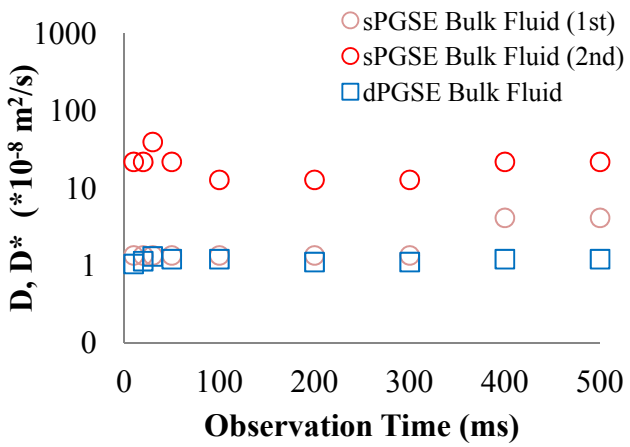

Figure A.17: 45 bar D and D* Coefficient vs. Observation Time

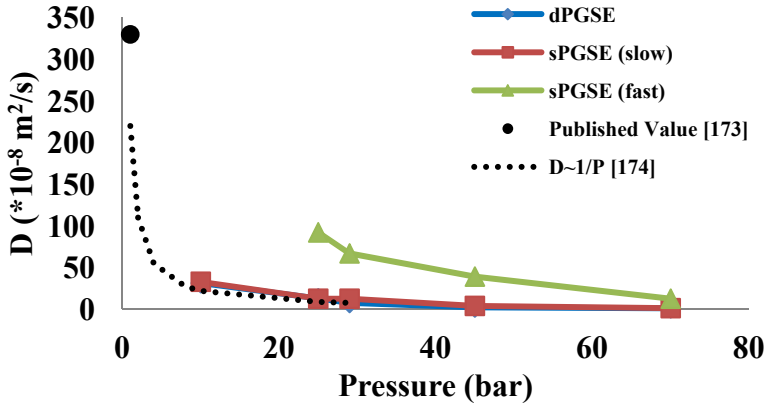

Figure A.18: Diffusion Coefficient vs. Pressure at 100 ms for T_{fluid} = 21 °C and $T_{surr.}$ = 21 °C taken from (Figure A.13 - Figure A.17). A low pressure approximation for diffusion in gases [174] and the value of diffusion for C_2F_6 at atmospheric pressure and room temperature is plotted [173].

A length scale was calculated from the fast component of diffusion for the sPGSE experiments. This was performed for all pressures that had a second component and plotted for each pressure as a function of the square root of the observation time. Plotting length scale vs. the square root of the observation time allows for easier viewing on any asymptotic behavior that can be due to pore restrictions.

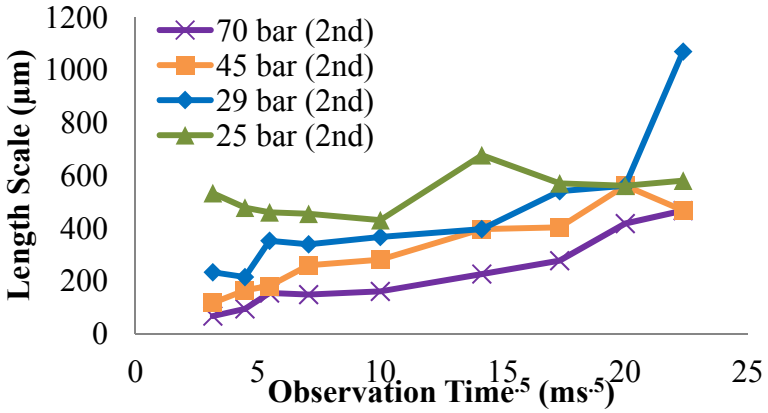

Figure A.19: sPGSE Length Scale vs. Observation Time of the fast diffusion component for T_{fluid} = 21 °C and $T_{surr.}$ = 21 °C.

Statistical Analysis

Statistical analysis was performed on the sPGSE and dPGSE non-flowing propagators for *P* = 10, 25, 29, 45, and 70 bar in bulk fluid corresponding to Figures A.20-A.24. The first four moments were calculated from the propagators, mean displacement (1st), variance (2nd), skew (3rd), and kurtosis (4th). The statistical variables are displayed as a function of displacement observation time Δ.

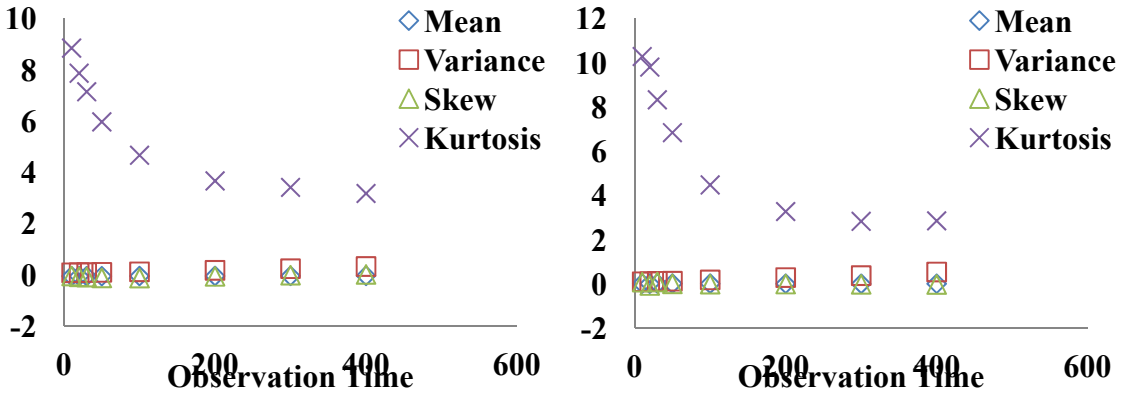

Figure A.20: Statistical analysis on non-flowing bulk fluid propagators at 10 bar for a) sPGSE and b) dPGSE.

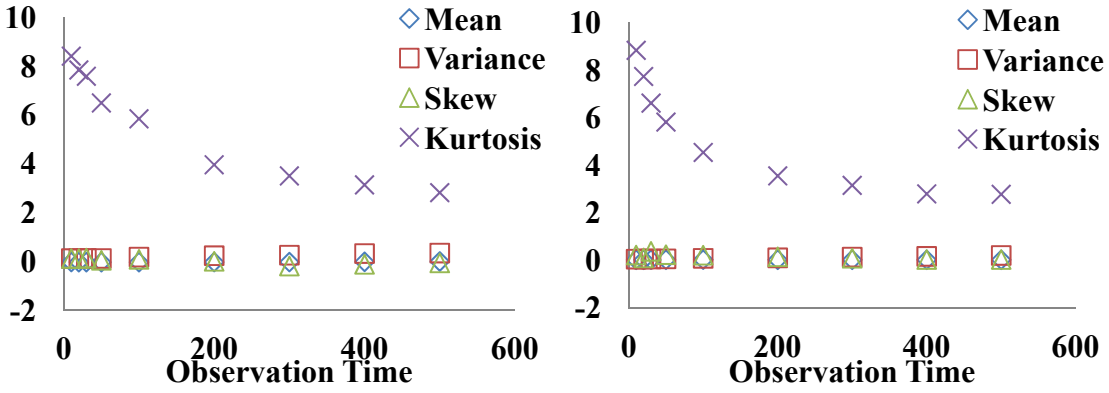

a b

Figure A.21: Statistical analysis on non-flowing bulk fluid propagators at 25 bar for a) sPGSE and b) dPGSE.

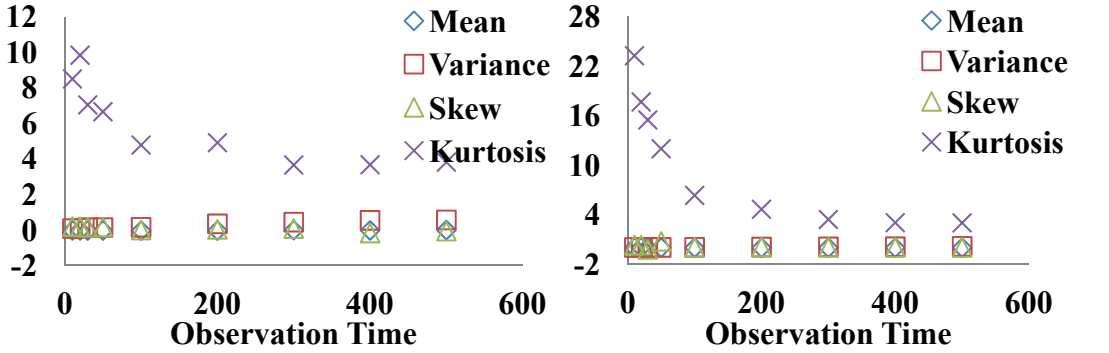

a b

Figure A.22: Statistical analysis on non-flowing bulk fluid propagators at 29 bar for a) sPGSE and b) dPGSE.

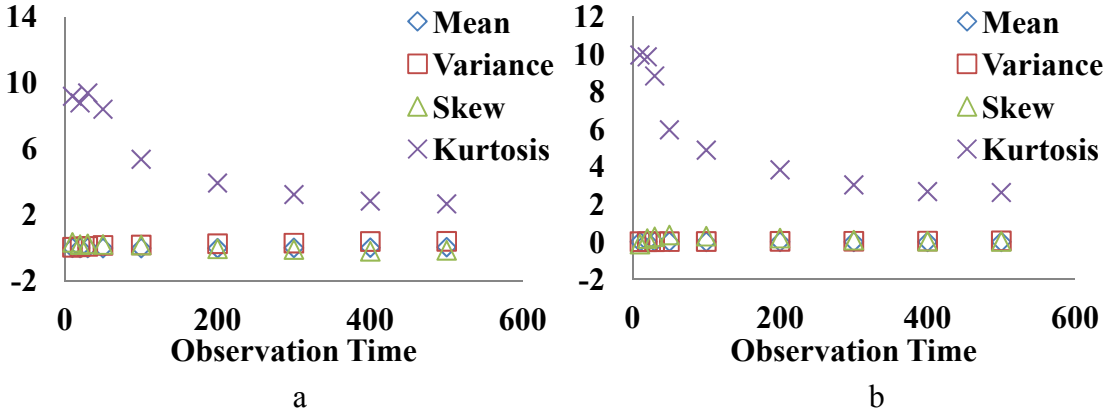

a b

Figure A.23: Statistical analysis on non-flowing bulk fluid propagators at 45 bar for a) sPGSE and b) dPGSE.

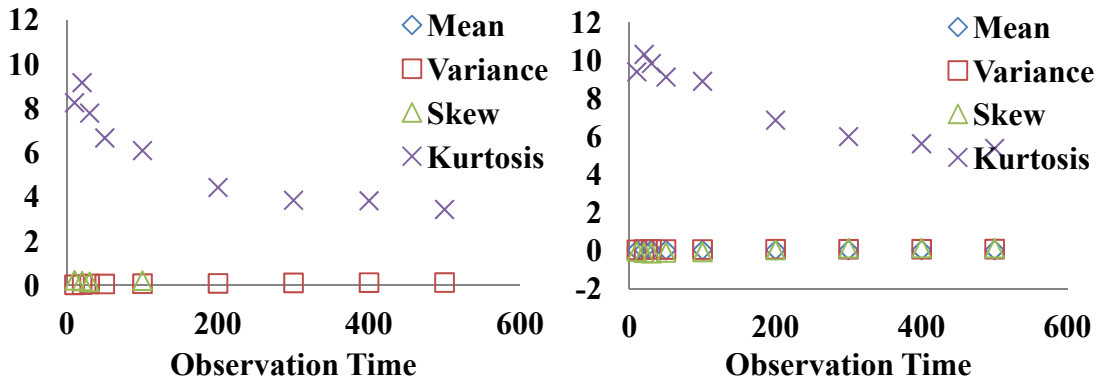

a b

Figure A.24: Statistical analysis on non-flowing bulk fluid propagators at 70 bar for a) sPGSE and b) dPGSE.

Results and Discussion

For no flow of the bulk fluid, two components of motion were present for pressures above 10 bar as was measured by sPGSE experiments. For the dPGSE measurements, only 1 component of motion was present and it matched the slow component observed with the sPGSE experiments (Figure A.18). 10 bar had an insignificant second population in the sPGSE experiments, but for pressures 25 bar and higher the second population was clearly visible (Figure A.13 - Figure A.17). For 25 bar (Figure A.14) the fast component of motion began to merge with the slower component at the longer observation times. The second component of diffusion at 29 bar and higher did not merge with the slower component. This fast component of motion was due to convective cells in the fluid due to minor temperature gradients. The motion is not akin to a diffusion motion because coherent motion is refocused in dPGSE and it was only present in sPGSE experiments. Therefore the motion is more a coherent motion more similar to a

bulk velocity motion. The first or slow component of motion was a diffusive motion and was observed in both sPGSE and dPGSE experiments.

The magnitude of the motion resulting from the cells and the size of the convective cells was a function of pressure (Figure A.13 - Figure A.17 and Figure A.19). The motion was only present for pressures near and above the critical point. The length scale and magnitude of the motion decreased with increasing pressure the farther the pressure was from the critical point. The second motional component for all observation times at the had decreasing magnitude separation from the slower component for increasing pressure indicating that eventually at pressures beyond 70 bar a return to only one component of motion may be occur.

APPENDIX B

SIGNAL PROCESSING AND DATA ANALYSIS NOTES

NMR Imaging

The procedure to process the data for MR imaging is described in this section. After completing the MR experiments on the samples, the data was transferred from the MR control computer to a local computer using a FTD program (WS_FTP95 LE, Ipswitch, Inc.). The data was then imported into Prospa V2.2.5 (Magritek) and analyzed. The process to import the data in Prospa was to select importData in the NMRI menu. After selecting the correct file in the correct working directory select "Paravision-LittleEndian" for the Type (Figure B.1).

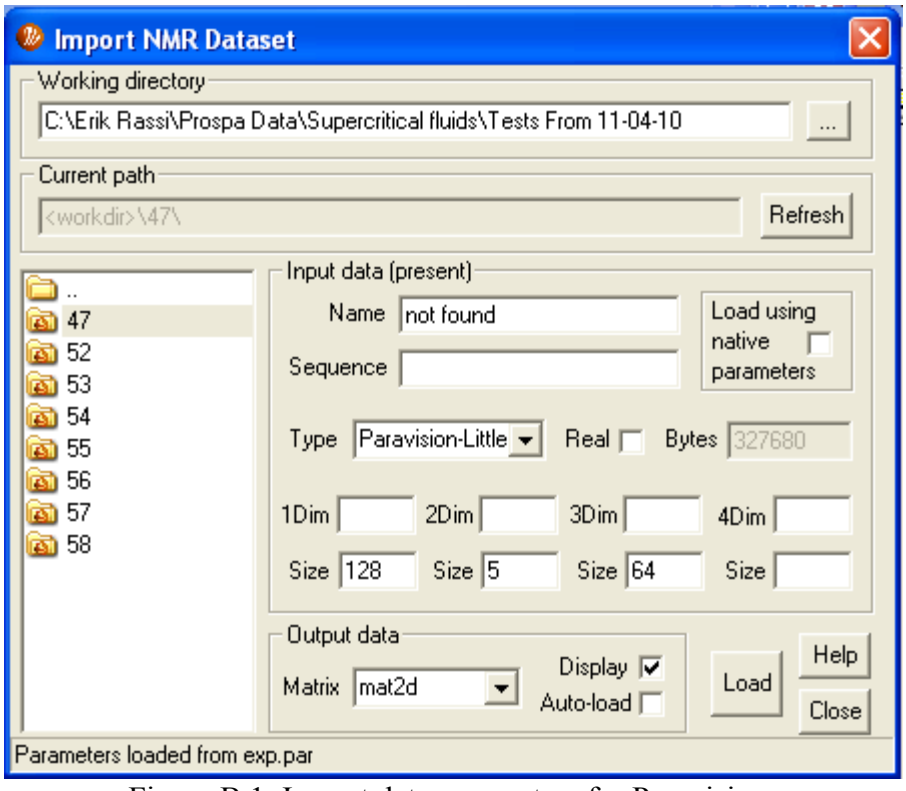

Figure B.1: Import data parameters for Paravision.

The size was input in the order of the x-direction number of points, the number of slices, and the y-direction number of points. The Output data Matrix name was set to the user's

naming convention but defaults to “mat2d.” Press the Load button to load the data. Once the data is loaded, in the Command Line Interface (CLI) transform the data matrix using the syntax A=trans(mat2d,yz). Select “nDFourierTransform” from the NMRI menu. Input the name of the transformed matrix in the “Input Matrix” field (A in this example, (Figure B.2). In the first two “Type” drop down menus “FTEcho” was selected. The last “Type” drop down menu displayed “none”. Magnitude was selected and the “Output Matrix” had a name of “AFt” a width, *w*, of the x-direction number of points (128), *h*, the y-direction number of points (64) and, *d*, the number of slices (5). The “Transform” button was pressed to Fourier transform the data. An example of the resultant image is shown in Figure B.3.

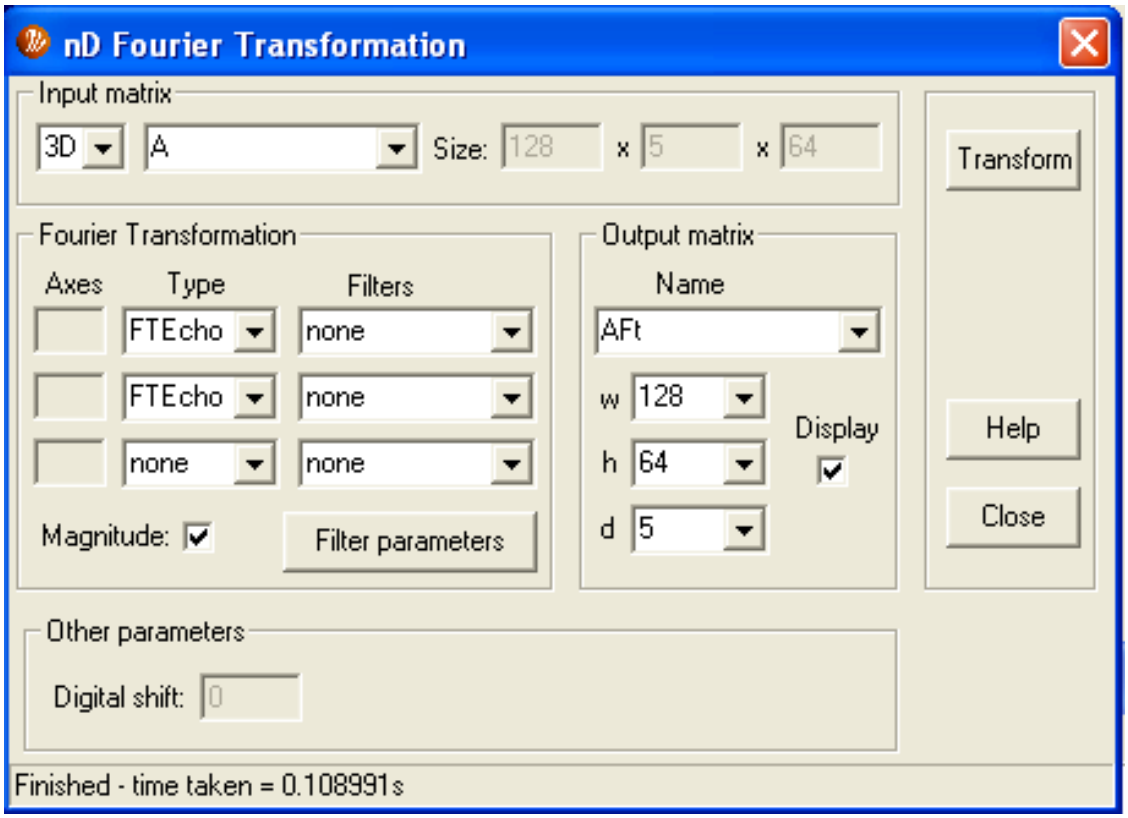

Figure B.2: nDFourier Transformation input box.

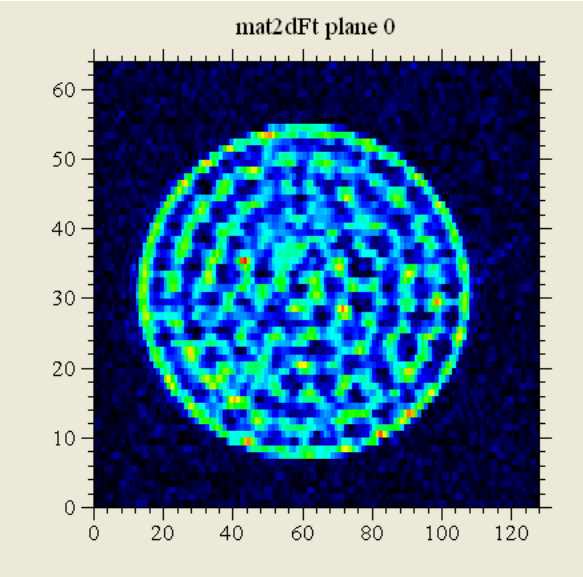

Figure B.3: MR Image Example.

In this example five slices or planes exist and were spaced according to input parameters used when taking the data. To toggle between the slices in Propsa go to the "3D" menu and select "selectPlane3D". Enter the correct 3D matrix name and select the xy button. Then toggle between the planes using the "Plane Position" slider.

One image was then filtered to reduce the noise to 0 magnitude using a custom written macro. The syntax for the code is below (Filter NMR Image Noise.mac):

```
#This program filters a 3D matrix.  For all points below the threshold,
#the magnitude of the point is set to 0.  This is useful in determining
#if a point is data or is noise.  Determine what the threshold should
#be that separates the noise from the signal.  Enter this into the
#"threshold=…" below.  The output matrix will be "A".

A = getplotdata("2d")
# n = column
# m = row
threshold=500000
t=0

for (m=0 to 63)
      for (n=0 to 127)
            if abs(A[n,m]) < threshold
```

```
            A[n,m]=0
            endif

            if A[n,m]>threshold
            t=t+1 #number of real signal points
            endif
      next (n)
next (m)
pr(t)
```

The filtered figure then became **Error! Reference source not found.**:

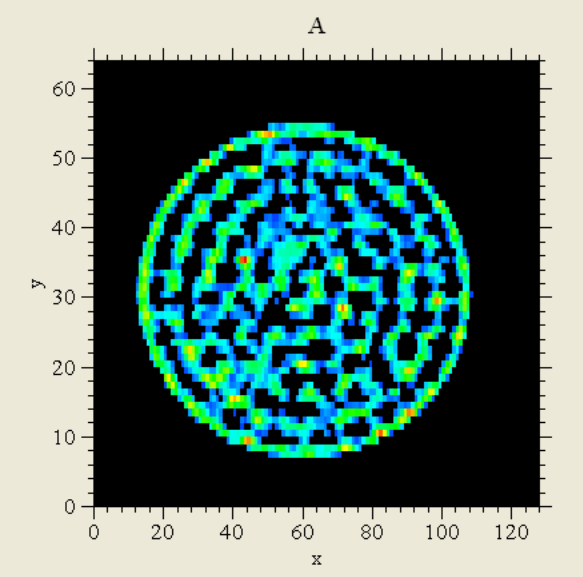

Figure B.4: Filtered MR image.

MR Velocity Imaging

The procedure to process the data for MR velocity imaging is described in this section. The process is identical to the MR Imaging section above up until the Fourier transform box. In the Fourier transform box, the magnitude was not selected for velocity imaging and the *d* is the number of *q*-space planes used to get the velocity data. For this work, 2 planes was used. All other parameters are defined similar to the MR imaging section.

Press the transform button and the image displayed is the resultant phase image of one plane instead of the magnitude image of one plane as was in the MR image. To cycle between the *q*-space planes the "selectPlane3d" under the 3D menu was used. Next, under the NMRI menu select "makeVelocitymap". The "Calculate Velocity Map" box will open (Figure B.5).

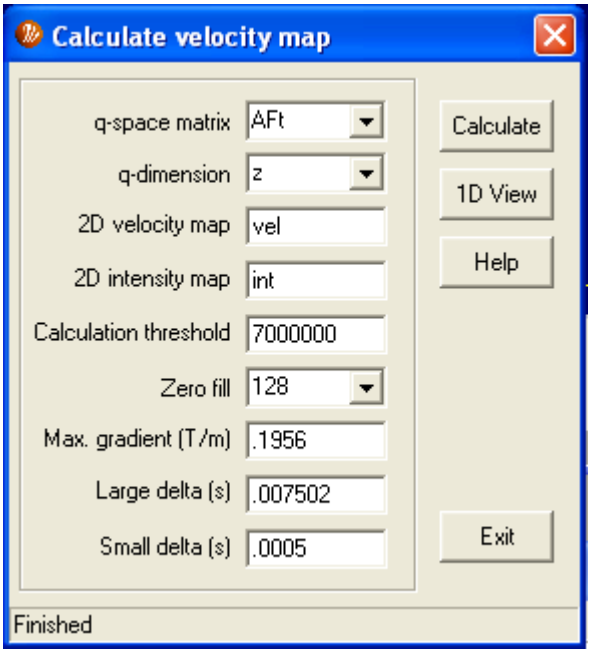

Figure B.5: Calculate Velocity Map Box.

The calculate velocity map macro takes the 2 *q*-space planes and determined the phase shift between each corresponding pixel in the planes. This phase shift was then used to determine the velocity per each pixel. This was correctly done in the calculate velocity map box, by typing in the correct Fourier transformed matrix name, the correct dimension of which the velocity map data was taken in the MR machine. The 2D velocity map and 2D intensity map matrix name was defined as desired although the intensity map was not used for this project. A threshold was entered to filter out the

noise. All values below the threshold are reduced to 0. The maximum gradient is the percentage of the flow encoding gradient used times 2. For instance, the AVANCE 300 had a maximum magnetic field gradient of 1.48 T/m. The flow encoding gradient in a velocity sequence is set to a percentage of this, for example 6.61%. The max. gradient entered for the velocity map calculation is 2 x .0661 x 1.48 T/m= .1956 T/m. The large delta is the flow encoding gradient separation time and the small delta is the flow encoding gradient pulse time. Once all the parameters were entered, the calculate button was pressed and the velocity map was displayed (Example in Figure B.6). The velocity map was then shifted using the "shiftRotate2D" function in the 2D menu.

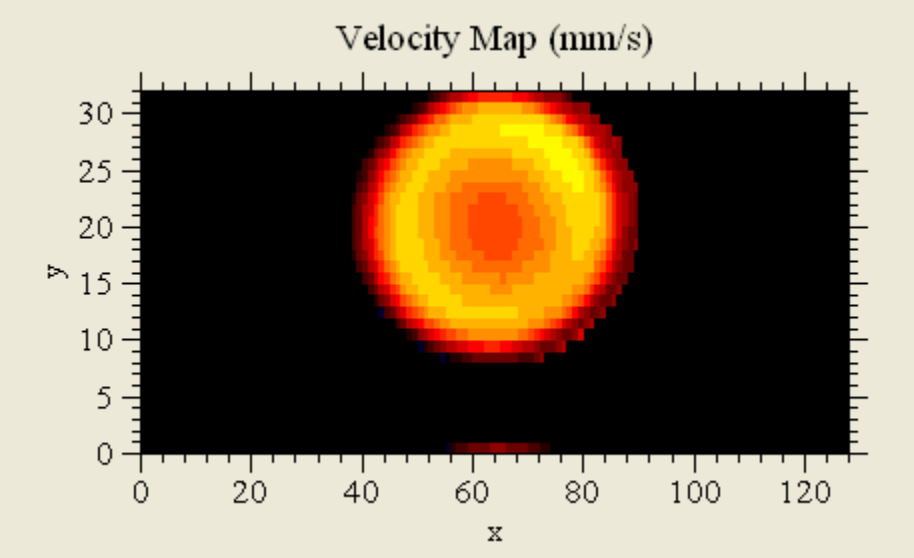

Figure B.6: Example Velocity Map.

MR Propagator

The procedure to process the data for MR propagators is described in this section. Once a s-PGSE or a d-PGSE sequence was completed in was transferred to a local computer using the FTD program discussed in the MR imaging section. The data was then

imported into Prospa by selecting the importData under the NMRI menu. The "LittleEndian" under the type drop down menu was selected (Figure B.7). The size of the matrix was the number of acquisition points in each FID (512), the number of FID or gradient steps, *G* (128), and 1 plane that the data was contained in. The matrix was defined as desired (mat1d) and the "load" button was pressed. For a s-PGSE or a d-PGSE sequence that was completed in Paravision the data was displayed unorganized as Figure B.8 is an example of. A s-PGSE or a d-PGSE sequence that was completed in Topspin was displayed organized and the following reordering data step can be ignored.

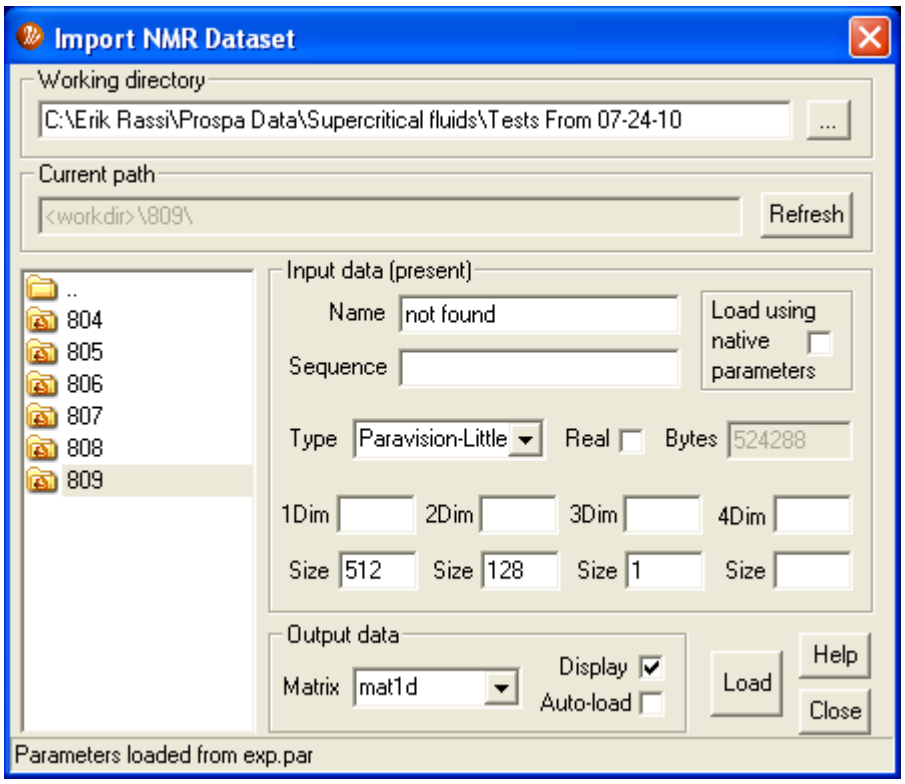

Figure B.7: Importing Propagator data into Prospa.

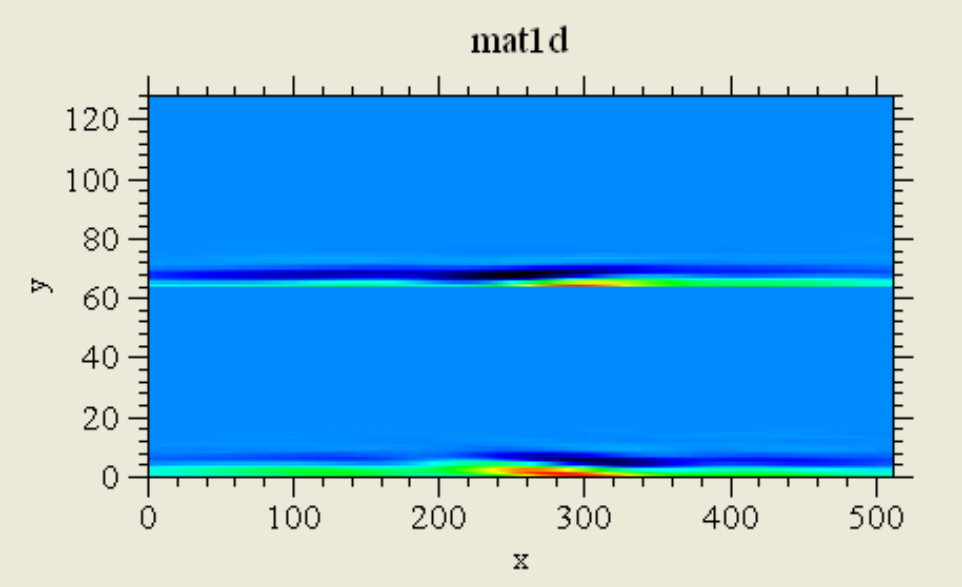

Figure B.8: Unorganized Paravision data before Fourier Transform.

To reorder the Paravision propagator data the following macro was used:

```
#######################################################
#                 Organise2dProp.mac
#
# Reorganise the positive and negative gradient values.
#
# Author: S Codd
#
#######################################################


procedure(Organise2dProp)

   n = :windowdefinition()
   showwindow(n)

endproc()

#######################################################
# Define the dialog to extract the parameters
#######################################################

procedure(windowdefinition)

   # Automatically generated window definition procedure.
   # Any code added manually will be removed if layout modified
interactively
   n = window("Reorganise 2D Propagator", -1, -1, 250, 200)

      # Define all controls with basic parameters
```

```
  statictext(3, 96, 25, "right", "Output Matrix Name")

       textbox(5, 103, 25, 89)



     # Set other control parameters
      setpar(n,5,"name","OutMat",
                  "tab_number",2)

       button(4, 12, 88, 70, 25, "Reorganise",
          :reorganise_data();)

       button(6, 136, 87, 50, 24, "Exit",
          closewindow(0);)


     # Set other control parameters
       setpar(n,4,"mode","default")

endproc(n)


#########################################################
# Reorganise the data
#########################################################

procedure(reorganise_data)

   (m,x,y) = getplotdata("2d")
   if(m == null)
      message("Information","No 2D plot data!")
      return
   endif

   (w,h) = size(m)


   (txt,lx,ly,nc,mode,x1,x2,y1,y2) = 2dpar:get()
   draw2d("false")

m1 = submatrix(m,0,w-1,1,h/2-1)
      m1=(reflect(m1,"horiz"))


m = insert(m,m1, 0 ,1)


OutMat = submatrix(m,0,w-1,2,h-1)
      2dpar:set(txt,lx,ly,nc,mode,x1,x2,y1,y2)
image(OutMat)
   title("Reorganised Prop")
   draw2d("true")
```

```
 assign(getpar(0,5,"text"),OutMat,"global")
endproc()
```

After running the macro and defining the newly reordered matrix, the "nDfouriertransform" was selected under the NMRI menu (Figure B.9). "FTEcho" was selected for both dimensions under the "Type" heading and none was selected for "Filters". The magnitude was selected and the output matrix was defined as desired. The width and height was entered as the same dimensions when the data was loaded initially. The transform button was pressed and a resultant Fourier transform of the data was displayed (Figure B.10). Under the 2D menu the "integrate2Dstrip" function was selected. The mouse button was selected in the "Integrate 2D Strip" box and the window was defined in the 2D plot. The resultant integration of the selected area was displayed in the 1D plot (Figure B.11).

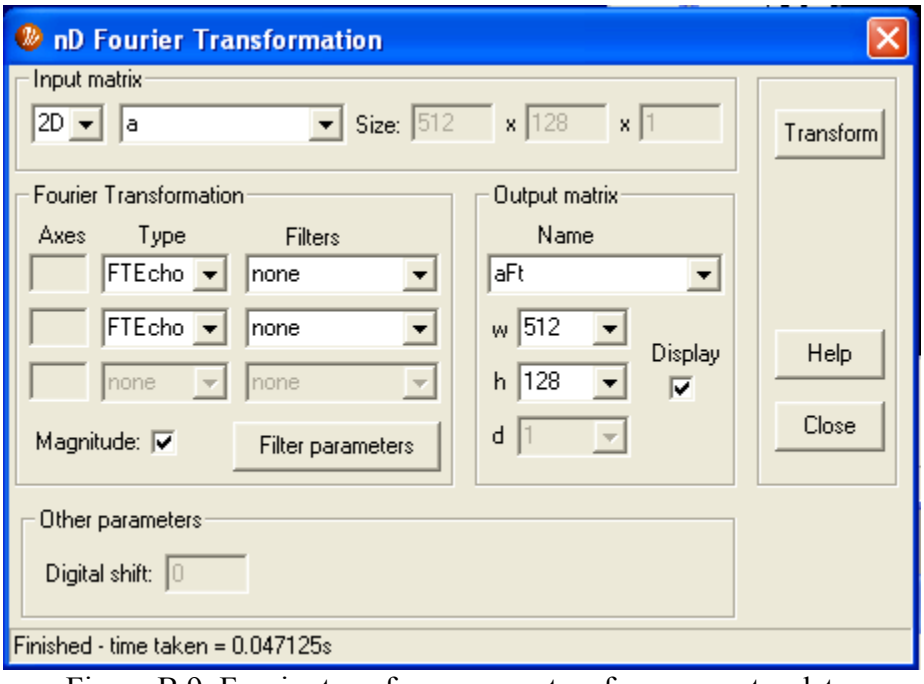

Figure B.9: Fourier transform parameters for propagator data.

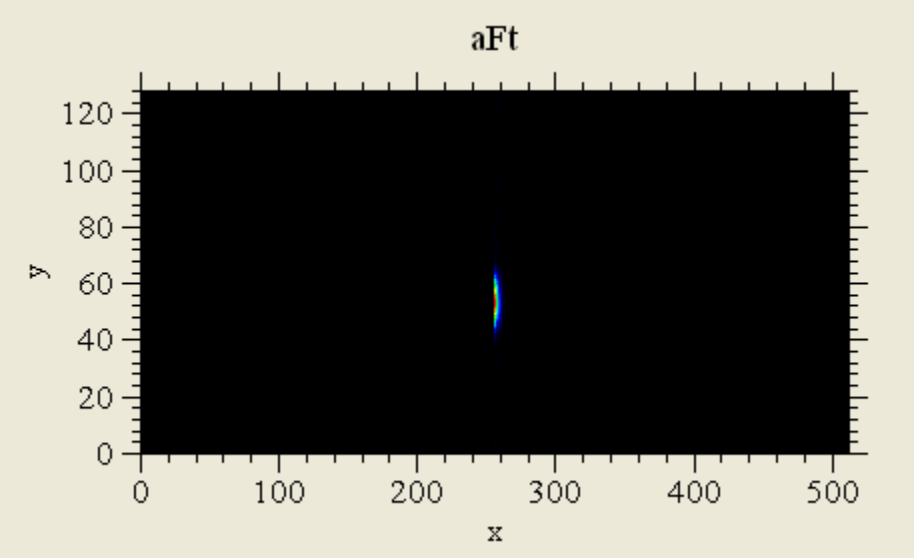

Figure B.10: Resultant plot of Fourier transform of propagator data.

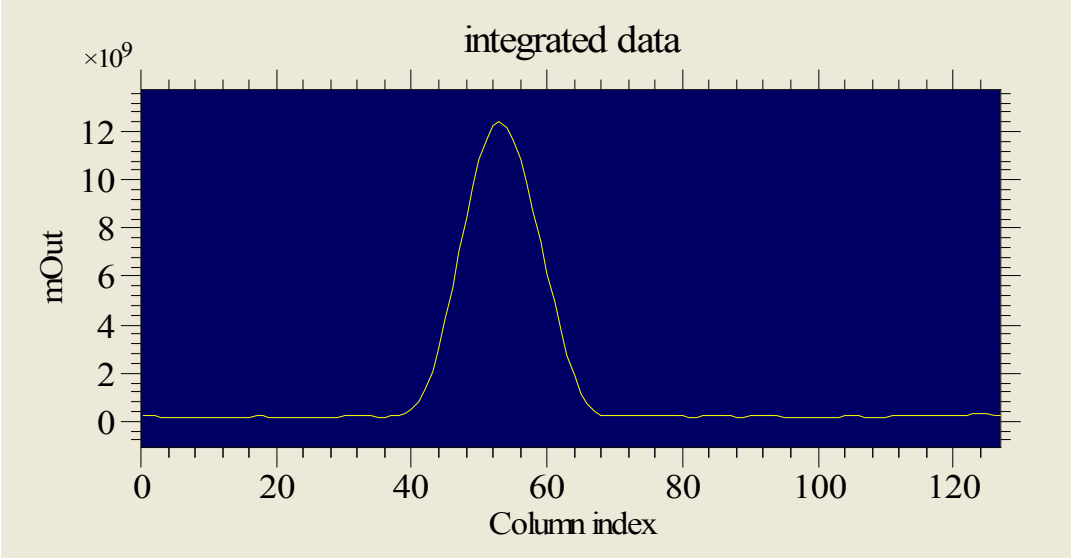

Figure B.11: The full propagator as a function of signal intensity vs. points.

The next step in processing the propagator data was to convert the full propagator from the signal intensity vs. points to the probability of displacement vs. displacement or the probability of velocity vs. velocity. To do this, a macro was run and the syntax is shown below.

```
#####################################################
#                propagator.mac
#
# Takes propagator from the 1D plot window
# (ie: data that was integrated using "integrate2dstrip"
# and plots against velocity or displacement
#
#
#####################################################

procedure(propagator)
   n = :windowdefinition()
   showwindow(n)

endproc()
#####################################################
# Define window
#####################################################

procedure(windowdefinition)

   # Automatically generated window definition procedure.
   # Any code added manually will be removed if layout modified
interactively
   n = window("Plot Propagator", -1, -1, 315, 562)

      # Define all controls with basic parameters
       windowvar(parlist.win)
       statictext(1,113, 26, "right", "Max gradient (T/m)")
       textbox(2, 121, 23, 71)
       statictext(3, 113, 68, "right", "Small delta (sec)")
       textbox(4, 121, 65, 71)
       statictext(5, 113, 110, "right", "Big delta (sec)")
       textbox(6, 121, 107, 71)
       statictext(7, 113 ,374, "right", "Normalized Prop")
       textbox(8, 121, 371, 71)
       button(9, 215, 128, 57, 26, "Exit",
# The load_control_values and save_control_values lines
# are used when you want to save and load parameters
# from an input matrix data file.  Don't do this in
# this program.
#         :save_control_values(getpar(0,2,"text"));
          closewindow(0);)
       button(10, 215, 18, 57, 26, "Calculate",
#          :save_control_values(getpar(0,2,"text"));
          :calculate();)
       statusbox(11)
       button(12, 215, 73, 57, 26, "Help",
          :showhelp();)
       radiobuttons(13,60, 185, 20, "vertical", "disp,vel","disp")
       statictext(14, 96, 185,"left","Displacement (mm)")
       statictext(15, 96, 205,"left","Velocity (mm/s)")
       groupbox(16, "", 5, 2, 205, 151)
       groupbox(17, "  Xaxis  ", 5, 160, 205, 80)
```

```
        groupbox(18," Output Matrices ",5, 350, 205, 151)
        statictext(19,113, 416,"right","Displacement")
        textbox(20, 121, 413,71)
        statictext(21,113,458,"right","Velocity")
        textbox(22, 121, 455,71)
        groupbox(23,"Normalization Integration Limits", 5,245,205,100)
        statictext(24, 113,269,"right","x1 (mm/s)")
        textbox(25,121,264,71)
        statictext(26,113,311,"right","x2 (mm/s)")
        textbox(27,121,308,71)

        setpar(n,8,"text","prop")
        setpar(n,20,"text","mm")
        setpar(n,22,"text","mms")
        setpar(n,25,"text","-100")
        setpar(n,27,"text","100")

endproc(n)


#####################################################
# Get the 1D plot data
#####################################################

procedure(calculate)
setpar(0,11,"text","Processing ...")
# Pull the integrated data off the 1D plot

   (x,prop) = getplotdata("1d","current")
   if(prop == null)
      message("Information","No 1D plot data!")
      return
   endif
   (w,h) = size(prop)

# Get all the gui parameters, ie: gmax, bigdel, lildel

gmax = getpar(0,2,"value")
ldel = getpar(0,4,"value")
bdel = getpar(0,6,"value")
x1 = getpar(0,25,"value")
x2 = getpar(0,27,"value")

# Generate the displacement and velocity vectors

mm = matrix(w)
      gradinc=gmax/(w/2)
      alpha=2.675E8
      qinc=alpha*ldel*gradinc/(2*pi)
   for  (q = 0 to w-1)
      mm[q] =((q-(w/2))/w)*(1/qinc)*1000
   next(q)
mms = matrix(w)
   for (t = 0 to w-1)
```

```
     mms[t] = (((t-(w/2))/w)*(1/qinc)*1000)/bdel
   next(t)

# Normalizes the propagator
# ie: area under the curve = 1
   sc = 1/(integvector(mms,prop,x1,x2))
   nprop = prop*sc
type = getpar(0,13,"text")
if (type == "disp")
   draw1d("false")
   plot(mm,nprop)
   xlabel("Displacement (mm)")
   draw1d("true")
elseif (type == "vel")
   draw1d("false")
   plot(mms,nprop)
   xlabel("Velocity (mm/s)")
   draw1d("true")
endif

# Assigning global variables, ie: so prop saved
# as a matrix in workspace
# Also connecting name in window with data set

     assign(getpar(0,8,"text"),nprop,"global")
     assign(getpar(0,20,"text"),mm,"global")
     assign(getpar(0,22,"text"),mms,"global")
     setpar(0,11,"text","Finished")
endproc()
```

When the program was run, it displayed a box to define the propagator parameters (Figure B.12). The max. gradient was the amplitude percentage used for the maximum displacement gradient. The small delta is the time of the pulse for the PGSE pair and the big delta is the time in between the pulse pair. For the Xaxis, the propagator plot was displayed either against the displacement or the velocity. The other parameters were left in the default values for this project. Once all the parameters were filled, the calculate button was pressed and the 1D graph was displayed with the proper probabilities vs. displacement or velocity (Figure B.13).

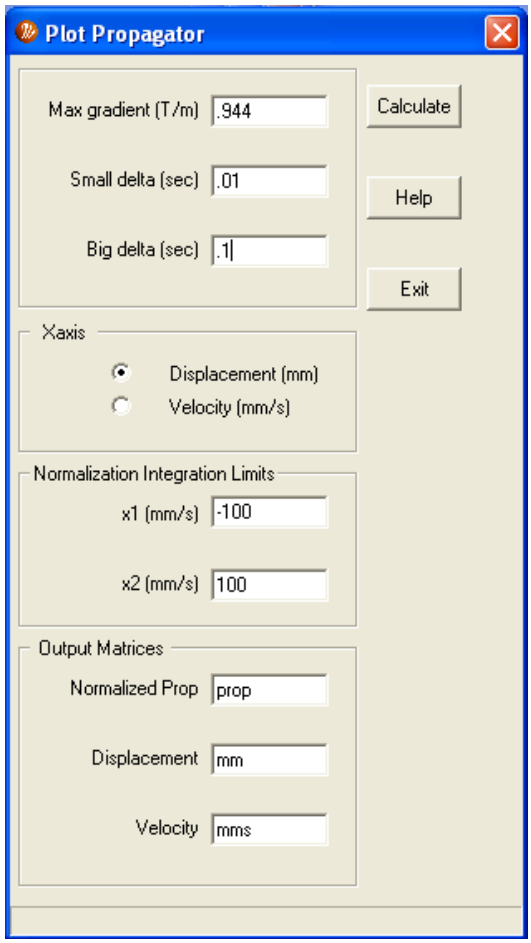

Figure B.12: Propagator parameter inputs.

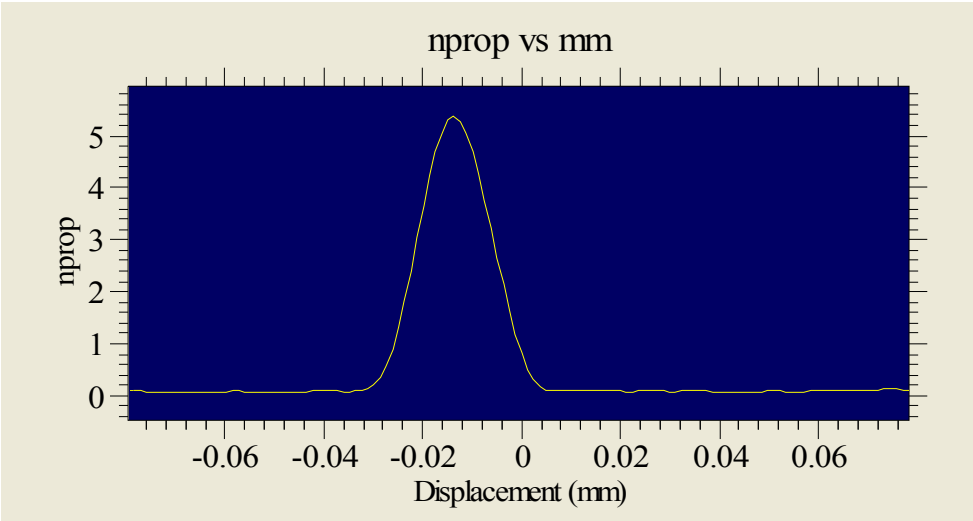

Figure B.13: Full propagator plotted as probability vs. displacment.

MR Topspin Diffusion

The procedure to process the data for MR diffusion and dispersion measurements using Topspin is described in this section. Once the s-PGSE or the d-PGSE sequence was completed in Topspin, the data was then processed in Topspin. These experiments were performed to determine the signal attenuation for a linear function of q. The G steps were taken with a 0 magnetic gradient to a positive gradient where as the full propagator was taken with G steps from –maximum gradient to +maximum gradient. The experiments showed FID attenuation into the noise for either 64 or 128 G steps. The first step was to Fourier transform the data in the second dimension by typing "xf2" in the command line. The next step was to go to the "Analysis" menu and select "T_1/T_2" relaxation. The relaxation module then popped up. In this module, the first step was to extract a slice and the 2nd FID was input. Next, the "Peak/Ranges" button was selected and the manual integration was selected. The mouse was then used to click and drag a 2D area across the peak. Once selected, the save icon was pressed and the export regions option was chosen. The next step was to click again on the "Peak/Ranges" button and then select the "manual peak picking". The down arrow was selected to bring the peak into view and the drag box was centered around the peak. The peak information was then exported by clicking the button left of save and export using the top line in the drop down menu. In the upper right hand corner of the screen, window 1 was selected and then the mouse was clicked on the relaxation window. Select the area button not intensity and then click the fitting function. This gave the diffusion coefficient from the signal attenuation data. In this module the plot parameters were adjusted to plot linearly,

square, or log of the data. Erroneous points were also deleted from individual experiments.

Here is a list of useful commands in Topspin:

Edc = edit copy

Iexpno = increments and clones the previous scan

Diff = runs the diffusion module to enter all important diffusion parameters such as big delta, little delta, # of G steps, and etc.
Gs = runs the test without saving data (similar to GSP in Paravision)
Zg = runs the current test
Multizg = runs a sequential number of experiments
Stop = stops the current test
To shim, with gs running select Spectrometer < accessories < digital lock system or type bsmsdisp in the command line.

MR Prospa Diffusion

The procedure to process the data for MR diffusion and dispersion measurements using Topspin to run the s-PGSE or the d-PGSE sequences, but importing the data into Prospa is described in this section. The data was transferred to a local computer using the FTD program discussed in the MR imaging section. The data was then imported into Prospa by selecting the importData under the NMRI menu. The "LittleEndian" under the type drop down menu was selected. The size of the matrix was the number of acquisition points in each FID (512), the number of FID or gradient steps, *G* (64 or 128), and 1 plane that the data was contained in. The matrix was defined as desired (mat2d) and the "load" button was pressed. For a s-PGSE or a d-PGSE sequence the data looked similar to that in (Figure B.14).

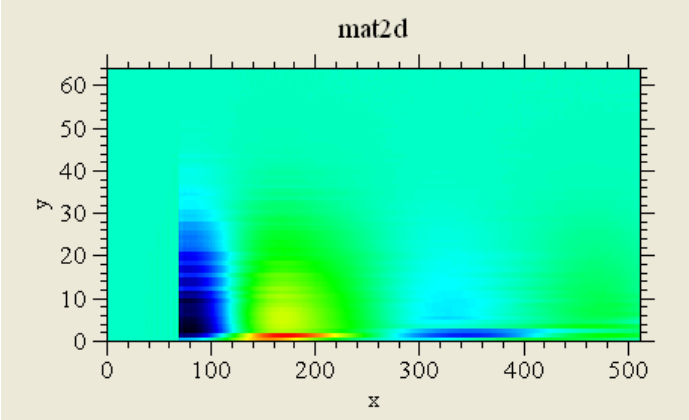

Figure B.1420: Signal attenuation data (before Fourier Transform) for determining diffusion or dispersion coefficient.

The "nDfouriertransform" was then selected under the NMRI menu (Figure B.15). "FTFid" was selected for the first dimension and none was selected for "Filters".

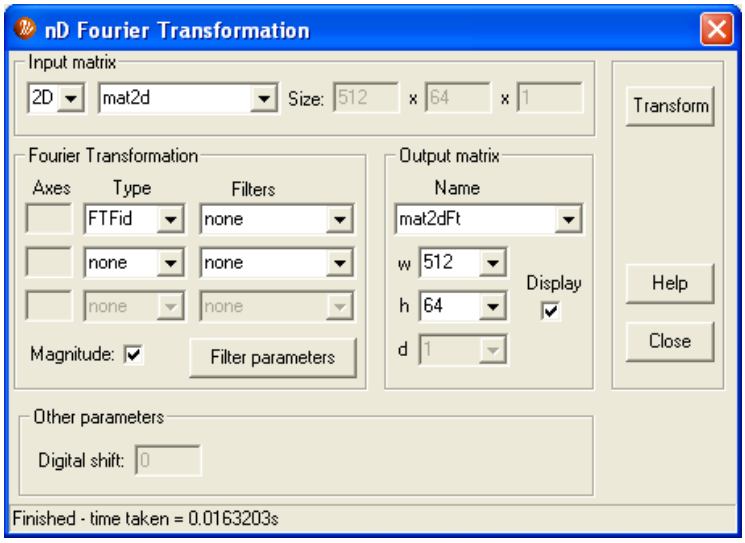

Figure B.15: Fourier transform parameters for signal attenuation data.

The magnitude was selected and the output matrix was defined as desired. The width and height was entered as the same dimensions when the data was loaded initially. The transform button was pressed and a resultant Fourier transform of the data was

displayed (Figure B.16). Under the 2D menu the “integrate2Dstrip” function was selected. The mouse button was selected in the “Integrate 2D Strip” box and the window was defined in the 2D plot.

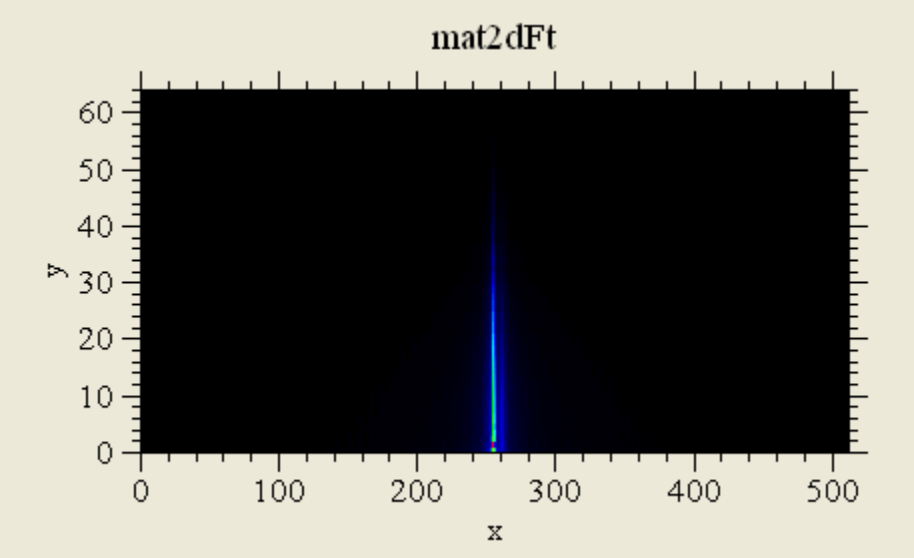

Figure B.16: Resultant plot of Fourier transform of signal attenuation data.

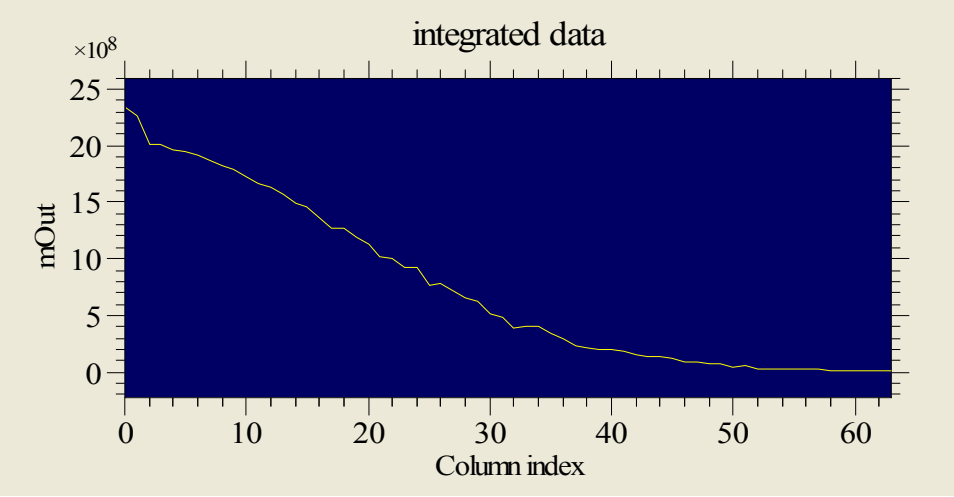

Figure B.17: The signal attenuation as a function of signal intensity vs. points.

The resultant integration of the selected area was displayed in the 1D plot (Figure B.17). The data was then exported using "File < Export Data < 2D" and saved with an appropriate name. The data was then imported into a spreadsheet program and then all the points in the y-direction were normalized to the maximum signal intensity. This normalization was performed for multiple experiments of the same testing conditions and then compared to each other to quantify relative signal attenuation (Figure B.18).

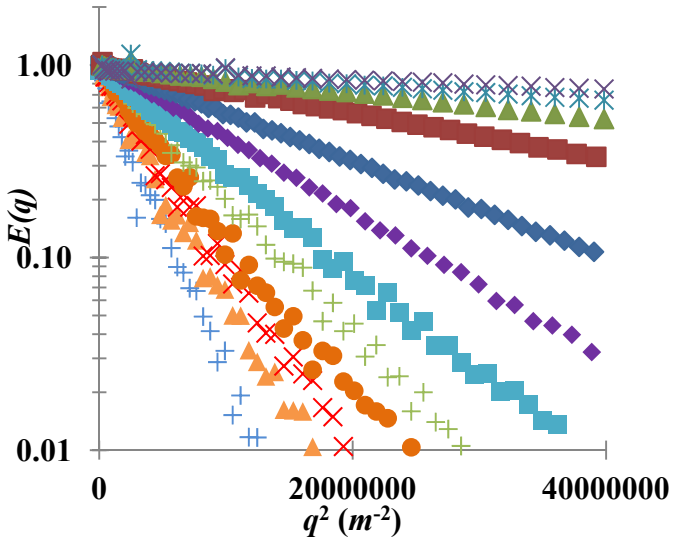

Figure B.18: Normalized signal attenuation for multiple experiments.

MR Relaxation and Diffusion Measurements

The procedure to process the data for MR T_1- T_2, T_2- T_2, and D- T_2 is described in this section. The data was transferred to a local computer using the FTD program discussed in the MR imaging section. The MATLAB program was opened. The "pathtool" command was entered in the command line and the following two folders were uploaded: msutbx and TwoDLaplaceInverse. These two folders contain multiple,

too many to enumerate here, matlab .m files created by Jim E. Maneval that were used in processing the relaxation data of T_1- T_2, T_2- T_2, and D- T_2. The file directory for these programs was C:\Erik Rassi\Matlab\. In matlab the first step was to load in the desired data file that was processed in the "Current Folder" line. Then the command "gett2t2", "gett1t2", or "getDt2" was typed into the command prompt. After going through the full series of questions that the program asked at the command line prompt, the next step was to type "TwoDLaplaceInverse" in the command line prompt. This opened a relaxation and diffusion module where the data was to be plotted. Then the data was imported into this module by loading the data file into the top line next to the button with the same name and loading the appropriate files into the time 1 and 2 positions corresponding to the x and y-axis, respectively (See Figure B.19 for an example).

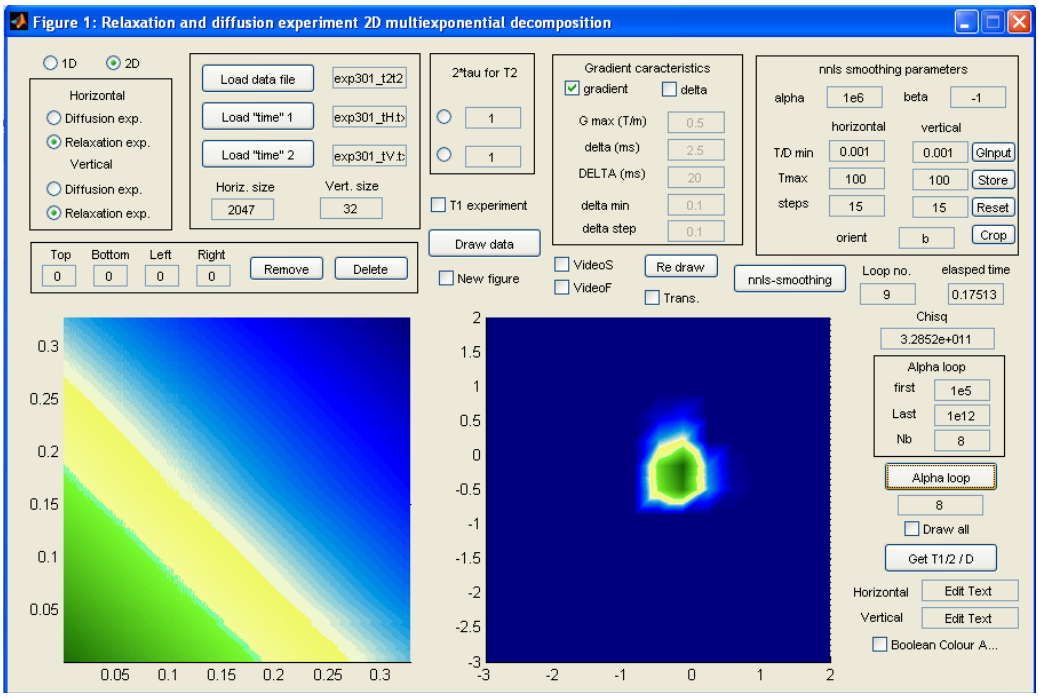

Figure B.19: Normalized signal attenuation for multiple experiments. The Relaxation and diffusion module was used to process T_1- T_2, T_2- T_2, and D- T_2data.

The radio button corresponding to the type of data that was imported was selected, *i.e.* for T_1- T_2 or T_2- T_2 the relaxation exp. was selected for both the horizontal and vertical options. For D- T_2, the diffusion exp. button was selected for the vertical option and the relaxation exp. for the horizontal option. The 2*tau for T_2 was always ignored. Once the data was loaded, the "Draw data" button was pressed and the data was drawn in the figure on the lower left hand corner. The "Gradient Characteristics" box was not used. Next, the "nnls smoothing" button was pressed and the data was drawn in the figure on the lower center graph. This was the T_1- T_2, T_2- T_2, and D- T_2 data with the vertical axis either T_1, T_2, or D and the horizontal axis T_2. The next step was to adjust the alpha loop values to the values shown in Figure B.19 where the box label first and last were 1e5 and 1e12, respectively and Nb was 8. After this, the "Alpha loop" button was pressed and the program ran an error estimation and plotted it similar to Figure B.20.

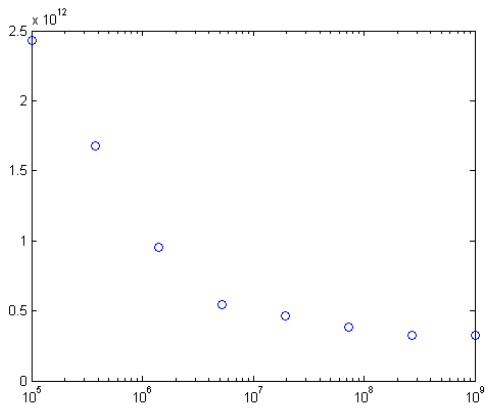

Figure B.20: Normalized signal attenuation for multiple experiments.Alpha loop error estimation plot.

From this graph it was determined with alpha value gave the best precision with the least amount of work. That value was chosen to be the relatively lowest point on the

graph with little change in value between itself and its neighbors (10^8 in this example). This value was then inserted into the "alpha" box under the "nnls smoothing parameters" cage. The steps box under this same cage was adjust to an number to increase resolution of the lower right hand graph. The horizontal and vertical *T/D* max and min were also adjusted if necessary on the "nnls smoothing" button was pressed again to redraw the graph. The "re draw" button and "new figure" option were also pressed if it was desired to have a standalone graph of the same figure separate from the relaxation and diffusion experiment window. The "Get T_1/ T_2/D" button was also pressed if it was desired to get T_1, T_2, or, D information directly off of the graph.